Air-Film Behaviour in an Air-Riding Face Seal



Amir A A M Ibrahim

St. Catherine's College

University of Oxford

A thesis submitted in fulfilment of the requirements for the degree of

Doctor of Philosophy in Engineering Science

Abstract

Increased cycle efficiency and reduced ownership costs of gas turbine engines can be facilitated by improvements in sealing between stationary and rotating engine components. Contacting seals have already improved performance but advanced non-contacting seals offer the possibility of high performance with near-infinite service life. This thesis investigates one potential style of non-contacting face seal which uses a thin film of air to maintain clearance between engine components at all engine operating conditions. Unlike conventional face seals, the seal must be capable of operating with moderate clearances in the order of tens to hundreds of microns and be deployable over large axial movements of several millimetres if it is to operate successfully in the jet engine environment where components are light, flexible and subject to extreme thermal growths. The level of leakage for this seal is intended to be similar to a brush seal at its end of life condition.

The thesis reports experimental analytical and numerical studies of the behaviour of the air-film in the primary sealing gap over a wide range of engine representative conditions. The effect of rotor distortions causing converging and diverging coning are characterised. Experimental pressure distributions are compared to 2D modelling tools based on Reynolds flow equations, used widely to design conventional face seals. These were found to be largely inadequate. High fidelity 3D Commercial CFD however, provided highly accurate predictions of the seal face behaviour, particularly if coupled to mechanical prediction of the distortion of sealing faces under pressure loads. Detailed measurements and modelling of diverging gaps experienced during thermal transients are reported for the first time.

On the basis of these results, a large axial movement prototype face seal was designed and tested. The seal was shown to be capable of running successfully without the addition of a thin, vulnerable to damage, front face typical of gas thrust bearings. A design strategy where passive hydrostatic balancing without the use of biasing springs was seen to be generally successful, although design for

tolerance to circumferential distortions was shown to be vital, as optimisation for leakage with a flat face made the seal liable to touch-down under extreme axial offset conditions. Steady state RANS 3D CFD model provided sufficient resolution to model the seal behaviour showing excellent agreement with experimental testing.

Acknowledgments

I would like to greatly thank my supervisor Prof David Gillespie for allowing me to pursue a DPhil and for his expert and invaluable knowledge, support and guidance throughout.

I would also like to thank my parents Atef and Nadia, and my brother Sameh whom without their unconditional love and support this work would not have been completed.

Thanks to all my friends in the lab, their support and company throughout has made this experience much more enjoyable.

Special thanks to Dr Andrew Owen and Mr Leo Verling for their help with setting up the experimental rig.

Nomenclature

A	Flow area (m^2)
B	Balance Ratio
D	Diameter (m)
Ep	Plastic strain energy (J)
ec	Effective clearance (μm)
F	Force (N)
h	Leakage path gap height (μm)
h_u	Minimum gap height in seal upstream gap (μm)
h_d	Minimum gap height in seal downstream gap (μm)
h_{step}	Radial step height (μm)
h_{coning}	Coning height (μm)
h_{bal}	Measured balance gap height (μm)
h_w	Swash wave amplitude (μm)
h_{avg}	Average gap height (μm)
I	Moment of inertia (kg m^2)
KE	Kinetic energy (J)
L	Leakage path radial length (mm)
M	Mach Number
m	Mass (kg)
$\dot{m}$	Mass flow leakage rate (kg s^{-1})
$\dot{m_{sas}}$	Secondary air system mass flow leakage rate (kg s^{-1})
p	Static pressure (barg – gauge) (bara – absolute)
*p**	Normalised pressure
p_{atm}	Atmospheric pressure (bar)
q_{in}	Heat input (J)
R	Specific gas constant (J kg^{-1} K^{-1})
Re	Reynolds number
Re_h	Reynolds number based on seal gap height

r	Radius (m)
$\|R^*\|$	Non-dimensional overall radial extent of seal
T	Static temperature (K)
t	Disc thickness (m)
U	Surface radial speed (m s^{-1})
u	Radial flow velocity component (m s^{-1})
V	Axial surface speed (m s^{-1})
v	Axial flow velocity component (m s^{-1})
W	Circumferential surface speed (m s^{-1})
w	Circumferential flow velocity component (m s^{-1})
w_c	Work required by compressor (J)
w_t	Work extracted by turbine (J)
$y+$	Wall y plus

Subscripts

u	Upstream
d	Downstream
IN, in	At the inlet plane
step	At the step location
AF	Air-film force
bal	Balance gap
w	Swash wave height
avg	Average

Greek

α	Coning angle (degrees)
ζ	Radial step position as percentage of seal radial length (%)
ε_f	Strain failure

ϕ_1, ϕ_2, ϕ_3	Labels given to characterize three different primary seal faces with varying outer radii
ρ	Density of air (kg m^{-3})
τ	Shear stress (N m^{-2})
ω	Rotational speed (RPM)
θ	Circumferential coordinate (radian)
μ	Dynamic viscosity (Pa s)
ν	Kinematic viscosity (m^2 s^{-1})
σ	Pre-defined offset (mm)
σ_y	Yield Stress (Pa)
σ_{UTS}	Ultimate tensile stress (Pa)
η	Efficiency
γ	Ratio of specific heat capacities

Acronyms

CFD	Computational fluid dynamics
FEA	Finite element analysis
FSI	Fluid-structure Interaction
sas	Secondary air system
HPC	High pressure compressor
HPT	High pressure turbine
IPC	Intermediate pressure compressor
LPC	Low pressure compressor
LPT	Low pressure turbine

Table of Contents

Abstract II
Acknowledgments IV
1 Introduction 1
1.1 Motivation for Seal Research 4
1.2 Existing Sealing Technologies 5
1.3 Primary Research Area 10
1.4 Thesis Content 12
2 Literature Review 14
2.1 Gas Film Lubrication 14
2.1.1 Hydrostatic Lubrication 14
2.1.2 Hydrodynamic Lubrication 20
2.2 Compliant Gas Bearings 27
2.2.1 Compliant Gas Thrust Bearings 27
2.2.2 Compliant Journal Foil Bearings 31
2.3 Self-Acting Face Seal 32
2.4 Compliant Foil Seal 35
2.4.1 Compliant Circumferential Foil Seal 36
2.4.2 Compliant Foil Face Seal 38
2.5 Literature Review Summary 39
3 Validation of Numerical Model against Existing Experimental Data and 3D CFD 42
3.1 The 2D Model 43
3.2 Validation with Experiments for Parallel Gaps With and Without Radial Steps 47
3.3 Numerical Model Validation against 3D CFD Model 54
3.3.1 Geometry and Mesh 54
3.3.2 Turbulence Modelling 56
3.3.3 Material Properties 56
3.3.4 Boundary conditions 56
3.3.5 Convergence Criteria 57
3.4 Results and Discussion 57
3.4.1 Parallel Gaps 58
3.4.2 Converging Coning 64
3.4.3 Diverging Coning 67
3.4.4 Converging coning with a radial step 73
3.4.5 Diverging coning with a radial step 76

3.5 Chapter Summary 82
4 Experimental Setup 85
4.1 Key components 88
4.1.1 Stator assembly 88
4.1.2 Rotor assembly 92
4.2 Instrumentation 94
4.2.1 Pressure measurement 95
4.2.2 Mass flow rate measurement 96
4.2.3 Axial force measurement 96
4.2.4 Temperature 96
4.2.5 Data acquisition and experimental procedure 97
4.2.6 Calibration 97
4.2.7 Uncertainty 98
4.3 Experimental Procedure 98
4.3.1 Determining touch-down location 99
4.4 Dimensional Analysis 104
5 Experimental and Numerical Study of Air-film Behaviour in Converging and Diverging Gaps 107
5.1 Parallel Gaps 108
5.1.1 Experimental Radial Pressure Distributions 108
5.1.2 Parallel Gaps: 3D CFD Radial Pressure Distributions 116
5.2 Converging Gaps 121
5.2.1 Experimental Radial Pressure Distributions 121
5.2.2 Converging Gaps: 3D CFD Radial Pressure Distributions 128
5.3 Diverging Gaps 134
5.3.1 Experimental Radial Pressure Distributions 134
5.3.2 Diverging Gaps: 3D CFD Radial Pressure Distributions 141
5.4 Air-film force behaviour in coned and parallel gaps 148
5.5 Effect of coning on leakage rate 151
5.6 Two-way Fluid-Structure Interaction 156
5.6.1 Two-way FSI: Model Setup 159
5.6.2 Two-way FSI: Results 165
5.7 Chapter Summary 168
6 Design and Testing of Prototype Seal 171
6.1 Key Components 173
6.1.1 Carrier Module 173

6.1.2 Interface Adaptor 174
6.1.3 Front face 175
6.2 Experimental Test Matrix 176
6.2.1 Radial Pressure Distributions 182
6.2.2 Air-film opening force 188
6.2.3 Change in Steady-state Balance Gap Height 190
6.2.4 Air-film Stiffness 191
6.2.5 Leakage rates 193
6.2.6 Swash: Radial pressure distributions 195
6.2.7 Swash: Effect on Air-film Opening Force 202
6.2.8 Swash: Effect on Steady-state Balance Gap Height 206
6.2.9 Swash: Effect on leakage rate 213
6.3 3D CFD Model for Prototype Seal 216
6.3.1 Models Parameters and Boundary Conditions 217
6.3.2 CFD Model Results: Radial pressure distributions and leakage rates 218
6.3.3 CFD Model Results: Rotation-induced Drop in Leakage Rate 222
6.4 Chapter Summary 229
7 Conclusions and Further Work 231
8 References 236
Appendix A 244
Derivation of the Two-dimensional Compressible Reynolds Equation 244
Appendix B 249
Chapters 3 and 5: 3D CFD model Mesh Independence 249
Chapter 6: 3D CFD model Mesh Independence 249

List of Figures

FIGURE 1-1TEMPERATURE –ENTROPY DIAGRAM FOR THE BRAYTON CYCLE 2
FIGURE 1-2: TYPICAL SECONDARY AIR SYSTEM ARCHITECTURE FOR A DOUBLE SPOOL JET ENGINE (CATY, 2012) 3
FIGURE 1-3: TYPICAL SEALING LOCATIONS IN A GAS TURBINE ENGINE, BILL, 1980. 6
FIGURE 1-4: BRUSH SEAL DESIGN, CHUPP ET.AL (2002) 7
FIGURE 1-5: BRISTLES OF A BRUSH SEAL, COURTESY OF TECHNETICS GROUP. 7
FIGURE 1-6: LABYRINTH SEAL FIN CONFIGURATIONS, BURCHAM ET.AL (1979). 8
FIGURE 1-7: TURBINE INTERSTAGE LABYRINTH STEPPED SEAL, LUDWIG ET.AL (1978). 8
FIGURE 1-8: CONVENTIONAL FACE SEAL, BROWN (1984) 9
FIGURE 1-9: PRESSURE BALANCING OF A CONVENTIONAL FACE SEAL, STEINETZ ET.AL (1997) 9
FIGURE 1-10: BALANCED AND UNBALANCED FACE SEALS, METCALFE (1971). 10
FIGURE 1-11: SCHEMATIC OF LARGE-AXIAL MOVEMENT FACE SEAL CONCEPT. 12
FIGURE 1-12: FACE SEAL TYPICAL FORCE BREAKDOWN 12
FIGURE 2-1: BOUNDARY CONDITIONS FOR EQ. 2.2 (LUBBINGE, 1999) 16
FIGURE 2-2 (LUBBINGE, 1999) 17
FIGURE 2-3: RADIAL GAP DISTORTIONS, (LUBBINGE, 1999) 18
FIGURE 2-4: RADIAL PRESSURE FOR CONING ANGLES $\alpha = 0 - 5$. 20
FIGURE 2-5: RADIAL PRESSURE H_{MIN} = 0.1 – 5. 20
FIGURE 2-6: INFINITE SLIDER BEARING, BREWE ET.AL (1997). 20
FIGURE 2-7: PRESSURE VARIATION WITH DISTANCE FROM SHOE, BREWE ET.AL (1997) 22
FIGURE 2-8: LIFT-GENERATING GEOMETRIES, AUSMAN (1964) 22
FIGURE 2-9: TYPICAL WAVINESS PROFILE, LEBECK (1977). 26
FIGURE 2-10: FILM CHARACTERISTICS OF NEAR SINUSOIDAL TWO-HUMPED PROFILE (BATCH AND INY, 1973) 27
FIGURE 2-11: FILM CHARACTERISTICS OF NEAR SINUSOIDAL THREE-HUMPED PROFILE (BATCH AND INY, 1973) 27
FIGURE 2-12: COMPLIANT FOIL THRUST BEARING, DYKAS ET.AL (2009). 28
FIGURE 2-13: COMPLIANT FOIL JOURNAL BEARING, KIM ET.AL (2005). 28
FIGURE 2-14: MECHANISM FOR ATTACHING TOP AND BUMP FOILS, DYKAS ET.AL (2008). 29
FIGURE 2-15: GAS THRUST BEARING AS MANUFACTURED BY DYKAS ET.AL (2008). 29
FIGURE 2-16: GAS THRUST BEARING WITH ORIFICE HOLES FOR HYDROSTATIC PRESSURE AUGMENTATION, LEE ET.AL (2010). 30
FIGURE 2-17: RADIAL BUMP FOIL ARRANGEMENT, LEE ET.AL (2010). 30
FIGURE 3-1: GEOMETRY NOTATION USED TO DEFINE GAP PROFILE. 45
FIGURE 3-2: FLOWCHART SHOWING METHOD OF SOLUTION OF 2D REYNOLD'S FLOW SOLVER. 46
FIGURE 3-3: SELF-CENTRING SEAL LEAKAGE PATH, ONLY UPSTREAM PORTION OF SEAL (HP TO IPC) IS CONSIDERED IN THIS STUDY, AUBRY (2011). 47
FIGURE 3-4: NON-DIMENSIONAL RADIAL PRESSURE DISTRIBUTION, P_{IN} =2.07 BARG, H_{MIN} = 200μM 49
FIGURE 3-5: NON-DIMENSIONAL RADIAL PRESSURE DISTRIBUTION, P_{IN} =3.45 BARG, H_{MIN} = 200μM 49
FIGURE 3-6: ABSOLUTE ERROR (BAR) AND RELATIVE ERROR, P_{IN} =2.07 BARG, H_{MIN} = 200μM 50
FIGURE 3-7: ABSOLUTE ERROR (BAR) AND RELATIVE ERROR, P_{IN} =3.45 BARG, H_{MIN} = 200μM 50
FIGURE 3-8: NON-DIMENSIONAL PRESSURE DISTRIBUTION, P_{IN} =2.07 BARG, H_{MIN} = 50μM 50
FIGURE 3-9: NON-DIMENSIONAL L PRESSURE DISTRIBUTION, P_{IN} =3.45 BARG, H_{MIN} = 50μM 50
FIGURE 3-10: ABSOLUTE ERROR (BAR) AND RELATIVE ERROR, P_{IN} =2.07 BARG, H_{MIN} = 50μM 51
FIGURE 3-11: ABSOLUTE ERROR (BAR) AND RELATIVE ERROR, P_{IN} =3.45 BARG, H_{MIN} = 50μM 51
FIGURE 3-12: NON-DIMENSIONAL RADIAL PRESSURE DISTRIBUTION, P_{IN} =1.03 BARG, H_{MIN} = 200μM, ζ=50%, H_{STEP} = 200μM 53
FIGURE 3-13: NON-DIMENSIONAL RADIAL PRESSURE DISTRIBUTION, P_{IN} =3.45 BARG, H_{MIN} =200μM, ζ=50%, H_{STEP} = 200μM 53
FIGURE 3-14: NON-DIMENSIONAL RADIAL PRESSURE DISTRIBUTION, P_{IN} =1.03 BARG, H_{MIN} = 50μM, ζ=50%, H_{STEP} = 200μM 53
FIGURE 3-15: NON-DIMENSIONAL RADIAL PRESSURE DISTRIBUTION, P_{IN} =3.45 BARG, H_{MIN} =50μM, ζ=50%, H_{STEP} = 200μM 53
FIGURE 3-16: NON-DIMENSIONAL PRESSURE DISTRIBUTION, P_{IN} =0.69 BARG, H_{MIN} =50μM, ζ =50, 75, 90%, H_{STEP} = 100μM 54
FIGURE 3-17: LEAKAGE PATH GEOMETRY, MESH AND BOUNDARY CONDITIONS. 55

FIGURE 3-18: DOMAIN BLOCKING, GREEN BLOCK = LAMINAR. 55
FIGURE 3-19: PARALLEL GAPS RADIAL PRESSURE DISTRIBUTION, P_{IN} =3.07 BAR (ABSOLUTE), H_{MIN} =50μM 58
FIGURE 3-20: PARALLEL GAPS RADIAL PRESSURE DISTRIBUTION, P_{IN} =4.45 BAR (ABSOLUTE), H_{MIN} =50μM 58
FIGURE 3-21: PARALLEL GAPS RADIAL PRESSURE DISTRIBUTION, P_{IN} =2.03 BAR (ABSOLUTE), H_{MIN} =20, 50, 100, 200, 300μM 60
FIGURE 3-22: PARALLEL GAPS RADIAL PRESSURE DISTRIBUTION, P_{IN} =4.45 BAR (ABSOLUTE), H_{MIN} =20, 50, 100, 200, 300μM 60
FIGURE 3-23: PRESSURE CONTOUR SHOWING FLOW SEPARATION AT GAP INLET, H_{MIN} = 200 μM, P_{IN} =2.03 BAR (ABSOLUTE). 60
FIGURE 3-24: PRESSURE CONTOUR SHOWING FLOW SEPARATION AT GAP INLET, H_{MIN} =200 μM , P_{IN} =4.45 BAR (ABSOLUTE). 60
FIGURE 3-25: ABSOLUTE ERROR (BAR) AND RELATIVE ERROR, P_{IN} =2.03 BAR (ABSOLUTE). 61
FIGURE 3-26: ABSOLUTE ERROR (BAR) AND RELATIVE ERROR, P_{IN} =4.45 BAR (ABSOLUTE). 61
FIGURE 3-27: EFFECT OF GAP HEIGHT ON OPENING FORCE. 63
FIGURE 3-28: VARIATION OF AIR-FILM STIFFNESS WITH GAP HEIGHT. 63
FIGURE 3-29: EFFECT OF GAP HEIGHT ON LEAKAGE RATE. 63
FIGURE 3-30: CONVERGING CONING RADIAL PRESSURE DISTRIBUTION, P_{IN} =2.03 BAR (ABSOLUTE), H_{MIN} = 20μM ... 66
FIGURE 3-31: CONVERGING CONING RADIAL PRESSURE DISTRIBUTION, P_{IN} =4.45 BAR (ABSOLUTE), H_{MIN} = 20μM ... 66
FIGURE 3-32: ABSOLUTE ERROR (BAR) AND RELATIVE ERROR, P_{IN} =2.03 BAR (ABSOLUTE), H_{MIN} = 20μM 66
FIGURE 3-33: ABSOLUTE ERROR (BAR) AND RELATIVE ERROR, P_{IN} =4.45 BAR (ABSOLUTE), H_{MIN} = 20μM. 66
FIGURE 3-34: CONVERGING CONING RADIAL PRESSURE DISTRIBUTION, P_{IN} =2.03 BAR (ABSOLUTE), H_{MIN} = 100μM 67
FIGURE 3-35: CONVERGING CONING RADIAL PRESSURE DISTRIBUTION, P_{IN} =4.45 BAR (ABSOLUTE), H_{MIN} = 100μM 67
FIGURE 3-36: ABSOLUTE ERROR (BAR) AND RELATIVE ERROR, P_{IN} =2.03 BAR (ABSOLUTE), H_{MIN} = 100μM. 67
FIGURE 3-37: ABSOLUTE ERROR (BAR) AND RELATIVE ERROR, P_{IN} =4.45 BAR (ABSOLUTE), H_{MIN} = 100μM. 67
FIGURE 3-38: DIVERGING CONING RADIAL PRESSURE DISTRIBUTION, P_{IN} =2.03 BAR (ABSOLUTE), H_{MIN} = 20μM 69
FIGURE 3-39: DIVERGING CONING RADIAL PRESSURE DISTRIBUTION, P_{IN} =4.45 BAR (ABSOLUTE), H_{MIN} = 20μM 69
FIGURE 3-40: DIVERGING CONING RADIAL PRESSURE DISTRIBUTION, P_{IN} = 2.03 BAR (ABSOLUTE), H_{MIN} = 100μM 70
FIGURE 3-41: DIVERGING CONING RADIAL PRESSURE DISTRIBUTION, P_{IN} =4.45 BAR (ABSOLUTE), H_{MIN} = 100μM 70
FIGURE 3-42: DIVERGING CONING RADIAL MACH NUMBER DISTRIBUTION, P_{IN} =2.03, 3.07, 3.76 & 4.45 BAR (ABSOLUTE), H_{MIN} = 100μM, α = -0.5°, CONING HEIGHT = -140 μM. 70
FIGURE 3-43: EFFECT OF CONING ON OPENING FORCE. 71
FIGURE 3-44: EFFECT OF CONING ON AIR-FILM STIFFNESS, AT TWO FIXED MINIMUM GAP HEIGHTS 72
FIGURE 3-45: EFFECT OF CONING ON LEAKAGE RATE. 73
FIGURE 3-46: CONVERGING CONING WITH RADIAL STEPS PRESSURE DISTRIBUTION, P_{IN} =2.03 BAR, H_{MIN} = 100μM, H_{STEP} = 80μM, ζ = -0.3°. 75
FIGURE 3-47: CONVERGING CONING WITH RADIAL STEPS PRESSURE DISTRIBUTION, P_{IN} =4.45 BAR, H_{MIN} = 100μM, H_{STEP} = 80μM, ζ = -0.3°. 75
FIGURE 3-48: EFFECT OF STEP POSITION ON OPENING FORCE, H_{MIN} = 100μM, H_{STEP} = 80μM, α = - 0.3°. 76
FIGURE 3-49: EFFECT OF STEP POSITION ON LEAKAGE RATE H_{MIN} = 100μM, H_{STEP} = 80μM, α = - 0.3°. 76
FIGURE 3-50: DIVERGING CONING WITH RADIAL STEPS PRESSURE DISTRIBUTION, P_{IN} =2.03 BAR, H_{MIN} = 100μM, H_{STEP} = 80μM, α=+0.5°. 80
FIGURE 3-51: DIVERGING CONING WITH RADIAL STEPS PRESSURE DISTRIBUTION, P_{IN} =4.45 BAR, H_{MIN} = 100μM, H_{STEP} = 80μM, α=+0.5°. 80
FIGURE 3-52: DIVERGING CONING WITH RADIAL STEPS: RADIAL MACH NUMBER, P_{IN} =2.03 BAR, H_{MIN} = 100μM,H_{STEP} = 80μM, α = +0.5° 80
FIGURE 3-53: DIVERGING CONING WITH RADIAL STEPS: RADIAL MACH NUMBER, P_{IN} =4.45 BAR, H_{MIN} = 100μM,H_{STEP} = 80μM, α = +0.5°. 80
FIGURE 3-54: EFFECT OF STEP POSITION ON OPENING FORCE H_{MIN} = 100μM, H_{STEP} = 80μM α = 0.5°. 81
FIGURE 3-55: EFFECT OF STEP POSITION ON LEAKAGE RATE H_{MIN} = 100μM, H_{STEP} = 80μM α = 0.5°. 81
FIGURE 4-1: GENERAL LAYOUT OF EXPERIMENTAL RIG AND AIR PRESSURE SYSTEM. 86
FIGURE 4-2: NON-CONTACTING SEALS RIG SCHEMATIC. 87
FIGURE 4-3: SEAL LEAKAGE PATH. 87
FIGURE 4-4: PRESSURE TAPPINGS ARRANGEMENT ON THE FRONT FACE OF THE REMOVABLE PART. 89
FIGURE 4-5: PRESSURE TAPPINGS ARRANGEMENT ON UPSTREAM HOUSING. 90
FIGURE 4-6: PRESSURE TAPPINGS ARRANGEMENT ON DOWNSTREAM HOUSING. 91

FIGURE 4-7: FULLY MODIFIED NON-CONTACTING SEALS RIG. 94
FIGURE 4-8: METHOD 1: LOAD CELL READING. 100
FIGURE 4-9: AXIAL DISPLACEMENT OF DISC UNDER PRESSURE. 101
FIGURE 4-10: MODIFIED ROTATING ASSEMBLY. 102
FIGURE 4-11: LIVE TORQUE READINGS. 103
FIGURE 4-12 104
FIGURE 5-1: GEOMETRY NOTATION FOR PARALLEL GAPS. 109
FIGURE 5-2: EXPERIMENTS, PARALLEL GAPS, RADIAL PRESSURE DISTRIBUTION AT P_{IN}=0.69 BARG. 110
FIGURE 5-3: EXPERIMENTS, PARALLEL GAPS, RADIAL PRESSURE DISTRIBUTION AT P_{IN}=1.03 BARG. 110
FIGURE 5-4: EXPERIMENTS, PARALLEL GAPS, RADIAL PRESSURE DISTRIBUTION AT P_{IN}=3.45 BARG. 110
FIGURE 5-5: SCHEMATIC OF SIMPLE CFD DOMAIN FOR INVESTIGATING EFFECT OF INCREASING CIRCUMFERENCE. 112
FIGURE 5-6: COMPARISON OF 2D AND AXISYMMETRIC (AXI.) CFD SIMULATIONS OF A SIMPLE PARALLEL GAP WITH THE INDICATED UPSTREAM INLET TOTAL PRESSURE, FOR LAMINAR AND TURBULENT FLOW (IN 300MICRON GAP CASES). 112
FIGURE 5-7: COMPARISON OF AVERAGE FACE PRESSURE (A) AND CENTRE OF PRESSURE (B) FOR 2D AND AXISYMMETRIC (AXI.) CFD SIMULATIONS OF A SIMPLE PARALLEL GAP SHOWN IN FIGURE 5-6. 113
FIGURE 5-8: EXPERIMENTS, PARALLEL GAPS, NORMALISED RADIAL PRESSURE DISTRIBUTION AT P_{IN}=3.45 BARG, 0 RPM. 115
FIGURE 5-9: EXPERIMENTS, PARALLEL GAPS, RADIAL PRESSURE DISTRIBUTION AT P_{IN}=3.45 BARG. 115
FIGURE 5-10: CFD, PARALLEL GAP, RADIAL PRESSURE DISTRIBUTION, H_{MIN} =50, P_{IN}=1.03 BARG. 117
FIGURE 5-11: CFD, PARALLEL GAP, RADIAL PRESSURE DISTRIBUTION, H_{MIN} =50, P_{IN}=3.45 BARG. 117
FIGURE 5-12: EXPERIMENTS, PARALLEL GAPS, RADIAL PRESSURE DISTRIBUTION AT P_{IN}=3.45 BARG. 117
FIGURE 5-13: CFD, PARALLEL GAP, RADIAL PRESSURE DISTRIBUTION, H_{MIN} =100, P_{IN}=1.03 BARG. 119
FIGURE 5-14: CFD, PARALLEL GAP, RADIAL PRESSURE DISTRIBUTION, H_{MIN} =100, P_{IN}=3.45 BARG. 119
FIGURE 5-15: CFD, PARALLEL GAP, RADIAL PRESSURE DISTRIBUTION, H_{MIN} =200, P_{IN}=1.03 BARG. 120
FIGURE 5-16: CFD, PARALLEL GAP, RADIAL PRESSURE DISTRIBUTION, H_{MIN} =200, P_{IN}=3.45 BARG. 120
FIGURE 5-17: CFD, PARALLEL GAP, RADIAL PRESSURE DISTRIBUTION, H_{MIN} =300, P_{IN}=1.03 BARG. 120
FIGURE 5-18: CFD, PARALLEL GAP, RADIAL PRESSURE DISTRIBUTION, H_{MIN} =300, P_{IN}= 3.45 BARG. 120
FIGURE 5-19: EXPERIMENTS, PARALLEL GAPS, RADIAL PRESSURE DISTRIBUTION AT P_{IN}=3.45 BARG. 121
FIGURE 5-20: GEOMETRY NOTATION FOR CONVERGING GAPS, UPSTREAM GAP. 122
FIGURE 5-21: EXPERIMENTS, CONVERGING CONING, RADIAL PRESSURE DISTRIBUTION, H_{MIN} =50, P_{IN}=0.69 BARG 124
FIGURE 5-22: EXPERIMENTS, CONVERGING CONING, RADIAL PRESSURE DISTRIBUTION, H_{MIN} =100, P_{IN}=0.69 BARG. 124
FIGURE 5-23: EXPERIMENTS, CONVERGING CONING, RADIAL PRESSURE DISTRIBUTION, H_{MIN} =200, P_{IN}=0.69 BARG. 125
FIGURE 5-24: EXPERIMENTS, CONVERGING CONING, RADIAL PRESSURE DISTRIBUTION, H_{MIN} =50, P_{IN}=2.07 BARG. 126
FIGURE 5-25: EXPERIMENTS, CONVERGING CONING, RADIAL PRESSURE DISTRIBUTION, H_{MIN} =100, P_{IN}=2.07 BARG. 126
FIGURE 5-26: EXPERIMENTS, CONVERGING CONING, RADIAL PRESSURE DISTRIBUTION, H_{MIN} =200, P_{IN}=2.07 BARG. 127
FIGURE 5-27: EXPERIMENTS, CONVERGING CONING, RADIAL PRESSURE DISTRIBUTION, H_{MIN} =50, P_{IN}= 3.45 BARG. 127
FIGURE 5-28: EXPERIMENTS, CONVERGING CONING, RADIAL PRESSURE DISTRIBUTION, H_{MIN} =100, P_{IN}= 3.45 BARG. 127
FIGURE 5-29: EXPERIMENTS, CONVERGING CONING, RADIAL PRESSURE DISTRIBUTION, H_{MIN} =200, P_{IN}=3.45 BARG. 128
FIGURE 5-30: CFD, RADIAL PRESSURE DISTRIBUTION, CONVERGING CONING, H_{MIN}=50μM, P_{IN} = 0.69 BARG. 130
FIGURE 5-31: CFD, RADIAL PRESSURE DISTRIBUTION, CONVERGING CONING, H_{MIN}=100μM, P_{IN} = 0.69 BARG. 130
FIGURE 5-32: CFD, RADIAL PRESSURE DISTRIBUTION, CONVERGING CONING, H_{MIN}=50μM, P_{IN} = 1.03 BARG. 131
FIGURE 5-33: CFD, RADIAL PRESSURE DISTRIBUTION, CONVERGING CONING, H_{MIN}=100μM, P_{IN} = 1.03 BARG. 131
FIGURE 5-34: CFD, RADIAL PRESSURE DISTRIBUTION, CONVERGING CONING, H_{MIN}=50μM, P_{IN} = 3.45 BARG. 131
FIGURE 5-35: CFD, RADIAL PRESSURE DISTRIBUTION, CONVERGING CONING, H_{MIN}=100μM, P_{IN} = 3.45 BARG. 131
FIGURE 5-36: ABSOLUTE ERROR IN NORMALISED RADIAL PRESSURES BETWEEN EXPERIMENT AND CFD PREDICTIONS, α = -0.5°. 133
FIGURE 5-37: : ABSOLUTE ERROR IN NORMALISED RADIAL PRESSURES BETWEEN EXPERIMENT AND CFD PREDICTIONS, α = -1.0°. 134
FIGURE 5-38: GEOMETRY NOTATION FOR DIVERGING GAPS, UPSTREAM GAP. 135
FIGURE 5-39: EXPERIMENTS, DIVERGING CONING, RADIAL PRESSURE DISTRIBUTION, H_{MIN}=50μM, P_{IN}=0.69 BARG. 137
FIGURE 5-40: EXPERIMENTS, DIVERGING CONING, RADIAL PRESSURE DISTRIBUTION, H_{MIN}=100μM, P_{IN}=0.69 BARG. 137
FIGURE 5-41: EXPERIMENTS, DIVERGING CONING, RADIAL PRESSURE DISTRIBUTION, H_{MIN}=200μM, P_{IN}=0.69 BARG. 137
FIGURE 5-42: EXPERIMENTS, DIVERGING CONING, RADIAL PRESSURE DISTRIBUTION, H_{MIN}=50μM, P_{IN}=2.07 BARG. 138
FIGURE 5-43: EXPERIMENTS, DIVERGING CONING, RADIAL PRESSURE DISTRIBUTION, H_{MIN}=100μM, P_{IN}=2.07 BARG. 138

FIGURE 5-44: EXPERIMENTS, DIVERGING CONING, RADIAL PRESSURE DISTRIBUTION, H_{MIN}=200μM, P_{IN}=2.07 BARG. 138
FIGURE 5-45: EXPERIMENTS, DIVERGING CONING, RADIAL PRESSURE DISTRIBUTION, H_{MIN}=50μM, P_{IN}=3.45 BARG. 139
FIGURE 5-46: EXPERIMENTS, DIVERGING CONING, RADIAL PRESSURE DISTRIBUTION, H_{MIN}=100μM, P_{IN}=3.45 BARG. 139
FIGURE 5-47: EXPERIMENTS, DIVERGING CONING, RADIAL PRESSURE DISTRIBUTION, H_{MIN}=200μM, P_{IN}=3.45 BARG. 139
FIGURE 5-48: EXPERIMENTS, DIVERGING CONING, RADIAL PRESSURE DISTRIBUTION, H_{MIN}=50μM, α = +1.0°. 141
FIGURE 5-49: EXPERIMENTS, DIVERGING CONING, RADIAL PRESSURE DISTRIBUTION, H_{MIN}=50μM, α = +2.0°. 141
FIGURE 5-50: EXPERIMENTS, DIVERGING CONING, RADIAL PRESSURE DISTRIBUTION, H_{MIN}=100μM, α = +1.0°. 141
FIGURE 5-51: EXPERIMENTS, DIVERGING CONING, RADIAL PRESSURE DISTRIBUTION, H_{MIN}=100μM, α = +1.0°. 141
FIGURE 5-52: CFD, RADIAL PRESSURE DISTRIBUTION, DIVERGING CONING, H_{MIN}=50μM, P_{IN} = 0.69 BARG. 143
FIGURE 5-53: CFD, RADIAL PRESSURE DISTRIBUTION, DIVERGING CONING, H_{MIN}=100μM, P_{IN} = 0.69 BARG. 143
FIGURE 5-54: CFD, RADIAL PRESSURE DISTRIBUTION, DIVERGING CONING, H_{MIN}=50μM, P_{IN} = 1.03 BARG. 143
FIGURE 5-55: CFD, RADIAL PRESSURE DISTRIBUTION, DIVERGING CONING, H_{MIN}=100μM, P_{IN} = 1.03 BARG. 143
FIGURE 5-56: CFD, RADIAL PRESSURE DISTRIBUTION, DIVERGING CONING, H_{MIN}=50μM, P_{IN} = 2.07 BARG. 145
FIGURE 5-57: CFD, RADIAL PRESSURE DISTRIBUTION, DIVERGING CONING, H_{MIN}=100μM, P_{IN} = 2.07 BARG. 145
FIGURE 5-58: CFD, RADIAL PRESSURE DISTRIBUTION, DIVERGING CONING, H_{MIN}=50μM, P_{IN} = 3.45 BARG. 145
FIGURE 5-59: CFD, RADIAL PRESSURE DISTRIBUTION, DIVERGING CONING, H_{MIN}=100μM, P_{IN} = 3.45 BARG. 145
FIGURE 5-60: CFD, RADIAL AVERAGE MACH NUMBER DISTRIBUTION, DIVERGING CONING, H_{MIN}=50μM, α = +1.0°. 147
FIGURE 5-61: CFD, RADIAL AVERAGE MACH NUMBER DISTRIBUTION, DIVERGING CONING, H_{MIN}=100μM, α = +1.0°. 147
FIGURE 5-62: CFD, RADIAL AVERAGE MACH NUMBER DISTRIBUTION, DIVERGING CONING, H_{MIN}=50μM, α = +2.0°. 147
FIGURE 5-63: CFD, RADIAL AVERAGE MACH NUMBER DISTRIBUTION, DIVERGING CONING, H_{MIN}=100μM, α = +2.0°. 147
FIGURE 5-64: CFD, MASS FLOW RATE THROUGH PRIMARY GAP, DIVERGING CONING, H_{MIN}=50μM AND 100μM, α = +1.0° AND +2.0°. 148
FIGURE 5-65: EXPERIMENTS, CHANGE OF AIR-FILM FORCE WITH CONING ANGLE, MINIMUM GAP HEIGHT AND INLET PRESSURE. 149
FIGURE 5-66: CONTOUR MAP ILLUSTRATING THE CHANGE IN AIR-FILM FORCE F_{AF} WITH THE FULL RANGE OF CONING ANGLES AND MINIMUM GAP HEIGHTS TESTED AT P_{IN}= 0.69 BARG. 151
FIGURE 5-67: CONTOUR MAP ILLUSTRATING THE CHANGE IN AIR-FILM FORCE F_{AF} (N) WITH THE FULL RANGE OF CONING ANGLES AND MINIMUM GAP HEIGHTS TESTED AT P_{IN}= 1.03 BARG. 151
FIGURE 5-68: CONTOUR MAP ILLUSTRATING THE CHANGE IN AIR-FILM FORCE F_{AF} WITH THE FULL RANGE OF CONING ANGLES AND MINIMUM GAP HEIGHTS TESTED AT P_{IN}= 2.07 BARG. 151
FIGURE 5-69: CONTOUR MAP ILLUSTRATING THE CHANGE IN AIR-FILM FORCE F_{AF} WITH THE FULL RANGE OF CONING ANGLES AND MINIMUM GAP HEIGHTS TESTED AT P_{IN}= 3.45 BARG. 151
FIGURE 5-70: METHOD OF BLOCKING PRIMARY SEAL GAP TO CHARACTERIZE LEAKAGE THROUGH SECONDARY SEAL. 153
FIGURE 5-71: EXPERIMENTS, CHANGE OF LEAKAGE RATE WITH CONING ANGLE AND MINIMUM GAP HEIGHT, P_{IN}=0.69 BARG. 154
FIGURE 5-72: EXPERIMENTS, CHANGE OF LEAKAGE RATE WITH CONING ANGLE AND MINIMUM GAP HEIGHT, P_{IN}=1.03 BARG. 154
FIGURE 5-73: EXPERIMENTS, CHANGE OF LEAKAGE RATE WITH CONING ANGLE AND MINIMUM GAP HEIGHT, P_{IN}=2.07 BARG. 154
FIGURE 5-74: CONTOUR MAP ILLUSTRATING THE CHANGE IN LEAKAGE RATE $\dot{M}_{PRIMARY}$ WITH THE FULL RANGE OF CONING ANGLES AND MINIMUM GAP HEIGHTS TESTED AT P_{IN}=0.69 BARG. 156
FIGURE 5-75: CONTOUR MAP ILLUSTRATING THE CHANGE IN LEAKAGE RATE $\dot{M}_{PRIMARY}$ WITH THE FULL RANGE OF CONING ANGLES AND MINIMUM GAP HEIGHTS TESTED AT P_{IN}=1.03 BARG. 156
FIGURE 5-76: CONTOUR MAP ILLUSTRATING THE CHANGE IN LEAKAGE RATE $\dot{M}_{PRIMARY}$ WITH THE FULL RANGE OF CONING ANGLES AND MINIMUM GAP HEIGHTS TESTED AT P_{IN}=2.07 BARG. 156
FIGURE 5-77: CONTOUR MAP ILLUSTRATING THE CHANGE IN LEAKAGE RATE $\dot{M}_{PRIMARY}$ WITH THE FULL RANGE OF CONING ANGLES AND MINIMUM GAP HEIGHTS TESTED AT P_{IN}=3.45 BARG. 156
FIGURE 5-78: SOLUTION ALGORITHM FOR ONE AND TWO COUPLING FSI, BENRA *ET.AL.* 2011. 158
FIGURE 5-79: FLOWCHART OF ANSYS STAGGERED TWO-WAY COUPLING ALGORITHM. 159
FIGURE 5-80: FSI MODEL DOMAIN. 160
FIGURE 5-81:FSI, ROTOR DISC WITH BOUNDARY CONDITIONS HIGHLIGHTED. 162
FIGURE 5-82: RADIAL PRESSURE DISTRIBUTION, CONVERGING CONING, H_{MIN}=50μM, P_{IN} = 1.03 BARG. 166
FIGURE 5-83: RADIAL PRESSURE DISTRIBUTION, CONVERGING CONING, H_{MIN}=50μM, P_{IN} = 2.07 BARG. 166
FIGURE 5-84: RADIAL PRESSURE DISTRIBUTION, CONVERGING CONING, H_{MIN}=50μM, P_{IN} = 2.76 BARG. 166

FIGURE 5-85: RADIAL PRESSURE DISTRIBUTION, CONVERGING CONING, H_{MIN}=50μM, P_{IN} = 3.45 BARG. 166
FIGURE 5-86: FSI, MESH DISPLACEMENT, CONVERGING CONING, H_{MIN}=50μM, α = -0.5°. 167
FIGURE 5-87: ABSOLUTE ERROR IN NORMALISED RADIAL PRESSURES IN CFD AND FSI PREDICTIONS, H_{MIN}=50μM, α = -0.5,° , P_{IN} = 1.03 AND 2.07 BARG. 168
FIGURE 6-1: EMBODIMENT OF THE PROTOTYPE SEAL SHOWING ITS PRIMARY AND SECONDARY LEAKAGE PATHS. 172
FIGURE 6-2: CARRIER MODULE. 174
FIGURE 6-3: INTERFACE ADAPTOR 175
FIGURE 6-4: COMPRESSIVE SPRING PINS. 175
FIGURE 6-5: SPRING PLUG WITH ANCHOR FOR USING TENSION SPRINGS 175
FIGURE 6-6: 3D PRINTED PRESSURE TUBE ADAPTORS. 175
FIGURE 6-7: REAR FACE OF THE SEALING FACE WITH 3D PRINTED PRESSURE ADAPTORS IN PLACE. 175
FIGURE 6-8: COMPLETE PROTOTYPE SEAL ASSEMBLY FRONT FACE SHOWN IN BLUE AND PRESSURE TAPPING BLOCKS IN GREEN. 176
FIGURE 6-9: GEOMETRY NOTATION OF PROTOTYPE SEAL. 179
FIGURE 6-10: RADIAL PRESSURE DISTRIBUTION, Φ_1, P_{IN}=0.69 BARG. 184
FIGURE 6-11: RADIAL PRESSURE DISTRIBUTION, Φ_1, P_{IN}=1.03 BARG. 184
FIGURE 6-12: RADIAL PRESSURE DISTRIBUTION, Φ_1, P_{IN}=2.07 BARG. 184
FIGURE 6-13: : RADIAL PRESSURE DISTRIBUTION, Φ_1, P_{IN}=2.76 BARG. 184
FIGURE 6-14: RADIAL PRESSURE DISTRIBUTION, Φ_2, P_{IN}=0.69 BARG. 185
FIGURE 6-15: RADIAL PRESSURE DISTRIBUTION, Φ_2, P_{IN}=1.03 BARG. 185
FIGURE 6-16: RADIAL PRESSURE DISTRIBUTION, Φ_2, P_{IN}=2.07 BARG. 186
FIGURE 6-17: RADIAL PRESSURE DISTRIBUTION, Φ_2, P_{IN}=2.76 BARG. 186
FIGURE 6-18: RADIAL PRESSURE DISTRIBUTION, Φ_3, P_{IN}=0.69 BARG. 187
FIGURE 6-19: RADIAL PRESSURE DISTRIBUTION, Φ_3, P_{IN}=1.03 BARG. 187
FIGURE 6-20: RADIAL PRESSURE DISTRIBUTION, Φ_3, P_{IN}=2.07 BARG. 187
FIGURE 6-21: RADIAL PRESSURE DISTRIBUTION, Φ_3, P_{IN}=2.76 BARG. 187
FIGURE 6-22: RADIAL PRESSURE DISTRIBUTION, Φ_3, P_{IN}=3.45 BARG. 188
FIGURE 6-23: CHANGE OF AIR-FILM FORCE WITH OFFSET. 189
FIGURE 6-24: CHANGE OF AIR-FILM FORCE WITH BALANCE GAP HEIGHT. 189
FIGURE 6-25: FORCE ON SEAL, Φ_1 190
FIGURE 6-26: FORCE ON SEAL, Φ_3 190
FIGURE 6-27: CHANGE OF BALANCE GAP HEIGHT WITH OFFSET. 191
FIGURE 6-28: AVERAGE SEAL STIFFNESS VS INLET PRESSURE 192
FIGURE 6-29: EFFECT OF OFFSET ON LEAKAGE RATE. 194
FIGURE 6-30: EFFECT OF OFFSET ON LEAKAGE RATE. 194
FIGURE 6-31: EFFECTIVE CLEARANCE CALCULATED AT AN AVERAGE RADIUS OF R = 77.1 MM. 195
FIGURE 6-32: ROTOR WITH KAPTON TAPE SECTORS TO INTRODUCE SWASH. 196
FIGURE 6-33: AMPLITUDE AND PERIOD LENGTH OF SWASH USING KAPTON TAPE SECTORS ON ROTOR. 196
FIGURE 6-34: NO -ADDED SWASH, RADIAL PRESSURE DISTRIBUTION, Φ_3, P_{IN}=0.69 BARG 198
FIGURE 6-35: NO -ADDED SWASH, RADIAL PRESSURE DISTRIBUTION, Φ_3, P_{IN}=1.03 BARG 198
FIGURE 6-36: NO -ADDED SWASH, RADIAL PRESSURE DISTRIBUTION, Φ_3, P_{IN}=2.07 BARG 198
FIGURE 6-37: 3-WAVE SWASH, RADIAL PRESSURE DISTRIBUTION, Φ_3, P_{IN}=0.69 BARG 200
FIGURE 6-38: 3-WAVE SWASH, RADIAL PRESSURE DISTRIBUTION, Φ_3, P_{IN}=1.03 BARG 200
FIGURE 6-39: 3-WAVE SWASH, RADIAL PRESSURE DISTRIBUTION, Φ_3, P_{IN}=2.07 BARG 200
FIGURE 6-40: 5-WAVE SWASH, RADIAL PRESSURE DISTRIBUTION, Φ_3, P_{IN}=0.69 BARG 202
FIGURE 6-41: 5-WAVESWASH, RADIAL PRESSURE DISTRIBUTION, Φ_3, P_{IN}=1.03 BARG 202
FIGURE 6-42: 5-WAVE SWASH, RADIAL PRESSURE DISTRIBUTION, Φ_3, P_{IN}=2.07 BARG 202
FIGURE 6-43: EFFECT OF ROTATIONAL SPEED ON AIR-FILM FORCE, σ = 12 MM, P_{IN} = 0.69 BARG 203
FIGURE 6-44: EFFECT OF ROTATIONAL SPEED ON AIR-FILM FORCE, σ = 12 MM, P_{IN} = 1.03 BARG 203
FIGURE 6-45: EFFECT OF ROTATIONAL SPEED ON AIR-FILM FORCE, σ = 12 MM, P_{IN} = 2.07 BARG 204
FIGURE 6-46: EFFECT OF ROTATIONAL SPEED ON AIR-FILM FORCE, σ = 12 MM, P_{IN} = 2.76 BARG 204
FIGURE 6-47 OPENING, CLOSING AND NET FORCES ON SEAL, 3-WAVE SWASH, σ = 12 MM. 204

FIGURE 6-48: : EFFECT OF ROTATIONAL SPEED AND VARYING OFFSET ON AIR-FILM FORCE, P_{IN} = 0.69 BARG 206
FIGURE 6-49: EFFECT OF ROTATIONAL SPEED AND VARYING OFFSET ON AIR-FILM FORCE, PIN = 2.76 BARGEFFECT OF ROTATIONAL SPEED ON AIR-FILM FORCE, PIN = 2.76 BARG 206
FIGURE 6-50: : EFFECT OF ROTATIONAL SPEED ON MEASURED H_{BAL}, σ = 12 MM, P_{IN} = 0.69 BARG 207
FIGURE 6-51: EFFECT OF ROTATIONAL SPEED ON MEASURED H_{BAL}, σ = 12 MM, P_{IN} = 1.03 BARG 207
FIGURE 6-52: EFFECT OF ROTATIONAL SPEED ON MEASURED H_{BAL}, σ = 12 MM, P_{IN} = 2.07 BARG 208
FIGURE 6-53: EFFECT OF ROTATIONAL SPEED ON MEASURED H_{BAL}, σ = 12 MM, P_{IN} = 2.76 BARG 208
FIGURE 6-54: NO-ADDED SWASH, CONTOUR MAP ILLUSTRATING THE CHANGE IN MEASURED H_{BAL} RATE AT THE FULL RANGE OF OPERATING PRESSURES AND SPEEDS. 209
FIGURE 6-55: 3-WAVE SWASH, CONTOUR MAP ILLUSTRATING THE CHANGE IN MEASURED H_{BAL} RATE AT THE FULL RANGE OF OPERATING PRESSURES AND SPEEDS. 209
FIGURE 6-56: 5-WAVE SWASH, CONTOUR MAP ILLUSTRATING THE CHANGE IN MEASURED H_{BAL} RATE AT THE FULL RANGE OF OPERATING PRESSURES AND SPEED. 210
FIGURE 6-57: EFFECT OF ROTATIONAL SPEED AND VARYING OFFSET ON MEASURED H_{BAL}, P_{IN} = 0.69 BARG 212
FIGURE 6-58: EFFECT OF ROTATIONAL SPEED AND VARYING OFFSET ON MEASURED H_{BAL}, P_{IN} = 1.03 BARG 212
FIGURE 6-59: EFFECT OF ROTATIONAL SPEED AND VARYING OFFSET ON MEASURED H_{BAL}, P_{IN} = 2.07 BARG 213
FIGURE 6-60: EFFECT OF ROTATIONAL SPEED AND VARYING OFFSET ON MEASURED H_{BAL}, P_{IN} = 2.76 BARG 213
FIGURE 6-61: EFFECT OF ROTATIONAL SPEED AND VARYING OFFSET ON LEAKAGE RATE WITH AND WITHOUT ADDED SWASH, σ = 12 MM, P_{IN} = 0.69 BARG 214
FIGURE 6-62: EFFECT OF ROTATIONAL SPEED AND VARYING OFFSET ON LEAKAGE RATE WITH AND WITHOUT ADDED SWASH, σ = 12 MM, P_{IN} = 1.03 BARG 214
FIGURE 6-63: EFFECT OF ROTATIONAL SPEED AND VARYING OFFSET ON LEAKAGE RATE WITH AND WITHOUT ADDED SWASH, σ = 12 MM, P_{IN} = 2.07 BARG 214
FIGURE 6-64: EFFECT OF ROTATIONAL SPEED AND VARYING OFFSET ON LEAKAGE RATE WITH AND WITHOUT ADDED SWASH, σ = 12 MM, P_{IN} = 2.76 BARG 214
FIGURE 6-65: NO-ADDED SWASH, CHANGE IN BALANCE GAP HEIGHTS AND EFFECTIVE CLEARANCES AT THE FULL RANGE OF INLET PRESSURS. 216
FIGURE 6-66: 3-WAVE SWASH, CHANGE IN BALANCE GAP HEIGHTS AND EFFECTIVE CLEARANCES AT THE FULL RANGE OF INLET PRESSURES. .. 216
FIGURE 6-67: SCHEMATIC OF THE SOLID AND FLUID DOMAINS FOR THE PROTOTYPE SEAL. 218
FIGURE 6-68: RADIAL PRESSURE DISTRIBUTION, CFD VS EXPERIMENT, Φ_1, σ = 12 MM, ... 219
FIGURE 6-69: RADIAL PRESSURE DISTRIBUTION, CFD VS EXPERIMENT,Φ_3, σ = 12 MM, ... 220
FIGURE 6-70: TOTAL CONTRIBUTION TO AIR-FILM FORCE BY THE PORTION OF THE SEAL LENGTH DOWNSTREAM OF THE RADIAL STEP, σ = 12 MM. 221
FIGURE 6-71: LEAKAGE RATE, CFD VS EXPERIMENT,Φ_1, σ = 12 MM. 222
FIGURE 6-72: LEAKAGE RATE, CFD VS EXPERIMENT,Φ_3, σ = 12 MM. 222
FIGURE 6-73: EFFECT OF ROTATIONAL SPEED ON LEAKAGE RATE, CFD VS EXP, Φ3, σ = 12 MM 223
FIGURE 6-74: VELOCITY CONTOUR AND VELOCITY VECTORS HIGHLIGHTING THE EFFECT OF ROTATION ON THE FLOW FIELD, Φ3, σ = 12 MM, PIN = 0.69 BARG. 224
FIGURE 6-75: CHANGE IN EFFECTIVE CLEARANCE, CALCULATED FOR THREE DIFFERENT EXIT PRESSURES, WITH ROTATIONAL SPEED, Φ_3, σ= 12 MM P_{IN} = 0.69 BARG. 226
FIGURE 6-76: PRESSURE DIFFERENCE CONTOUR BETWEEN ω = 0 RPM AND ω = 15 KRPM CASES, Φ_3, σ = 12 MM P_{IN} = 0.69 BARG. 227
FIGURE 6-77: CFD, EFFECT OF ROTATIONAL SPEED ON AIR-FILM FORCE, Φ_3, σ = 12 MM, P_{IN} = 0.69 BARG. 228
FIGURE 6-78: CFD, EFFECT OF ROTATIONAL SPEED ON CLOSING FORCE, Φ_3, σ = 12 MM, P_{IN} = 0.69 BARG. 228

1 Introduction

In the gas turbine, as embodied in an aircraft jet engine, air is drawn into the engine through a fan which then passes some of the air to a compressor where a pressure increase takes place. The highly pressurized air is guided to the combustion chamber where energy is added to it through the combustion of fuel. This process produces a high temperature-high pressure flow which expands through a turbine providing shaft work which in turn drives the compressor and a high momentum exiting jet. Figure 1-1 shows the Brayton cycle which describes the working concept of a gas turbine engine. The thermodynamic cycle is represented on a temperature-entropy *T-s* diagram, the solid and dashed lines denote the ideal and the actual cycles, respectively. In the ideal cycle case, the air enters the compressor at $\boldsymbol{p_{atm}}$ and $\boldsymbol{T_{atm}}$. The flow is isentropically decelerated relative to the engine creating conditions $\boldsymbol{p_1}$ and $\boldsymbol{T_1}$. In the core compressor of the engine its pressure and temperature rise in an isentropic (adiabatic and reversible) process (*1-2i*). Subsequently, fuel is burnt in the combustion chamber raising the temperature of the air in an isobaric process (*2i-3i*). The hot air then enters the turbine where its pressure falls isentropically as it expands and useful work is extracted to drive the compressor (*3i-4i*). Eventually, the high momentum exhaust jet accelerates through the nozzle as the pressure drops back to $\boldsymbol{p_{atm}}$ at *5i*, thus providing the required thrust. However, in practice there are losses due to rises in entropy associated with the expansion and compression processes, frictional losses and losses due to mixing and heat transfer. For instance, in an actual engine a greater temperature rise is required to compress the air (*1-2a*) and there is a pressure drop in the combustion chamber and the actual process is better described by (*3a-4a*). The compressor and turbine efficiencies relate the actual work per unit mass to an ideal engine with

an equivalent change in pressure. Hence, cycle efficiencies for the ideal cycles are bound to always be higher than the actual cycles due to the associated losses.

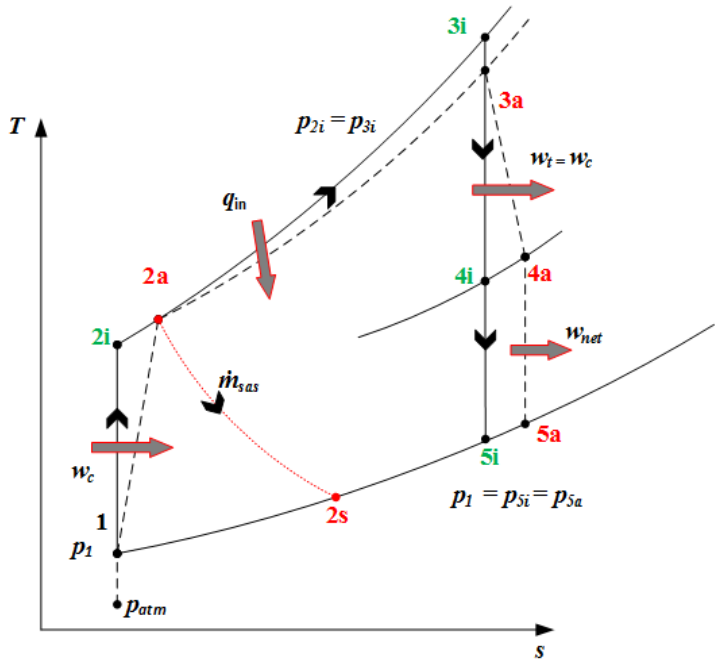

Figure 1-1Temperature –Entropy Diagram for the Brayton Cycle

Gas turbine engines work under extreme pressure and temperature conditions. As the demand for more efficient engines is high, these conditions are expected to become more extreme and post considerable challenges for future engine designers. In order to obtain higher cycle efficiencies, higher compression ratios, higher compressor discharge temperatures and higher turbine inlet temperatures are required. To enable this aggressive cooling of engine components is required using compressed uncombusted air, represented by line *2a – 2s* on Figure 1.1. The air intake that goes through the engine core is divided into a primary airflow that passes through the main gas stream and the combustor and a secondary airflow where air is bled from the compressor into passages to be used for critical applications such as sealing, bearing applications and cooling. Figure 1-2 outlines a typical secondary air system architecture for a double spool jet engine, the main functions of each numbered cycle are described in Table 1.1.

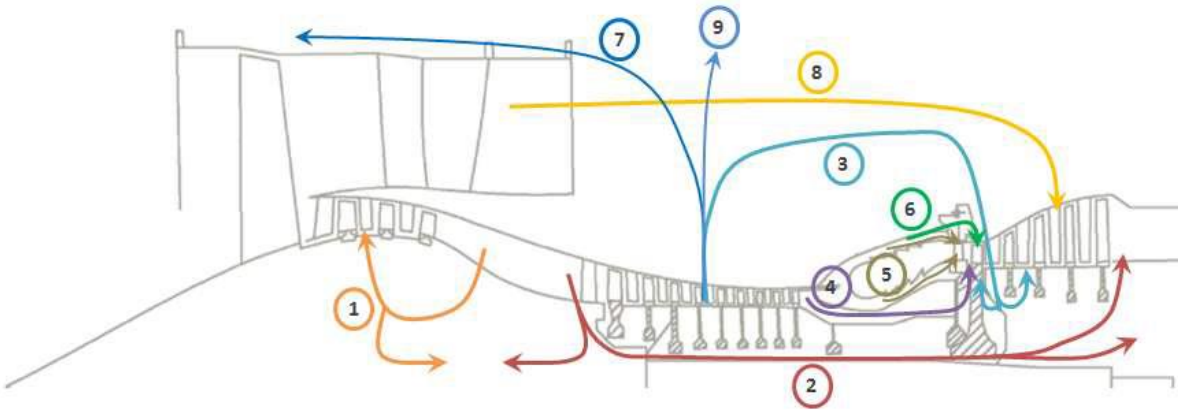

Figure 1-2: Typical secondary air system architecture for a double spool jet engine (Caty, 2012)

Table 1.1: Main functions of secondary air system (Caty, 2012)

Cycle Number	Main Functions
1	- LPC rotor cooling - Front bearing chamber pressurisation (front end)
2	- Front bearing chamber pressurisation (rear end) - HPC, HPT and LPT disc cooling (final stage) - Pressurisation of rear bearing chambers - LPT rear cavity purge
3	- HPT rear cavity cooling and purge - LPT nozzle cooling - LPT front cavity cooling and purge
4	- HPT front cavity purge and rotor blade cooling
5	- HPT nozzle and HPT lower part cooling
6	- HPT upper part cooling
7	- Nacelle anti-icing
8	- LPT active clearance control
9	- Customer bleed and wing anti-icing.

To channel cooling flows and bearing flows and prevent parasitic flows in the engine seals are required between static and rotating parts and this is the focus of the research presented in this thesis. With increasing pressure ratios and turbine inlet temperatures, differential thermal growths are larger during transient operation than ever before, and can also result in larger steady state clearances between components. Advanced sealing technologies which can cope with such changing conditions while also contributing to an improvement in propulsive efficiency are required to enable high efficiency engines.

1.1 Motivation for Seal Research

Until recently, most research has been focused on increasing efficiency by investing in improvements in larger mainstream gas path components such as fans, compressor and turbine components. As long ago as 1977, Stocker et.al (1977) identified that reducing the compressor rotor exit seal leakage by 1% would produce the same results as a 0.91% increase in compressor efficiency. Moreover, arriving at the same improvement in efficiency through improving performance of compressor and turbine components was suggested to be 4 to 5 times more expensive than that achievable by an equivalent improvement in seal technology (Stocker, 1977), (Smith, 1994). In military engine there have already been major benefits from the introduction of advanced seals: Mahler (1993) for example reported a 0.75% decrease in fuel consumption when replacing labyrinth seals with brush seals at the compressor discharge location in the PW4168 engine (Steinetz et.al, 1997). Hendricks et.al (1994) also used brush seals instead of labyrinth seals in the compressor discharge location of a GE-T700 helicopter engine and reported decreased leakage, increased pressure and 1% drop in specific fuel consumption.

Steinetz et.al (1998) performed a study that involved installing 3 advanced seals at turbine rim seal locations in an Allison AE3007 regional jet engine. The findings correlated well with the trend observed above. It was found that by holding the rotor inlet temperature constant, a 0.9% reduction in specific fuel consumption is achievable. Similarly, with rotor inlet temperature held constant these savings could be translated into a 2.5% increase in thrust. As a result, a 0.89% reduction in direct operating cost of the regional aircraft was estimated.

1.2 Existing Sealing Technologies

Gas turbine shaft seals can be found in multiple locations, with as many as 50 (Ludwig, 1978a) separate duties in a jet engine. Figure 1.3 shows typical sealing locations which split into two main categories; air-to-oil seals and air-to-air seals. Seals near bearings are suitable for very close toleranced seals but far from bearings and at high radius the relative movements of the rotating and static components may be large and poorly understood. Typical air-air seals where large performance improvements may be achieved are the compressor and turbine interstage seals, which are the primary means of metering cooling airflow to the turbine blades and vanes and also preventing gas recirculation (Munson, 1992a). Also of interest for improving performance are at vane-blade gap loations, and seals at high radius such as the front and rear bearing housings and the fan seal. While sealing air-to-air locations in the turbine offer the greatest performance improvement potential, (Munson, 2009), the extreme temperature environment here mean that robust conventional seals are typically used.

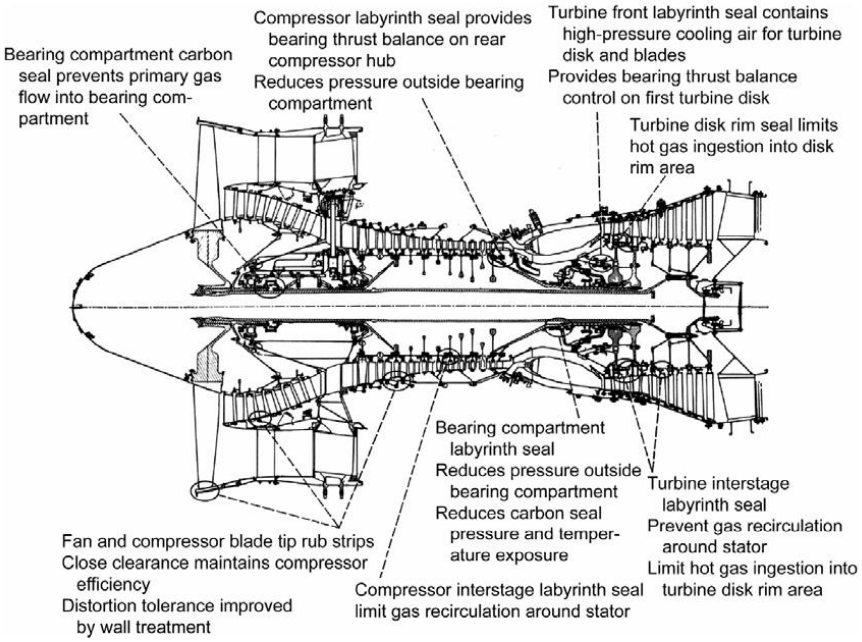

Figure 1-3: Typical Sealing Locations in a Gas Turbine Engine, Bill, 1980.

Seals can be contacting or non-contacting. The main contacting seal used in jet engines is the brush seal. Brush seals offer much lower leakage rates than conventional non-contacting seals, as low as 20% of labyrinth seals, which translates directly to higher cycle efficiencies. They were initially introduced by Ferguson (1988), and have the additional benefit of requiring much less axial space to produce the same pressure drop (Aubry, 2011). They consist of densely packed bristles placed at an acute lay-angle attached to a backing plate which supports them from turning downstream Figures 1.4, Figure 1.5. The bristles are able to move in response to shaft excursions at start-up/shutdown, rotor surface run-out and other transient conditions (Chupp et.al 2006). While they display reasonable stiffness and can be manipulated to apply only low blowdown forces on the shaft, their wear characteristics have limited their use to large civil aero-engines which have high maintenance intervals. Frictional heat generation and heat input into the rotor is another key risk associated with brush seals.

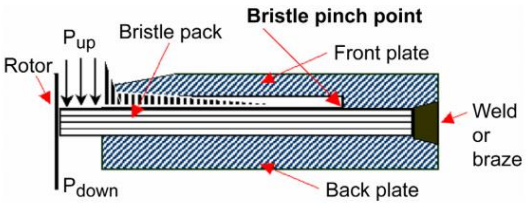

Figure 1-4: Brush Seal Design, Chupp et.al (2002)



Figure 1-5: Bristles of a Brush seal, Courtesy of Technetics Group.

Non-contacting seals can be separated into two types: labyrinth seals and *advanced* non-contacting seals. Labyrinth seals require clearances greater than the net thermal and centrifugal growths between components. Nonetheless they are the most commonly used seals in gas turbines. They consist of a finned surface, fins being in the form of very thin teeth, usually on the rotating part of the seal, which sits against a stationary surface. Remarkably they remain of similar design to those introduced by Perkins in his steam turbines of 1877. The stationary surface is often coated with an abradable material to reduce wear if contact occurs between the labyrinth teeth and the stationary surface (Steinetz et.al, 1997). The arrangement of cavities and constrictions formed by the fin geometry will causes the kinetic energy of the flow to dissipate as it flows through the rigorous labyrinthine path which increases friction and turbulence (Steinetz et.al, 1997). This ensures a pressure drop across the seal minimised leakage. The primary design parameters of a labyrinth seal are the number of teeth, cavity geometry and seal clearance. Figure 1.6 shows various configurations of labyrinth seal fins; straight, staggered and interlocking combinations. Figure 1.7 illustrates the location of a turbine interstage stepped labyrinth seal.

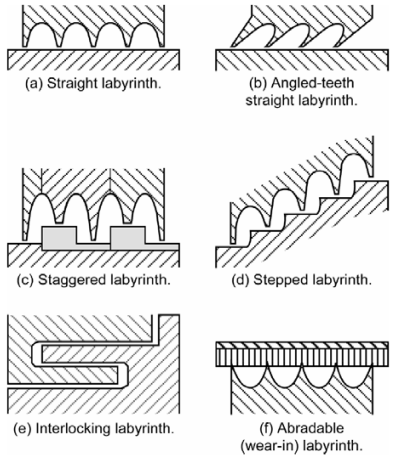

Figure 1-6: Labyrinth Seal Fin Configurations, Burcham et.al (1979).

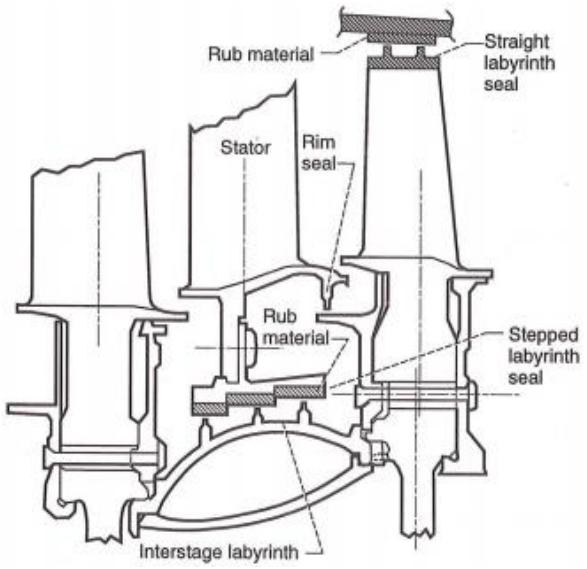

Figure 1-7: Turbine interstage labyrinth stepped seal, Ludwig et.al (1978).

Labyrinth seals can be operated under conditions as high as a running speed of 460 m/s, pressure differentials in excess of 1.7MPa, and operating temperatures up to 705 °C. Their main disadvantage, however, has been their high leakage rate. Moreover, for a stable response to dynamic loads, an increase in the number of teeth and cavities is required thus increasing the axial length and weight of the seal. They are particularly vulnerable to unstable forcing when there are circumferential distortions of the engine casing.

Advanced (non-contacting) seals typically operate by maintaining an air-film between two sealing surfaces; one of which is rotating. They offer much lower leakage rates and remarkably reduced levels of wear compared to contacting seals. However, non-contacting seals necessitate the application of stringent geometric control to minimise the level of distortion of the sealing faces to ensure surface flatness remains within tight limits thus maintaining a sufficiently stiff air-film to keep the faces separated. This condition is more easily achievable in land-based industrial engines. One of the objectives of this thesis is to investigate whether an advanced seal can be designed to be tolerant to the level of transient distortions typical of an aero-engine.

Conventional face seals have been considered as potential replacements for labyrinth seals to reduce leakage rates wear through non-contacting operation. Figure 1-8 shows the main constituents of a conventional face seal; a primary ring or the nosepiece (stator), the seal seat (rotor), a secondary seal and a preload spring. The nosepiece, usually made of carbon, is designed to move in the axial direction due to the effect of the spring thus accommodating engine thermal expansion (Steinetz et.al, 1997). The preload spring exercises an axial mechanical force on the nosepiece which is also loaded pneumatically by the sealed pressure, $P_{high,}$ (Steinetz et.al, 1997). The force balance of a conventional face seal is illustrated in Figure 1.9. The pressure of the fluid in the gap tends to open it and is opposed a preload spring. The seal can operate in a balanced or a mixed lubrication regime dependent on the relative size of the opening and closing forces. The film thickness under which this equilibrium is achieved is the operating clearance of the seal (Steinetz et.al, 1997), and is in the order of microns. Figure 1-10 highlights the distinction between a balanced and unbalanced seal. Balanced seals are commonly used in high pressure applications where hydraulic forces can be used to balance the forces on the sealing rings. The less complexly configured unbalanced seals are usually used in low pressure applications where some surface contact is allowed (Metcalfe, 1973).

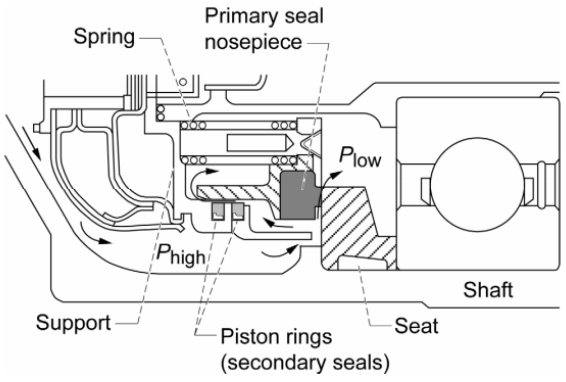

Figure 1-8: Conventional Face Seal, Brown (1984)

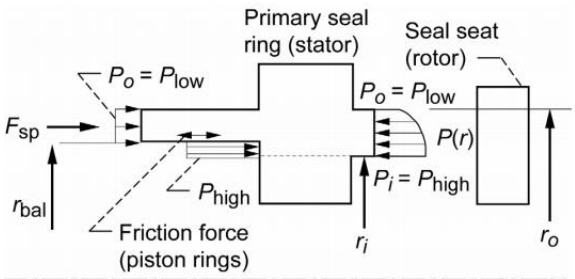

Figure 1-9: Pressure Balancing of a Conventional Face Seal, Steinetz et.al (1997)

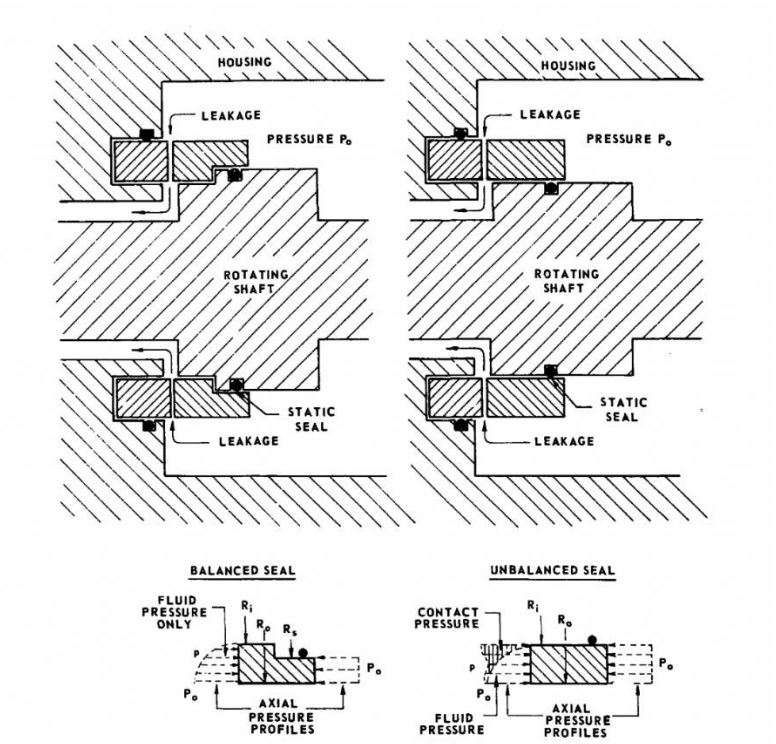

Figure 1-10: Balanced and Unbalanced Face Seals, Metcalfe (1971).

Although they exhibit very significantly lower leakage rates than labyrinth seals their operation is limited to lower pressure differentials (0.69MPa) and temperatures (480°C) (Steinetz, et.al 1997). In locations where high temperatures and high rubbing speeds are prevalent, the sealing faces tend to distort and to the author's knowledge no method of providing sufficient cooling to the carbon nosepiece to reduce wear and maintain surface flatness to enable non-contacting operation has yet been devised. The seals are discussed further in the literature review. For the aero-engine the potentially catastrophic failure mode of the carbon element of the seal has limited their application.

1.3 Primary Research Area

In this thesis, the idea of a large axial movement face seal that is able to run against a slightly distorted rotor is considered. An air-riding face seal for large diameter applications cannot have the close running clearances of a small diameter mechanical face seal. In such seals the running clearances are of the order a few microns, and out of flatness causes large changes in the forces

experienced by the seal. In the case of gas thrust bearings the considerations are similar. Here very tight tolerancing is required to sustain very high axial loads in the absence of a pressure gradient. The current concept is considered for application in more conventional sealing locations in the aero-engine where there may be large radial and axial movements of the stator and rotor sections. The leakage targets for the seal are similar to those of a brush seal installed in this location, and an order of magnitude better than an equivalent labyrinth seal. i.e. not the ultra-low leakage requirement of many small diameter mechanical face seals or carbon seals. Thus the motivation for the current research is to determine the operating conditions, leakage, film-forces and equilibrium operating conditions of a potential seal design for an aero-application. The work is experimental and numerical in nature and has been conducted, in its initial stages, with considerable support from Rolls-Royce plc., and the E-Break Framework 7 research programme funded by the European Commission.

The seal concept consists of a primary sealing face mounted on a movable carrier such that axial movements are possible over a range of several millimetres: a schematic of a large-axial movement face seal along with the associated force breakdown are shown in Figure 1-11 and Figure 1-12, respectively. This movement might be provided by a spring, but because of the large pressure differences across the seal is more appropriately implemented using the pressure difference between the front and back of the carrier. Basic operation with balancing of front and back pressure to cause movement is often expressed in terms of the balance ratio (***B***) which is defined as the ratio between the area over which the closing forces act to area over which opening forces act. A balance ratio of $\boldsymbol{B} = 1$ and would naturally close the gap. It requires the air-film to generate most of the net force and in the case loss of pressurisation would tend to blow or be pulled open by a spring. A balance ratio of $\boldsymbol{B} = 0$ requires the closing force provided by the spring and a generally smaller air-film force to open the seal. In the event of loss of

pressurisation, this seal will tend to close up (rub). The seal targeted for this research has a balance ratio that lies within the range ($0 < \boldsymbol{B} < 1$) and uses the balance between the opening force from the air-film and the closing forces from the sealed pressure to move the primary sealing surface into close proximity with the rotor. ***B*** is set by changing the radial position of the secondary seal, while the axial position influences the coning moment on the primary face.

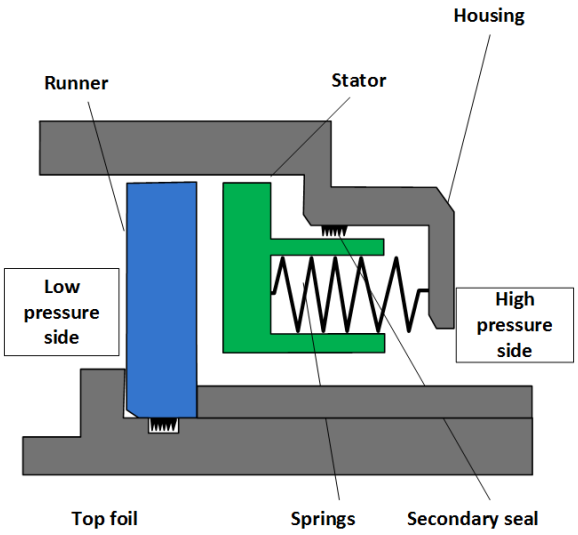

Figure 1-11: Schematic of large-axial movement face seal concept.

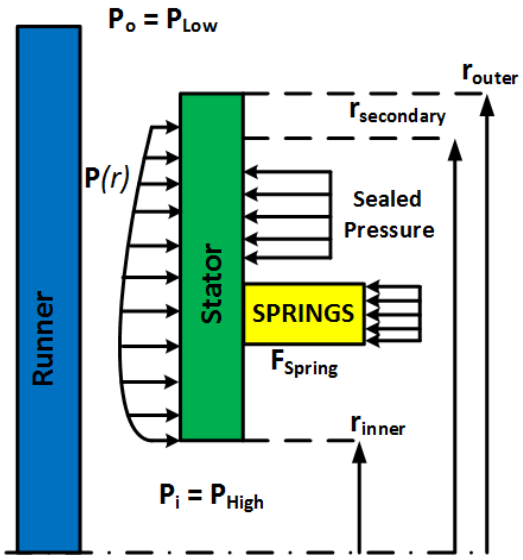

Figure 1-12: Face seal typical force breakdown

1.4 Thesis Content

Because the range of clearances is large compared to conventional face seals there are surprisingly few existing data in the literature to use to aid the design process. The research conducted has therefore been undertaken as follows:

Initial research was focussed on the primary sealing face. 2D modelling tools suitable for conventional face seals were used to model the pressure distribution and associate film forces in an isolated engine representative, primary sealing face. The engine representative conditions here refer to pressure differentials and the range of gap heights decided with the industrial

partner. These predictions were compared both to experimental data and separately developed high fidelity 3D Commercial CFD.

- In *chapter 3*, both models are developed and validated against a set of existing experimental results over a range of plain gap heights, *i.e.* with no added hydrostatic or hydrodynamic features.
- *Chapter 4* describes the modification of and existing experimental test rig, to allow the extension of the primary sealing face validation data for a range of gaps with radial coning distortions on the primary sealing face. The key performance parameters considered here are the radial pressure distributions within the primary gap, air-film forces and mass flow leakage rates.
- In *Chapter 5*, data are reported for a series of tests conducted in this test rig with the displacement of the primary sealing face relative to the rotor prescribed: a wide range of coning angles and displacements are tested in a very well-controlled environment. Results from this campaign were used to further asses the capability of 3D CFD and a further refined model employing two-way fluid structure interaction.
- In *chapter 6*, the design test and modelling of a prototype large axial movement seal containing the features shown in Figure 1-11 is reported. The prototype seal featured an axially-flexible front face mounted on a set of springs to the show effect of offset and determine the feasibility of pull in / push out seal. Additionally, the seal was subjected to high levels of swash representative of distortion of its rotating counterface. Finally results from 3D CFD modelling of the system are reported and compared to the reported experimental results.
- Conclusions are drawn from the work at the end of each chapter with overall conclusions concerning seal, modelling and future research in *chapter 7*.

Some of the initial results were reported in a poster at the ASME IGTI 2016, and the primary face pressure distributions were presented in detail at ISROMAC 2017.

2 Literature Review

Gas film lubrication forms the basis for non-contacting technologies used in bearings and seals. Although non-contacting compliant technologies have traditionally been applied to bearings, realizing the benefits this technology could have on sealing performance, in terms of lower leakage rates and reduced wear, has fast-tracked the need for its adoption in gas turbine applications. This section presents a literature review focusing on fundamentals of fluid film lubrication applied to non-contacting compliant technologies for bearings and seals.

2.1 Gas Film Lubrication

The purpose of fluid film lubrication is to maintain a sufficiently pressurized thin film fluid in a clearance gap between two surfaces to keep them apart and minimise any contact that could occur. The lubricant is the medium through which forces are transmitted between the two surfaces (Brewe et. al, 1997). Two main categories of bearings exist; thrust bearings and journal bearings. The former is used to support axial loads on the shaft while the latter supports radial loads. Much lower friction is achievable with air lubricants thus increasing the life of the component. Additionally, lower levels of noise, vibration and contamination are evident when using gas-based lubricants (Hughes, 1992).

2.1.1 Hydrostatic Lubrication

A fluid film between two surfaces can be created and maintained by imposing a pressure differential along the clearance gap using pressure supplied from an external source. Due to

the pressure difference a force is created which acts to keep the surfaces separated. Hydrostatic seals and bearings rely on hydrostatic pressure generation to maintain non-contacting operation. It is particularly useful at locations where little or no relative motion exists between the two surfaces and at start-up and shutdown conditions to maintain clearance between surfaces and reduce wear. The Reynolds' Equation has been used extensively in thin film flow applications. The equation relates lubricant viscosity, film thickness, pressure and surface speed. The main assumptions made in the derivation of the Reynolds equation are; 1- Laminar Flow within the gap, 2-Viscous forces are dominant and inertial force are neglected, 3-Curvature effects are neglected and 4- The pressure across the film is constant (Brewe et.al (1997)). Refer to Appendix A for a full derivation of Reynolds equation. The 2D compressible Reynold's equation in polar co-ordinates can be written as,

$$\frac{\partial}{\partial r}\left(\frac{rph^3}{\mu}\frac{\partial p}{\partial r}\right)+\frac{1}{r}\frac{\partial}{\partial \theta}\left(\frac{ph^3}{\mu}\frac{\partial p}{\partial \theta}\right)=6r\omega\frac{\partial(ph)}{\partial \theta} \qquad \textbf{Eq. 2.1}$$

Lubbinge (1999) briefly discussed the effect of the ratio of seal radii (r_{inner}/r_{outer}) and radial coning on the hydrostatic pressure distribution in the sealing gap. Consider a static situation with parallel sealing faces and assuming the flow is incompressible, equation 2.1 reduces to,

$$\frac{\partial}{\partial r}\left(r\frac{\partial p}{\partial r}\right)=0. \qquad \textbf{Eq. 2.2}$$

Integrating equation 2.2 according to the following boundary conditions,

$$p=p_i \quad \text{at} \quad r=r_i$$
$$p=p_o \quad \text{at} \quad r=r_o.$$

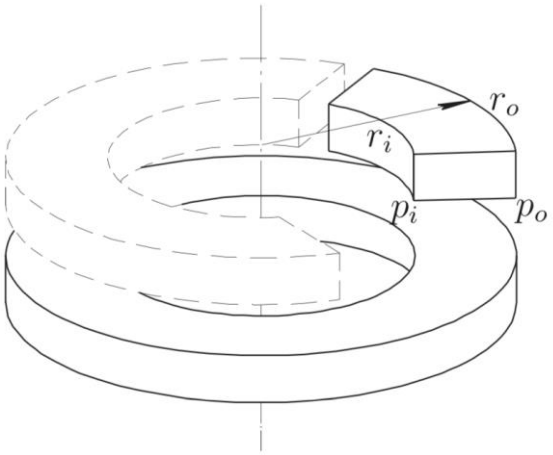

Figure 2-1: Boundary conditions for Eq. 2.2 (Lubbinge, 1999)

yields the solution for the hydrostatic pressure distribution within a seal gap (Lubbinge, 1999),

$$p = \frac{p_i \ln \frac{r}{r_o} + p_o \ln \frac{r_i}{r}}{\ln \frac{r_i}{r_o}}. \qquad \textbf{Eq. 2.3}$$

Now introducing the non-dimensional parameters,

$$\tilde{r} = \frac{r}{r_o}, \tilde{p} = \frac{p}{p_i - p_o} \text{ and } \xi = \frac{r_i}{r_o}$$

for different values of ξ the pressure distributions in Figure 2-2 can be plotted (Lubbinge,1999).

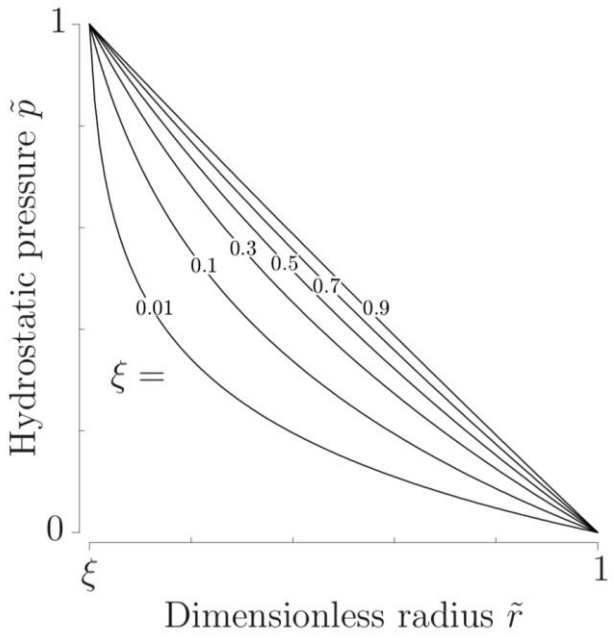

Figure 2-2: Pressure distribution for an inside pressurised face seal (Lubbinge, 1999)

It is apparent from the pressure distributions that at large values of ξ there the hydrostatic pressure distribution tends to a linear distribution. This is range for most applications they investigated where the value of ξ is approximately 0.9, (Lubbinge, 1999). Another parameter which heavily influences the levels of hydrostatic pressure maintained is the coning or radial taper of the gap in the direction of the flow. Figure 2-3 shows a geometric representation of the three possible coned radial gap profiles; parallel (no coning) gap, a converging gap and a diverging gap.

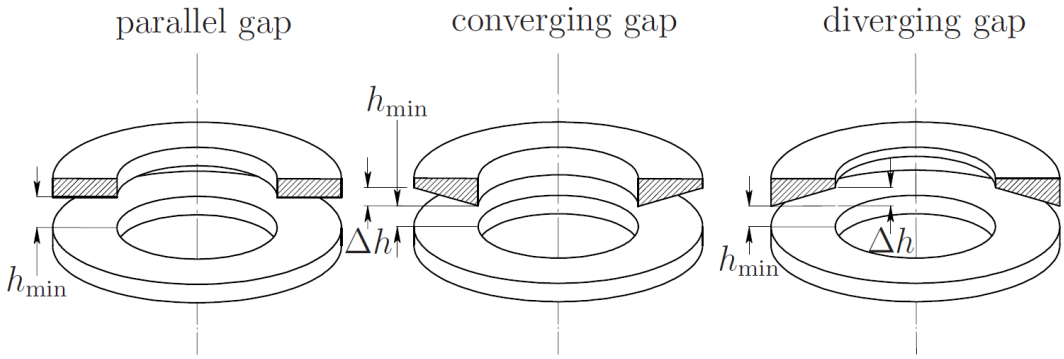

Figure 2-3: Radial gap distortions, (Lubbinge, 1999)

Consider the 2D incompressible form of the Reynolds equation shown hereunder in non-dimensional form,

$$\frac{\partial}{\partial X}\left(H^3\frac{\partial P}{\partial X}\right)+\frac{\partial}{\partial Y}\left(H^3\frac{\partial P}{\partial Y}\right)=6\frac{\partial H}{\partial X} \qquad \textbf{Eq. 2.4}$$

Assuming no pressure gradient in the ***X*** direction and no rotational speed for a radially-coned gap equation 4 reduces to,

$$\frac{\partial}{\partial Y}\left(H^3\frac{\partial P}{\partial Y}\right)=0 \qquad \textbf{Eq. 2.5}$$

For a gap with a converging coning, the film thickness ***H*** can be described by,

$$H = H_{\min}+\alpha Y \qquad \textbf{Eq. 2.6}$$

Solving equation 5 for a converging gap results in the following expression for the hydrostatic pressure distribution,

$$P(Y,H_{\min},\alpha,P_f)=P_f Y\frac{(H_{\min}+\alpha)^2(2H_{\min}+\alpha Y)}{(2H_{\min}+\alpha)(H_{\min}+\alpha Y)^2} \qquad \textbf{Eq. 2.7}$$

Similarly, the film thickness for a diverging gap can be written as,

$$H = H_{\min} + \alpha(1 - Y) \qquad \textbf{Eq. 2.8}$$

Hence, the hydrostatic pressure distribution for a diverging gap becomes,

$$P(Y, H_{\min}, \alpha, P_f) = -P_f Y \frac{{H_{\min}}^2(\alpha Y - 2H_{\min} - 2\alpha)}{(2H_{\min} + \alpha)(\alpha Y - H_{\min} - \alpha)^2} \qquad \textbf{Eq. 2.9}$$

Using the expressions derived above by Lubbinge (1999), the pressure distributions for a range of coning angles denoted by $\boldsymbol{\alpha}$ and for a range of minimum gap heights $\boldsymbol{H_{min}}$ were plotted in Figure 2-4 and Figure 2-5, respectively. The converging configurations are represented by the solid lines, the diverging by the dashed lines and the parallel (no-coning) gap is denoted by $\boldsymbol{\alpha}$ = 0. The plots suggest that film pressure increased with increasing the converging angle and vice versa in the case of a diverging gap. Lubbinge explains that for converging gaps, the resistance in the direction of the flow increases resulting in the convex profile exhibited by the cases highlighted here. On the other hand, diverging gaps resulted in a more concave pressure profile and led to the lowest film pressures. It is clear that film pressure is heavily influenced by both the coning present on the sealing faces and the minimum gap the seal is operating with. The effect of varying the minimum film thickness for a given coning angle is plotted in Figure 2-5. Even with a certain degree of coning, film thickness still influences the pressure distribution where smaller gaps resulted in higher film pressures.

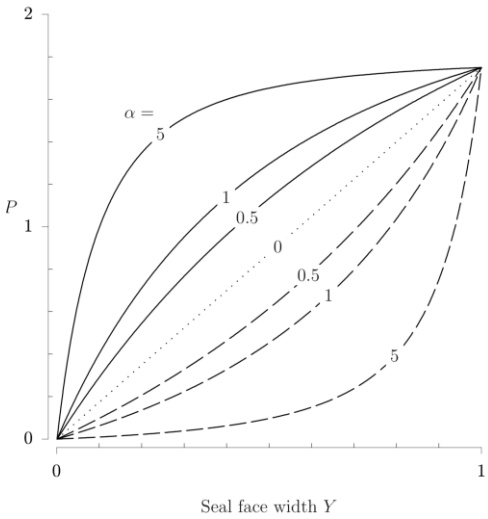

Figure 2-4: Radial pressure for coning angles $\alpha = 0 - 5$.

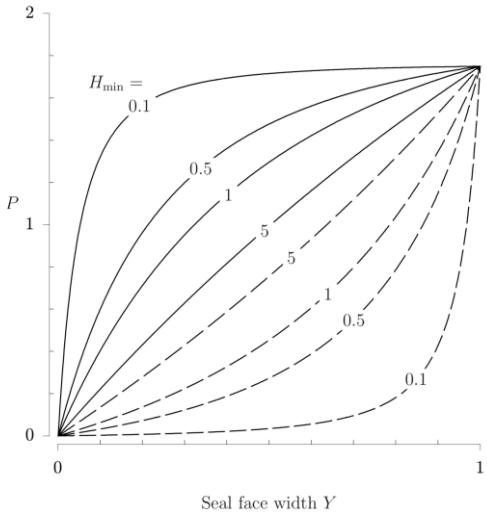

Figure 2-5: Radial pressure H_{min} = 0.1 – 5.

2.1.2 Hydrodynamic Lubrication

A pressure build up in the clearance gap can be created purely due to the relative motion between the two surfaces where there occurs a change in gap height in the direction of motion. Bisson and Anderson (1964) performed an analysis on an infinitely long slider bearing, Figure 2.1, using a 1-D incompressible form of Reynold's equation, Eq. 2.1,

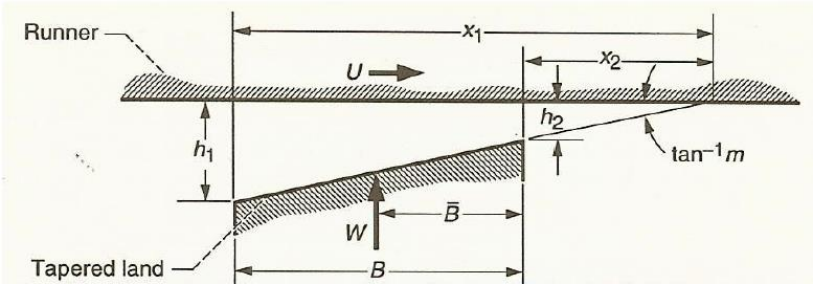

Figure 2-6: Infinite Slider Bearing, Brewe et.al (1997).

$$\frac{\mathrm{d}}{\mathrm{d}x}\left(h^3\frac{\mathrm{d}p}{\mathrm{d}x}\right) = 6\mu U\frac{\mathrm{d}h}{\mathrm{d}x} \qquad \textbf{Eq. 2.10}$$

Applying the boundary conditions $p = p_a$ *at* $h = h_1$ $(z = 0)$ and $h = h_2$ $(z = B)$ and integrating the above equation yields,

$$p - p_{atm} = 6\mu UB\frac{(h_1 - h)(h - h_2)}{(h_1^2 - h_2^2)h^2} \qquad \textbf{Eq. 2.11}$$

According to the above result, above ambient pressure could be generated between two surfaces by having a converging gap in the direction of motion. The results from the same study show that as the ratio (h_1/h_2) increases the point of maximum pressure is moved further downstream as seen in Figure 2.2. In addition to the tapered geometry alternative lift-generating geometries can also be used to generate hydrodynamic pressure, Figure 2.3.

Self-acting seals and bearings rely on hydrodynamic lubrication between surfaces to produce a force that maintains the face separation. If the resultant force is sufficient to keep the faces apart, *i.e.* support any self-weight plus steady and unsteady loads, the seal or bearing is said to be 'self-acting' or 'air-riding'. Note that, 'Air-riding' will be used for bearings and seals which are self-supported in this thesis independently of whether such lift is generated through hydrostatic and hydrodynamic means (or both), commonly bearing designs that combine hydrostatic and hydrodynamic capabilities are referred to as hybrid bearings. Ausman (1964) suggested that the highest hydrodynamic lift is obtained by using a spiral groove geometry. Due to the absence of external pressurization, self-acting geometries do not always produce sufficient lift force to maintain contactless operation at start-up and shutdown. Moreover, they require fine clearances to operate in a non-contacting mode which are hard to maintain at times when surface distortions occur under thermal and centrifugal growths and shaft movements.

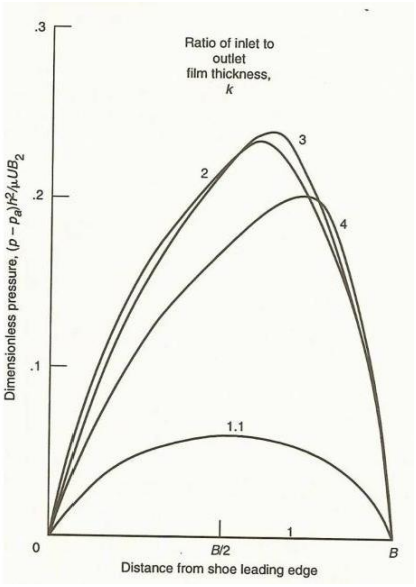

Figure 2-7: Pressure Variation with Distance from Shoe, Brewe et.al (1997)

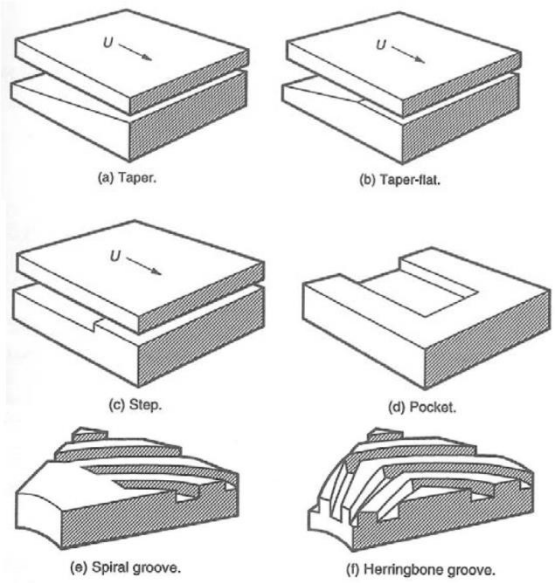

Figure 2-8: Lift-generating Geometries, Ausman (1964)

Face seals were typically designed to operate in mixed lubrication regimes where the load is shared by both the rubbing contact of the sealing faces and the fluid film pressure in the sealing gap, given that the resulting levels of wear and friction are acceptable. Here friction refers to start-up and shut-down rubbing of the sealing faces in addition to transient rubbing during operation. The level of transient rubbing will differ depending on whether the face seal is contacting or non-contacting. The former category is expected to operate in a mixed lubrication regime where the load is supported by both the air-film and rubbing contact. The latter category is typically used in higher pressure applications compared to the contacting face seals and ideally would have the load supported by the air-film. In this type of seal, lower levels of transient wear are expected. However with the move towards higher speeds, pressures and temperatures, it is not possible to maintain acceptable levels of wear and friction and it will be necessary to maintain a non-contacting mode of operation. To achieve this, sufficient hydrodynamic fluid pressure needs to be created to support higher load capacities. This is not only achieved through the aforementioned geometric patterns but can also be due to large scale

waviness, micro-asperities and various types of misalignment and vibration (Young and Lebeck, 1982). It should be noted that in high-pressure, low viscosity applications the hydrostatic component driven by the pressure drop across the sealing faces is expected to be the dominant source of load support. Cheng *et al.*, (1968) defined the ratio of hydrodynamic load to the hydrostatic load, ϕ, as,

$$\varphi = \frac{f_b 6\mu U b}{(p_2 - p_1)h^2} \qquad \textbf{Eq. 2.12}$$

The ratio ϕ is a function of viscosity, surface speed, seal width, pressure differential and minimum gap height. It can be used to demonstrate the effectiveness of the hydrodynamic action in load support. The factor f_b depends on the geometry of the hydrodynamic pattern, for Rayleigh steps and spiral grooves it is taken to be f_b = 0.025. Cheng *et.al.* (1968) report values of ϕ = 0.05625 for a submarine propeller shaft application and a value of ϕ = 0.0375 for a non-contacting face seal used in the end and interstages of a jet engine compressor. For both examples ϕ indicates a weak hydrodynamic action compared to the hydrostatic one. The minimum gap height for the jet engine compressor case was taken to be 25.4 μm, now if this gap size is reduced down to 5.08 μm it will result in a value of ϕ = 0.94. In other words, for smaller minimum gaps the hydrodynamic action will be more pronounced which will have a positive effect on the load capacity of the seal as well as its stiffness.

Investigating sources of hydrodynamic pressure generation in face seals became an area of interest in the early 1960's. Early experimental work by Denny (1961) describes a set of experiments to study the pressure between plane parallel thrust surfaces applied to radial face seals. Experiments were carried out with fluids pressures of 0.0375 bar and 1.013 bar and pressure generation due to shaft rotation was evident. The pressures generated exceeded the applied fluid pressure in some cases and became insignificant when face separation was larger

than 2.5 μm. With a face separation of 7.5 μm and in the absence of any extra hydrodynamic pressure generation, face pressures were still 10% higher than those predicted theoretically. This was found to be due a hydrostatic pressure build-up in the gap, where wear was found to result in a converging taper in the direction of the flow. Interestingly, 'negative' leakage was also reported where with small applied pressures the fluid showed a tendency to flow radially inwards (leakage flow direction is from inner to outer radius) regardless of the pressure difference. In other words, inward pumping implies fluid leaking in the opposite direction to the hydrostatic pressure drop within the sealing gap. Attempts were made to estimate the stalling pressure of this inward pumping action but results were found to vary significantly. Nonetheless, the inward pumping action remained evident in all cases.

Findlay (1968) lists four possible mechanisms to explain the development of hydrodynamic effects (including inward pumping) in mechanical face seals: 1- lubricant cavitation and non-parallel sealing surfaces, 2- axial seal vibration coupled with variable lubricant properties, 3- variable lubricant properties and non-parallel surfaces and 4- inertia effects. In an attempt to explain Denny's work (1961), Findlay formulated a model based on the incompressible form of the 2D Reynold's equation based on the short bearing approximation and including an approximation of cavitation effects. This was motivated by findings reported by Nau (1964) where cavitation was observed to play a part in the in the inward pumping action in the transparent face seal tested. However, Findlay's analytical model concluded that the presence of gas cavities did not affect the load on the seal. On the other hand, Nau (1968) showed experimentally that his initial observations regarding inward pumping due cavitation were valid and that only inward pumping occurred in his experiments. Findlay (1969) then extended his initial model (Findlay, 1968) to account for radial eccentricity, misalignment and waviness (one circumferential wave). Model predictions were compared to a radially misaligned

eccentric face seal with a fully developed fluid film (no gas cavities present) and good agreement was reported. The main conclusions drawn from this work were: 1- a net hydrodynamic force can be created through cavitation, however it does not alter the leakage, thus eliminating inward pumping as a consequence of cavitation. 2- pumping leakage can be produced through a coalition of radial eccentricity, misalignment (or tilt) or one-wave waviness. 3- pumping leakage can be either inward or outward. The direction is dictated by the relationship between radial eccentricity, misalignment and the direction of rotation. 4- in eccentric seals, cavitation diminished the pumping effect rather than caused it. 5- given the existence of a fully developed fluid film, pumping leakage is not affected by the hydrostatic pressure drop through the sealing gap (Findlay, 1969). In some instances, inward pumping can prove detrimental to the seal's life if the pressure due to the pumping action exceeds that of the sealed pressure. In that case, the fluid film in the clearance between both sealing rings will be ejected causing both faces to come into contact. It could also lead to undesignated leakage into the region targeted for sealing which can have catastrophic effects on the seal's life. To this extent, Batch *et.al* (1971) recommend the use of 'inside' pressurised seals for moderate to high sealed pressures in order to utilize the inward pumping action to reduce leakage. For low pressure applications, it would be more beneficial to use an 'outside' pressurised seal as it would aid in avoiding the aforementioned issue.

As mentioned previously, surface waviness along with misalignment, eccentricity and vibrations were reported to be sources of hydrodynamic pressure generation in face seals. Batch and Iny (1970) showed analytically that surface waviness can generate hydrodynamic pressure. Iny (1971) reported on the two-humped waviness surface profile significant capability in generating hydrodynamic pressure. Regarding sources of waviness, Batch *et.al* (1971) showed experimentally that considerable hydrodynamic pressure was generated after the carbon face

wear resulted in a wavy profile. Interestingly, the carbon face was found to repeatedly wear into a wavy profile, approximated by a near-sinusoidal wave. A typical waviness profile is shown in Figure 2-9. Further measurements were performed by Batch and Iny (1973) where two profiled cast iron seal faces were used: the first had a near sinusoidal two-humped profile and the second had a three-humped profile, film characteristics and test conditions for both configurations are outlined in Figure 2-10 and Figure 2-11, respectively.

Furthermore, measurements performed by Lebeck (1974) on carbon rings from a 'contacting' face seal after a period of operation showed that values of waviness amplitudes to have increased to (0.5 μm to 8 μm) when compared to their initial 'as-lapped' condition (0.25 μm to 0.5 μm). The primary sources of waviness reported by Lebeck (1974,1977) are mechanical loading, tangentially non-uniform face temperatures and material properties, clamping and mounting distortions.

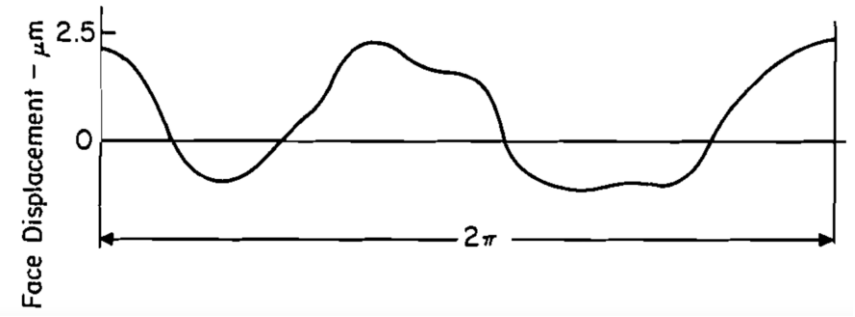

Figure 2-9: Typical waviness profile, Lebeck (1977).

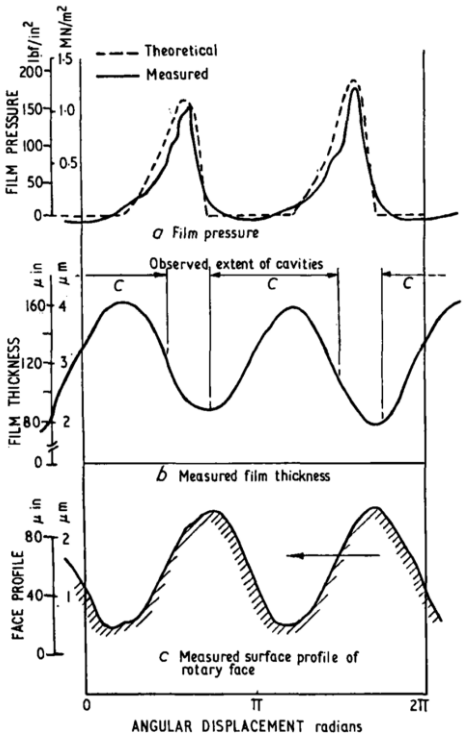

Test conditions. Speed 235 rev/min; sealing oil viscosity 6 cSt under a head of 15 cm; face loading 150 kN/m².

Figure 2-10: Film characteristics of near sinusoidal two-humped profile (Batch and Iny, 1973)

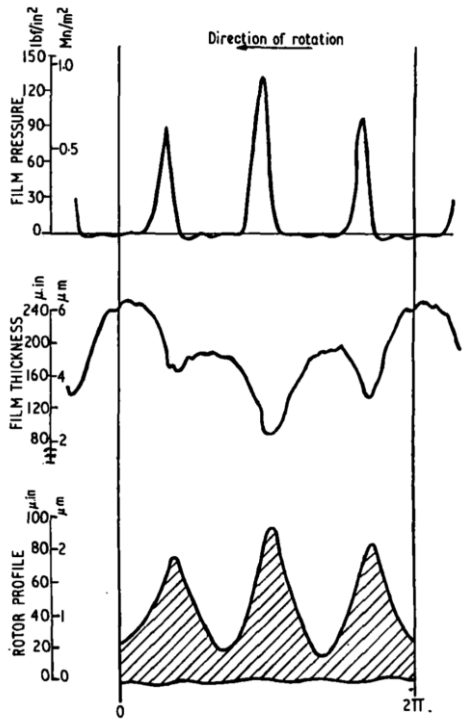

Test conditions. Three-humped cast-iron seal face rotating at 600 rev/min. Sealing oil of viscosity 6·5 cSt under a head of 40 cm. Face loading 80 kN/m².

Figure 2-11: Film characteristics of near sinusoidal three-humped profile (Batch and Iny, 1973)

2.2 Compliant Gas Bearings

2.2.1 Compliant Gas Thrust Bearings

In an attempt to lessen the stringent requirements for clearance control in self-acting gas seals and bearings, a ‘foil bearing’ was used. Essentially, rather than a rigid stator face, segmented pads with flexible elements of low mass and very low inertia are added. The compliant surface provided by the flexible elements, typically strips of corrugated bump foils, Figures 2.4, 2.5, acts as a spring causing the top foil to deform and hence define the profile of the film thickness. This will allow the stator to track larger distortions and misalignments of the runner, thus increasing the operational envelope of the seal/bearing. Furthermore, the load carrying capacity

can be optimised by designing the leading edge of the foil to have a converging wedge in the direction of rotation to maximise pressure build up.

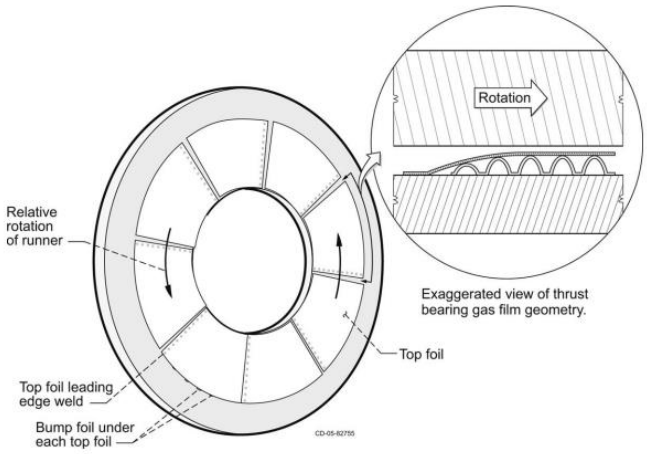

Figure 2-12: Compliant Foil Thrust Bearing, Dykas et.al (2009).

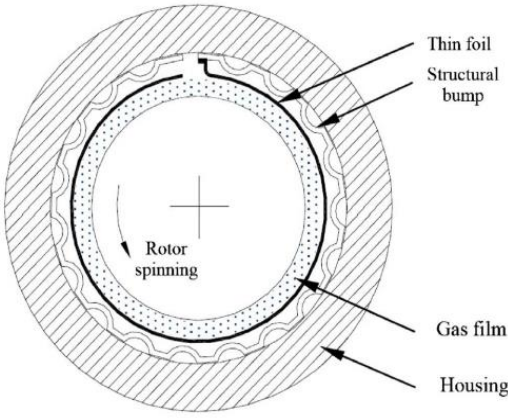

Figure 2-13: Compliant Foil Journal Bearing, Kim et.al (2005).

A thorough analysis of foil bearings performance was executed by Heshmat et.al (1983, 1984, 1991, 1999, and 1998). These types of bearings have been reported to perform at temperatures up to 650 °C and surface velocities up to 620 m/s (Heshmat et.al 1999). A compliant gas thrust bearing design by Heshmat (1998) consisted of eight segmented top foil pads supported on bump foils. A numerical model was presented by Heshmat et.al (1999) based on the aforementioned design which coupled 2D Reynolds equation with finite element methods to predict the bearing performance. Experiments showed that the bearing operated successfully and supported a maximum thrust load of 64 kg at 176 m/s surface speed. Additionally, results from experiments agreed well with model predictions.

Dykas et.al (2008) aimed to establish a simplified and a more experimentally-versatile manufacturing process for gas thrust bearings aimed at researchers in an attempt to yield a

wider adoption of this technology in experimental studies. Their recommendations included using semi-circular slots as a method of attaching top foils and bump foils to the backing plate instead of spot welding, Figure 2-14. The end product is shown in Figure 2-15, inner and outer diameters were 5.08 cm and 10.16 cm respectively. The prototype was tested experimentally at temperatures up to 425°C and subjected to a constant axial load and accelerated from 0 to 20 kRPM. A rapid increase in torque was seen at 125 N indicating the maximum load capacity of the bearing has been reached.

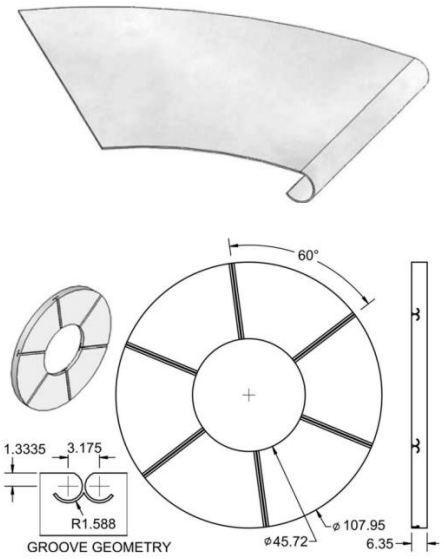

Figure 2-14: Mechanism for attaching top and bump foils, Dykas et.al (2008).

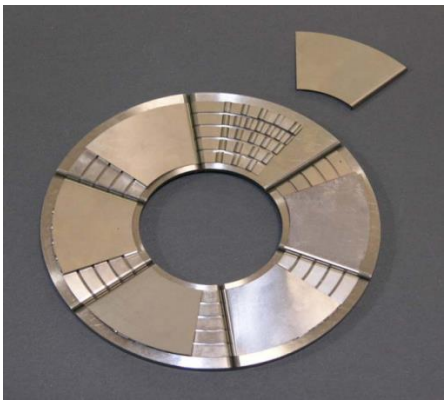

Figure 2-15: Gas Thrust Bearing as manufactured by Dykas et.al (2008).

Balducchi et.al (2013) used the same prototype introduced by Dykas et.al (2008) to experimentally investigate the torque, lift-off speeds and thermal features of the gas thrust bearing under mild loading conditions. The load deflection results were in reasonable agreement compared with those reported by Dykas et.al (2008). At a constant static load of 15 N and speeds up to 35 kRPM a sharp increase in torque at start-up and shutdown was seen indicating rubbing between the foils and the runner face. The torque decreased as the

hydrodynamic film started developing and stabilized once lift-off has been achieved. Further tests were run with loads up to 60 N at the same speeds. The torque measured at start-up, shutdown and after lift-off was found to vary in a linear fashion with the applied load while showing less dependency on speed. Balducchi et.al (2014) presented a 2DOF dynamic model for the same rig used before but higher loads up to 150 N were considered and measurements agreed well with model predictions. The same foil thrust bearing design was used in experimental work by Dickman (2010) and Bruckner et.al (2012) and performed successfully.

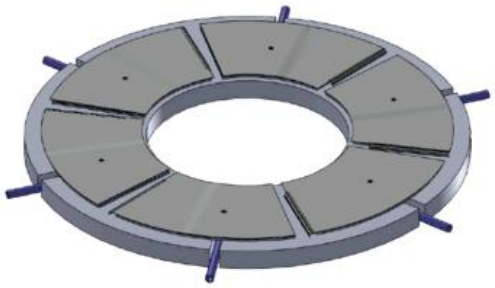

Figure 2-16: Gas Thrust Bearing with orifice holes for hydrostatic pressure augmentation, Lee et.al (2010).

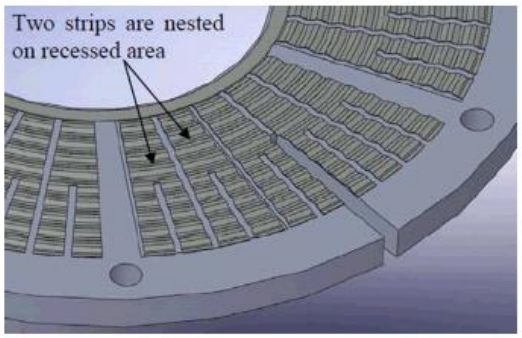

Figure 2-17: Radial Bump Foil arrangement, Lee et.al (2010).

Work by Lee and Kim (2010) included designing and testing a hybrid (journal) air foil bearing (HAFB). The hybrid design combined the hydrodynamic effect of the air bearing along with the hydrostatic augmentation of the load capacity at start-up and shutdown. The results were encouraging as higher load capacities at lower speeds were obtained and significantly reduced friction during start-up and shutdown was observed. Lee and Kim (2010) further extended this work to include a hybrid six-pad air foil thrust bearing (HAFTB). Each of the six pads is supplied with externally pressurized air discharged from orifice holes on the top of the pad, Figures 2.8, 2.9. The study revealed that at low speeds the highest load capacity was obtainable with orifice located on the centre of the pad while at higher speeds the highest load capacity

was achieved with the pressurised orifices closer to the leading edge. Higher minimum film thicknesses were reported compared to a hydrodynamic gas thrust bearing at zero rotational speed which is expected to reduce contact at start-up and shutdown. However, no experimental data were included to verify the validity of the model or dynamic operability.

2.2.2 Compliant Journal Foil Bearings

Walton et.al (2004) tested a compliant foil bearing's ability to support a rotor in a miniature turbojet engine. The study focused on assessing the capability of the compliant foil to withstand high temperatures (290°C) and its dynamic response to shock tests at speeds up to 150 kRPM. The bearings did not show wear signs at high temperatures and acceptable levels of vibrations were encountered. At a speed of 100 kRPM under a load of 38g, rotor displacements were reported to be well damped and stabilized in less than 80 milliseconds. For all test runs no evidence of rubbing was observed and the foil bearing orbit size remained below 2 μm.

Heshmat et.al (2006) experimentally investigated the performance of a foil journal bearing in a small gas turbine engine. Tests were run at maximum speed of 120 kRPM and temperatures up to 750°C and a thrust of 134N. The foil bearing's performance was compared against a standard fluid lubricated ball bearing and was found to reduce fuel consumption by 10%. Moreover, the component life of the foil bearing was reported to be longer than the ball bearing's life. Based on this study the authors predicted a 30% reduction in engine weight is achievable with a completely oil-free bearing.

Analytical work by Kim and San Andres (2005) coupled the Reynolds Equation with a simple elastic foundation model to investigate static and dynamic characteristics of a compliant foil journal bearing (CFJB). At high static loads, above 60 N, agreement of minimum film thickness and journal attitude angle with experimental data was found to be good, however for static

loads below 60 N a discrepancy was evident which the authors contributed to fabrication issues. San Andres and Kim (2007) then presented an improved analytical model that uses 1D and 2D finite elements to account for the deflection of the top foil instead of the previous simple elastic foundation model. The FE model was coupled with the Reynolds equation for the hydrodynamic gas film to assess the performance of the foil bearing. The 2D model over-predicted the minimum film thickness at the centreline and underestimated it at the bearing edges. The 1D model gave the best correlation compared to experimental data and was less expensive computationally. Both the 1D and 2D models predicted lower stiffness and damping coefficients compared to simple elastic foundation model.

The previous work formed the basis for a predictive tool used by NASA, XLGFBTH, which was validated by Howard and San Andres (2010). The predicted critical speeds were found to be in excellent agreement with the measured ones. On the other hand, a considerable disparity in the amplitudes of motion was realized, although the correct trend was captured. Errors in the balancing procedure of the rotor assembly due to measurement uncertainty in addition to the prediction of the bearing initial clearance could be possible reasons for the disagreement. In summary, the analytical tool's capability in accurately predicting critical speeds appears to be its strongest point.

2.3 Self-Acting Face Seal

As mentioned in *section 1.2.3*, rubbing contact and the affiliated thermal deformations limit the operational capabilities and performance of conventional face seals. To achieve non-contacting operation Johnson and Ludwig (1969) described the 'Self-acting Face Seal'. The seal incorporated lift-generating features, influenced by the design of gas lubricated self-acting thrust bearings where the stationary part included Rayleigh step pads for lift generation. The

Rayleigh step pads were used to generate extra lift, thus aiding in keeping the seal faces in a non-contacting mode of operation.

Such a self-acting face seal was tested by (Ludwig, 1971) in a rig which simulated a gas turbine engine bearing sump. The seal was subjected to pressure differentials ranging from 0.35 to 2.07 MPa, temperatures up to 650 °C. Endurance runs amounting to 320 hours under a sliding speed of 122 m/s were performed. Additionally, leakage rates were found to be a tenth of that of a labyrinth seal. Lynwander (1973,1974), ran a series of tests on a self-acting seal with circumferential Rayleigh steps including a 500-hour endurance test and the outcome agreed well with what Ludwig presented before, minimal wear was incurred by the sealing faces implying that lift off had been successfully achieved and maintained. Lipchitz (1984) also described an early concept of a film-riding seal which remains in contact when the shaft is stationary but lifts off when the shaft is rotating due to hydrodynamic effects.

Lift generating features are not limited to Rayleigh steps, spiral grooves have also been used and offered the same effect as lift pads. Ludwig (1978b) replaced the Rayleigh steps with a spiral groove geometry and ran a 54-hour endurance test under engine representative conditions and the seal was reported to successfully lift-off and minimal wear was observed. The leakage rate was much lower than an equivalent conventional face seal while the load capacity was higher.

Zheng (2005) attempted to optimize the design of the spiral groove for a medium sized film-riding face seal. The author varied the following parameters; spiral groove angle, circumferential land to groove ratio, groove depth and the number of spiral grooves. A 2D model that solves the Reynolds equation was used to predict the pressure field in the sealing gap and was compared to a 3D CFD model. The 3D CFD opening force prediction was

consistently higher than the 2D model. The author attributed this to the inertial effects ignored by the 2D model. The seal was described as working very well by the author, however no details of the length of runs or running conditions were mentioned. Additionally, no conical or surface run-out distortions were tested. Although the author claims the seal design has great potential in aerospace gas turbines, the effects of distortion that are a primary reason why the seal has not yet been applied to aerospace gas turbines have to be assessed.

Later developments were presented by Munson (1992a). Munson attempted to modify an existing film-riding seal model used for pipeline compressors to one that would operate successfully in gas turbine environment. The seal outer and inner diameters were 183 and 163 mm respectively. Twelve spiral grooves were used for hydrodynamic lift generation. Initial runs reported that the seal failed due to mechanical distortion cause by the divergent coning of the mating ring. A stiffer support arrangement was applied to mitigate the divergent coning. The seal was tested at 22,500 RPM, 0.7MPa differential pressure and 570°C operating temperature. The seal ran successfully for 50 hours before rubbing was detected. The results showed good potential as the seal produced sufficient opening force and exhibited a low leakage rate.

Munson (1992b) also considered a design for a self-acting face seal for use at the compressor discharge location in a gas turbine engine instead of labyrinth seals. Two hydrodynamic lift generating features were considered; Rayleigh step pads and spiral grooves. Gas film analysis was performed using compressible 2D Reynolds equation to arrive at a set of operating conditions for the seal to be tested. The analysis considered radial coning deformations and misalignment. However, only converging coning was considered as the author ignored a

diverging coning possibility due to its undesirable effects. This assumption proved costly as will be seen in the next study.

The prototype seal underwent testing by Munson (1993). Pressure differentials ranged from 0.345 MPa to 4.1 MPa, temperatures ranged from 316°C to 649°C and rotational speeds up to 25 kRPM were considered. Dynamic tests for the spiral groove case revealed that the seal achieved lift-off at low pressure differentials and exhibited the predicted level of low leakage. The leakage rate increased with increasing pressure differential and rotational speed. The Rayleigh step seal static test showed very high levels of torque and upon investigation it was realized that a radial divergent coning has decreased the opening force compared to what had been predicted in a previous analysis that did not account for divergent coning. Leakage rates for the film riding face seal were reported to be one tenth of a labyrinth seal for a range of pressure differentials.

2.4 Compliant Foil Seal

Although the concept of the 'film riding face seal' proved to be successful in industrial compressors and in the pipeline industry, it did not find the same success in aerospace gas turbine engines, despite its excellent performance in terms of leakage and hence reduced fuel consumption. Large thermal gradients and shaft movements, particularly at engine transients, in an aerospace engine increase the severity of the sealing faces distortions. As a result, keeping the surface flatness within confined limits to maintain non-contacting operation cannot be guaranteed. Clogging and rubbing-off of the fine lift features is another issue that obstructs the seal's ability to lift-off. Compliant bearings as discussed before have shown potential in increasing the compliance of the stationary face to track an out-of-flat runner, this combined with the self-acting face seal ability to track axial movements of the runner due to thermal

growth and shaft excursions could help establish this technology in aerospace gas turbines (Munson, 2009).

2.4.1 Compliant Circumferential Foil Seal

Munson et.al (2001) developed a circumferential foil seal with the intention of using it in turbine rim locations. The seal was broken into 18 individual segments distributed around its circumference. The segments were free to tilt about a pivot point the same way a tilt pad bearing to give it more compliance. Two methods of producing hydrodynamic pressure were tested. The first method included Rayleigh steps on the segmented pads and the second had no fine lift geometry and was rather dependent on the tilting of the pads to create hydrodynamic lift. The leakage rate was reported to be slightly higher than a self-acting seal but was considerably lower than of a brush seal. However, the seal concept was abandoned as it eventually failed due to issues related to curvature mismatch between the segments and the runner at high operating temperatures.

Salehit et.al (1999) performed numerical and experimental investigations on applying foil seals (journal) to gas turbine engines. For a pressure differential of 0.224 MPa and a rotational speed of 30 kRPM the leakage rate for the compliant foil seal was approximately three times lower than that of the rigid one. Additionally, the leakage rate showed very little variation with increasing eccentricities for the compliant seal, unlike the rigid seal. The compliant seal was then tested at differential pressure up to 4bar and rotational speeds up to 40 kRPM. The seal lifted-off successfully. Additionally, the foil seal exhibited much lower leakage rates than an equivalent labyrinth seal at all pressure differentials. The leakage rates were compared with the analytical model and were found to be in good agreement. However, the claimed near-constant leakage rate with varying eccentricity was not validated experimentally.

Salehi et.al (2000b) then tested the performance of a compliant foil seal experimentally in a small gas turbine simulator under high temperatures (up to 600°C) and rotational speeds as high as 56kRPM. Rotordynamic behaviour showed the seal's response to be well damped and performed in a stable manner. A brush seal was tested on the same simulator and clear signs of wear were found on the runner surface due to friction with the bristles. Contrariwise, neither the compliant foil surface nor the journal surface showed any signs of wear. The leakage rate of the two seals was also compared at pressure differentials up to 0.97 bar at 40 kRPM. It was reported that the leakage rate for the compliant seal was almost four times lower than that of the brush seal. However, the load capacity parameter was not included in this study.

Further experiments were carried out by Salehi et.al (2002) on a larger diameter seal at higher pressure differentials than considered earlier, up to 0.62 MPa. The study asserted that the performance of the seal, particularly in terms of leakage rate, was more of a function of the inlet pressure rather than the rotational speed. The relationship between leakage rate and inlet pressure was observed to be linear. Dynamic tests at 14 kRPM for pressure differentials of 0.345 MPa and 0.55 MPa were executed showing the seal displacements to be well-damped. The minimum lift-off speed achieved was 1000 RPM and the seal was able to maintain non-contact operation successfully with rotor eccentricities up to 0.15mm. The seal was a subject of a patent by Heshmat *et.al.* (2003). Although the study reports a capability for high temperature testing, the tests reported were performed at room temperature.

Heshmat et.al (2010) tested a compliant foil seal for application in a high-speed hydrogen compressor. Static and dynamic tests were performed at elevated temperatures (260 °C) and rotational speeds up to 60 kRPM. The study focused on leakage rates which were reported to be very low. Dynamic tests showed lower leakage rates due to the centrifugal growth of the

runner and hydrodynamic film developed in the gap. The leakage was highly dependent on the inlet pressure and the radial clearance between the shaft and the top foil. Additionally, lower leakage rates were observed at higher temperatures.

2.4.2 Compliant Foil Face Seal

Munson et.al (2001) considered implementing a foil face seal by combining the thrust-bearing part found on the stationary face of a compliant foil gas thrust bearing with a conventional face seal concept instead of the circumferential design. The process focused on optimizing the compliant foil thrust bearing part having a high film stiffness, load capacity and maximum flexibility of the foil elements. The seal diameter was 11.43 cm; the primary seal ring design consisted of segmented top foil thrust bearings supported by corrugated bump foils. Coning distortions and circumferential-out-of flatness (waviness) of the rotor were assessed. Instead of incorporating lift-generating geometries, the seal would rely on tilting of the pads to generate hydrodynamic pressure. Relying on the tilt of the segmented foil pads to distort and create sufficient hydrodynamic lift is reported to have been successful for this study. This is encouraging as no machining of fine features is required which alleviates the risk of them being clogged in operation. Collectively, seal testing reported that the seal successfully tracked the motion of the wavy plates tested. The range of distortions covered was reported to be over two orders of magnitude larger than a conventional face seal would be capable of handling.

Munson *et.al.* (2002) further tested yet another proof of concept foil face seal. For the circumferential out-of-flatness, three and five waves were machined on the surface on the runner with an amplitude of 76 microns. In this study, three different bump foil stiffnesses were considered; 12784, 11558 and 5604 N/mm. Running at 45 kRPM, the stiffest bump foil produced the largest load capacity, 280N, against the three-wave runner and 218N against the five-wave runner. It was also noticed that introducing waviness decreased the load capacity of

the seal. The leakage rate decreased with an increasing load indicating the gap height between the top foil and the runner is reduced while it increased at higher rotational speeds. Additionally, higher pressure ratios showed higher leakage rates. It was also found that the lift-off speed was higher at larger axial loads. The lift-off speed versus load curve showed that the lift-off speed is a function of the square root of the applied load. The seal design was later patented by Agrawal, Munson and Patel (2007).

Munson (2009) performed tests on a larger diameter (0.305 m) foil face seal to be used at the outer fan location in the Trent 1000. The initial design omitted the use of bump foils and the top foil was mounted on a less compliant foil in attempt to reduce leakage. The seal failed to conform to radial coning distortions and rotor waviness. The absence of the compliance provided by the bump foils has hindered the performance of the seal. Hence, a re-design took place and the bump foils were included within the seal setup. However, unexpected high levels of torque were measured at the start of the testing procedure which led to the damage of the top foil. The author explains that a lack of analytical methods to predict the force balance between opening and closing forces for this type of seal constituted an issue for the current design and caused its failure. A design methodology formulated for this novel seal is seen as a necessity for a successful working concept.

2.5 Literature Review Summary

A brief overview of the fundamentals of fluid film lubrication and its application to bearing and sealing technologies has been presented. The benefits of non-contacting compliant seals and their potential gains have been highlighted. The difficulty in maintaining surface flatness and handling distortion were the main obstructions deterring the application of such seals in aerospace engines. Increasing the compliancy of the sealing faces was presented as a potential

solution to increase the capability of the seal to handle a wider range of distortions. The literature survey presented here shows that the emphasis of the majority of face seal research focused on widening the operational envelope of face seals while holding the ultra-low leakage characteristic as the primary objective. As previously discussed, it would not be possible for a conventional face seal with the very small gaps typical of those seals to survive in an aero-engine. However, the ability of a face seal to provide large axial movements while sacrificing some leakage can aid in establishing the technology in engine locations where movements due to thermals are quite large but poorly understood, for instance the tail bearing housing (TBH) location. Hence, there is an evident gap in the literature studying the pressure fields in larger gaps (> 50 μm) both numerically and experimentally which would be necessary to develop an understanding of the air-film behaviour under a range for face distortions.

The closest viable concept of an air-riding flexible face seal to the current work was that described by Munson (2009), however the seal failed to perform as expected due to the absence of a predictive tool that produced an accurate force balance for this specific type of seal. The pressure balance on the seal's faces due to the gap profile was described as a crucial design parameter for this type of seal. This would require a thorough understanding of the pressure field in the sealing gap, which is one of the main objectives of this project. A design methodology is deemed necessary if this concept was to progress to a higher technological level. Consequently, Rolls-Royce Plc have provided a MATLAB code based on the 2D Compressible Reynolds Equation to predict the pressure field in the sealing gap. The author has in turn done initial validation work using existing experimental data and 3D CFD modelling covered in *chapter 3* . An experimental campaign took place after the validation process was completed to obtain pressure field data in radially distorted gaps. Further numerical models were formulated to support the experimental data, reported in *chapter 5*. Subsequently, the data

collected from the previous two steps were utilized to design and test a more-engine realistic seal in *chapter 6*. The seal underwent a series of tests under representative engine conditions and the results were reported to supplement the knowledge included in this literature review.

3 Validation of 2D Reynolds Flow Model against Existing Experimental Data and 3D CFD

This chapter reports on the validation process of a finite volume code supplied by Rolls-Royce that predicts the radial pressure distribution along the seal gap. The code is based on the 2D compressible form of the Reynold's equation for thin film flows and is derived in the Appendix of this thesis for reference. The objective of the numerical model is to predict that pressure distribution in the primary gap of the seal which subsequently allows for the air-film force to be computed. The code is capable of predicting the radial pressure distribution in the gap for parallel gaps as well as radially coned gaps, both converging and diverging. Moreover, radial steps can also be modelled within the seal gap. The code is intended as a quick design tool for face seals. Previously seen behaviour near the entrance to face seal suggests that inertially dominated effects must be modelled requiring validation process prior to widely accepting the use of this tool for further design purposes (Aubry, 2011).

An existing set of experimental data was used to make a preliminary validation of the pressure fields predicted. These data include radial pressure distributions for parallel gap geometries over a range of minimum gap heights, in addition to parallel gaps with radial steps at different locations along the seal's radial extent. Due to the lack of pressure distributions for radially converging and diverging gaps in both relevant literature and the lab's database, it was decided to formulate a surrogate 3D CFD model to allow the validation of the numerical model for radially coned gaps. Further robust validation is provided by an experimental campaign to obtain data for the aforementioned gap configurations, refer to *chapter 4*. Regarding radial steps, only experimental data for parallel gaps with radial steps were available. Hence, in this

research the 3D CFD model was used to model radially coned gaps with radial steps and these were then used to assess the applicability of the numerical model.

3.1 The 2D Model

The numerical code was developed by Dr. John Garratt of Rolls-Royce and is an implementation of the 2D compressible Reynolds equation (see Appendix A) subject to isothermal conditions. Using the formulation of Hughes (1992) this may be written in polar coordinates as.

$$\frac{\partial}{\partial r}\left(\frac{rph^3}{\mu}\frac{\partial p}{\partial r}\right)+\frac{1}{r}\frac{\partial}{\partial \theta}\left(\frac{ph^3}{\mu}\frac{\partial p}{\partial \theta}\right)=6r\omega\frac{\partial(ph)}{\partial \theta} \qquad \textbf{Eq. A.24}$$

The above equation is implemented and discretised in the code in its non-dimensional form. The following non-dimensional parameters govern the flow:

$$\boldsymbol{P}=\frac{p}{p_{out}}, \qquad \boldsymbol{H}=\frac{h}{h_{min}}, \qquad \boldsymbol{R}=\frac{r}{r_{outer}}, \qquad \boldsymbol{\theta}=\boldsymbol{\theta}, \qquad \boldsymbol{M}=\frac{\mu}{\mu_o}$$

as:

$$\frac{\partial}{\partial R}\left(\frac{RPH^3}{M}\frac{\partial P}{\partial R}\right)+\frac{1}{R}\left(\frac{PH^3}{M}\frac{\partial P}{\partial \theta}\right)=\boldsymbol{\Lambda}\,R\,\frac{\partial}{\partial \theta}\,(PH) \qquad \textbf{Eq. A.25}$$

Where $\boldsymbol{\Lambda}$ is a dimensionless parameter referred to as the bearing number or the compressibility factor (Hamrock, 1991).

$$\boldsymbol{\Lambda}=\frac{6\,\mu_o\,r_{outer}^2\,\omega}{p_{out}\,h_{min}^2} \qquad \textbf{Eq. A.26}$$

The bearing number relates the level of fluid compressibility to the sliding speed and film thickness (Vasco, 2009). The closer the bearing number is to zero, the more incompressible the flow is. Commonly, bearing numbers of $\boldsymbol{\Lambda} > 20$ are considered to be large. Note that, in the

code the walls of the domain are assumed to be isothermal such that as the flow is compressible, the kinematic viscosity (ν) changes while the dynamic viscosity (μ) remains unchanged. The code employs Sutherland's Law, Eq. A.27, to model dynamic viscosity wherein the effect of temperature variation is accounted for.

$$\frac{\mu}{\mu_{ref}} = \left(\frac{T}{T_{ref}}\right)^{3/2} \frac{T_{ref}+S}{T+S}, \quad \text{where for air} \qquad \textbf{Eq. A.27}$$

$\mu_{ref} = 1.789\times10^{-5}$ kg/ms , T_{ref} is 288K and S=110K.

The assumptions made in the derivation of the Reynolds equation are listed below:

1- The flow is laminar.
2- Viscous shear forces are much larger than inertia and body forces, so the effects of the latter are neglected (due to very small aspect ratios).
3- The weight of the fluid and body forces are negligible
4- No-slip exists at the fluid-solid interface
5- The pressure across the film depth (rotating face to static face) is constant.

The inputs to the code are; 1- inlet pressure, 2- outlet pressure, 3- runner Speed, 4- air-film temperature, 5- inner and outer radii, 6- coning height, step height and position. The geometry notation used in the code is illustrated in Figure 3-1. The viscosity is calculated using Sutherland's Law.

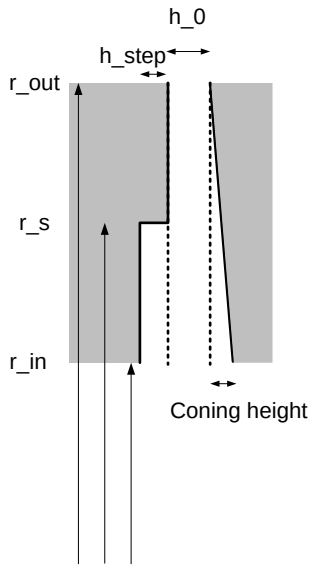

Figure 3-1: Geometry notation used to define gap profile.

The code is an implicit solver and the finite volume discretization method (FVM) is employed to approximate the 2D compressible Reynolds equation. The flow chart shown in Figure 3-2 outlines the solution methodology applied in executing the code. First, the boundary conditions of the problem are specified. The solver then computes the flow domain geometry taking into account coning (both converging and diverging) and the presence of radial features (radial steps), if any. A structured grid is then created based on the number of radial and azimuthal elements defined by the user. Note that for unknown values at cell faces, a first order upwind differencing scheme is used for interpolation. Subsequently, an initial guess is made to evaluate the pressure field $\boldsymbol{P_{vec}(i_0)}$ followed by evaluating the velocity field $\boldsymbol{v(i_0)}$. The initial fluxes $\boldsymbol{q_0}$ are then computed and the system of non-linear equation is assembled. At the start of the solution loop, the Jacobian matrix [$\boldsymbol{J}$] of the non-linear system of equations is evaluated. This then allows the system to be linearly approximated and solved using Newton's Method such that

$$x_1 - x_0 = \Delta = [\boldsymbol{J}]^{-1}\boldsymbol{f}(x_0) \qquad \textbf{Eq. 3.1}$$

The pressure field is then updated using the solution vector $\boldsymbol{\Delta}$ such that

$$\boldsymbol{P_{vec}}(i_1) = \boldsymbol{P_{vec}}(i_0) - \Delta \qquad \textbf{Eq. 3.2}$$

Based on the updated pressure field $\boldsymbol{P_{vec}}$, a new velocity field $\boldsymbol{v}$ is evaluated. The residual is then calculated and convergence monitored. The solver terminates if convergence criteria are met. Otherwise, more iterations are executed till either convergence or the maximum number of iterations is reached.

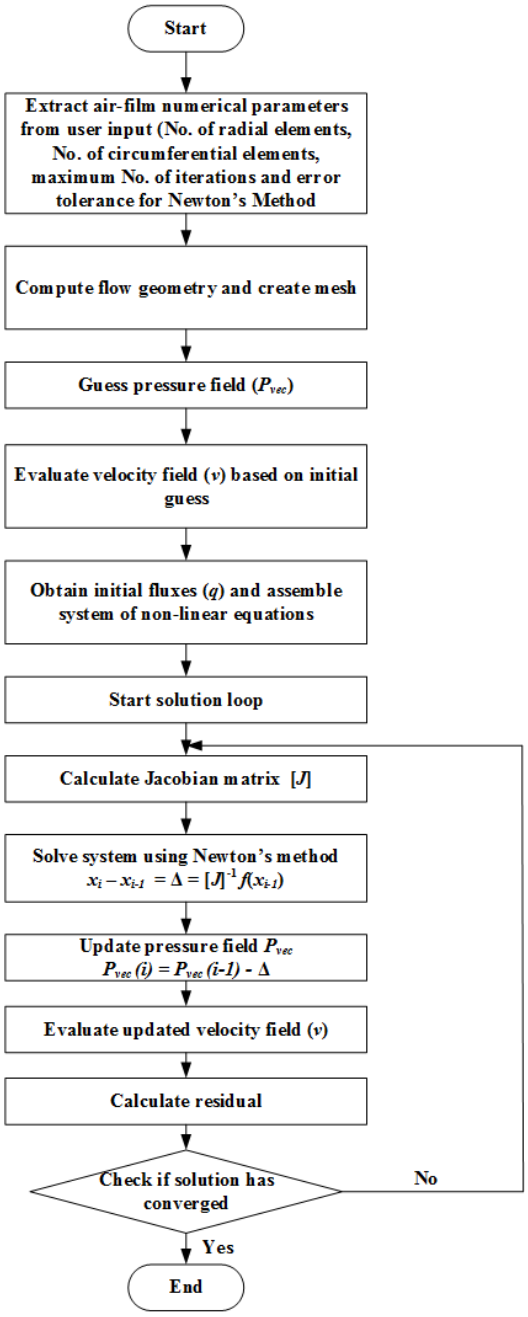

Figure 3-2: Flowchart showing method of solution of 2D Reynold's flow solver.

3.2 Validation with Experiments for Parallel Gaps With and Without Radial Steps

In the early stages of research independent experimental data were not available. Hence, work performed by Aubry (2011) on another face seal concept, a self-centring face seal, generated a set of experimental pressure distribution data that were used to validate the analytical model. The seal's leakage path is described in Figure 3-3. The radial leakage path length (***L***) is 11 mm and the total seal gap height, $(h_u + h_d)$ is 400 µm. Experimental pressure data from the upstream leakage path was used for validation. Initially, parallel gap profiles were considered. The minimum gap heights tested were h_{min} = 200 µm and 50 µm at inlet pressures of 2.07 and 3.45 bar (gauge), downstream pressure being atmospheric.

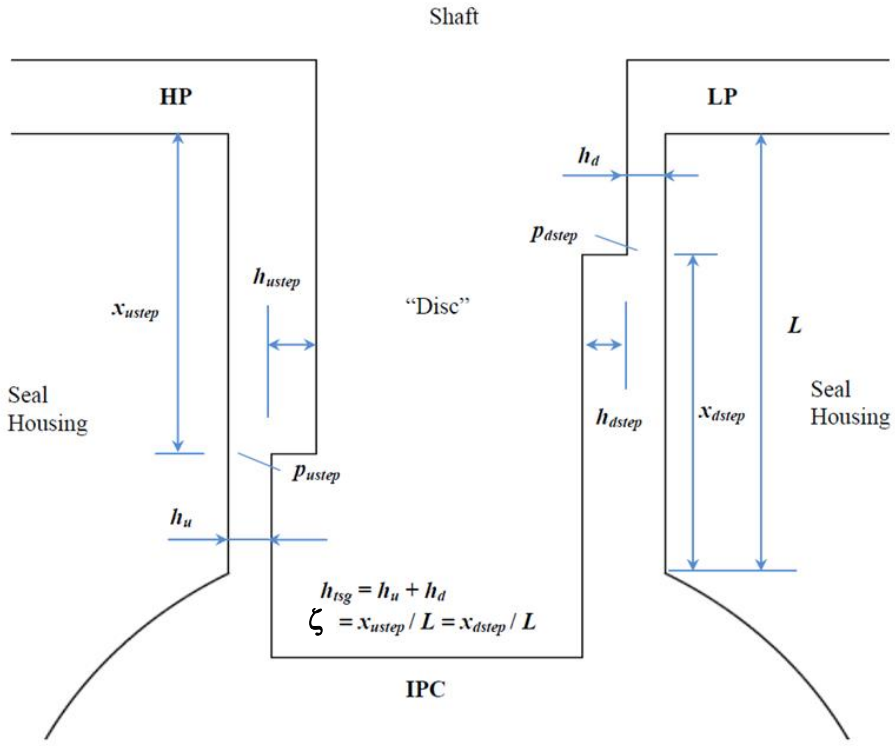

Figure 3-3: Self-centring seal leakage path, only upstream portion of seal (HP to IPC) is considered in this study, Aubry (2011).

Figure 3-4, Figure 3-5, Figure 3-8 and Figure 3-9 show the non-dimensional radial pressure against the non-dimensional radial position. The local pressure was non-dimensionalised by the inlet pressure ($p(r)/p_{in}$). The non-dimensional radial position at 0 denotes the inner radius and at 1 represents the outer radius. Figure 3-4 and Figure 3-5 show the radial pressure distribution for a minimum gap height of 200 μm. The pressure drops almost linearly from the inlet until the flow exits the gap. An important aspect to note is the significant pressure drop at the entrance to the sealing gap, *i.e.* the value is not unity. The numerical model assumes that the flow is dominated by viscous forces, and does not account for finite accelerations losses due to inertial forces as the flow turns a sharp corner and is accelerated into the sealing gap. To allow comparisons of the pressure distributions within the gaps, the inlet pressure loss obtained experimentally was used to set the inlet pressure in the gap, keeping the outlet pressure as atmospheric. Comparing the two cases, a higher normalised inlet loss is seen for the lower inlet pressure case (2.07 barg). For the same inlet pressures, but smaller minimum gap height, Figure 3-8 and Figure 3-9, the numerical model prediction showed similar trends to the larger gap height particularly in terms of the entry loss followed by a viscous drop till the gap exit. In these pressure distributions the characteristic curvature associated with the compressible Reynold's flow solution is clearly seen, however at the lower upstream pressure shown the experimental results remain surprisingly linear. Unlike the larger gap height, the numerical predication agreed better with experiments at the higher inlet pressure (3.45 barg),

In order to quantify the error in the numerical prediction, the absolute and relative errors for each of the considered cases were computed and plotted in Figure 3-6, Figure 3-7, Figure 3-10 and Figure 3-11. The absolute error was calculated as the difference between the experimental results and the numerical model and has the units of bar, Eq. 3.3. The relative error was taken

as the ratio between the absolute error at a given data point and the experimentally measured value, Eq. 3.4.

$$Absolute\ Error = Experimental\ Measurement - Code\ Prediction \qquad \textbf{Eq. 3.3}$$

$$Relative\ Error = \frac{Absolute\ Error}{Experimental\ Measurement} \qquad \textbf{Eq. 3.4}$$

The relative error for the 200 μm gap case shown in Figure 3-6 and Figure 3-7 for both inlet pressures, showed a maximum error magnitude of 3% for the lower inlet pressure case and a maximum error of less than 2% for the high inlet pressure case. Note, that the error was zero at the inlet and outlet to the gap as they are prescribed boundary conditions in the code. The inlet pressure prescribed in the code is based on the experimentally measured value after accounting for the entry loss. The relative error for the 50 μm case shown in Figure 3-10 and Figure 3-11 was higher than the 200 μm case for both inlet pressures considered. For P_{IN} = 2.07 barg, a maximum relative error of 10% was computed while half this value was recorded for the highest inlet pressure case.

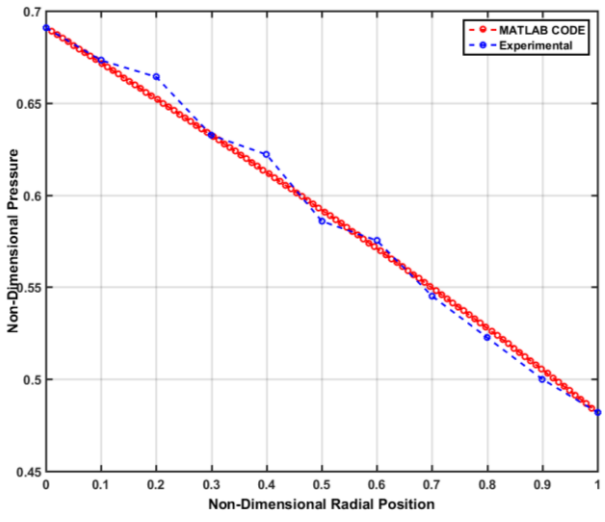

Figure 3-4: Non-Dimensional Radial Pressure Distribution, P_{in} =2.07 barg, h_{min} = 200μm

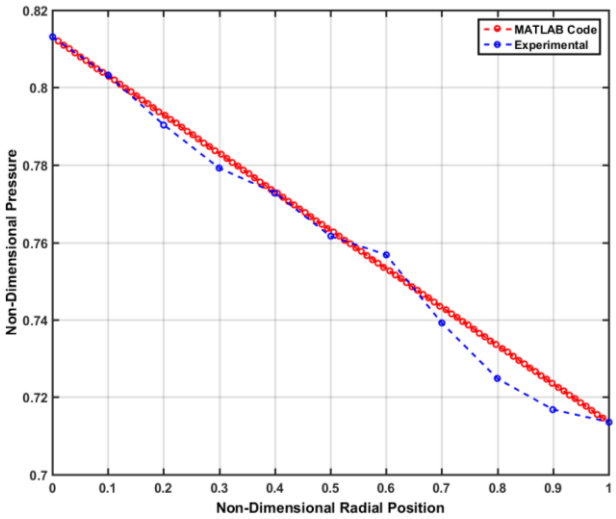

Figure 3-5: Non-Dimensional Radial Pressure Distribution, P_{in} =3.45 barg, h_{min} = 200μm

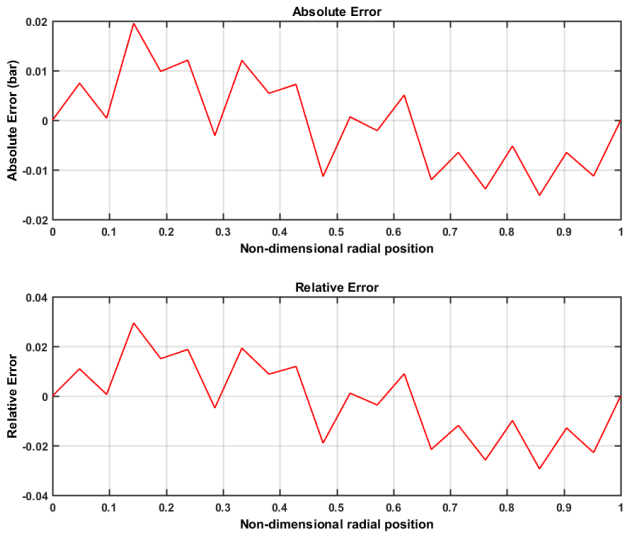

Figure 3-6: Absolute error (bar) and relative error, P_{in} =2.07 barg, h_{min} = 200µm

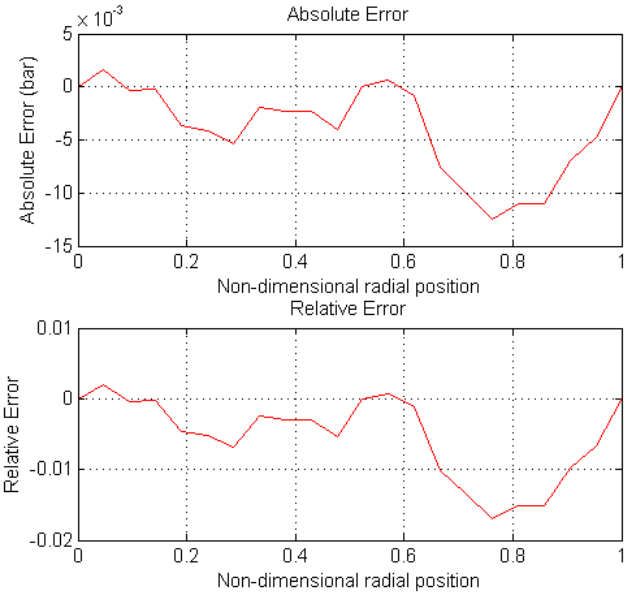

Figure 3-7: Absolute error (bar) and relative error, P_{in} =3.45 barg, h_{min} = 200µm

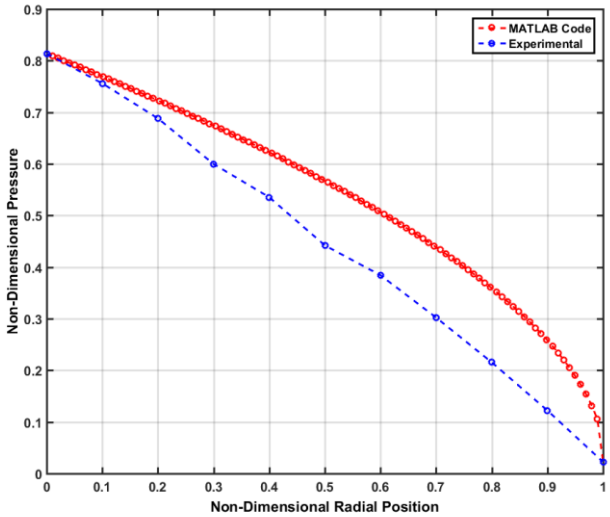

Figure 3-8: Non-Dimensional Pressure Distribution, P_{in} =2.07 barg, h_{min} = 50µm

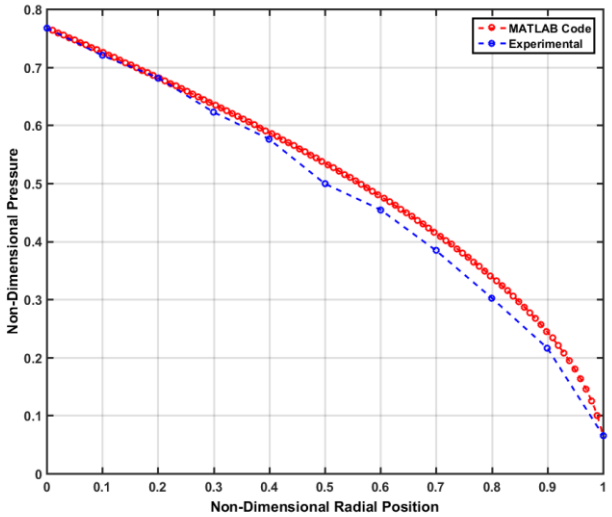

Figure 3-9: Non-Dimensional l Pressure Distribution, P_{in} =3.45 barg, h_{min} = 50µm

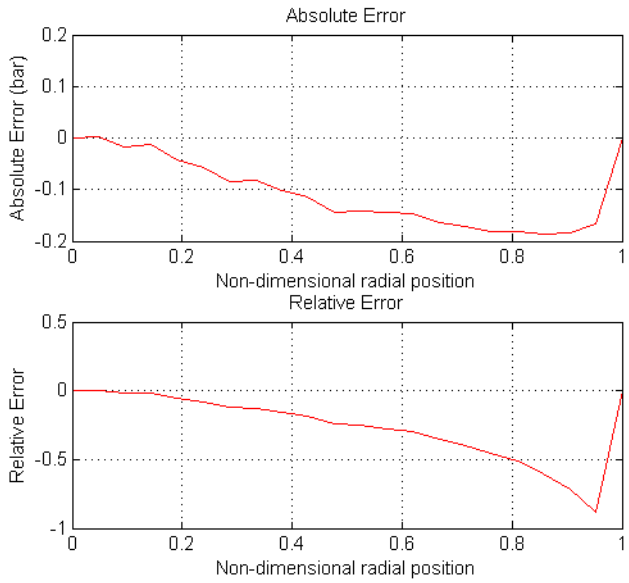

Figure 3-10: Absolute error (bar) and relative error, P_{in} =2.07 barg, h_{min} = 50µm

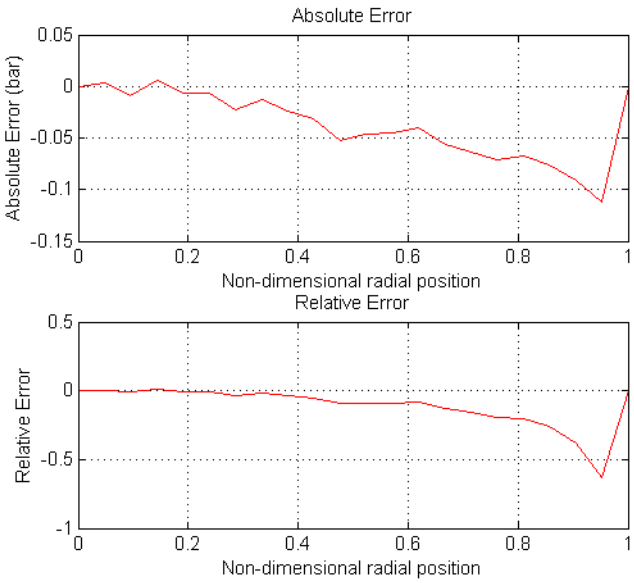

Figure 3-11: Absolute error (bar) and relative error, P_{in} =3.45 barg, h_{min} = 50µm

The effect of incorporating radial steps along the seal was considered next. The position of the step is described as a percentage of the total radial length (L = 11 mm), denoted by ζ. A schematic of the leakage path was described in Figure 3-3. Three radial step locations were considered, at ζ = 50%, 75% and 90% of the total radial length. Figure 3-12 and Figure 3-13 consider a 200 µm radial step located at ζ = 50% for a minimum gap height of 200 µm, i.e. the step reduces the gap height from 400µm at the inlet to 200 µm at ζ =50%. Figure 3-14 and Figure 3-15 are the pressure profiles for a 50 µm gap height and the same step height and position as before. Results are shown for 1.03 and 3.45 bar (gauge) inlet pressure.

As with the no radial step case the pressure drop at the gap inlet was evident, however it was not as significant as most of the pressure drop occurred downstream of the step due to the relative change in gap height. Furthermore, another inertial loss was encountered as the flow accelerates into the smaller gap height at the step position. Such discontinuity is clearly seen in experimental data but not captured by the numerical model. The viscous pressure drop downstream of the step then continues until the flow exits the gap.

The effect of varying the radial position of the step was investigated and the pressure distributions are shown in Figure 3-16. The cases show varying the step position for a 50 μm minimum gap height and a 100 μm step height at 0.69 bar (gauge) inlet pressure. From the information presented, it can be concluded that moving the step further down the radial length delays most of the pressure drop until the step location. This implies that the seal's opening film force would benefit from adding a radial step closer to the primary gap's exit as it will aid in maintaining most of the film pressure along a large portion of the gap's radial extent.

In conclusion, the numerical model gave accurate predictions for the pressure distribution of parallel sealing faces only when the inlet pressure loss was accounted for by the user prior to running the simulation. This is due to the assumptions postulated when deriving the 2D compressible Reynold's equation where the flow is assumed to be viscously dominated and inertial forces are ignored. The inclusion of radial steps has further highlighted that another significant pressure drop due to acceleration losses at the radial step position is not captured by the numerical model. The inability of the numerical model to capture the aforementioned losses is again due to inertial forces which tend to be significant at discontinuities such as the sharp corner leading into the gap or the sudden gap height reduction introduced by the radial step. All cases shown are for stationary conditions. As per Reynold's equation, hydrodynamic lift will be generated only if there is a change in gap height in the direction of rotation i.e. the circumferential direction.

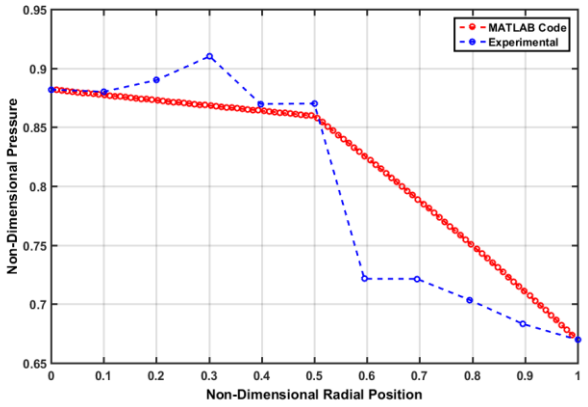

Figure 3-12: Non-Dimensional Radial Pressure Distribution, P_{in} =1.03 barg, h_{min} = 200µm, ζ=50%, h_{step} = 200µm

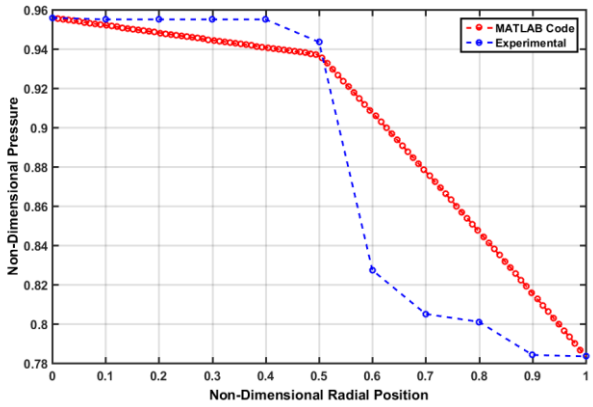

Figure 3-13: Non-Dimensional Radial Pressure Distribution, P_{in} =3.45 barg, h_{min} =200µm, ζ=50%, h_{step} = 200µm

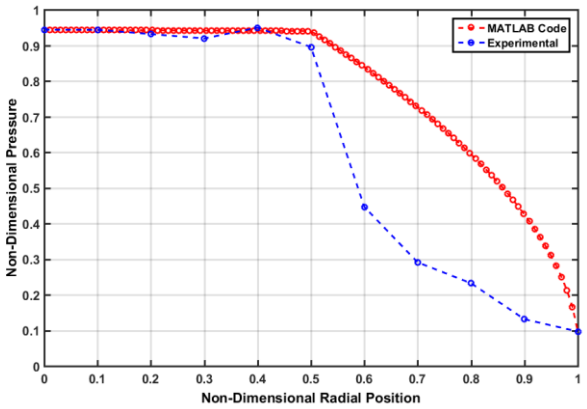

Figure 3-14: Non-Dimensional Radial Pressure Distribution, P_{in} =1.03 barg, h_{min} = 50µm, ζ=50%, h_{step} = 200µm

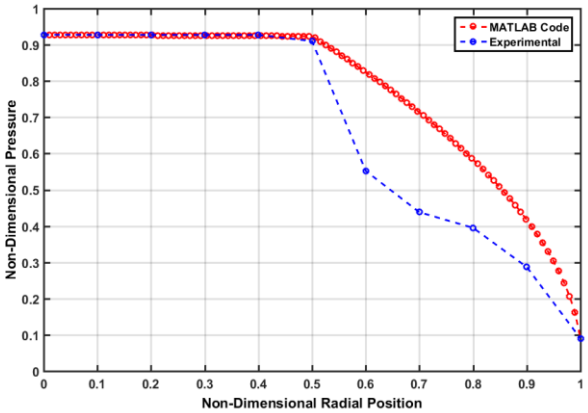

Figure 3-15: Non-Dimensional Radial Pressure Distribution, P_{in} =3.45 barg, h_{min} =50µm, ζ=50%, h_{step} = 200µm

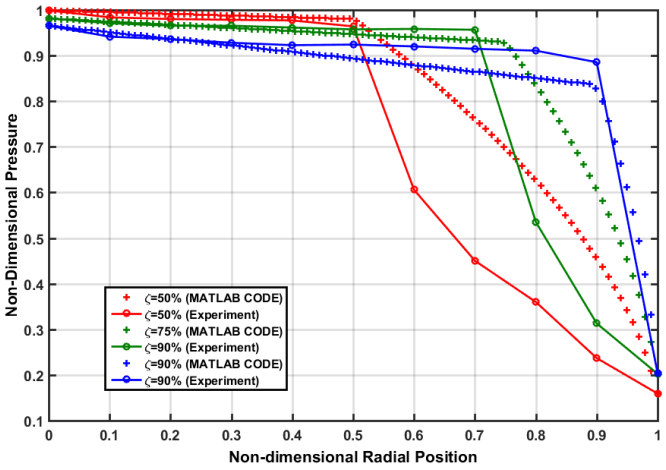

Figure 3-16: Non-Dimensional Pressure Distribution, P_{in} =0.69 barg, h_{min} =50µm, ζ =50, 75, 90%, h_{step} = 100µm

3.3 Numerical Model Validation against 3D CFD Model

The primary out-of-flatness distortions of interest in the current project are characterized by radial coning distortion, and circumferential waviness. Within this chapter only radial coning distortions are considered. Coning results in the sealing gap taking up a converging or a diverging path which alters the pressure distribution and affects the seal's performance. It is most likely to occur due to inhomogeneous thermo-mechanical loads but could also result from misalignment of one of the sealing rings or due to machining tolerances or be added by design. It is of paramount importance to investigate the resultant flow-field in the gap due to expected distortions. To do that, the author opted to formulate a CFD model and perform an initial investigation of the flow field under different radial coning configurations to be validated at a later stage by a set of experiments reported in *chapter 5*. The CFD results are compared to results from the numerical model, where possible.

3.3.1 Geometry and Mesh

A 3D CFD model of a 36-degree sector of the primary leakage path is shown in Figure 3-17. A 3D model allows the changing circumferential length scale to be correctly captured and also

periodic boundary conditions to be defined. Enforcing the cyclic periodicity boundary conditions enables the modelling of a sector rather than the complete domain. The cyclic boundary conditions, pressure inlet and outlet and salient features of the mesh are highlighted in Figure 3-17. Refer to Figure 3-1 for an outline of the geometry notation used to describe the minimum gap height, coning height, radial step position and height.

A multi-block structured mesh was built using ANSYS ICEM. The blocking of the domain is illustrated in Figure 3-18. The blocking was split into two zones; the green block represents a laminar zone for the seal gap while the rest of the domain was considered turbulent and is represented by purple blocks. The assumption of a laminar region in the primary gap is common in modelling seal flows due to the highly viscous flow expected the sealing gap, though this restriction can be further explored in simulations. A grid independent solution was obtained with 20 nodes along the primary seal gap, see *Appendix B*. The total number of elements was 1.4 million for all gap geometries tested.

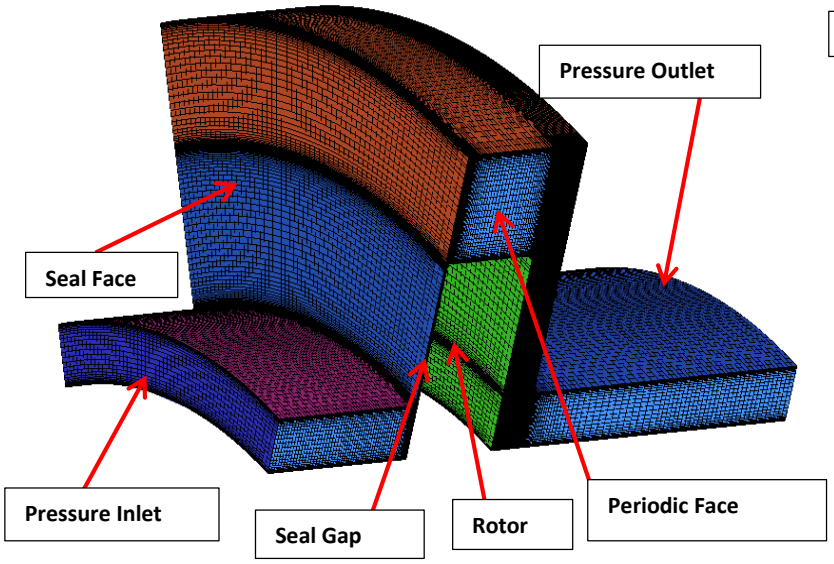

Figure 3-17: Leakage Path Geometry, Mesh and Boundary Conditions.

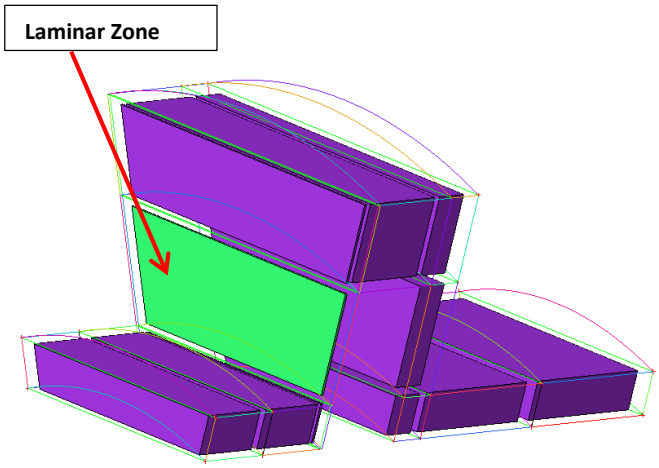

Figure 3-18: Domain Blocking, Green Block = Laminar.

3.3.2 Turbulence Modelling

The realizable k-ε model was applied in the turbulent zones (purple blocks). The initial values prescribed for the solution were based on the default settings in the solver, ANSYS Fluent. Since the seal gap is very small, the $y+$ values are inherently small and a $y+$ value of less than 1 was maintained within the seal gap. Enhanced wall treatment was used to allow for the laminar sub-layer to be adequately resolved. The choice of the k-ε turbulence model was based on the validity of an earlier setup to model a self-centring seal by Aubry, 2011.

3.3.3 Material Properties

The flow was treated as an ideal gas (air) making it necessary to solve the energy equation. The viscosity was set to be calculated using Sutherland's Law as per the numerical model. Furthermore, thermal conductivity, specific heat and molecular weight values were set to be constant.

3.3.4 Boundary conditions

The inlet and outlet were set as a pressure inlet and a pressure outlet respectively, based on atmospheric reference values. Only the inlet pressure was varied as the outlet pressure was assigned to be at atmospheric pressure for all cases in line with experimental conditions. The direction of the bulk flow was assigned to be along the axial direction. The walls were set to be isothermal walls and stationary, unless otherwise stated. The rotational/cyclic periodic boundary conditions set the periodicity of the model to be about the x-axis (axial direction). A *Second Order Upwind Scheme* was used for spatial discretisation and the *SIMPLE* scheme was chosen for pressure-velocity coupling.

3.3.5 Convergence Criteria

The solution is said to have converged when the continuity and velocity components scaled residuals fell below *1e-3* and the energy equation scaled residuals fell below *1e-6* and have reached a plateau. While the aforementioned values are arbitrary in ANSYS Fluent, the mass imbalance between the inlet and out mass flow rate was also monitored and had to be in the order of *1e-7* to consider the solution fully converged. Results and Discussion

Results from the effect of coning angle on the runner face are reported below. In the results a *-ve* angle represents a convergent coning while a *+ve* angle represents a divergent coning. The criteria used to assess the sealing performance are; pressure distribution within the gap, opening force acting on the primary sealing face (stator) and mass flow leakage rate. The combined effects of radial steps with a coned gap geometry are also presented Additionally, the result of adding radial steps within coned gaps is also presented, as this is the most likely embodiment of a final seal design.

To gain confidence in the CFD modelling procedure, radial pressure distributions from CFD model were compared against experimental data and the MATLAB code first for parallel gaps before further models were formulated. Figure 3-19 and Figure 3-20 show the radial pressure distribution for a parallel gap with a minimum height of 50 μm at 3.07 and 4.45 bar (Absolute). The pressure on the vertical axis and the radial position were normalised in the same manner as before. Note that the leakage path used for comparison was that of the upstream leakage path of the seal previously installed on the rig. Unlike when using the analytical model, the inlet pressure for the CFD was set blind of any knowledge of the inlet pressure loss, as the entire purpose of resorting to a CFD model is to capture entry losses and losses at other geometric discontinuities.

In general, pressure predictions from the CFD show better agreement with experiments compared to the analytical model. It also uncovers a feature not previously captured in experiments nor in the numerical model due to lower resolution and lack of inertial terms, respectively. CFD pressure predictions showed a region of pressure recovery downstream of the initial inlet loss which suggests that there is significant flow separation around the corner as flow comes into the seal gap followed by a region of re-attachment. Predictions from the 3D CFD model show excellent agreement with experiments in terms of capturing the inlet loss to the system.

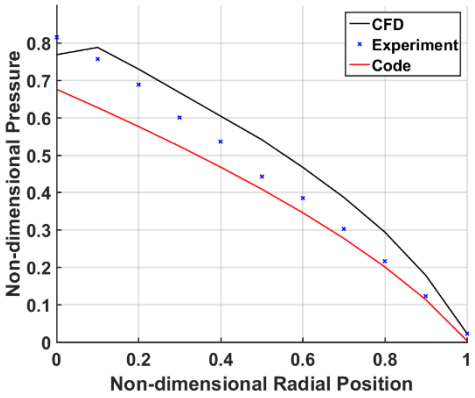

Figure 3-19: Parallel Gaps Radial Pressure Distribution, P_{in} =3.07 bar (Absolute), h_{min} =50µm

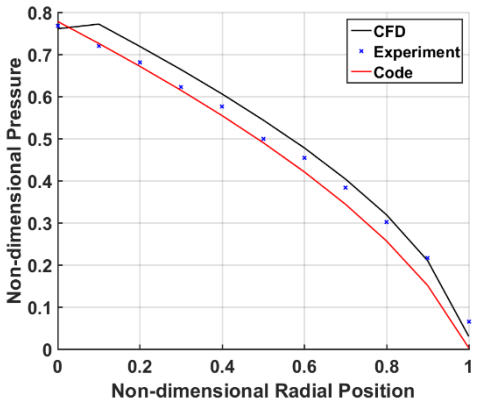

Figure 3-20: Parallel Gaps Radial Pressure Distribution, P_{in} =4.45 bar (Absolute), h_{min} =50µm

3.3.6 Parallel Gaps

3.3.6.1 Radial Pressure Distribution

Figure 3-21 and Figure 3-22 show the radial pressure distributions for inlet pressures of 2.03 bara and 4.45 bara at 20, 50,100, 200 and 300 µm minimum gap heights. The leakage path modelled is that of the new experimental setup with a radial length (***L***) of 15.5 mm.

It was evident that at smaller gaps the inlet pressure loss was less signficant than that of a larger gap at a given inlet pressure. This can be explained by considering the ratio of the fluids inertial

forces to the viscous forces (Reynolds Number) where at smaller gaps the mass flow rate is much lower and the flow tends to be dominated by viscous forces. As the gap height increases, so does the mass flow rate and therefore the inertia forces, giving rise to higher dynamic head with which the pressure loss at the gap inlet scales. Another point to observe is the pressure recovery following the loss at the inlet which is very pronounced at for the largest gaps (> 100 μm). Refer to Figure 3-23 and Figure 3-24 for absolute pressure contours illustrating the flow seperation around the corner and re-attachement for the 200 μm gap case at 2.03 and 4.45 bara, respectively. Additionally, at smaller gap heights a higher film pressure was maintained through the gap for any given inlet pressure. Clearly, this is desirable effect as provides for a higher permissible axial load. However, where a transition to inertially significant losses occurs there is a very rapid change in the overall load.

The CFD model and the analytical model results agreed well at the smallest gap height (20 μm) at all inlet pressures which is unsprising as the inertial terms, neglected in the model are insignifcant here. On the other hand, at larger gaps, the numerical model results deviate severly from the CFD predictions. Figure 3-25 and Figure 3-26 highlight the absolute and relative discrepency between the CFD results and the numerical model for all cases considered. For both inlet pressures considered, the magnitude of relative error increased with gap height. This is mainly down to the pressure recovery region that exits downstream of the gap inlet not being captured by the MATLAB code. The recovery region tends to be more significant for larger gaps due to the increased mass flow rate giving more way to inertial forces to get involved. For the smallest minimum gap (20 μm), a maximum local relative error magnitude of 10% was seen at P_{IN} = 2.03 bar and 20% at P_{IN} = 4.45 bar, at the same radial location at $r \sim 0.082$ m. Those values rose to over 50% for the largest gap height (300 μm) at locations just downstream

of the gap inlet. Note that, the absolute error here is taking as the MATLAB code prediction subtracted from the 3D CFD model predictions.

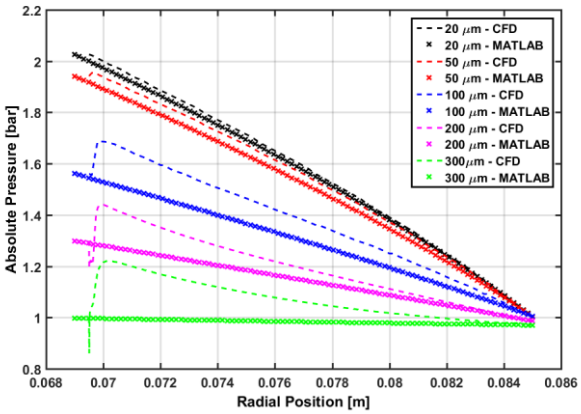

Figure 3-21: Parallel Gaps Radial Pressure Distribution, P_{in} =2.03 bar (Absolute), h_{min} =20, 50, 100, 200, 300µm

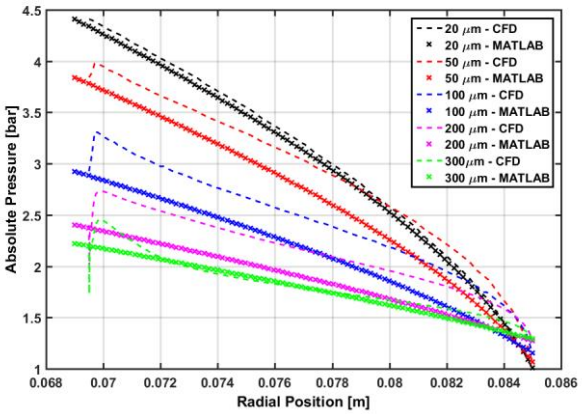

Figure 3-22: Parallel Gaps Radial Pressure Distribution, P_{in} =4.45 bar (Absolute), h_{min} =20, 50, 100, 200, 300µm

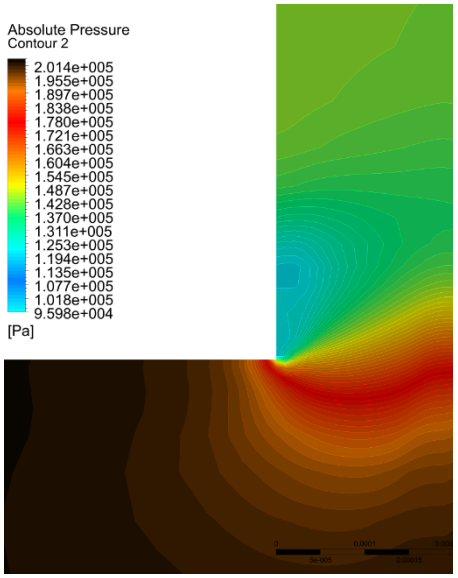

Figure 3-23: Pressure contour showing flow separation at gap inlet, h_{min} = 200 µm, P_{in} =2.03 bar (Absolute).

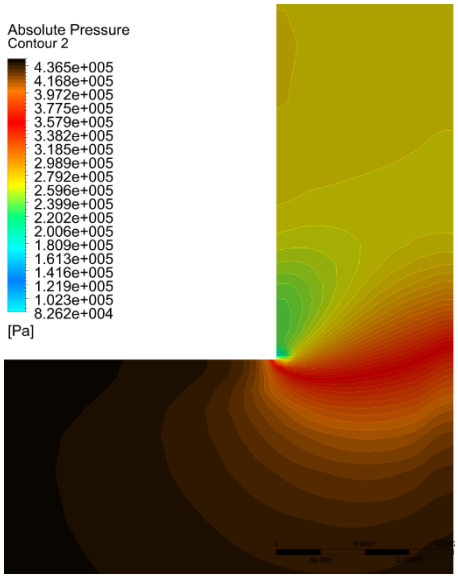

Figure 3-24: Pressure contour showing flow separation at gap inlet, h_{min} =200 µm , P_{in} =4.45 bar (Absolute).

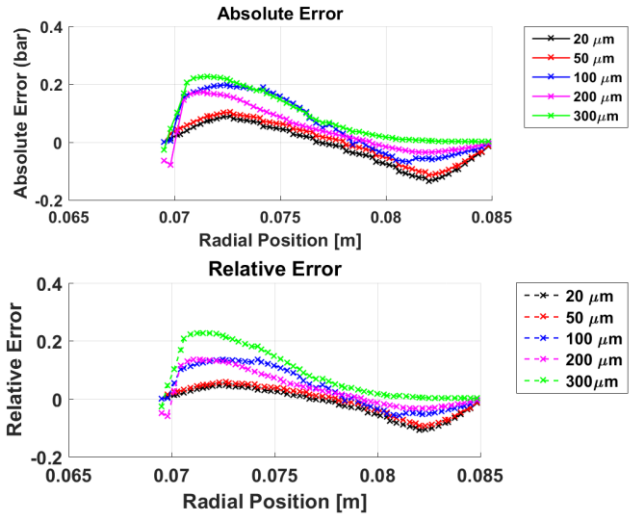

Figure 3-25: Absolute error (bar) and relative error, P_{in} =2.03 bar (Absolute).

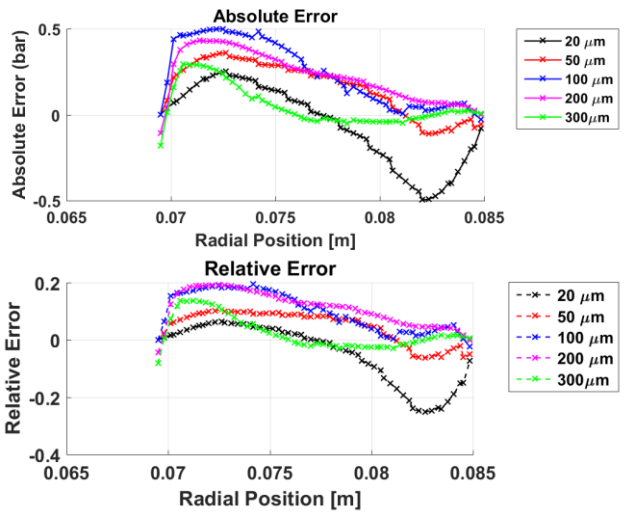

Figure 3-26: Absolute error (bar) and relative error, P_{in} =4.45 bar (Absolute).

3.3.6.2 CFD - Opening Force, Air-film Stiffness and Leakage rate

Figure 3-27 and Figure 3-28 show the force on the seal face due to the pressure generated by the air film and the air-film stiffness as predicted by the CFD through the integration of the pressure field over the seal face (stator). The air-film stiffness is defined as the rate of change of opening force with gap height.

From Figure 3-27 it is evident that at all inlet pressures the force dropped markedly as the minimum gap height increased. Moreover, at a given minimum gap height the opening force increased with increasing inlet pressure. The trend ties in well with the previously shown pressure distributions, as smaller gap heights maintained a higher film pressure and hence the increase in load capacity. Figure 3-28 shows the change in air-film stiffness with minimum gap height and inlet pressure. The highest air-film stiffness was yielded by the 50 μm gap and dropped progressively as the minimum gap height increased. Additionally, the air-film stiffness increased with increasing operating pressure for a given minimum gap height. It should be

noted however that a central differencing numerical scheme was employed to calculate the film-stiffness. Consequently, the points at either boundaries (20 μm and 300 μm) of the envelope were calculated using forward and backward differencing schemes. This exlpains the apparently higher stiffness calculated for the 50 μm compared to the 20 μm case as the slope of the curve is greater.

Figure 3-29 shows the mass flow leakage rate through the seal gap expressed as effective clearance, as a function of the minmum gap height at different inlet pressures. The effective clearance (*ec*), Morgan (2004) and represents the equivalent gap size for an isentropic flow in a seal with the same inner diameter that under the same pressure differential would give the same mass flow rate. Effective clearance can be used to compare leakage rates for seals of different geometries and can be expressed as follows;

$$ec = \frac{\dot{m}\sqrt{T}}{\pi\, p_u\, D\, Q} \qquad \textbf{Eq. 3.5}$$

$$Q = \begin{cases} \sqrt{\frac{2\gamma}{R(\gamma-1)}\left(\left(\frac{p_u}{p_d}\right)^{\frac{-2}{\gamma}} - \left(\frac{p_u}{p_d}\right)^{-\frac{\gamma+1}{\gamma}}\right)} & \left(\frac{p_u}{p_d}\right) < \left(\frac{2}{\gamma+1}\right)^{-\frac{\gamma}{\gamma-1}} \\ \sqrt{\frac{\gamma}{R}\left(\frac{2}{\gamma+1}\right)^{\frac{\gamma+1}{\gamma-1}}} & \left(\frac{p_u}{p_d}\right) > \left(\frac{2}{\gamma+1}\right)^{-\frac{\gamma}{\gamma-1}} \end{cases} \qquad \textbf{Eq. 3.6}$$

where;

Q	Dimensionless Flow function
$\dot{m}$	Mass flow rate (*kg/s*)
T	Upstream Temperature (*K*)
P_u	Upstream Pressure (*Pa*, Absolute)
P_d	Downstream Pressure (*Pa*, Absolute)
A	Flow area (m^2)

R Gas Constant ($R = 287\ J/kg/K$ for air)

γ Ratio of specific heats

The results collapse and to become essentially independent of inlet pressure with the exception of the lowest pressure case, where the flow may remain laminar at all gap heights and so no longer scale directly with the inlet pressure.

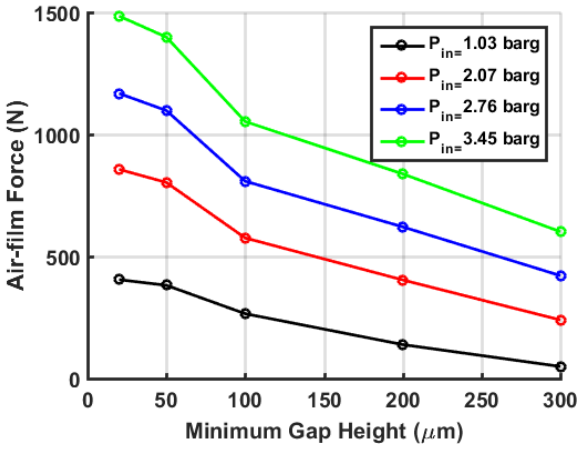

Figure 3-27: Effect of gap height on Opening Force.

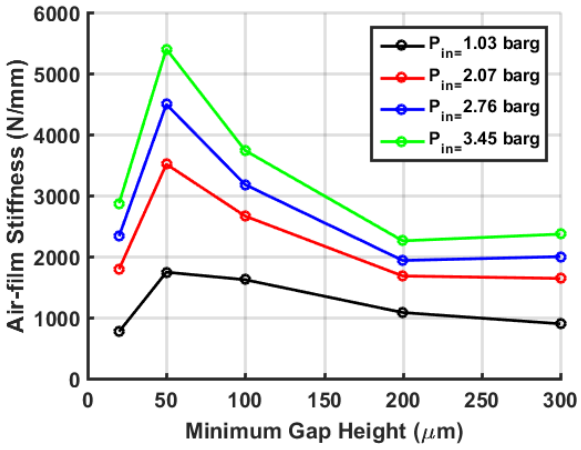

Figure 3-28: Variation of air-film stiffness with gap height.

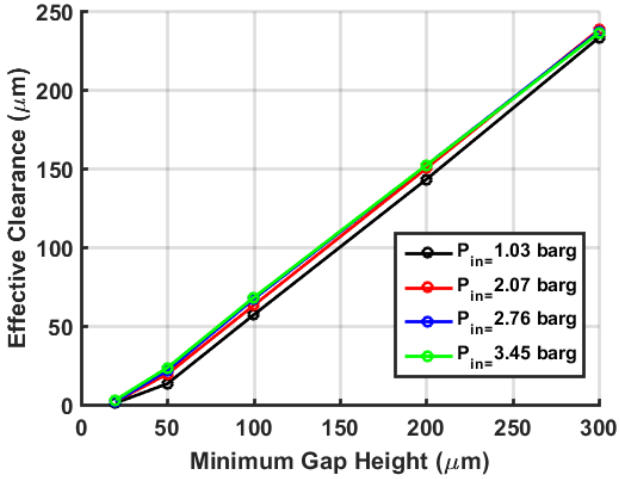

Figure 3-29: Effect of gap height on leakage rate.

3.3.7 Converging Coning

3.3.7.1 Radial Pressure Distribution

Figure 3-30, Figure 3-31, Figure 3-34 and Figure 3-35 show the radial pressure distributions both predicted by CFD and the analytical model for two minimum gap heights; 20 and 100 µm at inlet pressures of 2.03 and 4.45 bar. The coning angle, α, was increased from $\alpha = 0^o$ (parallel case) to $\alpha = -0.1^o$, -0.3^o and -0.5^o. Note that the aforementioned coning angles correspond to coning heights of 30 µm ($\alpha = -0.1^o$), 80 µm ($\alpha = -0.3^o$) and 140 µm ($\alpha = -0.5^o$), refer to Figure 3-1 for the definition of coning height (h_{coning}).

For the 20 µm gap case, it was evident that the film pressure within the gap increased with increasing the coning angle. Additionally, all coned cases showed a higher film pressure compared to the parallel gap case. This could be explained as follows, as the fluid enters through a larger gap height at the inlet than at the outlet, the working fluid is compressed generating a pressure build up, unlike parallel faces where no pressure build-up is encountered.

Regarding the 100 µm minimum gap case, Figure 3-34 and Figure 3-35, similar trends to the smaller gap height case are observed whereby the film pressure increases with increasing coning angle and remains higher than the parallel gap pressure distribution. Whereas the pressure loss at the inlet was negligible for the previous case, it was significant for the 100 µm gap cases where higher mass flow rates are seen and inertial forces become dominant. Interestingly, the inlet pressure loss decreases with higher coning angles while this is in line with the typical hole inlet considerations, the size of the reduction in loss is still surprising. This could be due to the higher film pressure generated at larger coning angles. The numerical model predictions were not in good agreement with the CFD at the larger gap heights due to

the inertia-driven pressure loss at the gap inlet followed by the zone of pressure recovery immediately downstream of the gap inlet.

Figure 3-32, Figure 3-33, Figure 3-36 and Figure 3-37 highlight the absolute and relative errors for both minimum gaps considered in this study ($\boldsymbol{h_{min}}$ = 20 and 100 μm) at the full range of coning angles and operating pressures. For the 20 μm case at P_{IN} = 2.03 bar, the relative error showed a different trend for the parallel case compared to the coned configurations. The relative error for the parallel case showed two peaks: one at r = ~0.0725 m and another at r = ~0.0825 m with relative error magnitudes of 5% and 10%, respectively. However, the coned cases for the lowest inlet pressure showed almost no error up until r = ~0.084 m where all converging configurations showed a relative error of 15%. At the highest inlet pressure for the 20 μm case, Figure 3-33, the trends reported above held true with the parallel case showing two peaks at the same radial positions as the lower pressure case with relative error magnitudes of 5% and almost 25%. The coned configurations for the higher inlet pressure showed one peak at the same location reported for the lower pressure cases, however in this case the relative error magnitude decreased with an increase in coning angle, peaking at ~25%. For the 100 μm parallel case at P_{IN} = 2.03 bar, relative error magnitudes showed the same two peaks highlighted before at the same radial locations, relative error magnitudes of 15% and 5% were estimated. Regarding coned gaps, larger relative error magnitudes were sustained at more upstream radial locations compared to the smaller gap height case. Additionally, two peaks in relative error magnitude were realised at r = 0.07 m (immediately downstream of gap inlet) at and another at r ~ 0.084 m. Furthermore, the relative error magnitude showed a subtle drop with an increase in coning angle. At the highest inlet pressure, Figure 3-37, the same trends discussed previously remained evident but larger relative error magnitudes were recorded. The primary source of error for the larger gap cases is the pressure recovery region just downstream of the gap inlet

which was more pronounced in the 100 µm gap case and not captured by the numerical model. Another, although less significant, source of error is related to the gap exit pressure. When prescribing boundary conditions in the CFD model, the outlet pressure was set to be that of the air exiting the entire domain not the gap. This approach was chosen in order to assess the CFD model capability in predicting the pressure drop within the gap based on the working conditions of the experimental rig.

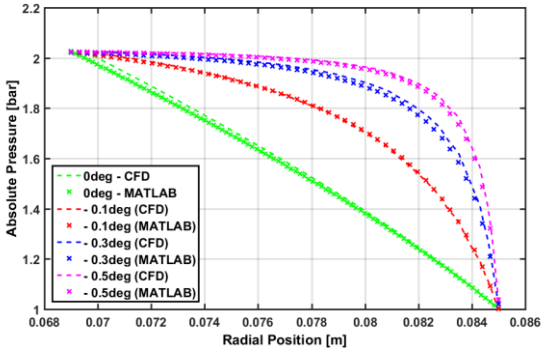

Figure 3-30: Converging Coning Radial Pressure Distribution, P_{in} =2.03 bar (Absolute), h_{min} = 20µm

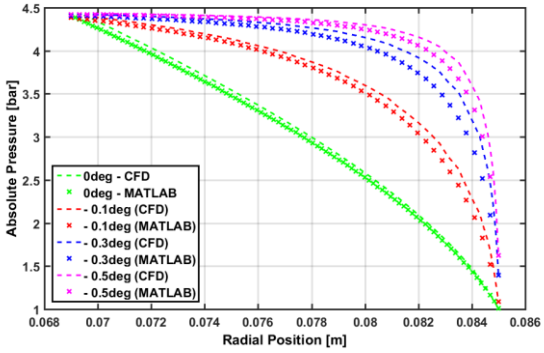

Figure 3-31: Converging Coning Radial Pressure Distribution, P_{in} =4.45 bar (Absolute), h_{min} = 20µm

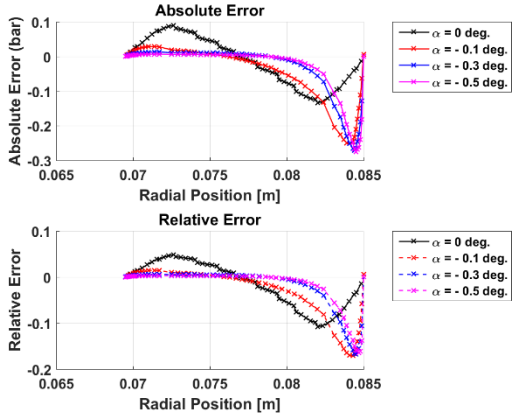

Figure 3-32: Absolute error (bar) and relative error, P_{in} =2.03 bar (Absolute), h_{min} = 20µm .

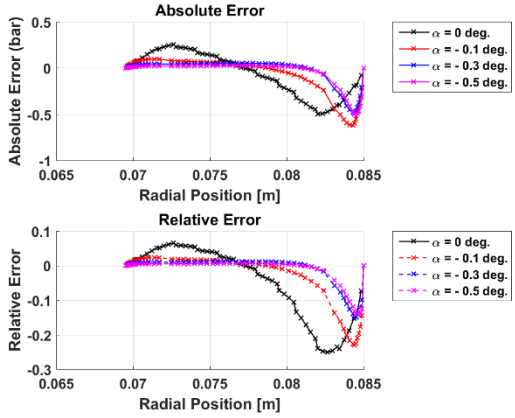

Figure 3-33: Absolute error (bar) and relative error, P_{in} =4.45 bar (Absolute), h_{min} = 20µm.

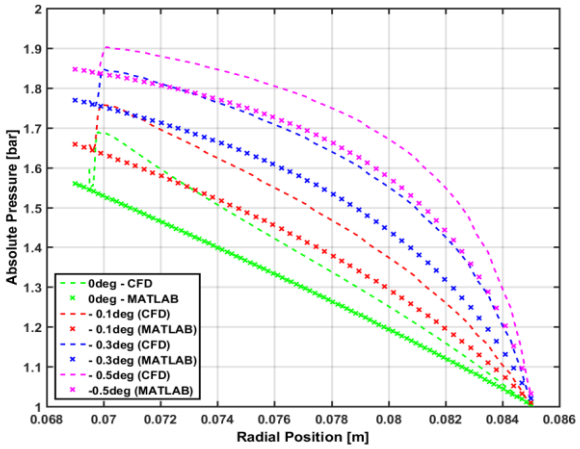

Figure 3-34: Converging Coning Radial Pressure Distribution, P_{in} =2.03 bar (Absolute), h_{min} = 100µm

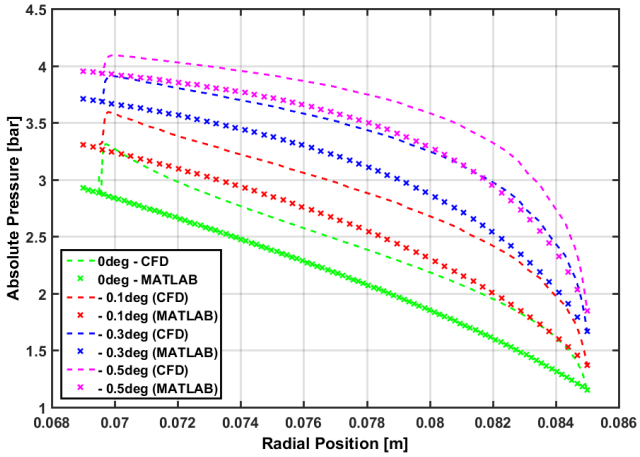

Figure 3-35: Converging Coning Radial Pressure Distribution, P_{in} =4.45 bar (Absolute), h_{min} = 100µm

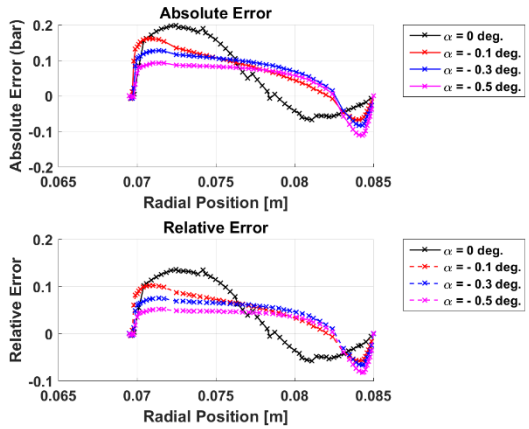

Figure 3-36: Absolute error (bar) and relative error, P_{in} =2.03 bar (Absolute), h_{min} = 100µm.

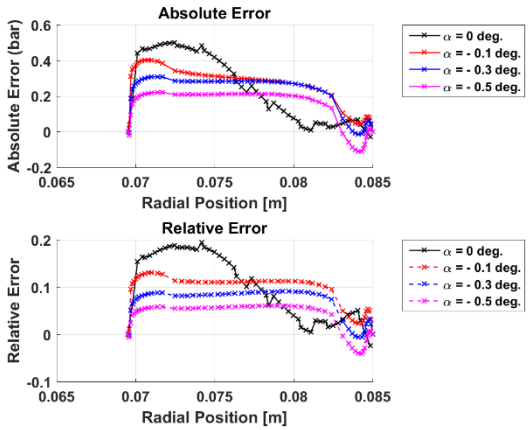

Figure 3-37: Absolute error (bar) and relative error, P_{in} =4.45 bar (Absolute), h_{min} = 100µm.

3.3.8 Diverging Coning

3.3.8.1 Radial Pressure Distribution

Similar to the converging case, the same coning angles were used but with a *+ve* sign to simulate the diverging geometry. The CFD models along with the numerical model were run at the same pressure conditions as before. Figure 3-38 to Figure 3-41 show the radial pressure distributions for the diverging coning and the corresponding parallel cases.

The most noticeable difference observed was the substantial drop in film pressure for the diverging coning compared to parallel and converging coning cases. Considering the h_{min} = 20 μm case, the drop in film pressure increased with increasing the divergence angle where a severe pressure drop at the gap inlet decreased the film pressure compared to parallel and converging coning cases. Also, this is believed to be the reason behind the significant drop in inlet pressure loss seen for the first time in the 20 μm gap case. The inlet pressure loss increased with increasing divergence angle for all inlet pressures. The predictions from the numerical model did not agree well with the CFD for this case. The substantial drop in film pressure which persists within the seal gap was not correctly captured by the numerical model either. As shown before for both the parallel and converging configurations at the same minimum gap height, the pressure recovery region downstream of the gap inlet was not significant.

For the 100 μm gap height case, Figure 3-40 and Figure 3-41, there was a significantly higher entry loss was conceded followed by a region of pressure recovery which was not present in the 20 μm cases. The pressure loss was far more significant compared to parallel and converging coning cases, particularly at lower inlet pressures. In fact, for the $\alpha = 0.5^o$ case at P_{in} = 2.03 bar, the pressure at the gap exit was higher than at the inlet. Furthermore, the film pressure was seen to drop as the diverging coning angle increased. Moreover, for larger diverging coning angles, $\alpha = 0.3^o$ and $\alpha = 0.5^o$, an unexpected behaviour was noticed. Downstream of the pressure drop at the inlet there existed a region where pressure started recovering again. The recovery region was observed to shift further downstream as the inlet pressure increased. A possible explanation for this behaviour could be achieved by thinking of the flow at the inlet to the diverging gap as choked flow in a throat of a *de Laval* nozzle. At the inlet pressures considered, the flow reaches supersonic speeds within the gap, refer to Figure 3-42 for the radially-averaged Mach Number distributions for the (h_{min} = 100 μm, $\alpha = 0.5^o$) at

all inlet pressures. Hence, as the flow chokes at the gap inlet a region of supersonic flow will exist where the flow accelerates further downstream as the area increases. The supersonic region is eventually terminated by a series of very weak shockwaves that cause a progressive deceleration of the flow towards subsonic conditions at the gap exit, marked by the sudden pressure rise. As the inlet pressure increases, the Mach number also increases and so the supersonic region will extend further in the radial direction. This explains the downstream-shifting of the recovery region at higher pressures. Numerical model predictions did not match CFD predictions: 1- the drop in film pressure was not correctly predicted by the code for either gap height, 2- the inlet pressure loss and subsequent recovery for the larger gap were not captured and 3- the second pressure recovery upstream of the gap exit due to compressibility effects for the 100 µm gap also was not captured. Errors were not assessed for the diverging configurations as predictions from both methods were fundamentally different.

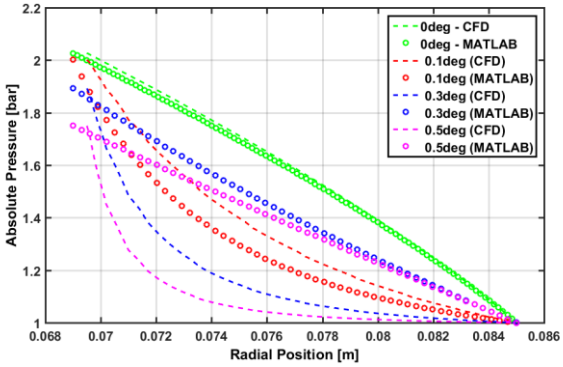

Figure 3-38: Diverging Coning Radial Pressure Distribution, P_{in} =2.03 bar (Absolute), h_{min} = 20µm

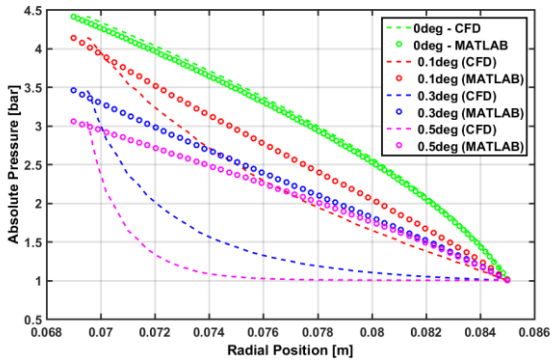

Figure 3-39: Diverging Coning Radial Pressure Distribution, P_{in} =4.45 bar (Absolute), h_{min} = 20µm

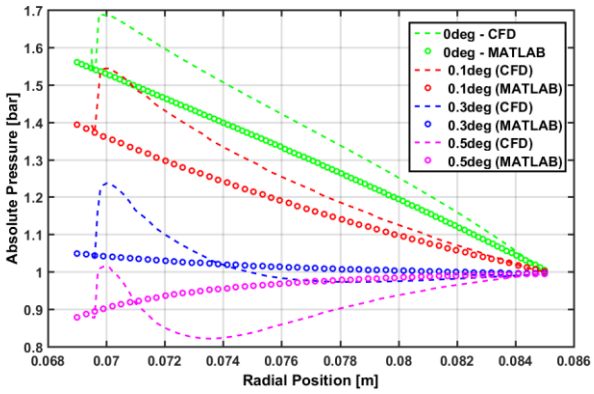

Figure 3-40: Diverging Coning Radial Pressure Distribution, P_{in} = 2.03 bar (Absolute), h_{min} = 100µm

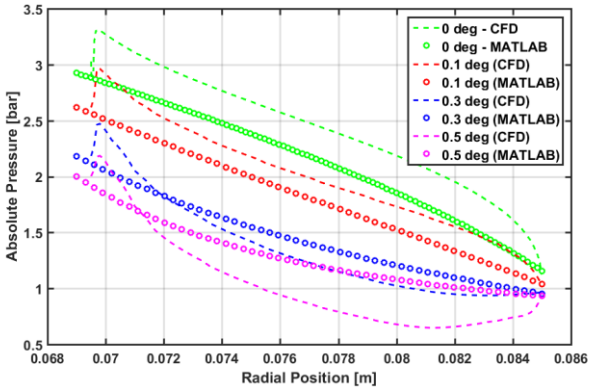

Figure 3-41: Diverging Coning Radial Pressure Distribution, P_{in} =4.45 bar (Absolute), h_{min} = 100µm

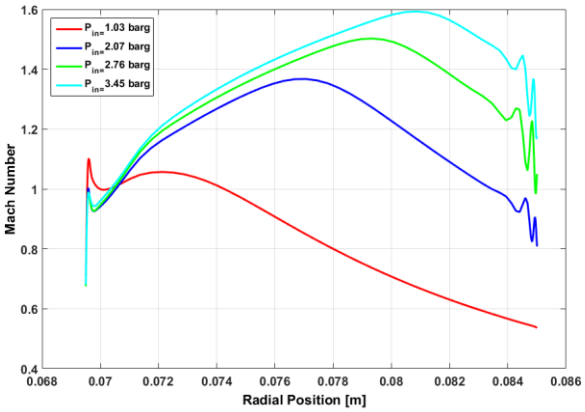

Figure 3-42: Diverging coning radial Mach number distribution, P_{in} =2.03, 3.07, 3.76 & 4.45 bar (Absolute), h_{min} = 100µm, α = 0.5°, Coning height = -140 µm.

3.3.8.2 CFD Coned Air-Gap - Opening Force and Leakage Rate

Figure 3-43 and Figure 3-44 show the change in the opening force acting on the stationary seal face and the air-film stiffness as a function of the minimum gap height (20 and 100 µm), inlet pressure (2.03 up to 4.45 bara) and coning angle (α = -0.5° to α = 0.5°).

The trend shown in the chart agrees well with the pressure profiles presented earlier, where with an increasing converging coning angle the opening force increased compared to the

parallel gap case. The opening force also increased at smaller minimum gap heights and higher inlet pressures. For the region to the left of the graph the opening force decreased markedly as the diverging angle increased compared to both the parallel and converging cases. For the converging cases, the delay of the pressure drop is translated to an increase in film pressure, which is reflected by an increasing force on the seal face. On the contrary, the diverging gap showed a substantial drop in film pressure which reduces the capabilities of the seal to tolerate large axial movements and will eventually lead to asperities rubbing resulting in friction and wear. The air-film stiffness, Figure 3-44, was highest for parallel. The drop in air-film stiffness for converging gaps is believed to be a result of the larger gap heights caused by introducing coning on the seal face. While for diverging gaps, the collapse of the fluid film and the associated drop in film force lead to a diminishing air-film stiffness.

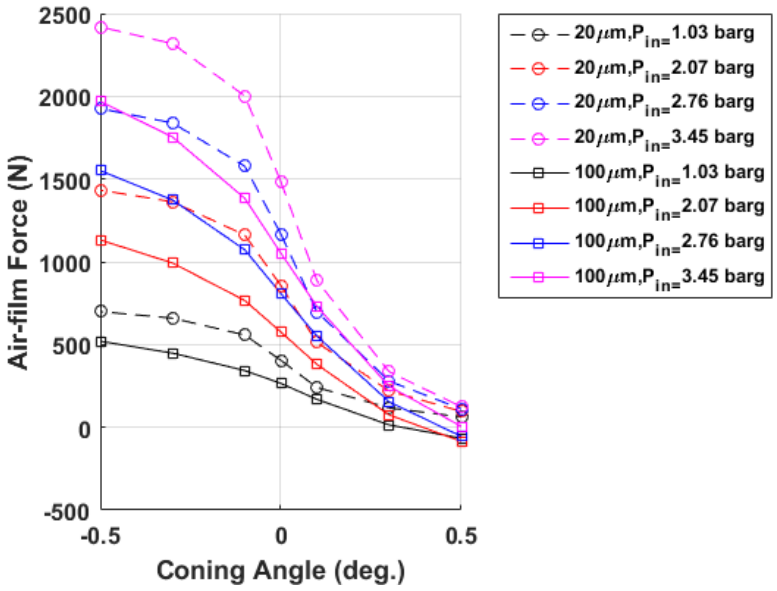

Figure 3-43: Effect of coning on opening Force.

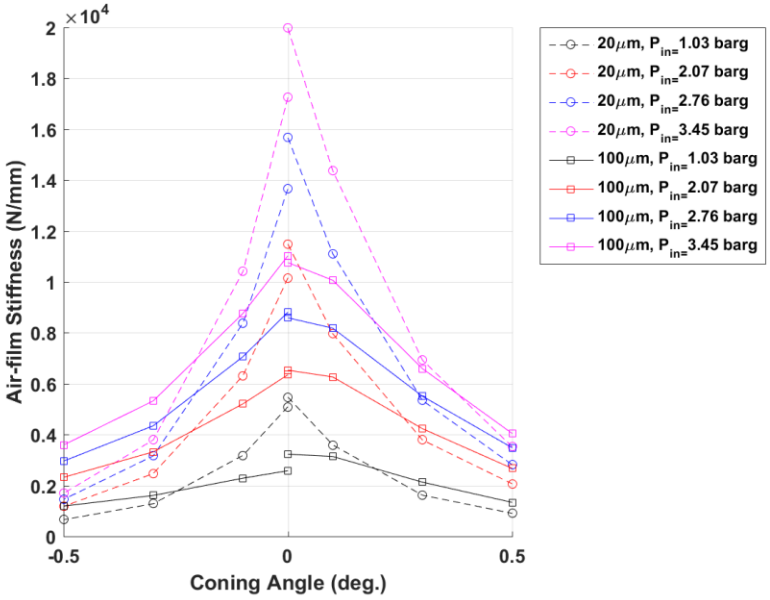

Figure 3-44: Effect of coning on air-film stiffness, at two fixed minimum gap heights

Figure 3-45 shows the leakage rate through the seal gap as a function of the aforementioned parameters. Compared to a parallel gap, the leakage rate increased as the coning angle increased, for both converging or diverging configurations. A higher leakage rate was evident at higher inlet pressures and larger minimum gap heights. Although keeping the leakage rate as low as possible is key to efficient performance of a seal, sufficient leakage needs to get through to generate enough pressure in the sealing gap. Therefore, a trade-off would have to be made between converging gap pressure generation capabilities and its higher leakage rate compared to a parallel gap. On the contrary, a diverging gap should be avoided throughout the operational envelope of the seal as it underperforms in terms of opening force generation and leakage rate.

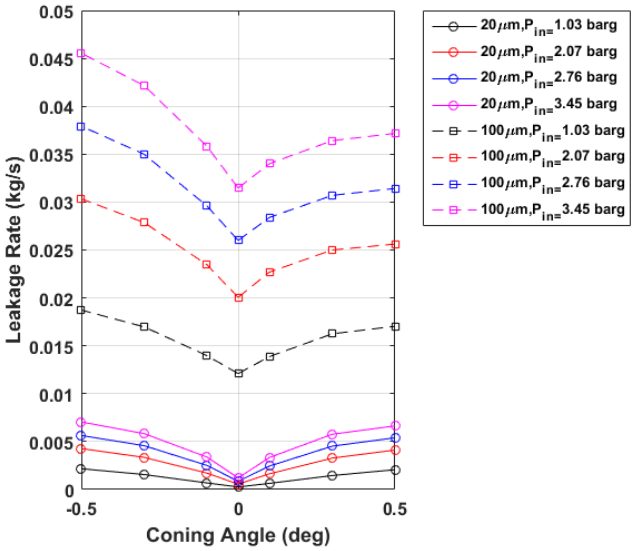

Figure 3-45: Effect of coning on leakage rate.

3.3.9 Converging coning with a radial step

3.3.9.1 Radial Pressure Distribution

This section investigates the influence adding a radial step at three different radial positions will have on the pressure distribution within a converging seal gap and compares the CFD predictions to the numerical code. The step causes a decrease in minimum gap height in the direction of the radial flow. A single case of minimum gap and coning was considered with a minimum gap height of h_{min} = 100 µm and coning angle of α = - 0.3º. The step height was h_{step} = 80 µm. The three radial step positions were at ζ = 50%, 75% and 90%, where ζ denotes the radial step position as a percentage of the total radial length (L = 15.5 mm), refer to figure 6 for a schematic of the leakage path with radial steps. Simulations were run at P_{in} = 2.03 and 4.45 bara.

Figure 3-46 and Figure 3-47 show the pressure distributions resulting from adding a radial step and varying its location along the coned gap. The figures show that at all pressures and radial step positions the entry loss did not vary significantly and the acceleration loss followed by the

recovery downstream was evident in all cases. A sizeable pressure loss (inertial) was experienced at the location of the step as the flow accelerates into a smaller gap height. The loss was followed by a recovery region and then a viscous pressure drop for the remaining length of the gap. At ζ=50%, 75% and 90%, the pressure upstream of the step was always higher than that of the plain (no step) converging gap. While downstream of the step, acceleration losses caused the pressure to drop at the step position below that of the plain converging gap for the ζ = 50% and 75% cases. However, for ζ = 90%, the pressure downstream of the step initially dropped to a level below the plain converging gap but quickly recovered to match it. The results show that including a radial step dictates where most of the pressure drop occurs within the gap due to the relative change in gap height at the step position. The same conclusion was drawn from adding radial steps to parallel gaps in *section 3.2*. The step position at the furthermost location along the gap length appeared to maintain the highest pressure within the gap which has a positive effect on the load capacity of the seal. Step positions at the ζ= 50% and 75% would not be as beneficial, at least for parallel and converging configurations.

Numerical model predictions did not match CFD predictions; the inertia-driven pressure drop at the radial step position was not captured by the model due to the previously discussed assumptions related to Reynold's equation. Similarly, the gap inlet pressure drop and recovery were not modelled. Moreover, the pressure upstream of the step was consistently underestimated in the code. On the contrary, due to the numerical model not capturing the significant acceleration losses at the step position, it over predicts pressure downstream of the step. The trend remained unchanged at all inlet pressures.

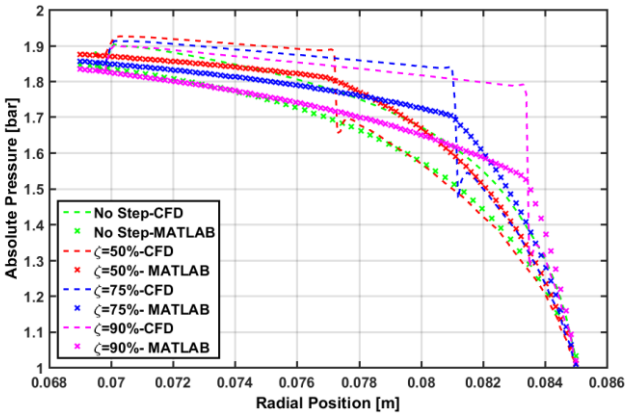

Figure 3-46: Converging Coning With Radial Steps Pressure Distribution, P_{in} =2.03 bar, h_{min} = 100µm, h_{step} = 80µm, ζ = -0.3°.

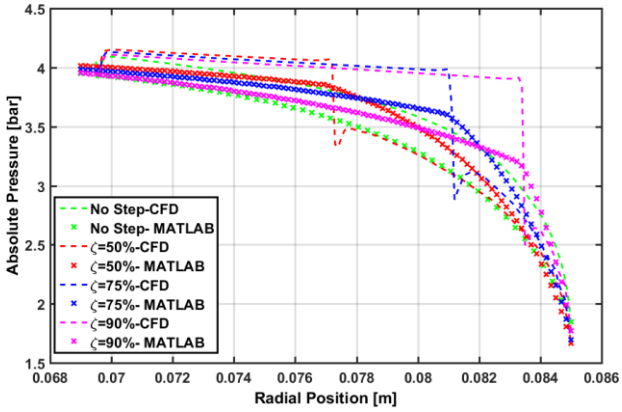

Figure 3-47: Converging Coning With Radial Steps Pressure Distribution, P_{in} =4.45 bar, h_{min} = 100µm, h_{step} = 80µm, ζ = -0.3°.

3.3.9.2 CFD – Opening Force and Leakage Rate

Figure 3-48 and Figure 3-49 illustrate the change in opening force and leakage rate with radial step position at different inlet pressures, respectively. Regarding the opening force, Figure 3-48 shows the predicted air-film force for a plain converging gap and with radial steps at ζ = 50%, 75% and 90%. For the no step case, the opening force was higher than the case with a radial step at ζ = 50%. Subsequently, the force started to increase again as the was step placed further downstream at ζ = 75% and produced an opening force slightly higher than that of the plain case. Moving the step position to outermost location, ζ = 90%, augmented the opening force even further as most of the pressure drop occurred downstream of the step. The force behaviour agrees well with the pressure distributions shown previously.

Figure 3-49 shows that the minimum leakage rate was obtained by positioning the radial step at ζ = 50%, corresponding to the lowest opening force. The leakage rate decreased starting from the no step case to the ζ = 50% radial position then gradually increased at the ζ = 75% and eventually reached its highest at the ζ = 90% position, which corresponds to the highest opening force attained.

For the converging cases, adding radial steps proved to have potential in increasing the seal's load capacity given that the radial step is located as close as possible to the gap exit. Locating the step at ζ = 90% has delayed the majority of the pressure drop towards the exit of the gap thereby maintaining a higher film pressure for most of the gap's length. Locating the step at positions further from the exit will tend to decrease the pressure upstream of the step and hence the opening force.

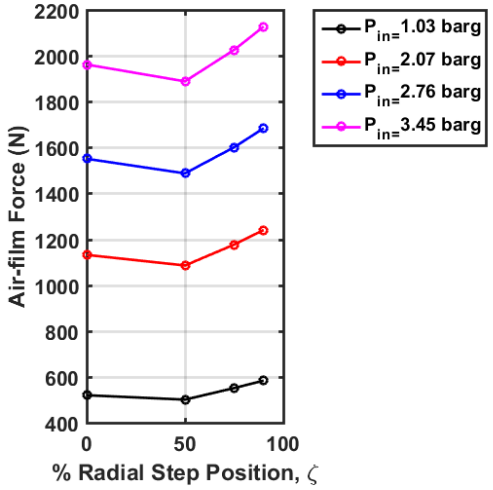

Figure 3-48: Effect of step position on Opening Force, h_{min} = 100µm, h_{step} = 80µm, α = - 0.3°.

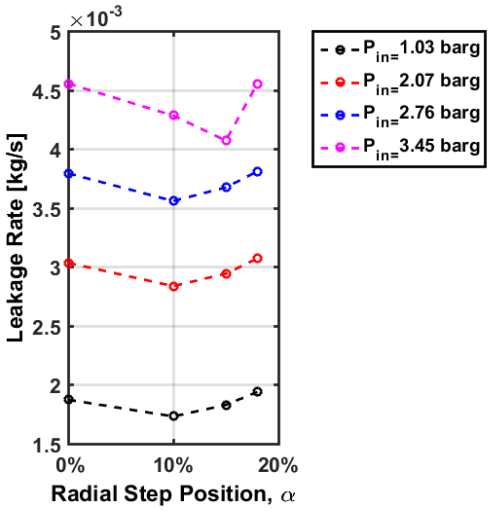

Figure 3-49: Effect of step position on Leakage Rate h_{min} = 100µm, h_{step} = 80µm, α = - 0.3°.

3.3.10 Diverging coning with a radial step

3.3.10.1 Radial Pressure Distribution

In *section 3.5.3*, 3D CFD pressure distributions for the diverging coning cases predicted a substantial drop in air-film pressure and revealed a compressible behaviour involving an abrupt pressure recovery towards the gap exit. This had a detrimental effect on the opening air-film force and to a lesser extent the leakage rate. Although it would be desirable to avoid operating with a diverging gap, it is not always achievable. In fact, Young and Lebeck (1982) reported on a mechanical face seal they tested in water at 3.45 bar and a rotational speed of 1800 RPM where they found that coning on the seal faces did not remain constant during operation due to

friction, wear, thermal stresses and pressure distortions. Thermal rotation due to the non-uniform temperature distribution in the seal ring along with misalignment can also lead to a divergent gap. For a contacting mechanical face seal some extent of rubbing contact between the sealing faces is expected and accounted for in design. However, if the seal was to maintain a non-contacting mode of operation the hydrostatic load support needs to be augmented further, for instance by adding radial features and/or by amplifying the amount hydrodynamic load generated. This section presents a set of data highlighting the effect of adding radial steps in diverging gap to investigate its potential in augmenting the hydrostatic load.

Figure 3-50 and Figure 3-51 show the effect of adding a radial step on the pressure distribution in a diverging gap with a minimum gap height of h_{min} = 100 µm, a coning angle of α = +0.5^o and a step height of h_{step} = 80 µm. Similar to the converging case, three different positions along the radial length were chosen at ζ = 50%, 75% and 90%. The case with no radial step (plain) is also highlighted. Additionally, Figure 3-52 and Figure 3-53 illustrate the change in Mach number with radial position for the three different step positions at the two inlet pressures considered (2.03 bar and 4.45 bar (absolute)).

For the ζ = 50% case, the entry loss did not change significantly compared to the no-step case. The pressure recovery downstream of the inlet was maintained until the step position and acceleration losses drove the pressure drop downstream of the step. The film pressure was higher upstream of the step when compared to the no-step case. However, downstream of the step, the film pressure dropped below that of the no-step case and then recovered towards the gap exit. The pressure drop downstream of the step increased with increasing inlet pressure and the unexpected pressure recovery, possibly due to a series of very small shockwaves, before the gap exit became more evident. The point at which the pressure recovered shifted further downstream as the inlet pressure increased.

Moving the step position further downstream, ζ = 75%, resulted in a much higher pressure drop at the inlet to the gap compared to all other cases and the film pressure remained below the no-step case over quarter of the radial length. A second pressure recovery upstream of the step drove the film pressure to increase beyond the no-step case but remained below the film pressure of the ζ = 50% case. As expected, head losses caused a substantial loss in pressure at the step position. Moreover, downstream of the step the film pressure showed a slight recovery towards the gap exit. Unlike the converging case, the film pressure with the step at ζ = 50% position maintained a higher film pressure compared to ζ = 75%.

The furthest downstream step position, ζ = 90%, incurred a slightly higher pressure drop at the gap inlet compared to the no-step and ζ = 50% cases. The pressure recovery was evident and film pressure was higher than the no-step case over the total radial length. The film pressure was lower than ζ = 50% case for the upstream portion but maintained a higher film pressure over the downstream portion followed by a drop at the stop position due to head losses and a quick recovery towards the gap exit. The quick pressure recovery just before the exit remained evident for all inlet pressures.

For the converging stepped cases, the entry loss increased, albeit very slightly, with moving the step further downstream (*i.e.* increasing ζ) but in all cases was less than that incurred by the corresponding plain case. On the other hand, the diverging stepped cases showed a slightly more abrupt trend for the entry loss where the largest entry loss was incurred by the ζ = 75% case (also resulting in the lowest film force, Figure 3-54) and the lowest by the ζ = 50% case. The plain face exhibited similar levels of entry loss to the ζ = 50% and 90% cases. In terms of film pressure behaviour downstream of the radial step, the stepped diverging cases differed from their converging counter parts in that the pressure recovery followed by the viscous drop seen for parallel and converging cases can sometimes lead to the sudden pressure

recovery by way of the previously mentioned weak shockwaves occurring just prior to the gap exit, this was apparent for the ζ = 50% and to a lesser extent for the ζ = 75% case at both the low and high inlet pressures. Nevertheless, the aforementioned behaviour was absent when placing the radial step at ζ = 90%.

For the converging stepped cases, the entry loss increased, albeit very slightly, with moving the step further downstream (*i.e.* increasing ζ) but in all cases was less than that incurred by the corresponding plain case. On the other hand, the diverging stepped cases showed a slightly more abrupt trend for the entry loss where the largest entry loss was incurred by the ζ = 75% case (also resulting in the lowest film force, Figure 3-54) and the lowest by the ζ = 50% case. The plain face exhibited similar levels of entry loss to the ζ = 50% and 90% cases. In terms of film pressure behaviour downstream of the radial step, the stepped diverging cases differed from their converging counter parts in that the pressure recovery followed by the viscous drop seen for parallel and converging cases can sometimes lead to the sudden pressure recovery by way of the previously mentioned weak shockwaves occurring just prior to the gap exit, this was apparent for the ζ = 50% and to a lesser extent for the ζ = 75% case at both the low and high inlet pressures. Nevertheless, the aforementioned behaviour was absent when placing the radial step at ζ = 90%.

The MATLAB code did not capture the inertial losses and subsequent recovery regions for all the cases considered. Therefore, it failed to yield a representative pressure field for the air film. The significance of inertial forces at discontinuities and in this case compressibility effects are believed to be the main reasons for the mismatch.

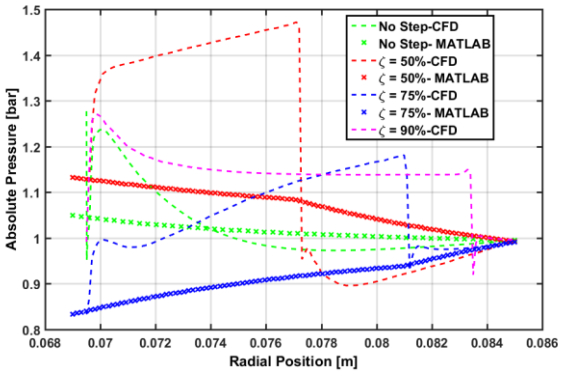

Figure 3-50: Diverging Coning With Radial Steps Pressure Distribution, P_{in} =2.03 bar, h_{min} = 100µm, h_{step} = 80µm, α=+ 0.5°.

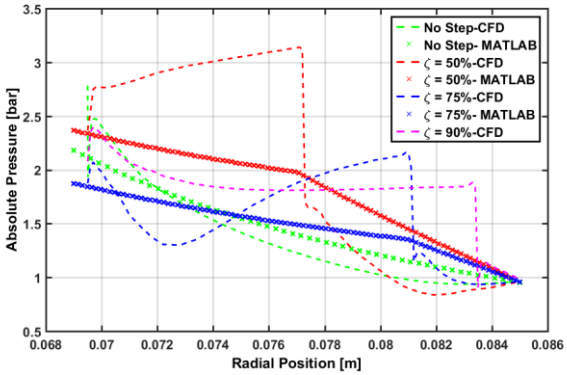

Figure 3-51: Diverging Coning With Radial Steps Pressure Distribution, P_{in} =4.45 bar, h_{min} = 100µm, h_{step} = 80µm, α= +0.5°.

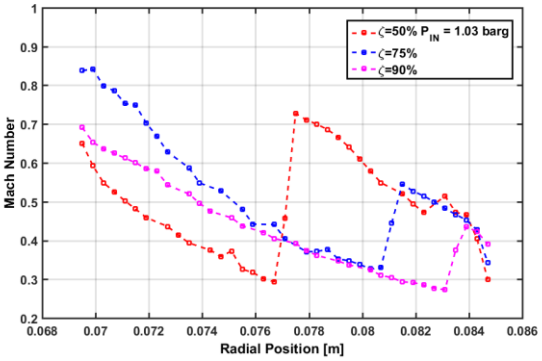

Figure 3-52: Diverging Coning With Radial Steps: Radial Mach Number, P_{in} =2.03 bar, h_{min} = 100µm,h_{step} = 80µm, α = +0.5°

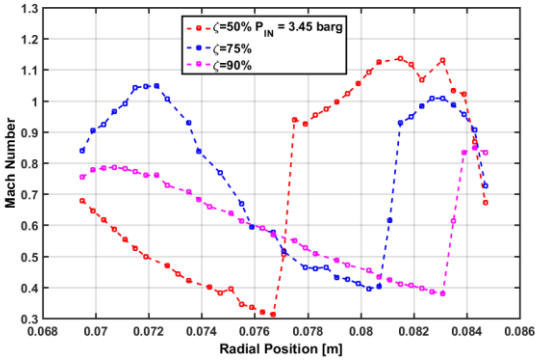

Figure 3-53: Diverging Coning With Radial Steps: Radial Mach Number, P_{in} =4.45 bar, h_{min} = 100µm,h_{step} = 80µm, α = +0.5°.

3.3.10.2 CFD – Opening Force and Leakage Rate

Figure 3-54 and Figure 3-55 show the variation of the opening force and the leakage rate, respectively, for the step positions considered. The largest opening force was achieved when the step was located at ζ = 50%. The force then drops markedly as the step position moves to ζ = 75%, which is the opposite of what had been seen in the converging case. At ζ = 90%, the force increases again and was observed to be higher than the plain case but lower than ζ = 50% case by nearly 10 N. The trend does not follow what has been seen in the converging case, as the highest gain in opening force for the diverging case was obtained with the step is located

at the upstream-most position. The recovery of the opening force at the ζ = 90% position is a good sign as it suggests that placing the radial step at this position is beneficial for both converging and diverging coning. This location also showed no abrupt pressure recovery driven by the weak shockwaves experienced in the other two configurations.

It should, however, be noted that for all the radial step locations considered, the film force associated with a stepped diverging gap was an order of magnitude lower than the corresponding converging configurations.

Leakage rate was found to be lowest for the no-step case, Figure 3-55, while highest leakage rate occurred at ζ = 75% position and dropped again as the step moved further downstream. Once more, the trend suggests that placing the radial step at ζ = 90% will improve the seal performance for a coned gap, whether converging or diverging, compared to a plain no-step case.

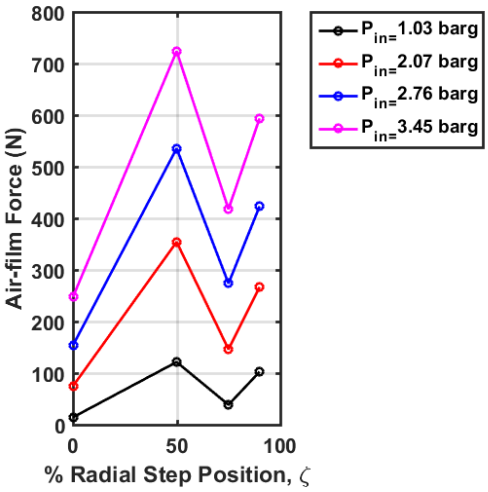

Figure 3-54: Effect of step position on Opening Force h_{min} = 100µm, h_{step} = 80µm α = 0.5°.

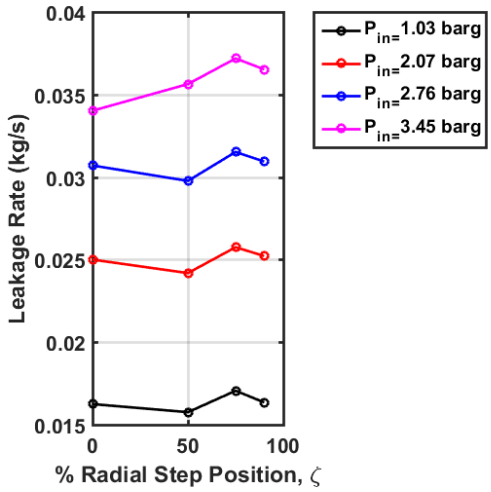

Figure 3-55: Effect of step position on Leakage Rate h_{min} = 100µm, h_{step} = 80µm α = 0.5°.

3.4 Chapter Summary

In this chapter, a derivation of the 2D compressible form of Reynold's equation was presented along with a numerical model which was developed to investigate the pressure field the air-film operates within for a range of coning distortions and operating clearances. The numerical model was validated using a set of previously existing experimental data. To extend the validation scope a 3D CFD was formulated and used to investigate radial distortions on sealing faces with and without radial steps. The study investigated the characteristics of a thin air film for parallel, converging and diverging sealing faces. The cases with a radial step were also analysed with and without coning. An inlet pressure loss was seen to be significant for larger gap heights for all configurations considered which needs to be accounted for to obtain an accurate prediction of the opening force. For parallel gaps, the opening force was higher at smaller gap heights and increased with an increase in inlet pressure. Additionally, lower leakage rates were achievable at smaller gap heights and were found to increase at higher inlet pressures.

For coned gaps, increased converging coning enhanced opening force while increased diverging coning diminished it due to the large drop in film pressure. Leakage rate was lowest for the parallel gaps while it increased with an increase in coning angle and inlet pressure. The highest leakage rate (<50 g/s) was at the largest converging coning angle. Increased diverging coning also resulted in higher leakage rates but to a lesser extent compared to converging coning.

Adding a radial step at the outermost radial position for coned gaps resulted in a slight improvement in the opening force as the film pressure was maintained upstream of the step and the drop occurred only downstream of the gap thereby increasing the film pressure.

Incorporating the step at locations in the vicinity upstream of the gap exit has proved detrimental for both coning configurations in terms of opening force and leakage rate, although the sensitivity was low for the range considered. Interestingly, for step locations upstream of the gap exit for some divergent coning configurations the flow acceleration as the gap converges at the step location drove the film pressure to values lower than the downstream pressure. Such behaviour was evident in the CFD predictions but not captured by the numerical model.

The findings presented in this chapter suggest that it would be desirable for the seal to operate with narrow gaps to provide sufficient opening force and stiffness while exhibiting low leakage rates. Converging radial coning distortion could be accommodated as it increases the opening force; however it will be required to limit the magnitude of coning acceptable within the operating envelope of the seal as it negatively affects the stiffness of the air-film and the leakage rate. Divergent coning, on the other hand, is unlikely to be acceptable for practical design and should be avoided. Integrating radial steps for augmenting the opening force becomes useful if the radial step is located closer to the gap exit.

Furthermore, the investigation demonstrated that to produce a seal that does not contact under range of operating conditions a solid understanding of the behaviour of the film pressure under different distortions must be developed. Although, the results shown in this chapter focused on radial distortions (coning), further depreciation in sealing performance is also expected when adding the effects of circumferential out-of-flatness (waviness), which could result in a diverging gap in the circumferential direction and in larger gap heights. Ideally, maintaining a converging gap in the direction of the flow coupled with a low minimum gap height should produce a desirable sealing performance. An engine realistic face seal was tested under swash conditions and findings are reported in *chapter 6*. Moreover, the CFD film pressure predictions

were compared against an aerodynamic numerical model based on 2D compressible form of Reynold's equation, differences were highlighted and reasons for mismatch were discussed. Of interest was the inertia-influenced pressure loss incurred at the inlet to the sealing gap and at the radial step locations which was not captured by the code.

4 Experimental Setup

Experiments were performed to characterise both key elements generic to face seals and also specific assemblies of the current prototype seal being developed at the Osney Thermo-fluids Research Laboratory. The test rig was employed previously to test a self-centring face seal by Aubry, 2011. Hence, the rig served as a good basis for testing the type of face seal considered here, particularly in terms of instrumentation which did not require major modifications. However, the entire housing had to be redesigned to optimise it for the current seal. Additionally, a redesign of the pressure supply system was necessary to enable testing at higher differential pressures to be achieved at the larger gaps considered in this study. Furthermore, a new rotating assembly was designed and incorporated to allow operation at higher speeds and to enhance the accuracy of defining a datum position. The general layout of the test rig is shown in Figure 4-1. Component parts are further described below. Figure 4-7 shows a labelled photograph of the modified Non-Contacting Face Seals Testing Facility highlighting the key components. Figure 4-3 is a cross section view outlining the primary leakage path for the modified seal. The primary sealing occurs between the removable part of the housing (stator) and the rotor. This part is machined to obtain the necessary face geometry. Having a removable element allows different seal face geometries to be tested which include radial and circumferential features. This in turn allows for a wider range of gap profiles to be tested.

In summary, this experimental setup aims to generate a database of pressure distributions on a coned primary sealing face. In *chapter 3*, pressure data for parallel gaps with and without radial steps were presented and validated against the MATLAB code and the 3D CFD model. However, no experimental data were present for radially coned gaps which prompted setting up an experimental campaign to generate the aforementioned data which is presented in *chapter*

5. Understanding the air-film behaviour under a range of coning distortions (converging and diverging) is of paramount importance as it will shed light on practices that would augment the hydrostatic opening force as well as confirming the compressible behaviour seen in diverging gaps which was highlighted in *chapter 2* to have resulted in seal failures due to the collapse of the film force.

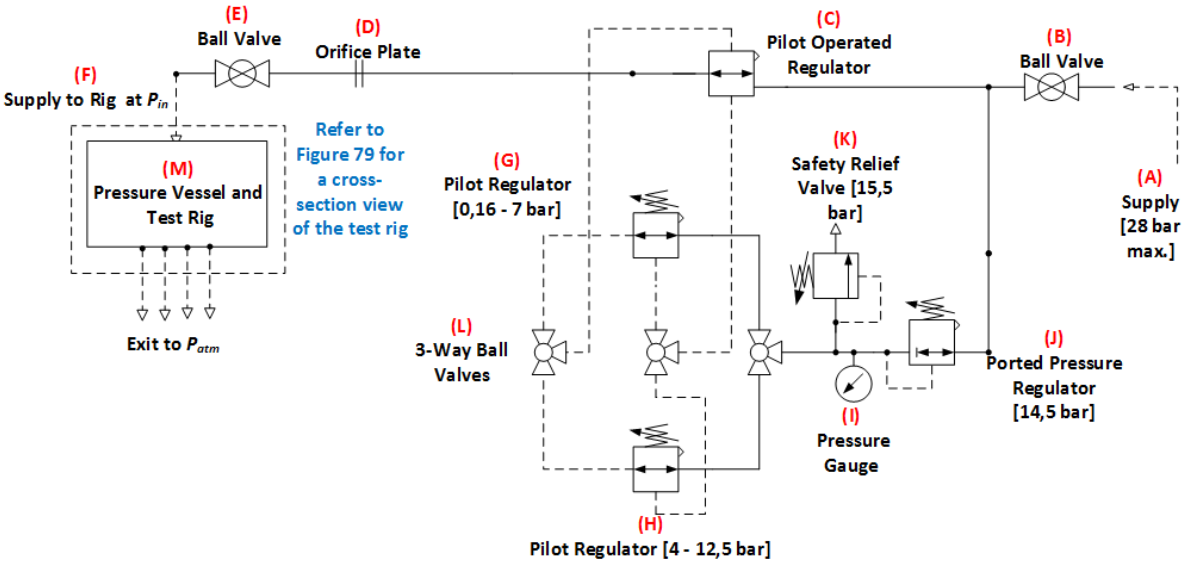

Figure 4-1: General Layout of experimental rig and air pressure system.

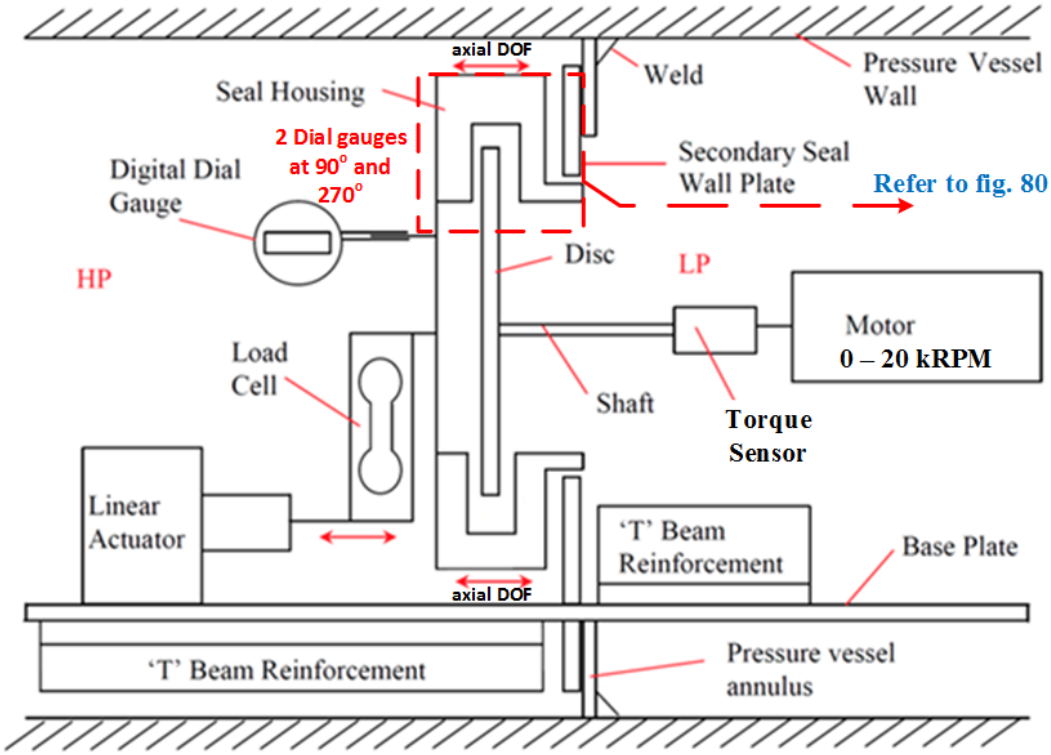

Figure 4-2: Non-Contacting Seals Rig Schematic.

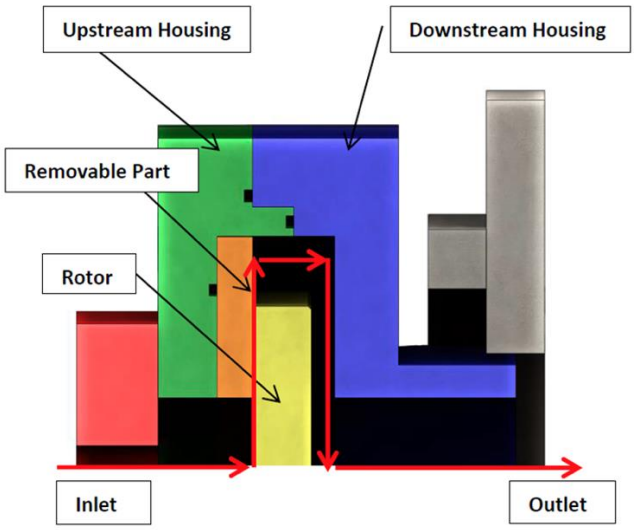

Figure 4-3: Seal Leakage Path.

Table 4.1 and Table 4.2 outline the seal's geometric specifications and the operating conditions the rig is capable of providing respectively.

Geometric specifications	
Seal inner diameter	139 mm
Seal outer diameter	170 mm
Total radial length	15.5 mm
Removable part thickness	6 mm
Rotating disc diameter	170 mm
Rotating disc thickness	10 mm
Total available gap height	4.1mm

Table 4.1: Seal geometric specifications.

Rig operating conditions	
Differential Pressure	Up to 3.45 bar
Downstream Pressure	Atmospheric
Axial movement	4.1 mm
Axial movement rate	18 mm/s
Speed	Up to 15 kRPM (133.5 m/s surface speed @ 170 mm diameter)
Temperature	Ambient temperature

Table 4.2: Rig operating conditions and capabilities.

4.1 Key components

The rig is made up of 3 component assemblies: the stator, the rotor and the pressure vessel. The stator assembly consists of the upstream and downstream seal housing and the removable part. These are axially moved relative to the rotor along a linear slide using a linear actuator. The rotor assembly is made up of the rotor, its driving motor, bearings and the torque sensor. The entire rig is mounted on a stiff base plate and housed in a pressure vessel whose exit is open to the atmosphere.

4.1.1 Stator assembly

4.1.1.1 Removable part

The removable part as noted above is the key sealing element. In the experimental test rig it is highly instrumented with pressure tappings. Those tappings exit onto the front surface of the test piece via 0.5 mm diameter holes and interface with tubulations with an outer diameter of

1 mm permanently housed in the upstream seal housing. In total, 130 pressure tappings are available which offer sufficient resolution to assess the pressure field within the sealing gap, see Figure 4-4 for tappings arrangement. Pressure tappings are placed at 0º, 90 º, 180 º and 270º around the circumference to allow periodicity to be measured. Tappings are arranged both radially and circumferentially to enable assessing the pressure field in case of adding circumferential features. The removable parts available are made of polycarbonate. The removable part surface was measured using an *Alicona* microscope and ***Ra*** value of 1.4663 µm was recorded.

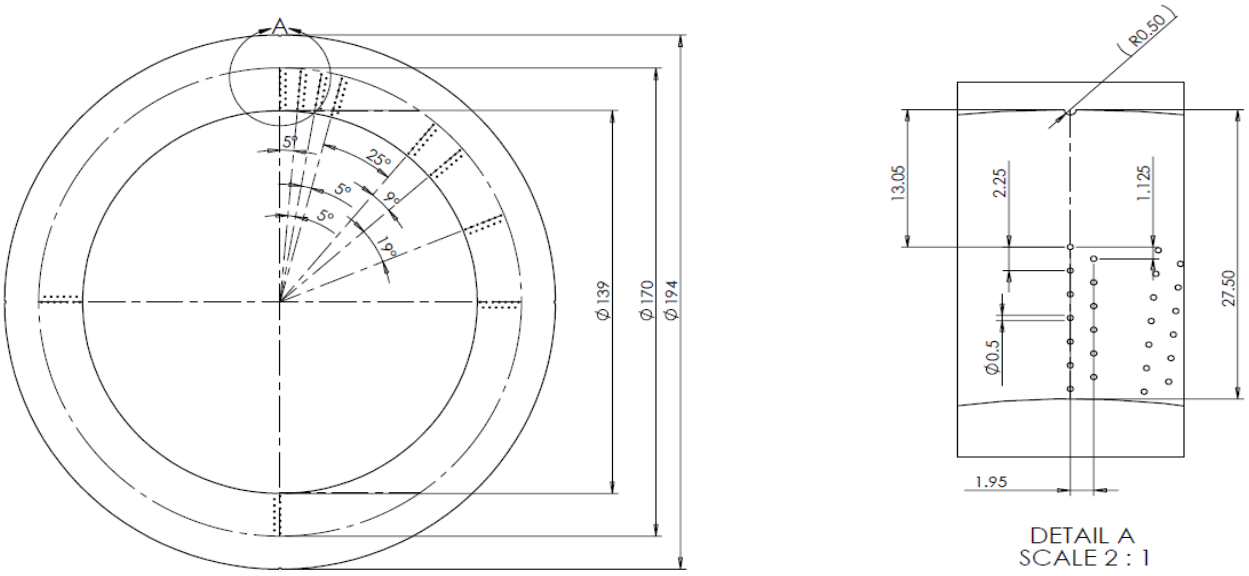

Figure 4-4: Pressure tappings arrangement on the front face of the removable part.

4.1.1.2 Upstream seal housing

The upstream housing is manufactured from with a cut-out that carries the removable part. The upstream housing was designed so that it features the same pressure tappings arrangement as the removable part, Figure 4-5. Each pressure tapping tube (1mm diameter) is surrounded by a

circular groove of (2 mm diameter) where an O-ring is placed to seal around each tubulation. O-ring grooves are also machined around the removable part and between the upstream and downstream housing to ensure the air flows only through its designated leakage path. The upstream housing is attached onto the downstream housing using a set of 12 M4 bolts placed equally around the circumference and 4 dowel pins to ensure precise relative location.

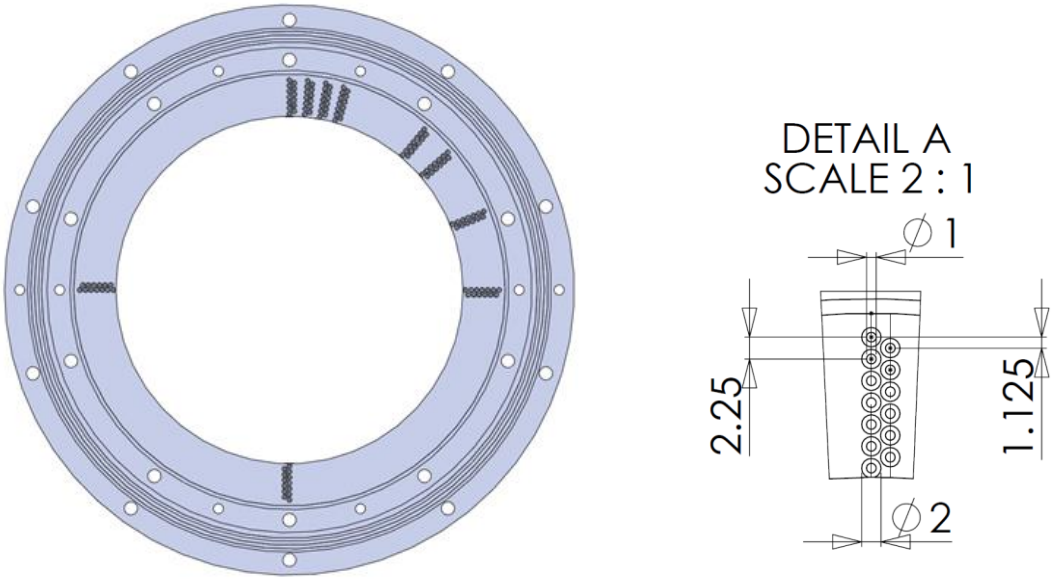

Figure 4-5: Pressure tappings arrangement on upstream housing.

4.1.1.3 Downstream seal housing

In the downstream the seal housing, also made of mild steel, four pressure tappings are installed to measure the pressure downstream of the seal. Figure 4-6 shows the downstream housing along with the associated pressure tappings arrangement.

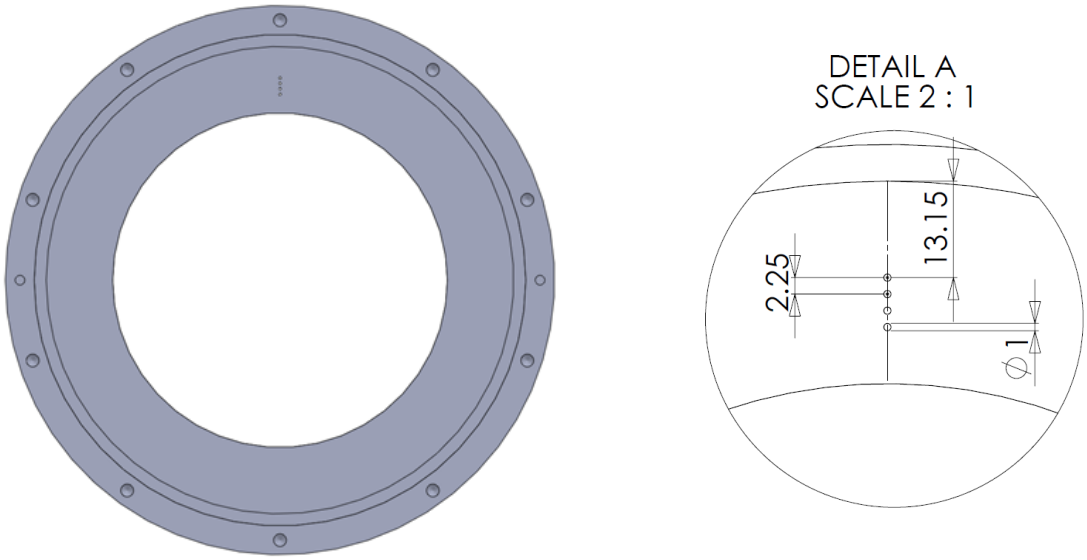

Figure 4-6: Pressure tappings arrangement on downstream housing.

4.1.1.4 Linear slide

The linear slide supports the weight of the seal housing assembly including the removable part and the perforated plate. It consists of a linear slide shaft and bushing. The shaft is 20 mm in diameter. The shaft slides into the bushing which consists of an array of ball bearings, with extremely low backlash. An anti-deflection assembly is in place to ensure the linear slide shaft and bushing axes remain parallel during operation. The slide assembly is concentric with the seal housing and only allows movement in the axial direction while providing a rotational constraint. The latter constriction is a necessity to alleviate the effects of any excessive torque on the seal housing that could be initiated by a high speed rotating disc touch-down.

4.1.1.5 Linear actuator

To alter the position of the housing with respect to the rotating disc, and hence the minimum gap height, a linear actuator, Zaber NA3460C, will be used to provide the axial motion required. This process cannot be performed manually as the whole rig assembly will placed inside the pressure vessel during operation. The aforementioned mechanism has proved to be successful in a previous setup and was found to produce sufficient force to overcome the axial

force on the seal housing due to differential pressure and it also provided sufficient linear resolution of (0.198 μm) allowing for very small gaps to be accurately obtained.

4.1.2 Rotor assembly

4.1.2.1 Rotor disc

The rotor installed is identical to that used by Aubry (2011). The rotor has a diameter (***D***) = 0.17 m and thickness (***t***) = 0.01 mm) and is made of steel with the following material properties: mass (***m*** = 1.77 kg), yield stress (σ_y = 240 MPa), ultimate tensile strength (σ_{UTS} = 480 MPa), and strain failure (ε_f = 0.14). Importantly, the surface roughness of the rotor and its flatness are known. The rotor surface was measured using an *Alicona* microscope and ***Ra*** value of 2.8224 μm was recorded. When installed in the test rig a run out of ± 20 μm was measured using a dial gauge. Thus subsequent experiments are subject to this underlying uncertainty.

4.1.2.2 Electric motor

For rotating cases, rotation is provided by an *Isel AC Motor*. The motor has an operational speed of to 20,000 RPM, which is sufficient to achieve surface speeds of above 100 m/s at the seal's outer radius, to mimic engine representative conditions. These surface speeds also allow significant hydrodynamic effects to be detected. The motion is transmitted to the downstream end of the rotating disc via a HUCO flexible coupling which is tolerant to slight misalignment.

4.1.2.3 Base plate

Prior to inserting the components into the pressure vessel, they are assembled on the base plate. The base plate is made of steel and is 650 mm in length, 127 mm in width and 12.7 mm in thickness. Due to the forces acting on the components during operation, the base plate has 3 supports: one upstream bolted onto the inner wall of the vessel, another downstream that is welded to the inner surface and finally a support provided by the flat surface of the pressure

vessel. In a further attempt to minimise the deflection of the base plate another T-section support was bolted to the base plate.

4.1.2.4 Pressure vessel

After the assembly of all components and ensuring that they are rigidly fitted onto the base plate, the whole assembly is inserted (upstream end first) into the pressure vessel. The aforementioned supports are then screwed in their respective positions and the secondary wall plate is screwed on an internal divider inside the pressure vessel. The vessel is made of section of a steel pipe rated to 40 bar. The vessel is 660 mm in length and 304.80 mm inner bore diameter. The upstream end plate is manufactured from a standard Victaulic component.

For cases where the disc is rotating, a containment calculation has been performed to ensure that there is enough containment on the rig in case the spinning disc bursts.

The moment of inertia, ***I***, of the rotor can be computed as follows,

$$I = m\left(\frac{D}{2}\right)^2 = 1.77(\frac{0.17}{2})^2 = 0.00063957\ kg.m^2 \qquad \textbf{Eq. 4.1}$$

The kinetic energy, $\boldsymbol{KE_{disc}}$ of the disc at a rotational speed $\boldsymbol{\omega}$ = 20 kRPM = 2094.4 rad/s is,

$$KE_{disc} = I\omega^2 = 0.00063957 * (2094.4)^2 = 14.02\ kJ \qquad \textbf{Eq. 4.2}$$

Regarding the pressure vessel, the plastic strain energy, $\boldsymbol{E_p}$, of taking the steel vessel from yield ($\boldsymbol{\sigma_y}$) to its ultimate tensile strength ($\boldsymbol{\sigma_{UTS}}$) can be calculated as,

$$E_p = \frac{\sigma_y + \sigma_{UTS}}{2} * \varepsilon_f * V_l = \frac{240 + 480}{2} * 0.14 * 0.00204 = 102.6\ kJ \qquad \textbf{Eq. 4.3}$$

Where, $\boldsymbol{V_l}$ is the volume of the cylindrical pressure vessel (steel). Therefore, the rotor kinetic energy at a speed above the planned operating speed is well within the limits of the plastic limit

of the steel pressure vessel, so in case of a burst any fragmentations should be safely contained within the vessel. Also, note that the disc is enclosed within its seal housing which has not been shown in the above calculations however it has a plastic strain energy of *40.13 kJ* which serves in enhancing the containment capability, providing an overall safety factor of $142/14.02 \approx 10$.

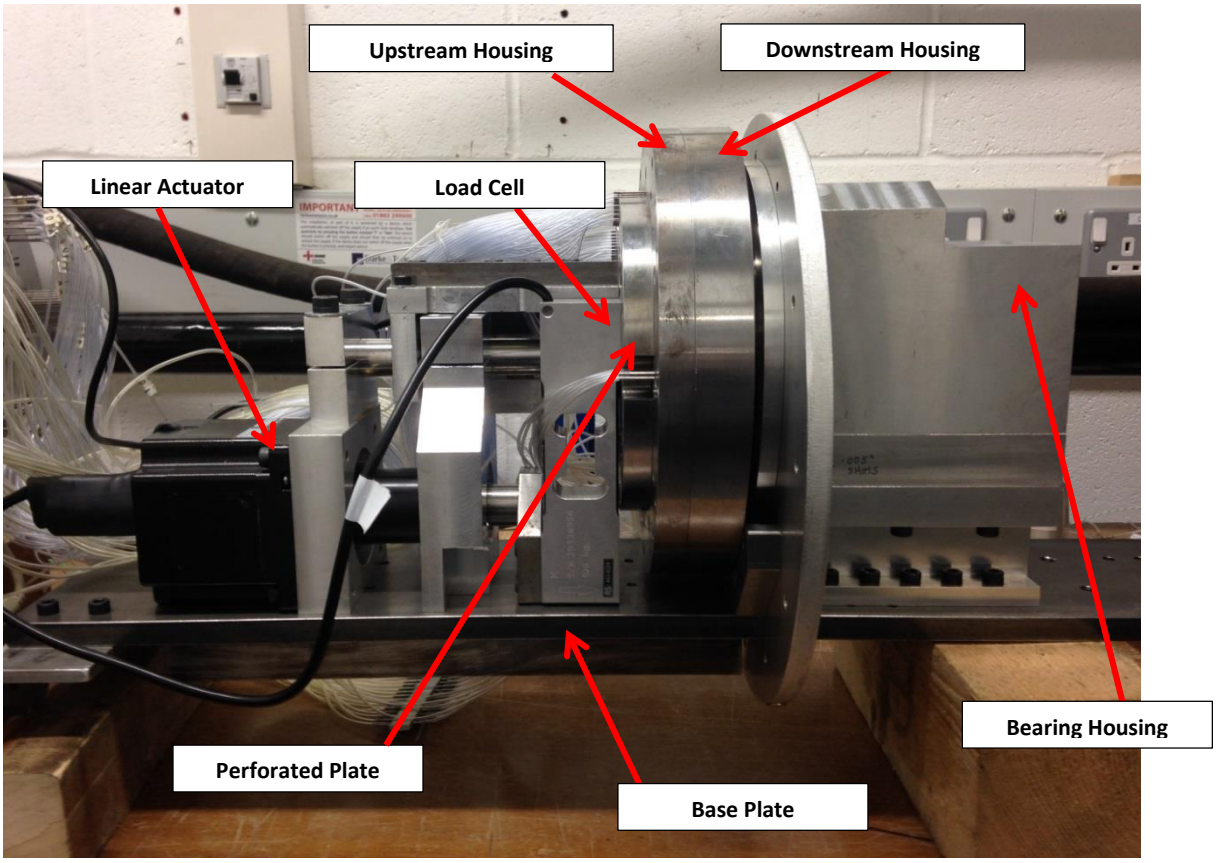

Figure 4-7: Fully Modified Non-Contacting Seals Rig.

4.2 Instrumentation

The key parameters to be quantified are; the pressure drop through primary seal gap, the pressure drop across the secondary seal, the pressure drop across the orifice plate, the seal housing axial displacement to measure the minimum gap height, the axial force on the seal housing and the temperature at the orifice meter. In terms of pressure capability, the rig supply line is connected to the 400-psi line which allows 3.5 barg differential pressure to be easily achieved. A list of the instruments used on the rig is shown in Table 4.3.

Measurement Application	Instrument
Data acquisition	National Instruments *NI BNC 2110*
Pressure measurement	SensorTechnics Pressure Sensors
	Scanivalve Pressure Tubing (*1mm*)
	Scanivalve Pressure Tubulations
	Scanivalve Tubulation reducers
	Scanivalve Multiplexers
Axial force	Tedea Huntleigh Single Point Load Cell (100 kg)
	SOEMER LAC 65.1 Analogue converter
Axial movement	*Zaber NA34C60* Linear Actuator Linear Actuator + Motor
Seal housing axial displacement measurement	*2 x* Mitutoyo Absolute Dial Gauge (Resolution: 0.001 mm)
Temperature	*k*-type Thermocouples + 4-channel NI USB 9211Thermocouples readers

Table 4.3: List of instruments.

4.2.1 Pressure measurement

The pressure drop across the orifice plate is measured by a low range differential SensorTechnics pressure transducer (0 - 1.03 barg). The pressure upstream of the orifice plate is measured by either a SensorTechnics (0 - 7 barg) or (0 - 1.03 barg) pressure transducer, depending on the inlet pressure. The pressure in the high pressure region is monitored by either a (0 - 1.03 barg) or a (0 - 7 barg) SensorTechnics pressure transducer, again depending on the inlet pressure. The pressure drop in the sealing gaps and across the secondary seal, for the 130 tappings on the upstream housing, removable part and downstream housing is measured with either 4 SensorTechnics (0 - 1.03 barg) or (0 – 7 barg) pressure transducers, depending on the inlet pressure. *Two* 2 x 24 channel Scanivalve multiplexers (*i.e.* 96 channels) are used to cover the large number of pressure tappings. The multiplexers alternate between all the pressure

tappings and the output is fed into the designated pressure transducer. All pressure transducers are connected to the data acquisition card through a NI BNC 2110 shielded connector block with 8 analogue inputs.

4.2.2 Mass flow rate measurement

The mass flow rate through the system is estimated by placing an orifice plate on the pipe upstream of the pressure vessel. The orifice plate was designed according to British and European Standards (ISO5167-2 2003). The data acquisition system is setup to read the pressure upstream and downstream of the orifice plate and the orifice temperature. An in-house MATLAB code uses an iterative scheme with the aforementioned parameters in addition to the pipe diameter, surface roughness, and orifice plate diameter as inputs to estimate the mass flow rate through the system. The maximum mass flow rate uncertainty was 3.2%.

4.2.3 Axial force measurement

The axial force on the seal housing is measured by a 100 kg capacity - TEDEA HUNTLEIGH single point load cell. The load cell is be connected to the data acquisition card via a Soemer LAC 65.1 load cell analogue converter. While the load cell provides an overall measure of the load on the system, it is subject to pressure loadings unique to the test rig, rather than the sealing faces, and thus, while useful in determining differences between geometric cases, the determination of surface forces by integration of the surface pressures was felt to be the most representative of those required for design of a real seal.

4.2.4 Temperature

The temperature of the flow at the orifice meter is measured by a *k*-type thermocouple. The flow is unheated. A thermocouple reader, 4-channel NI USB 9211, is then used to send the temperatures recorded to the data acquisition computer via a USB port. While for seal

installations it is desirable to run close to engine temperature, for the series of tests to be reported in the next chapter the purpose was to investigate the pressure and inertia induced forces on faces of known geometry and so tests are run at ambient conditions to avoid thermal distortion. Provided the non-dimensional parameters are matched, this is not a problem. Refer to *section 4.4* for the dimensional analysis of the system.

4.2.5 Data acquisition and experimental procedure

The graphical programming language *LabVIEW 2012* is used to monitor and record the data from all the instrumentation on the rig. 100 samples per channel are recorded at 50 Hz and then averaged to obtain the final measurement for each data point. Prior to taking the data acquisition programme, the upstream pressure regulator is set to the required pressure in the high pressure region. A pressure tapping in the high pressure monitors the upstream pressure in the cavity in real time. The position of the housing is altered to achieve the required seal gap height using the linear actuator and the data recording is begun. Finally, the recorded data are saved into a single precision tab-limited ASCII data file.

4.2.6 Calibration

For both pressure transducers and the load cell *insitu* calibration were performed using calibrated pressure regulators and calibrated weights, respectively. Linear regression is performed over the range of the transducers to give a linear relationship consisting of a gain and an offset for each device. The gain is only likely to change if the transducers are over-loaded. However, the offset is heavily influenced by the ambient temperature. Therefore, to account for this, automatic measurements of the pressure transducers' and load cell's offsets are programmed into the data acquisition software and are conducted at the start of each run of tests. All pressure transducers were calibrated *in situ* with the all the instrumentation in use connected to the data acquisition system to minimise calibration errors. A *Fluke 718 100G*

pressure calibrator was used to calibrate all pressure transducers. A device accuracy of *0.1 mbar* is quoted for the lowest range transducer, *0-25 mbar*, equating to approximately *0.4%* error, Aubry (2011).

4.2.7 Uncertainty

Two types of measurement errors exist; random and systematic errors. The former category is the type of error that varies every time the measurement of a quantity is repeated while the latter is an error that remains constant as the measurement of a quantity is repeated. Both errors combine to give the total measurement error. To assess the level of confidence in the measured data, an analysis performed on the same equipment being used estimated 95% confidence intervals for the measured results, Aubry (2011). The procedures used to perform the uncertainty analysis are outlined in; Moffat (1982), Abernathy et al. (1985), Rolls-Royce guidelines (2005) and Performance Test Codes (2005). Table 4.4 shows the systematic and random errors associated with the transducers used on the rig.

Measurement	Systematic Uncertainty	Random Uncertainty
Pressure Transducers (70 mbar)	64.7 Pa	49.3 Pa
Pressure Transducers (350 mbar)	272.6 Pa	239.4 Pa
Pressure Transducers (1 bar)	703.3 Pa	679.83 Pa
Pressure Transducers (5 bar)	6800 Pa	925 Pa
Displacement	None quoted	0.0015 mm
Temperature	2.89 K	0.154 K

Table 4.4: Test rig transducers uncertainties.

4.3 Experimental Procedure

Figure 4-2 shows a schematic of the experimental facility outlining the main components. Regarding operation, the rig is firstly inserted into the pressure vessel and the cover plate fitted on. The pressure is then increased to the required level: a pressure tapping placed in the

upstream cavity monitors the pressure. The range of axial displacement (upstream and downstream) is 4.1 mm. To set the running clearance under pressure, the position of contact between upstream face and the disc is determined, and the housing is displaced axially using the linear actuator to achieve the required gap. Two dial gauges are used to read the axial displacement of the housing relative to the disc. Once the required inlet pressure and gap height are reached, the DAQ system is charged to capture the data.

4.3.1 Determining touch-down location

The most challenging issue faced is trying to determine with certainty the location at which the disc and the upstream face are in contact such that a datum position can be defined. The difficulty arises because when the rig is pressurised the housing and in addition, the rotor displace axially and while it is possible to measure the displacement of the housing, the displacement and/or distortion of the rotor is not accounted for. Two methods were used and are outlined hereunder.

4.3.1.1 Method 1: Load cell

In the method initially employed, the load cell was used to determine the zero position; under unpressurised conditions the housing was pulled to a known location where the disc and the upstream face were not in contact then brought forwards in small increments while the load read by the load cell was monitored, a sudden increase in the load indicated the touch-down location. The readings from the dial gauges were recorded and that location was taken to be the zero position. Figure 4-8 illustrates load *vs* displacement found using this method used. The blue curve shows the trend as the housing is pushed towards the disc till it touches and the load starts increasing. It is then pulled away from the disc, represented by the green curve, to confirm the touch-down location. The vertical red line indicates the position of the touch down location. A hysteresis loop exists due to the internal friction within the system.

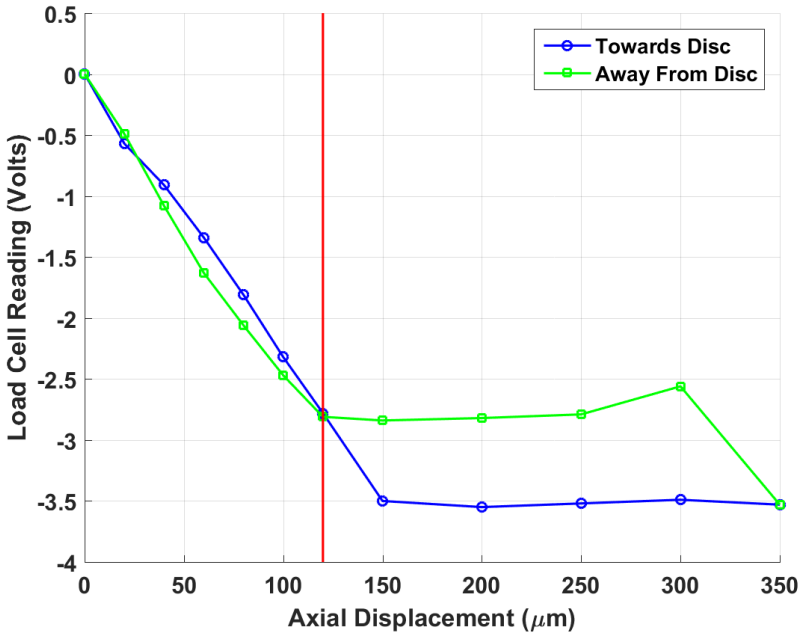

Figure 4-8: Method 1: Load Cell Reading.

Although the method applied was sufficient to confidently determine the touch-down location with no flow, once the rig is pressurized the load cell readings were significantly higher and affected by the changing gap at the sealing face. Thus, it was not possible to confidently determine whether the load being read was due to the pressure applied or the two faces coming into contact.

Another issue which hindered the use of this method was the axial displacement of the disc itself. The disc is fixed onto a stub shaft supported by a bearing. However, once pressure is applied the disc was found to move axially by a significant amount. To quantify the distance the disc displaces as a function of inlet pressure, an extension arm was manufactured for one of the dial gauges which allowed it to sit at a radius of 55 mm on the upstream face of the disc. The rig was then pressurised in increments up to 4.14 bar (gauge) and the axial displacement of the disc was recorded.

Inlet Pressure (barg)	Disc Displacement (μm)
0.69	20
1.03	30
2.07	60
2.76	75
3.45	100
4.14	120

Table 4.5: Axial displacement of disc under pressure.

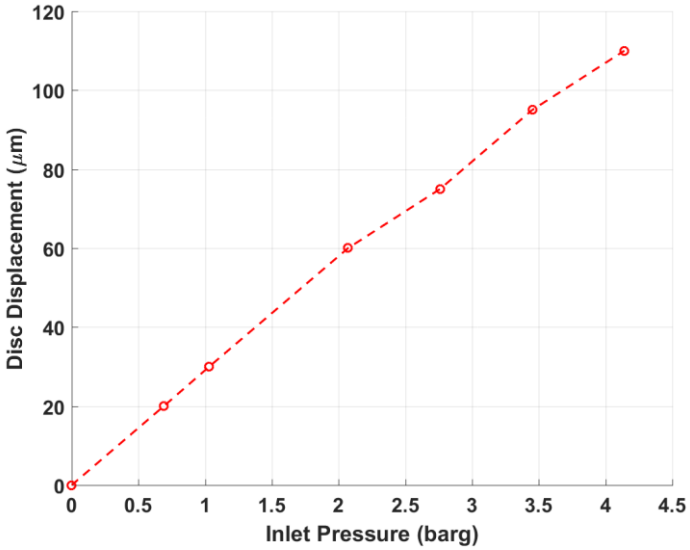

Figure 4-9: Axial displacement of disc under pressure.

Table 4.5 and Figure 4-9 show the results obtained for the displacement of the disc. The relationship is linear and the magnitude of displacement was found to be ~ 100 μm at 3.45 barg *i.e.* 200% larger than the smallest gap tested (**50 μm**). Therefore, a more robust method was developed to determine the zero-position, independent of any assumed position of the disc was vital for the research.

4.3.1.2 Method 2: Torque Measurement

A new modification to the setup aimed at alleviating the uncertainties related to the datum location was configured. The modification, shown in Figure 4-10 , was based on incorporating a torque sensor to the rotating assembly. The process was performed as follows; starting with the housing away from the disc to allow rotation, the disc was spun at low speed (**500-600 RPM**) and the housing was moved axially in small increments towards the disc while monitoring the torque. A sudden increase in torque implied the faces have come into contact and defined the touch-down location, associated with the motor stopping.

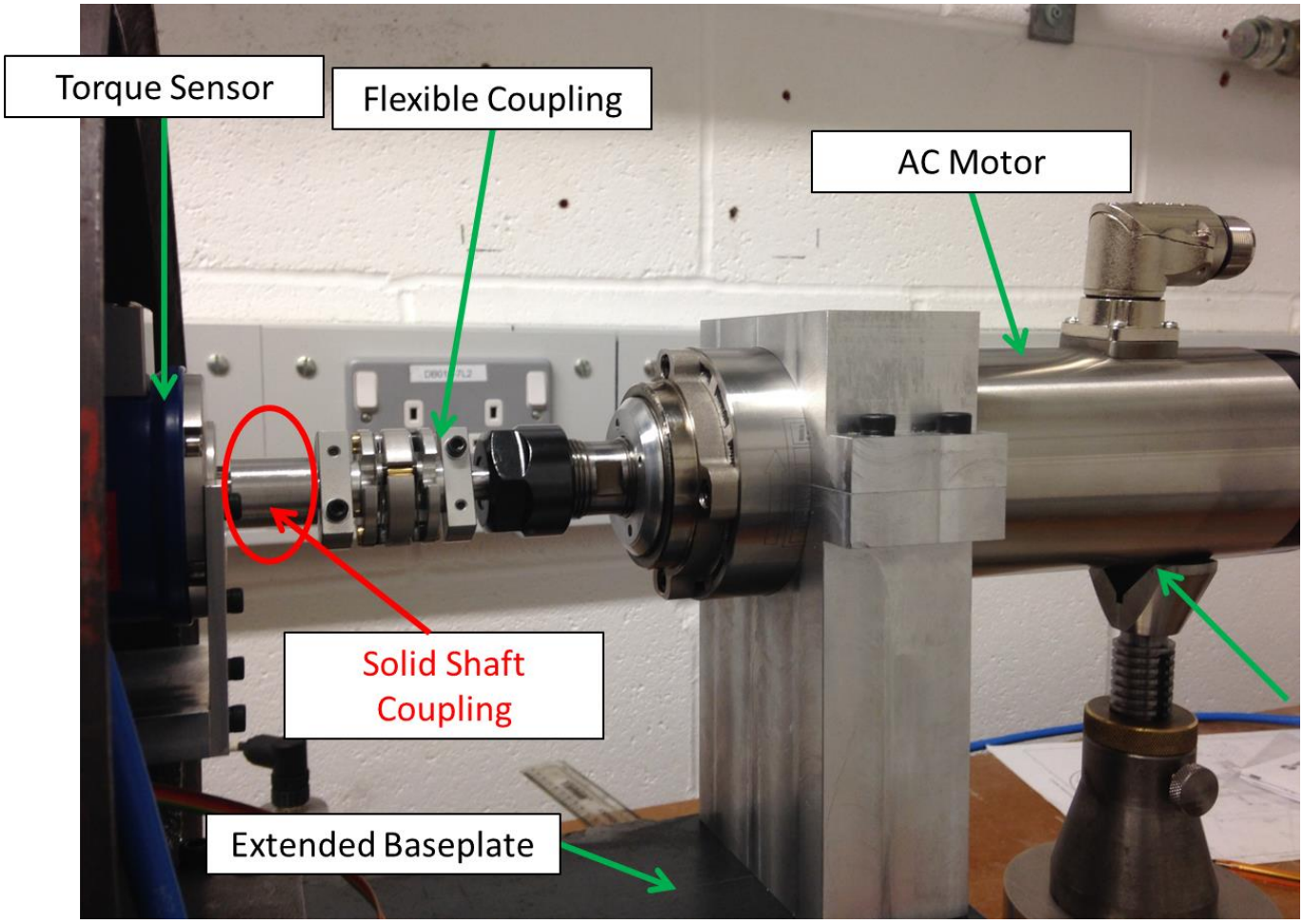

Figure 4-10: Modified rotating assembly.

Figure 4-11 shows an example of applying this method, on the *x*-axis is the time and the *y*-axis represents the torque reading. The fluctuations in the data indicate some misalignment in the setup of the rotating assembly, though not run-out on the disc itself. However, extreme care has been exercised to reduce these to a minimal level. The sudden jump in torque, represented by the vertical red line, signifies that touch-down has occurred. Accounting for the existing reading of the dial gauge, the housing is then pulled back to the required gap height. The main advantage of this method is that it is entirely independent of the movement of the disc under pressure. The results shown in this section used this method to define the reference location. Although other methods such as an electrical continuity test were considered, it was not

possible to adequately insulate the components of the rig to be able to rely on the aforementioned technique.

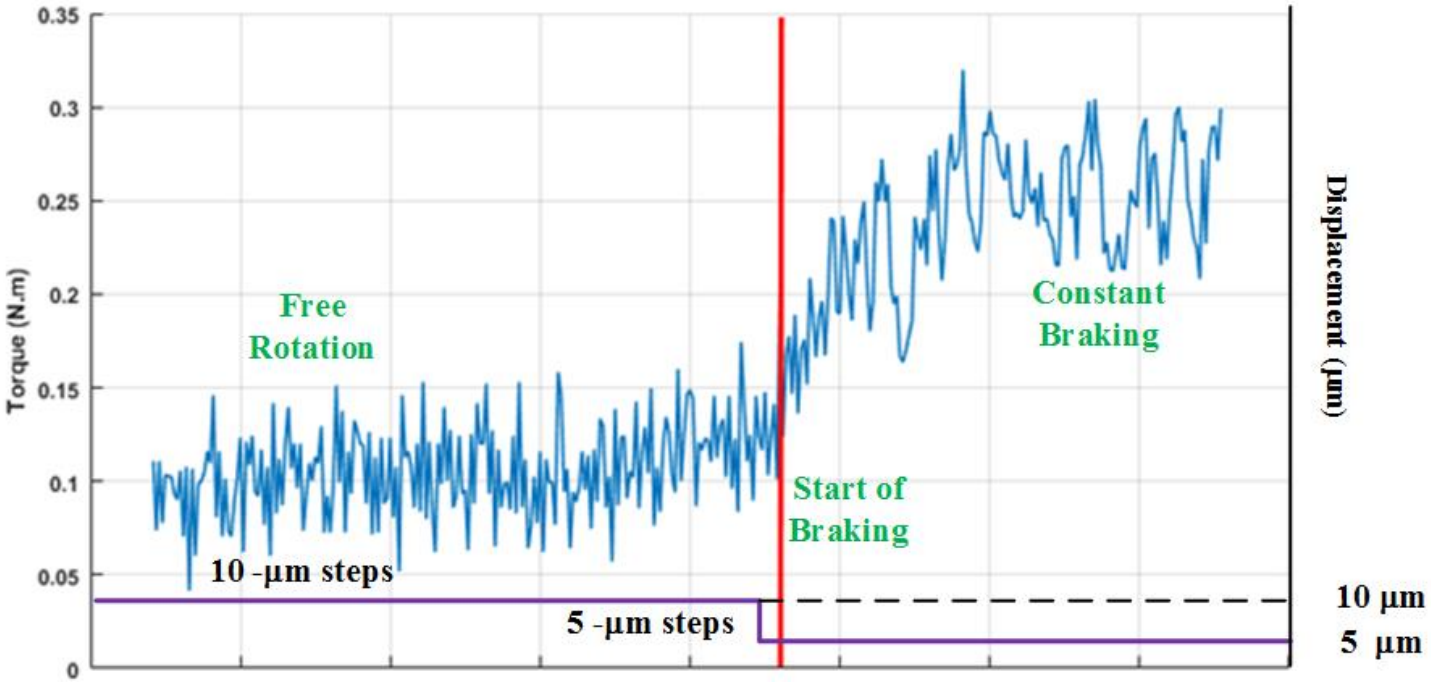

Figure 4-11: Live torque readings.

4.4 Dimensional Analysis

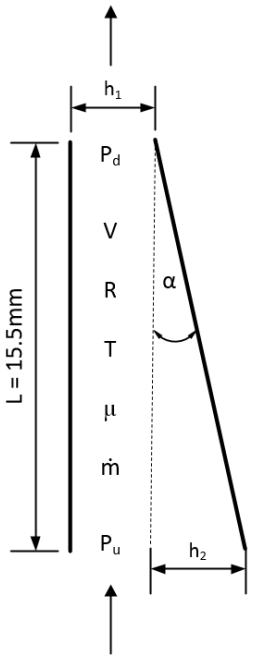

Figure 4-12

To match rig conditions to engine realistic conditions, the author performed a dimensional analysis. Compressible flow conditions were assumed and the flow parameters within the gap are shown in Figure 4-12, where $\dot{m}$ is mass flow rate, P_u and P_d are absolute upstream and downstream pressures respectively, R is universal gas constant, T is temperature, V is surface speed, μ is dynamic viscosity, h_1 is minimum gap height, h_2 is taper height, $L = 15.5\ mm$ is the radial length of the test seal and α is taper angle. According to these parameters the mass flow rate could be characterized as,

$$\dot{m} = f(P_u, P_d, \mu, R, T, V, h_1, h_2, L, \alpha, \gamma) \qquad \textbf{Eq. 4.1}$$

Hence, the dimensionless groups according to Buckingham Pi-Theorem can be represented as,

Table 4.6: Non-Dimensional Π Groups

Mass Flow Term	Reynolds Number Term	Pressure Ratio	Velocity Ratio	Coning Angle	Min. Gap to Coning Height Ratio
$\boldsymbol{\Pi_1} = \frac{\dot{m}\sqrt{\boldsymbol{RT}}}{\boldsymbol{P_u\, h_1^2}}$	$\boldsymbol{\Pi_2} = \frac{P_u h_1}{\mu\sqrt{RT}}$	$\boldsymbol{\Pi_3} = \frac{P_u}{P_d}$	$\boldsymbol{\Pi_4} = \frac{V}{\sqrt{RT}}$	$\boldsymbol{\Pi_5} = \alpha = \frac{h_2}{L}$	$\boldsymbol{\Pi_6} = \frac{h_1}{h_1 + h_2}$

Therefore,

$$\frac{\dot{m}\sqrt{RT}}{P_u\, h_1^2} = f\left(\frac{P_u h_1}{\mu\sqrt{RT}}, \frac{P_u}{P_d}, \frac{V}{\sqrt{RT}}, \alpha, \frac{h_1}{h_1 + h_2}\right) \qquad \textbf{Eq. 4.4}$$

Using these dimensionless groups, Table 4.6, along with engine data at a given operating cycle allows for scaling of experiments to engine conditions. An example is showed here where engine conditions at take-off, *i.e.* 'max dry' are as follows, P_u = 30 bar, P_d = 20 bar, T = 937 K, R = 287 J/ kg K and μ = 4.1x10^{-5} Pa s, V= 150 m/s, h_1 = 50x10^{-6} m and h_2 = 250x10^{-6} m.

Using the pressure ratio dimensionless group, $\boldsymbol{\Pi_3}$, and knowing that the downstream pressure for the rig conditions is at atmospheric pressure, the required upstream pressure to match engine conditions could be obtained as follows,

$$\frac{P_{u_E}}{P_{d_E}} = \frac{P_{u_R}}{P_{d_R}} = \frac{30}{20} = \frac{P_{u_R}}{1.01325} \;\Rightarrow\; P_{u_R} = 1.52\ bar \qquad \textbf{Eq. 4.5}$$

Where, double subscript ***E*** denotes engine conditions while ***R*** denotes rig conditions.

The rig pressure supply is connected to the 400 psi line, so that a differential pressure of 7 bar is achievable. Therefore, the required upstream pressure for this case is attainable. Note that, although the axial pressure ratio across the seal was matched to engine conditions the tests were run at room temperature to avoid any further distortions on the seal faces due to thermal loading. However, temperature scaling is accounted for in estimating the rig conditions for the minimum gap height, coning height and surface speeds as shown below.

Similarly, using the Reynolds Number group, $\boldsymbol{\Pi_2}$, scaling the minimum gap height to match engine conditions is obtainable as follows,

$$\left(\frac{P_u h_1}{\mu\sqrt{RT}}\right)_E = \left(\frac{P_u h_1}{\mu\sqrt{RT}}\right)_R \Rightarrow h_{1_R} = 245\ \mu m \qquad \textbf{Eq. 4.6}$$

Furthermore, the coning height could be matched using group $\boldsymbol{\Pi_6}$,

$$\frac{h_{1_E}}{h_{1_E} + h_{2_E}} = \frac{h_{1_R}}{h_{1_R} + h_{2_R}} \Rightarrow h_{2_R} = 1.225\ mm \qquad \textbf{Eq. 4.7}$$

Thus, the coning angle from $\boldsymbol{\Pi_5}$ is obtained as, $\alpha_R = \frac{h_{2_R}}{L_R} \approx 0.1°$

Finally, the velocity ratio non-dimensional group, $\boldsymbol{\Pi_4}$ can be used to match rig surface speeds to engine surface speeds,

$$\left(\frac{V}{\sqrt{RT}}\right)_E = \left(\frac{V}{\sqrt{RT}}\right)_R \Rightarrow V_R = 85\ m/s \qquad \textbf{Eq. 4.8}$$

The current inner and outer radii of the seal on the experimental rig are 69.5 and 85 mm, respectively. The rotational speed to give the required surface velocity is computed as follows,

$$\omega_R = \frac{V_R}{r_{outer} * 0.10472} = \frac{85}{0.085 * 0.10472} \Rightarrow \omega_R = 9550\ RPM \qquad \textbf{Eq. 4.9}$$

The maximum safe operating speed of the disc is 15 kRPM; hence the required surface is achievable.

5 Experimental and Numerical Study of Air-film Behaviour in Converging and Diverging Gaps

Throughout the operational envelope of a face seal it is difficult to maintain the flatness of both seal faces. The faces tend to take up a coned profile largely caused by thermal gradients which may be particularly high during engine transients, pressure gradients across the rotor faces, misalignment of either of the sealing rings, machining errors, or coning may be included by design. The resulting gap profile significantly affects the load capacity of the seal. Little data exit in the literature showing detailed pressure fields for the air-film under different distortions at the relatively large gaps considered in this thesis. This is particularly the case in terms of experimental data. Hence, in this chapter aims an experimental investigation of the effects of converging and diverging coning on the seal's performance in terms of its load capacity and leakage rate are reported. The coning configurations considered here are in the radial direction, see Figure 2-3, and the effect of swash is further considered in *chapter 6*.

The experimental campaign uses parallel gap configuration as a baseline test. Coning is then introduced gradually onto the primary sealing face and each configuration is tested accordingly. The range of likely gap heights, coning configurations and pressure differentials were populated following discussion with the industrial partners. The main parameters varied in experiments were; minimum gap height, $\boldsymbol{h_{min}}$, coning angle, $\boldsymbol{\alpha}$, coning height, $\boldsymbol{h_{coning}}$ and inlet pressure, $\boldsymbol{P_{in}}$. In all cases the downstream pressure was nominally atmospheric. Measurements were focused on assessing the following criteria; radial pressure distribution in the primary sealing gap, pneumatic opening force applied by the air-film on the sealing faces, leakage rate through the primary sealing gap.

The experimental data yield some very interesting results. The variation in air-film behaviour indicated by the assessing the pressure field was significant and very sensitive to the gap profile. The data give a clear indication of which gap profiles were favourable in terms of the seal's resulting load capacity and leakage rate. The conclusions drawn from this study were used as basis for designing an axially flexible sealing assembly, discussed in *chapter 6*. As experiment cannot be the primary means of seal design, and a simplified Reynolds flow based model has been shown to be inadequate, comparisons between radial pressure distribution predictions from a 3D CFD model are made to experiments for all gap configurations considered.

5.1 Parallel Gaps

5.1.1 Experimental Radial Pressure Distributions

The first set of experiments were performed on parallel sealing faces with no machined angles on either face. The parallel gaps are used as a benchmark to which other coning configurations will be compared. As mentioned previously in Table 5.1, the total available axial gap (the sum of the upstream gap height $\boldsymbol{h_u}$ and downstream gap height $\boldsymbol{h_d}$) is 4.1 mm. Figure 5-1 shows a schematic outlining the notation used. Note that, the upstream gap height is set to be the minimum gap height such that $\boldsymbol{h_{min} = h_u}$. This is at the lowest radial position on the disc as the disc undergoes slight bending under pressure. Table 5.1 lists the range of minimum gaps and downstream gaps tested. In some of the datasets presented here, the data are plotted against a normalised radial displacement. This is represented by the red line on Figure 5-1. The tappings are aligned such that the first tapping is coincident with the inner radius of the upstream housing and the 13th tapping is aligned with the rotor outer diameter. The overall extent is represented by $|R^*|$ and r is the local radial distance from the housing inner radius. Note that, the surface

finish of the disc and the static face is nominally smooth in all cases with measured ***Ra*** values of 2.8224 μm and 1.4663 μm, respectively.

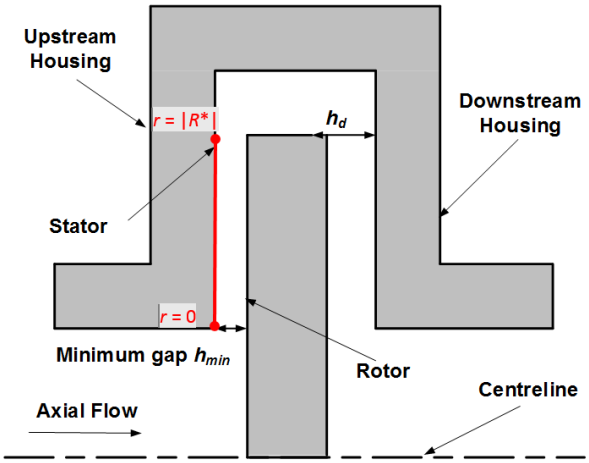

Minimum Gap $h_{min} = h_u$ (μm)	Downstream Gap h_d (μm)
50	4050
100	4000
200	3900
300	3800

Table 5.1: Axial upstream and downstream gap heights for parallel gaps.

Figure 5-1: Geometry notation for parallel gaps.

Figure 5-2 to Figure 5-4 show the average radial pressure (gauge) distributions for 4 different minimum gap heights (50 μm, 100 μm, 200 μm and 300 μm) at three different inlet pressures (0.69 barg, 1.03 barg and 3.45 barg). The pressure was averaged at 4 different locations around the circumference. Note that all tests were performed statically. As there are no changes in gap height in the circumferential direction, rotating the disc has little effect on the air-film pressure distribution.

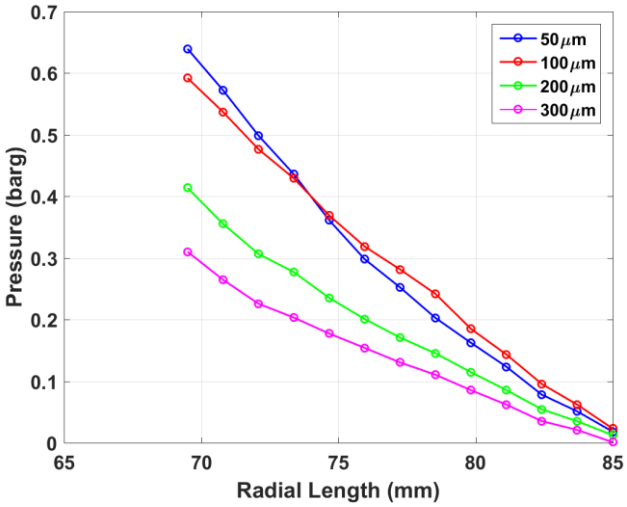

Figure 5-2: Experiments, Parallel gaps, Radial pressure distribution at P_{in}=0.69 barg.

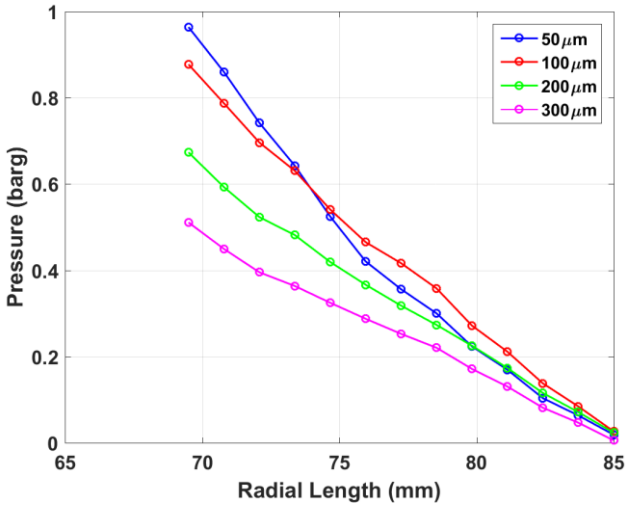

Figure 5-3: Experiments, Parallel gaps, Radial pressure distribution at P_{in}=1.03 barg.

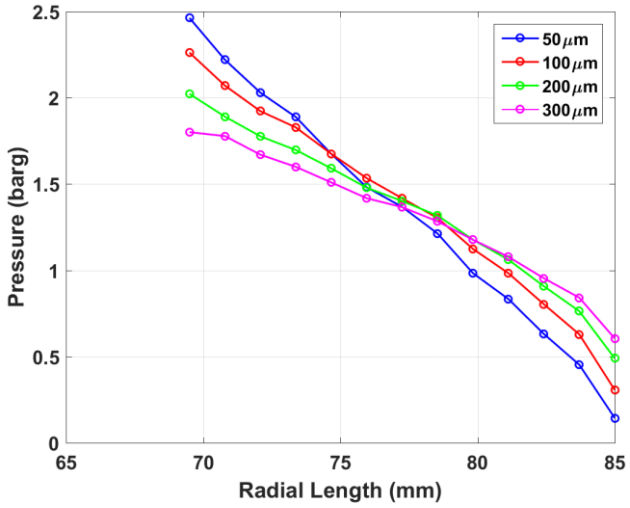

Figure 5-4: Experiments, Parallel gaps, Radial pressure distribution at P_{in}=3.45 barg.

As expected, the pressure distributions show that at smaller gaps a higher film pressure was maintained for a given inlet pressure. Possibly the most significant feature of the pressure distributions is the pressure drop evident at the entrance to the primary sealing gap. The entry loss is driven by both viscous and inertial forces as the flow accelerates around the sharp corner

at the inlet, with possible flow separation. As the mass flow increases non-linearly with increasing gap height the inertia-driven entry loss increases. With higher gaps it is noted that the exit pressure rises. This occurs as downstream of the seal there is still a complicated exit flow path from the test rig. In this region there are additional inertial exit losses which increase as the square of the exit dynamic head.

Notably, at 1.03 barg, the pressure distribution appears nearly linear with increasing radius, whereas for compressible Reynolds flow in a 2-D flow a parabolic profile might be expected. In fact the pressure distribution appears to be concave in shape. This might be expected near the entrance and there is likely some pressure recovery from an initial separation fighting pressure drop along the radial flow direction in this region. Furthermore, as the flow moves radially outwards, one might expect a more rapid decrease in pressure compared to a 2-D geometry linear geometry because of simple continuity requirements - the area increase is akin to having a diverging gap. Over the range 68 - 84 mm there is an increase in flow area for the parallel gap case of 23%, and simplistically this might be considered equivalent to a diverging angle of 4.6^{o} to 5.2^{o} over the range of gap sizes from 20μm to 300μm. However, it is clear that the pressure field does not conform to such a radically expanding geometry. Indeed, at higher inlet pressures the expected characteristic curvature in the pressure distribution is restored, particularly towards the exit region of the seal.

To try to quantify the effect of the change in flow area with increasing circumference a comparison was made between 2D and axisymmetric CFD predictions of two simple parallel gap cases (50 μm and 300 μm) over the radius range of the test rig to assess the effect of the increasing radius more realistically. The simulations were conducted using a uniform mesh of 5 x 5 μm resolution in each gap, at two inlet pressures of 200 kPa and 445 kPa with the outlet

pressure set at 100 kPa, a schematic of the domain is shown in. A laminar flow viscosity model was used in the case of the small gaps, and laminar and realizable-k-ε with enhanced wall treatment were used for the larger gap cases, the results are shown in Figure 5-6.

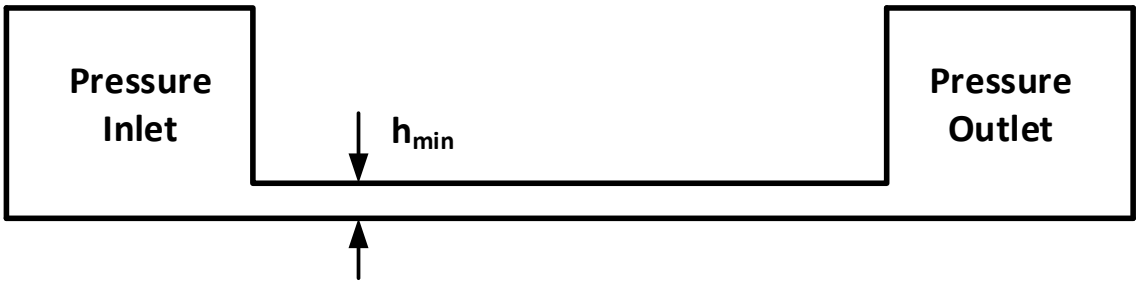

Figure 5-5: Schematic of simple CFD domain for investigating effect of increasing circumference.

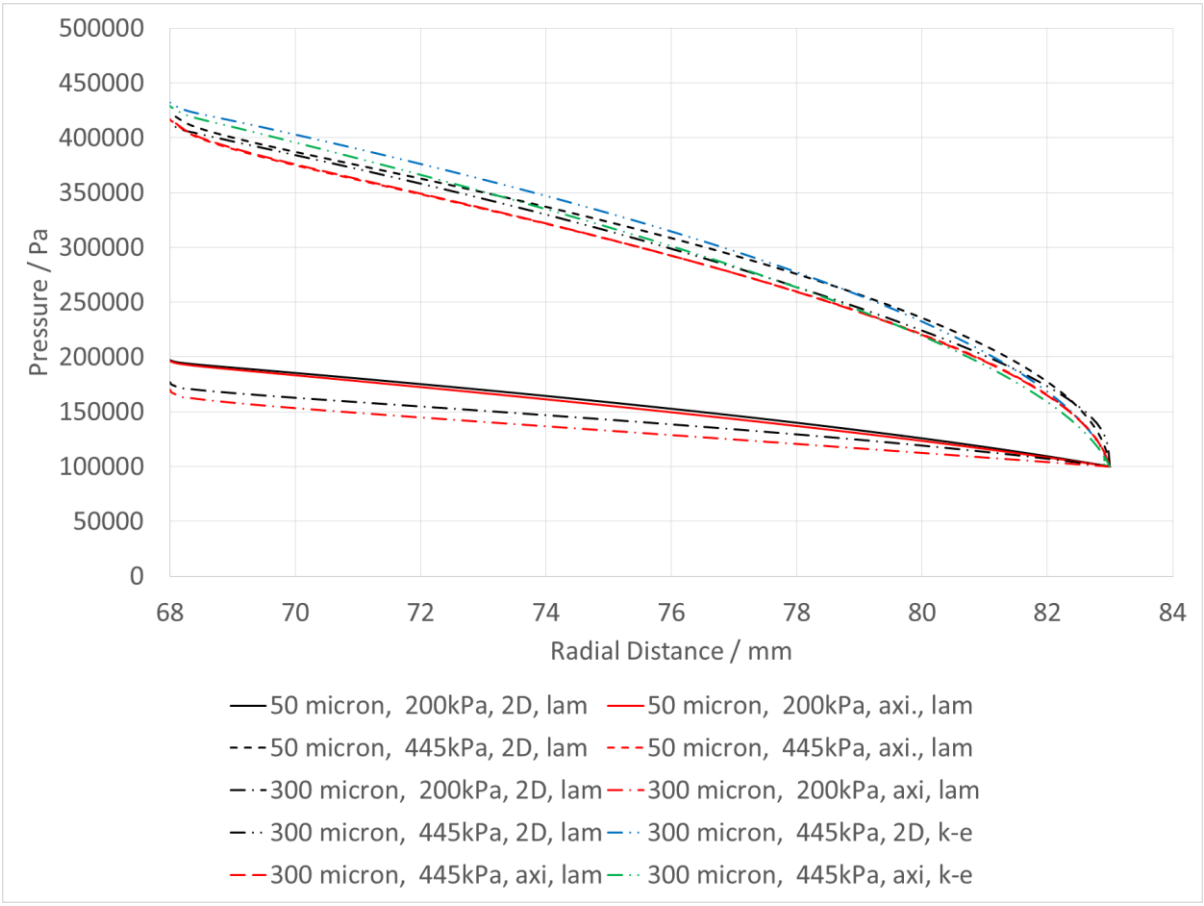

Figure 5-6: Comparison of 2D and axisymmetric (axi.) CFD simulations of a simple parallel gap with the indicated upstream inlet total pressure, for laminar and turbulent flow (in 300micron gap cases).

At low pressure there is surprisingly little difference in the pressure distribution between the cases seen, and the pressure distribution deviation appears to be dominated by the establishment of the boundary layer at the inlet of the system in the case of the 300 μm gap. At higher pressure the story is more complicated. In each case the 2D model slightly over predicts the pressure distribution compared to the axisymmetric case, whether running with a laminar or turbulent viscosity model, but the deviation is not large and can be assessed in terms of the average pressure on the face and the centre of pressure in the system. These are shown in Figure 5-7.

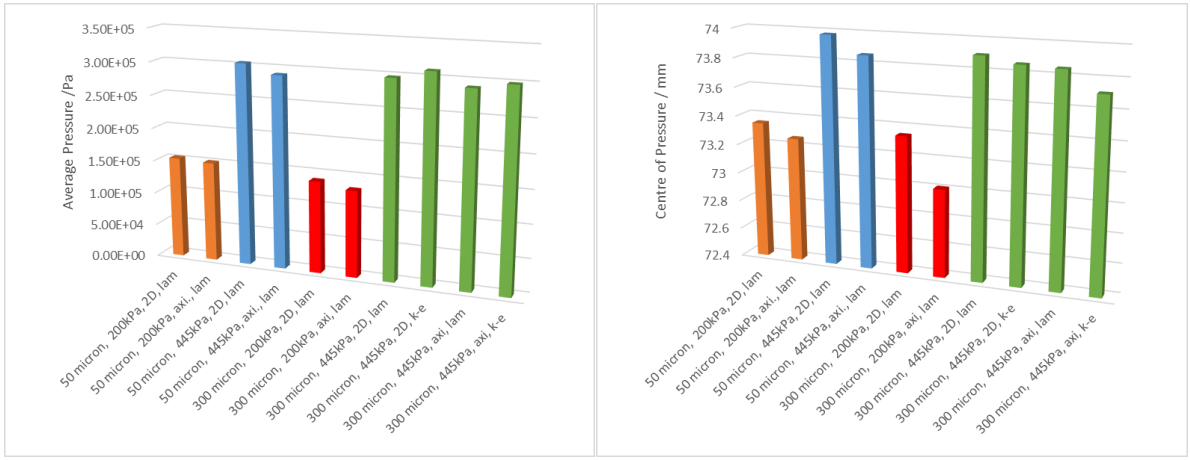

(a) **(b)**

Figure 5-7: Comparison of Average face pressure (a) and Centre of Pressure (b) for 2D and axisymmetric (axi.) CFD simulations of a simple parallel gap shown in Figure 5-6.

It is clear that for all of the cases the change in the position of the centre of pressure < 0.3 mm, and the change in average pressure and hence the force generated by the sealing face is 2 – 8% of the driving pressure difference, with the largest discrepancy being for the high gap low pressure case. For the larger gap at high pressure there is no reliably known solution, as the flow is not laminar, but there is close agreement between the 2D and the axisymmetric cases simulated using the same turbulence model. The change in the centre of pressure is insignificantly small here, as the seal will be embodied as a circumferential ring which will be

supported against twisting, while the change in average pressure may result in a changed equilibrium gap in the seal and hence a change in the leakage mass flow rate.

Considering further the pressure distributions in Figure 5-2 and Figure 5-3, a cross-over is observed in the pressure distribution curves for the 50 μm and 100 μm gap heights at 0.69 barg and 1.03 barg. This is likely caused by the relative unimportance of flow loss and recovery at the inlet of the 50 μm gap (low gap and low dynamic head), and the dominance of viscous loss in the latter region of the sealing face for the same geometry. An additional effect may the very slight bending under pressure loading of the disc which is more significant at smaller gap sizes. This feature is apparent particularly in the parallel gap cases where small deviations change the nature of the flow. At larger gap heights the effect of surface flatness becomes less prominent compared to the gap height. (For a given upstream pressure there are only small changes in pressure distribution over the face of the disc regardless of the minimum gap, so the deformation is approximately the same as shown below in Figure 5-19.)

At 3.45 barg, Figure 5-4, the pressure drop in the exit passage is significant causing the exit pressure to rise and a cross-over of pressure distributions at radial location r = ~ 78 mm. This cross over (at non-dimensional $r/|R^*|$ ~ 0.5 - 0.6) is, in fact, an artifice of the experimental test rig, as here the increased mass flow rate has caused a rise in the back pressure in the test rig. To assess whether there has been a change in the gap flow physics, the pressure drop from inlet conditions to the exit of the face seal should be considered as the driving pressure in the system. For comparative purposes then in this case the pressure is normalised on the basis that $p^* = \frac{p_{in} - p(r)}{p_{in} - p_{final\ tapping}}$ as shown in Figure 5-8. Here the normalisation is by the local driving pressure difference across the seal, however the inlet pressure is the same in all cases. Following normalisation it is clear that (*i*) there is increased load capacity at low gaps caused

by the lower leakage mass flow rate as expected (*ii*) there is no longer any cross-over behaviour in the pressure distributions.

Figure 5-9 shows the effect of rotating the disc (albeit slowly) on the resulting pressure distribution. (Much higher rotational speeds are considered later in the thesis – see *chapter 6*) Again for this plot it was necessary to normalise the local pressure distribution by the inlet to outlet pressure difference. For each of the stationary cases shown, the corresponding rotating case is represented by a dashed line. Little difference was observed between stationary and rotating cases.

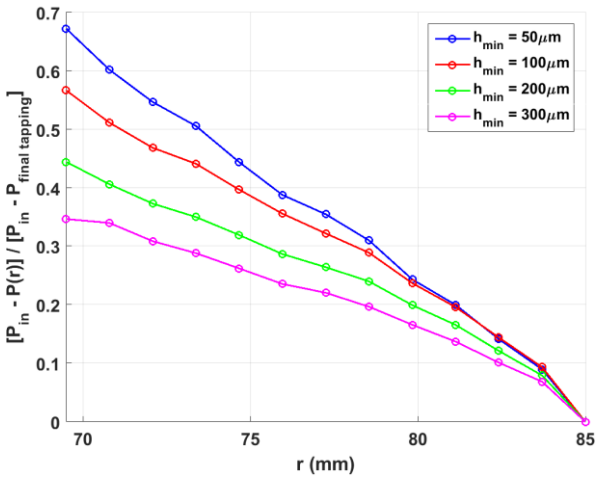

Figure 5-8: Experiments, Parallel gaps, Normalised Radial pressure distribution at P_{in}=3.45 barg, 0 RPM.

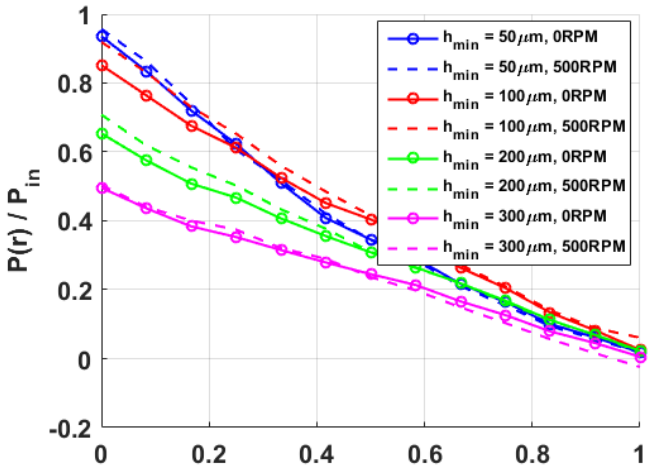

Figure 5-9: Experiments, Parallel gaps, Radial pressure distribution at P_{in}=3.45 barg.

It should be noted that although experimental data are plotted here the associated error bars have been omitted, as in all cases they are smaller in extent than the size of the data markers. Care has been taken to eliminate bias errors through the iterative use of a single pressure transducer, thus the error associated with each reading is the precision error. This error is not a percentile of the reading but rather an absolute value determined as a percentage of the full scale and allowing for misreading in the DAQ system and misreading of the offset at zero

pressure prior to the start of the tests. The data are taken in a manner which eliminates the systematic errors in pressure measurement when the non-dimensional pressure is reported. The error in non-dimensional pressure ranges from 0.027 – 0.037 at an inlet pressure of 3.45 barg rising to 0.0137 – 0.0190 at 0.69 barg inlet. The error at r = 85 mm is indeterminate.

5.1.2 Parallel Gaps: 3D CFD Radial Pressure Distributions

The CFD methodology and meshing strategy are fully described in *chapter 3*. In this is section, the results of the 3D CFD simulations of the primary leakage path though the seal for the parallel gap tests are shown. The results are compared to the radial pressure distributions obtained from experiments.

Figure 5-10 and Figure 5-11 show the pressure distributions across the 50 μm gap at two different inlet pressures (1.03 barg and 3.45 barg). Results show that the CFD overpredicts the pressure within the primary gap in both cases. At the lower inlet pressure (1.03 barg), the inlet loss is captured accurately by the CFD, however the concave pressure distribution is not properly predicted. For the higher inlet pressure (3.45 barg), the CFD significantly underestimates the inlet loss and subsequently a higher film pressure is maintained compared to the experimental case.

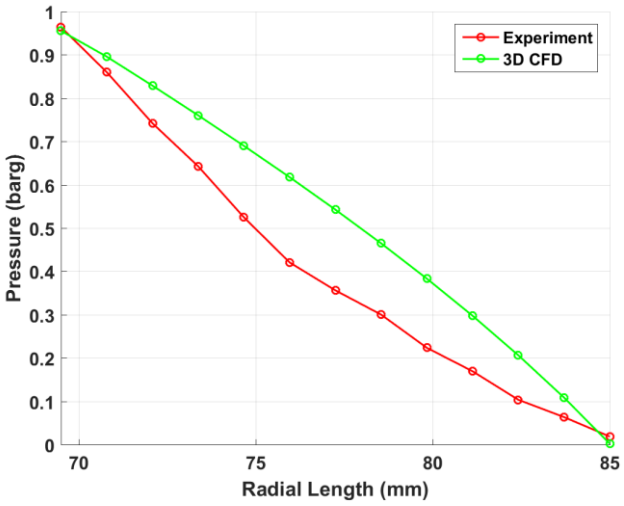

Figure 5-10: CFD, Parallel gap, Radial pressure distribution, h_{min} =50, P_{in}=1.03 barg.

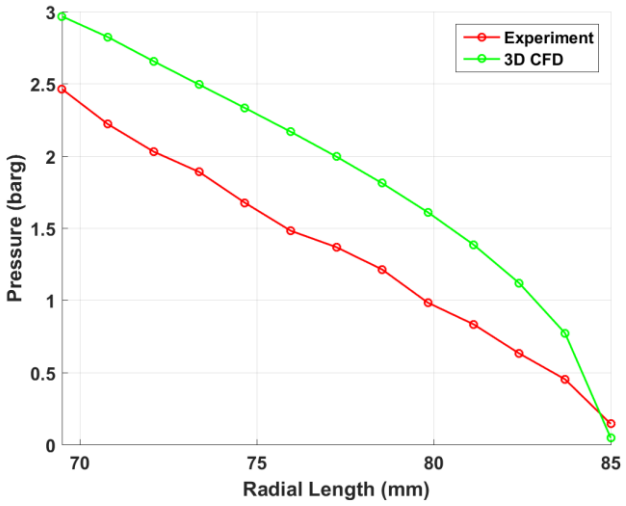

Figure 5-11: CFD, Parallel gap, Radial pressure distribution, h_{min} =50, P_{in}=3.45 barg.

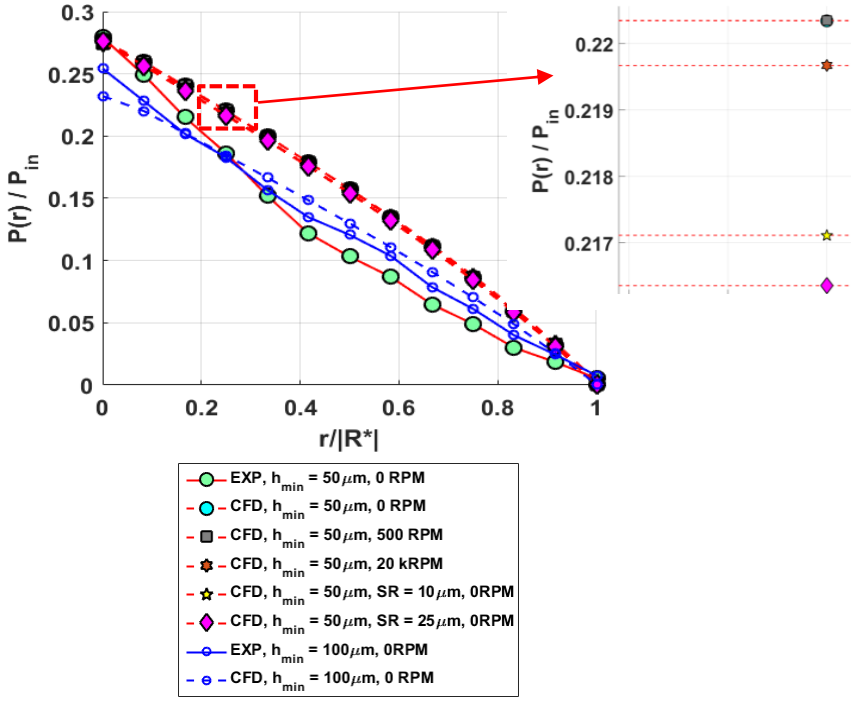

Figure 5-12: Experiments, Parallel gaps, Radial pressure distribution at P_{in}=3.45 barg.

Figure 5-12 shows the effect of varying the rotational speed and the surface roughness (*SR*) for the 50 µm gap case – these changes are affected using CFD. Changing the rotational speed by a factor of 40 resulted in almost no change in the predicted pressure distribution. Minor

differences were observed between the stationary CFD pressure distribution and both rotating cases (500 RPM and 20 kRPM). Similarly, varying the surface roughness height did not improve the CFD predictions. This is perhaps unsurprising. The effect of pumping would be to increase the pressure locally moving radially outwards, however, the pressure at the exit is prescribed and one might then expect small changes in the shape of the pressure distribution, but with similar endpoints if the entry loss is similarly captured. It should also be noted that the geometric inaccuracies inherent to the experiment in terms of the surface flatness of the sealing faces and the run-out of the disc (± 20 μm when installed on test rig) are contributing factors to the mismatches between CFD and experiments. Additionally, the level of corner radius-ing at the inlet to the gap (and step location) can be significant in setting the magnitude of inlet pressure loss to the system, however this has not been considered in this work.

The 100 μm minimum gap cases shown in Figure 5-13 and Figure 5-14, show strong agreement between CFD predictions and experimental data at both operating pressures (1.03 barg and 3.45 barg), apart from a slight variation in the magnitude of the inlet entry loss. Note that, for the 50 μm and 100 μm gaps, the fluid block representing the flow in the primary gap was assigned as a laminar zone. The rest of the blocks were defined as turbulent zones and the *realizable k-epsilon* turbulence model was used.

P_{in} (barg)	Minimum Gap h_{min} (μm)	Reynolds No. Re_h
1.03	50	1040
	100	4600
	200	10940
	300	8800
3.45	50	4040
	100	11340
	200	24800
	300	38000

Table 5.2: Reynolds Number in the Gap

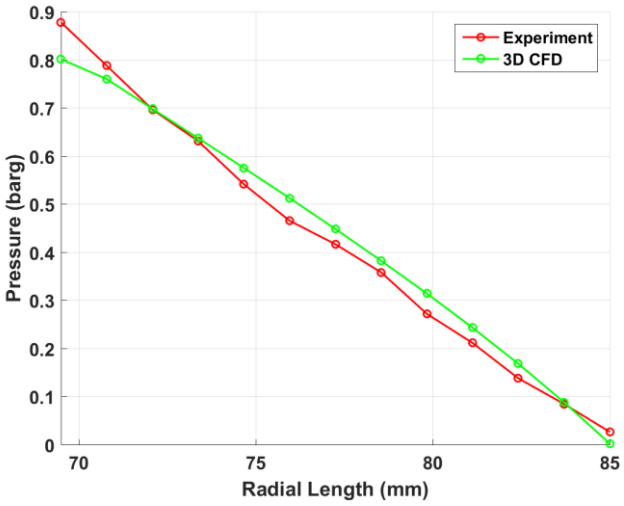

Figure 5-13: CFD, Parallel gap, Radial pressure distribution, h_{min} =100, P_{in}=1.03 barg.

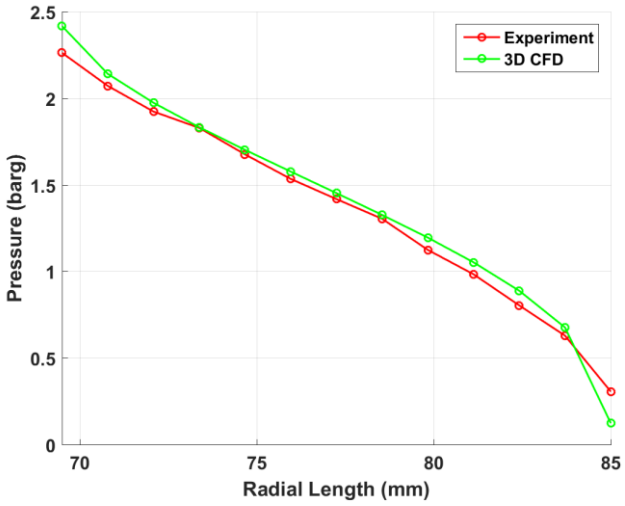

Figure 5-14: CFD, Parallel gap, Radial pressure distribution, h_{min} =100, P_{in}=3.45 barg.

Figure 5-15 to Figure 5-18 show the comparisons for the 200 and 300 μm gaps. The plots show the CFD predictions for both a laminar flow in the primary gap and another for a fully turbulent domain. The initial simulations were run with laminar flow in the gap, however the discrepancies between the CFD predictions and experiments were large. This lead to a reconsideration of the previously made assumption of laminar flow in the primary gap across all cases. Table 5.2 shows the *Reynolds Number*, Re_h, based on twice the minimum gap height (hydraulic diameter ≈ $2h_{min}$) at two inlet pressures (P_{in} = 1.03 and 3.45 barg) as obtained from CFD. If the onset of turbulence in an internal pipe or duct is accepted to occur at Re =2000 - 4000 then the cases with 200 and 300 μm gap heights lie well above that limit and the flow may be considered turbulent. Therefore, all cases with gaps larger than 100 μm are modelled as fully turbulent flow. The use of *realizable k-epsilon* model, however, limits the source terms to be small. A significantly improved agreement between CFD and experiments was achieved for larger gaps when a fully turbulent domain was imposed.

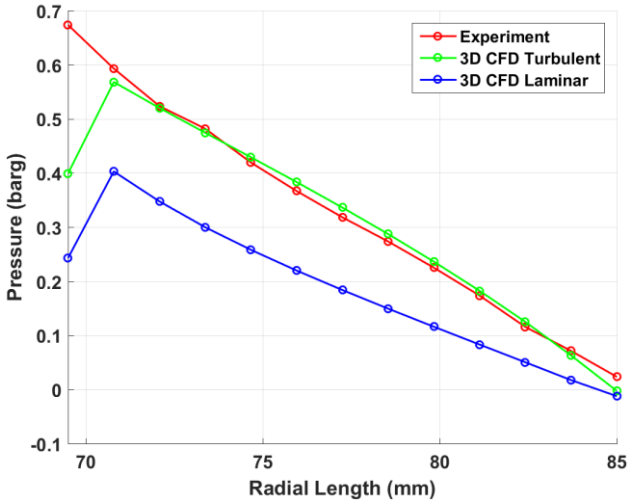

Figure 5-15: CFD, Parallel gap, Radial pressure distribution, h_{min} =200, P_{in}=1.03 barg.

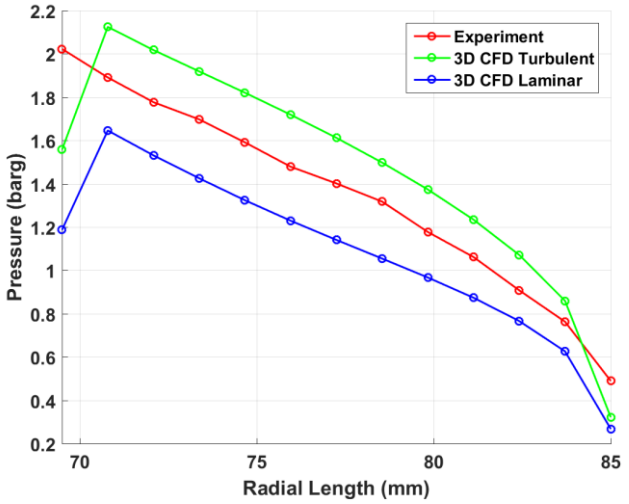

Figure 5-16: CFD, Parallel gap, Radial pressure distribution, h_{min} =200, P_{in}=3.45 barg.

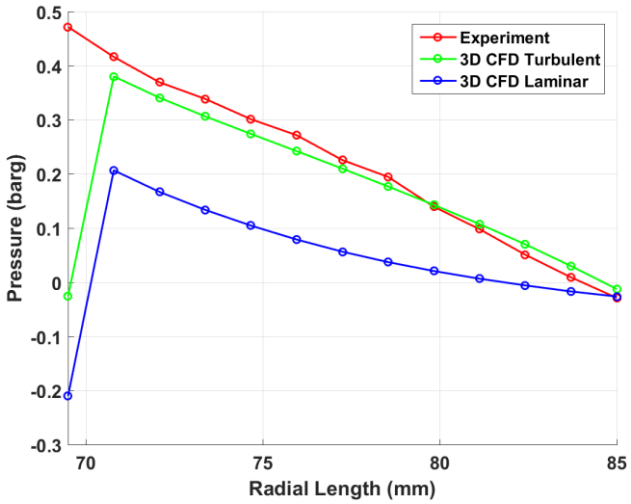

Figure 5-17: CFD, Parallel gap, Radial pressure distribution, h_{min} =300, P_{in}=1.03 barg.

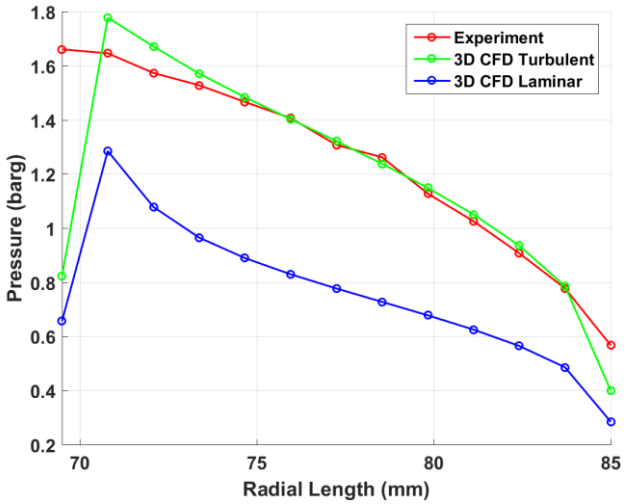

Figure 5-18: CFD, Parallel gap, Radial pressure distribution, h_{min} =300, P_{in}= 3.45 barg.

Figure 5-19 shows the resulting coning angle of the disc under a range of operating pressures at a range of initial gaps. An FEA model was set up where the pressure load from the air-film at different gap heights and inlet pressures was applied over the seal's radial length. The remainder of the disc was under the load from the inlet pressure. The loading was surprisingly high and at small gaps may cause displacement of the outer radius of the disc by as much as

50% of the gap height, however, because the datum touchdown clearance is actively controlled: being set at the beginning of each test, under pressure loading, the nominal seal clearance can be restored. There is, however, always a slight divergence in the range of 0.005° – 0.029° as shown in Figure 5-19.

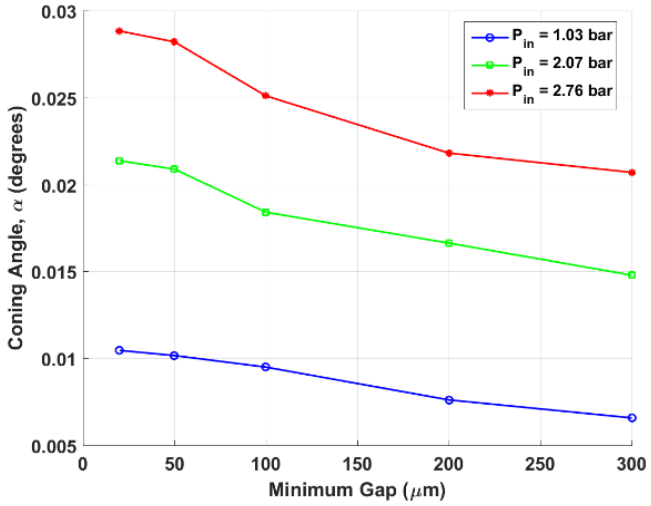

Figure 5-19: Experiments, Parallel gaps, Radial pressure distribution at P_{in}=3.45 barg.

5.2 Converging Gaps

5.2.1 Experimental Radial Pressure Distributions

The second set of tests investigated a converging gap (a converging path from gap inlet to gap outlet). The converging angle is denoted by α and is a given a negative sign to highlight its negative slope, refer to Figure 5-20 for a schematic describing the geometry of a converging gap, note that only the upstream gap geometry is shown as there are no changes in the downstream gap geometry from the parallel cases. The converging angle was machined on the static sealing face (removable face) by gradually removing material off the front face to give the desired angle. The same arrangement of pressure tappings was used to read the static pressures in the gap. Three converging angles were considered, α = -0.5°, -1.0° and –1.5°. Table

5.3 shows the range of coning angles, their corresponding coning heights and the minimum gaps considered. Note that, the local upstream gap is then the sum of the minimum gap height h_{min} and the coning height h_{coning}. The minimum gap lies at the outer radius of the sealing faces while the total gap is at the inner radius. The total axial length remained as 4.1 mm in these tests. The minimum gap for a given converging angle was altered by displacing the seal axially using the linear actuator. The touch-down location was determined in the same method applied before, see *section 4.3.1.2*. However, for the converging gap case touch down occurs first at the outer radius of the sealing face being the closest point to the rotating disc. The minimum gap is defined as the distance travelled from the touch-down location to a given location as read by the digital dial gauges.

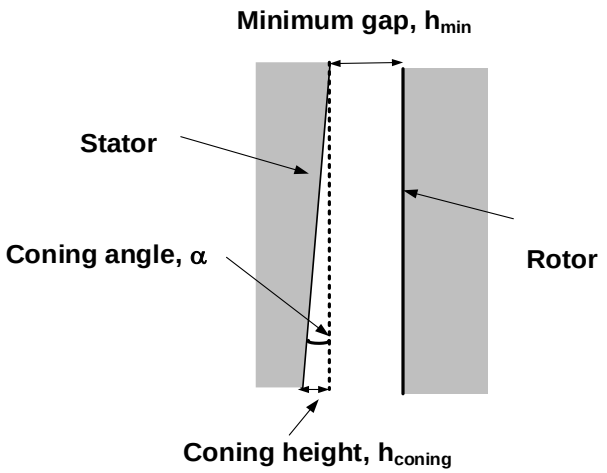

Figure 5-20: Geometry notation for converging gaps, upstream gap.

Coning angle (deg.)	Coning Height h_{min} (μm)	Minimum Gap h_{min} (μm)
-0.5	-135	50,100, 200, 300
-1	-270	50,100, 200, 300
-1.5	-405	50,100, 200, 300

Table 5.3: Range of minimum gap heights, converging coning angles and coning heights.

Figure 5-21 to Figure 5-29 show the circumferentially-averaged radial pressure distributions for all three converging angles considered. The minimum gap heights for a given converging angle ranged from 50 to 200 μm. The blue curve labelled $\alpha = 0^o$ represents the corresponding parallel case for the given minimum gap height.

A general trend is immediately evident from the range of pressure distributions shown below whereby a converging gap consistently maintained a higher film pressure for a given minimum gap and inlet pressure compared to a parallel gap. Moreover, increasing the converging angle resulted in an increase in average film pressure which is intuitively the case as the air-film gets *squeezed* into the converging gap, recovering some of the pressure loss compared to the parallel case.

As with the parallel gaps, an inlet pressure loss was evident and dominates the results for many conditions. Interestingly, the inlet loss appeared to be more a function of the minimum gap rather than the converging angle as minor changes were observed in the magnitude of the inlet loss over a range of converging angles at a given minimum gap. This, it is presumed, is because the minimum gap is dominant in setting the mass flow rate through the system, and the coning angle means that the proportional change of the geometry is smaller at the inlet than for the parallel cases. The pressure distributions for smaller gap heights (50 and 100 μm) at the two lowest inlet pressures (0.69 barg and 2.07 barg), Figure 5-21 and Figure 5-22, show that the entry loss for converging cases was consistently higher than the parallel configuration regardless of the gap size. This effect is consistent with a near constant loss coefficient at the inlet of to the seal. This can be seen by reference to Figure 5-71 which shows the mass flow rate through the converging gaps. Here, at a given inlet pressure the mass flow rate is seen to rise approximately with $\alpha^{0.5}$, whereas the inlet gap increases linearly with α. Thus the dynamic head at inlet is approximately constant. Also notable are the gap exit pressures, which are higher than the parallel cases and increased steadily with the converging angle. This is a direct result of the increased mass flow rate for all converging gaps compared to the parallel cases. The results also suggest the presence of a back pressure being created in the rig which implies

that the overall system leakage is also important as the path downstream participates in the sealing function.

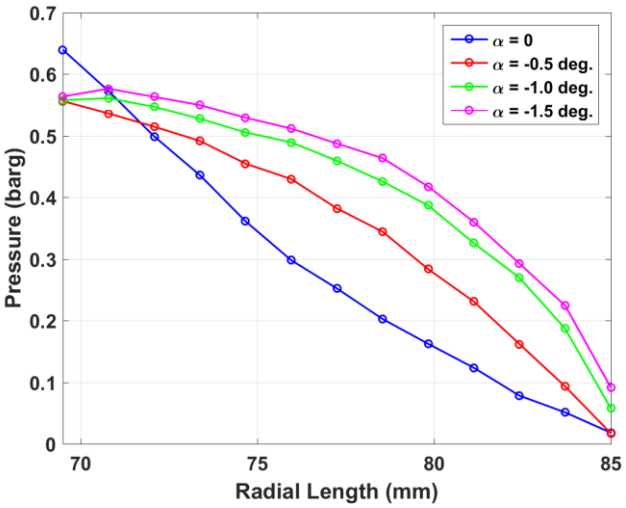

Figure 5-21: Experiments, Converging coning, Radial pressure distribution, h_{min} =50, P_{in}=0.69 barg

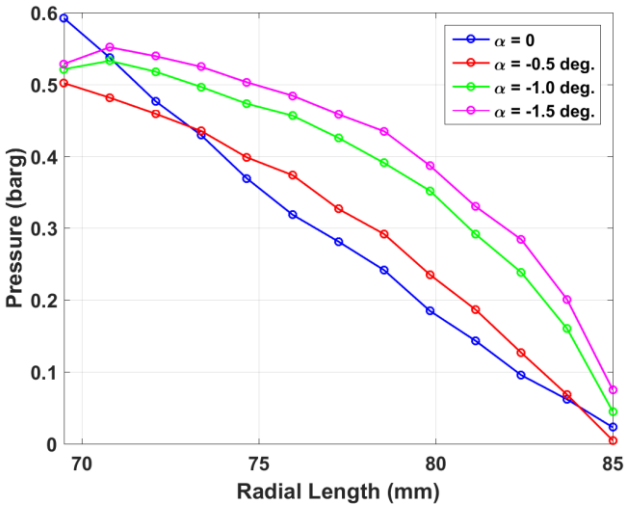

Figure 5-22: Experiments, Converging coning, Radial pressure distribution, h_{min} =100, P_{in}=0.69 barg.

The behaviour is reversed for the larger minimum gap height (200 μm), Figure 5-23, where the inlet loss for the converging cases is slightly lower than the corresponding parallel case. However, at higher inlet pressures (2.07 barg up to 3.45 barg) the inlet loss for converging cases was consistently lower than the parallel configuration regardless of the gap size, figures Figure 5-24 to Figure 5-28. As expected, the gap exit pressures were higher than the parallel cases and increased steadily with the converging angle. The larger inlet loss exhibited by converging cases in comparison to parallel cases could be due to the fact that the average gap height for a converging gap is inherently larger than a parallel gap. And as has been shown before in the parallel configuration results, larger gaps resulted in higher inlet losses as inertial forces became more significant.

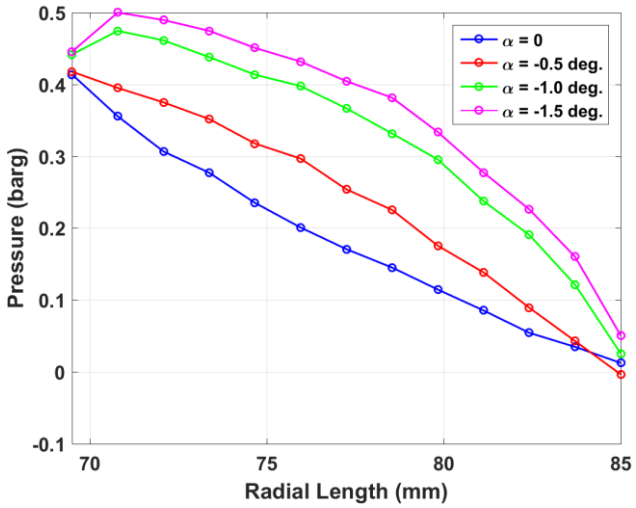

Figure 5-23: Experiments, Converging coning, Radial pressure distribution, h_{min} =200, P_{in}=0.69 barg.

Additionally, immediately downstream of the inlet loss location a region of pressure recovery exists as the flow separates around the corner and re-attaches further downstream. The recovery region was more pronounced in cases featuring larger angles (α = -1° and -1.5°) and minimum gap heights of 100 μm and greater, particularly at higher inlet pressures, Figure 5-25, Figure 5-26 and Figure 5-28.

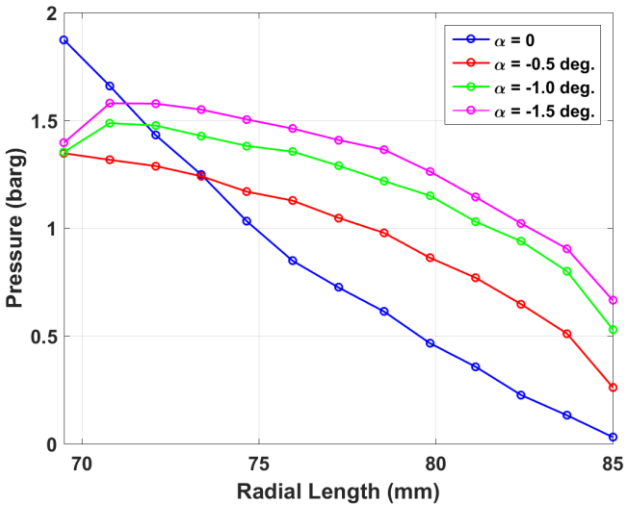

Figure 5-24: Experiments, Converging coning, Radial pressure distribution, h_{min} =50, P_{in}=2.07 barg.

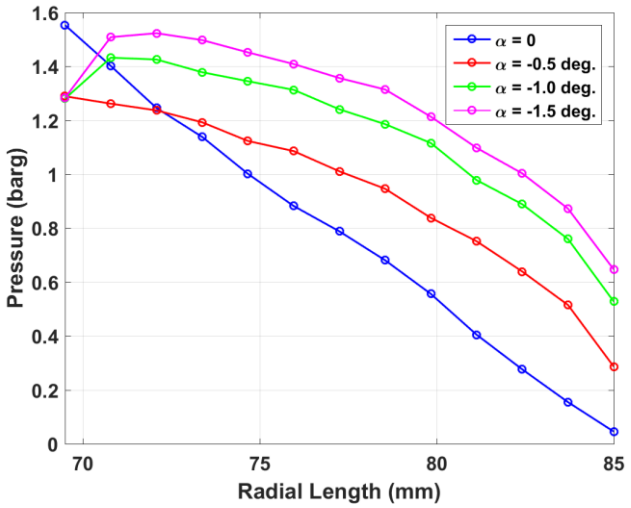

Figure 5-25: Experiments, Converging coning, Radial pressure distribution, h_{min} =100, P_{in}=2.07 barg.

At the highest inlet pressure (3.45 barg), Figure 5-28, only data for two converging angles (α = -0.5° and -1.0°) were obtained. This was because at α = -1.5° the large air-film force generated could not be overcome by the linear actuator as the housing was being pushed forward towards the rotating disc. As a result, it was not possible to determine the touch-down position with sufficient accuracy.

In general, the behaviour seen from having a converging coning in the primary sealing gap was favourable as it remarkably increased the air-film pressure. Further results in this section will illustrate in detail how the minimum gap and coning angle affect the leakage rate and the air-film force.

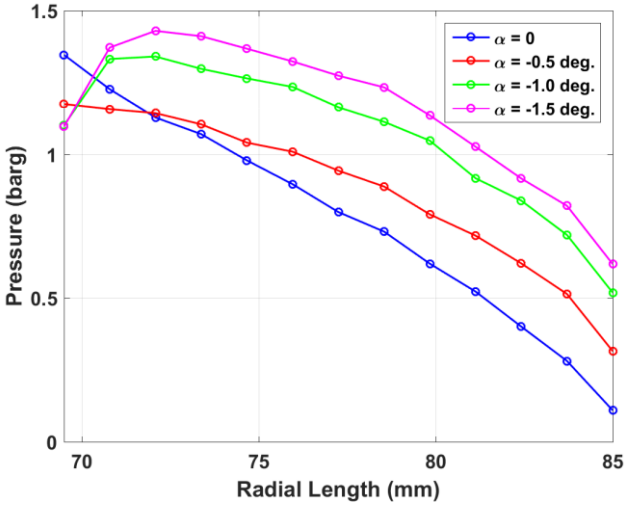

Figure 5-26: Experiments, Converging coning, Radial pressure distribution, h_{min} =200, P_{in}=2.07 barg.

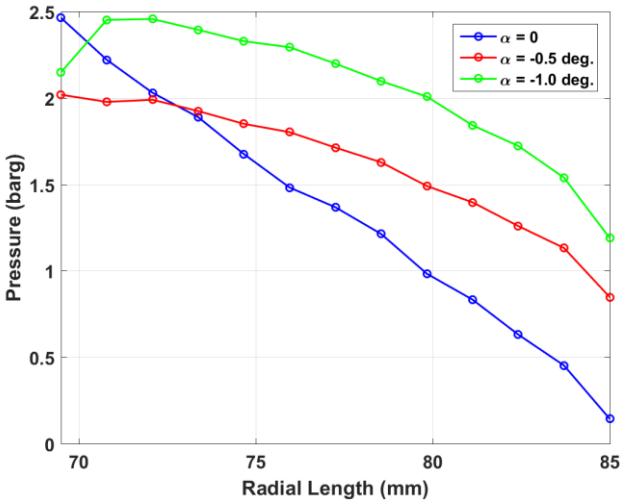

Figure 5-27: Experiments, Converging coning, Radial pressure distribution, h_{min} =50, P_{in}= 3.45 barg.

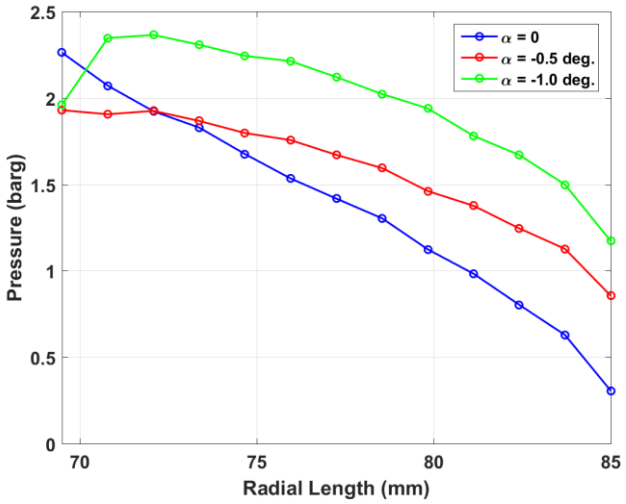

Figure 5-28: Experiments, Converging coning, Radial pressure distribution, h_{min} =100, P_{in}= 3.45 barg.

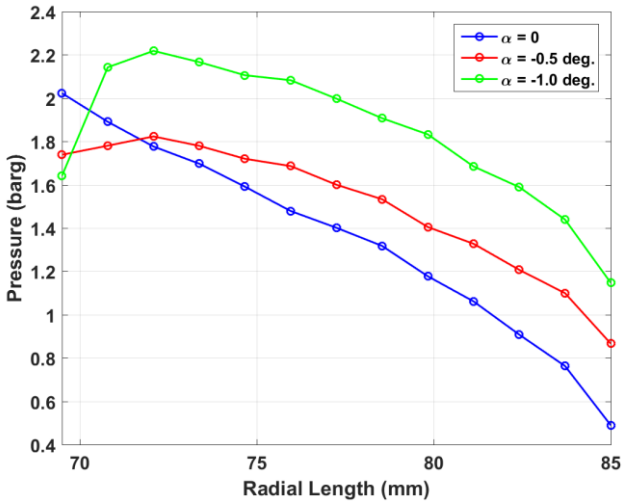

Figure 5-29: Experiments, Converging coning, Radial pressure distribution, h_{min} =200, P_{in}=3.45 barg.

5.2.2 Converging Gaps: 3D CFD Radial Pressure Distributions

This section compares the radial pressure distributions from the 3D CFD model against those obtained experimentally for the converging configuration. Each plot in Figure 5-30 to Figure 5-35 shows the pressure profile at a given inlet pressure (0.69 barg up to 3.45 barg) for a set minimum gap (50 μm and 100 μm) at two converging coning angles (α = -0.5° and -1.0°). Refer to Table 5.3 for corresponding coning heights.

Considering the full range of data shown, it is evident that the film pressure predicted by CFD is significantly higher than that obtained experimentally. However, the trend from both data sets matches fairly well. Unlike the inlet pressure loss shown experimentally, which is more sensitive to the minimum gap height rather than the coning angle, CFD predictions suggest that the larger coning angle (α = -1.0°) results in lower inlet loss, but this loss increases with increasing gap heights. The effect is clearly evident in Figure 5-31, Figure 5-33 and Figure 5-35.

The air-film pressure distribution predicted by the CFD for the smaller gap height (50 μm), illustrated in Figure 5-30, Figure 5-32 and Figure 5-34, shows that the air-film is maintained close to the upstream pressure in the gap before suddenly dropping in close proximity to the gap exit. The effect is most clearly illustrated at higher inlet pressures. Moreover, the discrepancy between both data sets significantly increases at higher inlet pressures, Figure 5-34, where the loss appears to be massively over-predicted. Although the trend from the experimental curve is similar, the air-film pressure was maintained over a smaller region and a considerable drop was already encountered before exiting the gap. More encouragingly, for the smaller angle case (α = -0.5°) CFD shows very little signs of pressure recovery downstream of the inlet loss location which agrees with what has been shown experimentally. On the other hand, the larger angle showed a recovery region in experiments but not CFD. Although the magnitude of inlet loss was markedly different between CFD and experiments they showed a similar trend whereby a very subtle difference in entrance loss was seen in for both angles at the smaller gap height (50 μm). Similar to experiments, increasing the coning angle increased the air-film pressure.

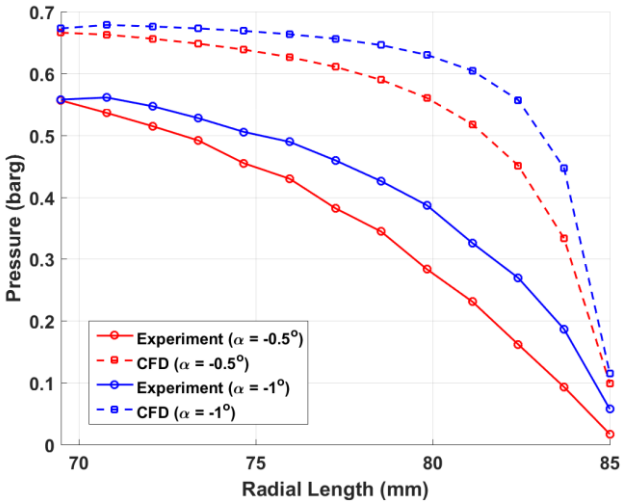

Figure 5-30: CFD, Radial pressure distribution, Converging Coning, h_{min}=50µm, P_{in} = 0.69 barg.

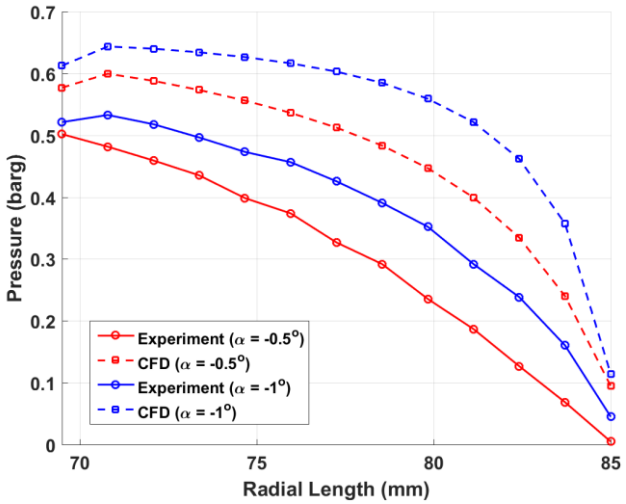

Figure 5-31: CFD, Radial pressure distribution, Converging Coning, h_{min}=100µm, P_{in} = 0.69 barg.

For the larger gap height case (100 µm), Figure 5-31, Figure 5-33 and Figure 5-35, the agreement between CFD predictions and experiments showed a slight improvement. Nevertheless, CFD pressure predictions were still larger in magnitude compared to experiments and the discrepancy continues to increasing at higher inlet pressures. Additionally, the inlet pressure loss was higher than smaller gap cases. However, and contrary to what experiments suggest, CFD predicted a lower inlet loss in cases featuring the larger angle. The trend of pressure recovery downstream of the entrance loss location was well captured by the CFD.

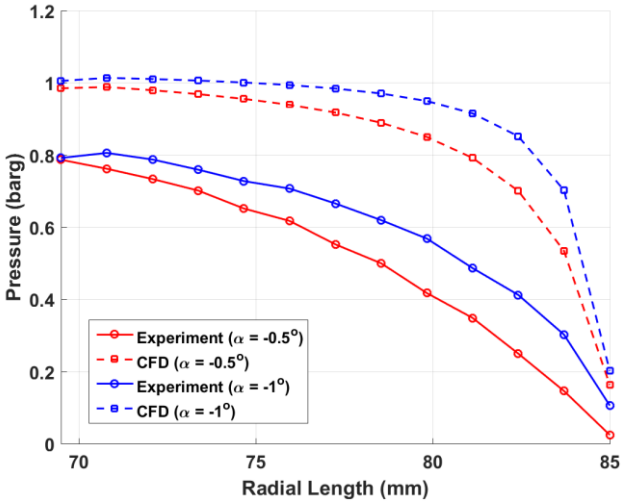

Figure 5-32: CFD, Radial pressure distribution, Converging Coning, h_{min}=50µm, P_{in} = 1.03 barg.

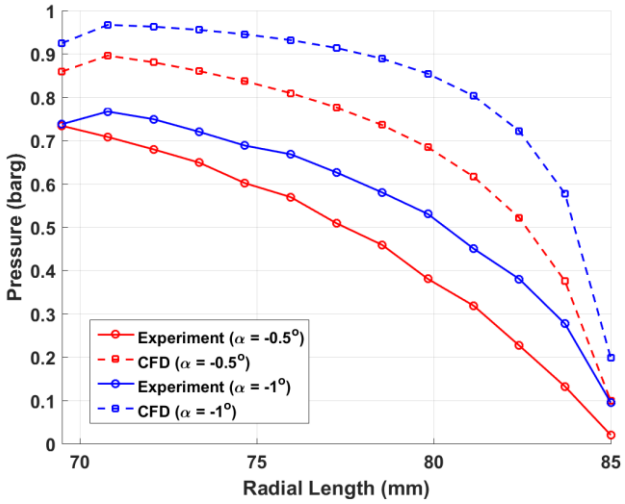

Figure 5-33: CFD, Radial pressure distribution, Converging Coning, h_{min}=100µm, P_{in} = 1.03 barg.

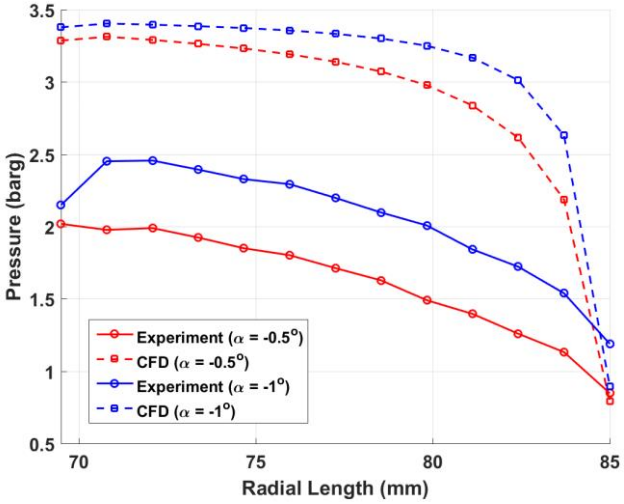

Figure 5-34: CFD, Radial pressure distribution, Converging Coning, h_{min}=50µm, P_{in} = 3.45 barg.

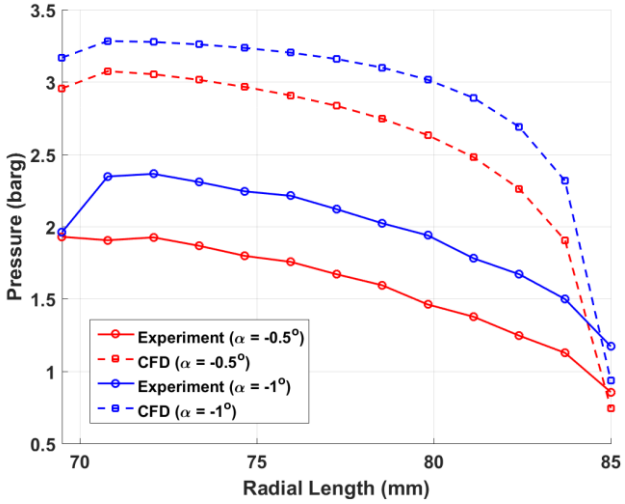

Figure 5-35: CFD, Radial pressure distribution, Converging Coning, h_{min}=100µm, P_{in} = 3.45 barg.

The main cause of discrepancy between the results is in part due to the inability of the CFD model to correctly capture the entry loss. While from an experimental point view, the accuracy of determining the touch-down location could also have contributed to this mismatch along with geometric deviations of both sealing faces in terms of the characterized surface flatness and run-out. The overall result was an over-prediction of film pressures across the range of

conditions considered here. Another aspect that could be a contributing factor is the structural deformation of the disc under the significantly increased air-film pressure in a converging configuration. This increase in gap height, if significant, will contribute to the drop in air-film pressure. At the end of this chapter, a two-way coupled Fluid-Structure Interaction (FSI) model is introduced to investigate this issue.

In an attempt to consolidate the suggested reasoning behind the discrepancy between CFD predictions and experimental data, the absolute error was calculated and plotted in figures Figure 5-36 and Figure 5-37 . The absolute error was calculated as follows,

$$Absolute\ Error = Experimental\ Measurement - CFD\ Prediction \qquad \textbf{Eq. 5.1}$$

To understand absolute error in predicting the shape of the pressure distribution in the channel, the radial pressures, for both CFD and experiment, were normalised in the same manner as before (refer to Figure 5-9) , *i.e.* $p^* = \frac{p_{in} - p(r)}{p_{in} - p_{final\ tapping}}$. This again makes the error at r = 85 mm indeterminate. Figure 5-36 shows the absolute error in percentage for the α = -0.5^o case at two minimum gap heights (50 μm and 100 μm) at three inlet pressures (0.69 barg, 1.03 barg and 2.07 barg). The red data points denote the 50 μm gap while the green data points correspond to the 100 μm gap. The three different marker shapes represent the three inlet pressures considered. The radial position is shown in *mm* on the *y*-axis. Figure 5-37 follows on the same format as described but represents the relative error for the α = -1.0^o case.

From both plots a trend can be observed where at the same inlet pressure and regardless of the gap height the absolute error increased towards the outer radius of the primary gap and increased with increasing pressure. The absolute error trends suggest that the differences are

dependent to an extent on the inlet pressure and the magnitude of force generated by the air-film.

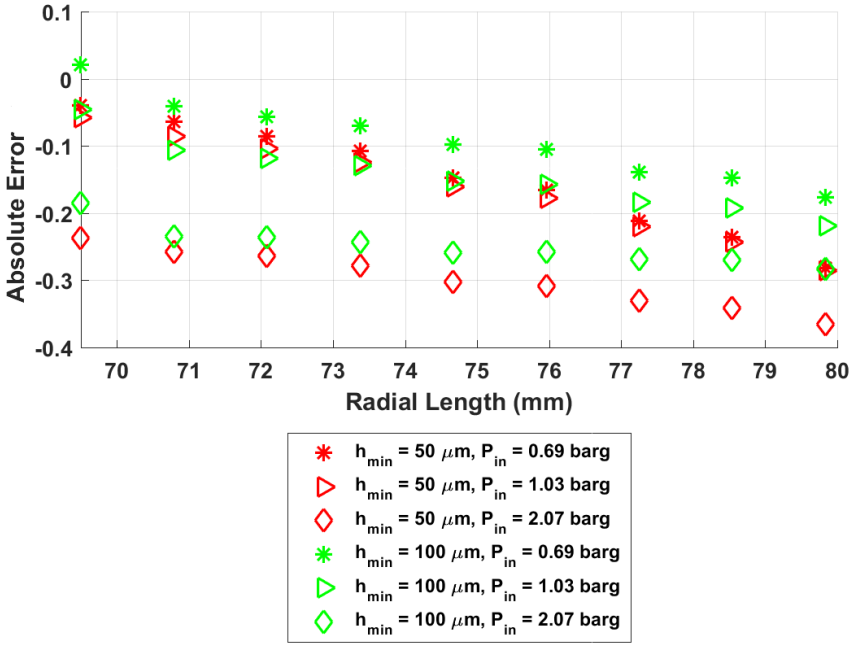

Figure 5-36: Absolute error in normalised radial pressures between experiment and CFD predictions, α = -0.5º.

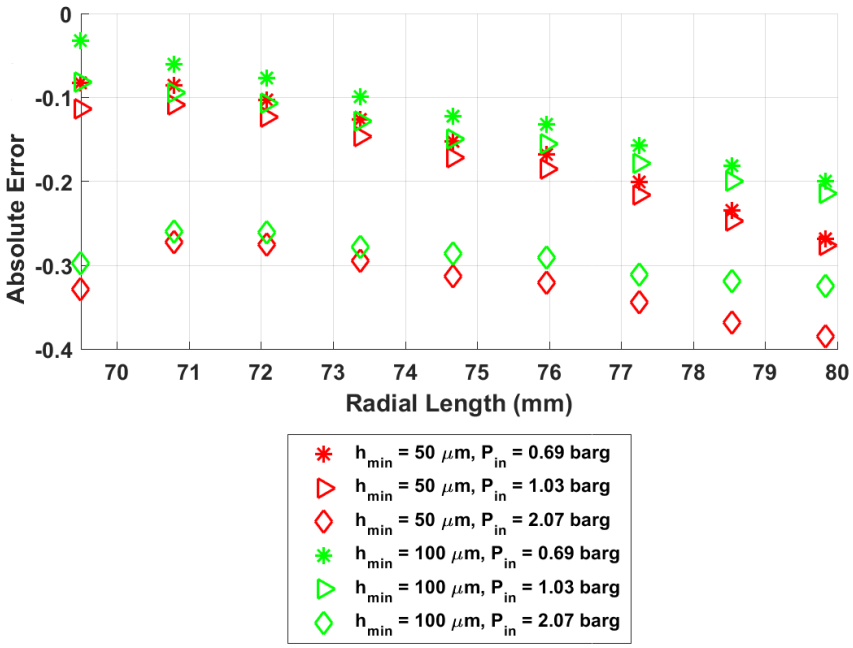

Figure 5-37: : Absolute error in normalised radial pressures between experiment and CFD predictions, α = -1.0º.

5.3 Diverging Gaps

5.3.1 Experimental Radial Pressure Distributions

The final set of tests of this campaign were conducted with a diverging angle machined on the face of the removable part. The diverging coning angle is also denoted by α but given a positive sign based on the positive slope of the straight line. Figure 5-38 shows a schematic outlining the geometry and notation for a diverging gap. The definition of the coning angle and height remain the same as the converging case. In the case of a diverging gap the minimum gap will be at the inner radius of seal face while the total gap height ($h_{coning} + h_{min}$) will be at the outer radius. Table 5.4 outlines the range of coning heights, angles and minimum gaps considered in this study.

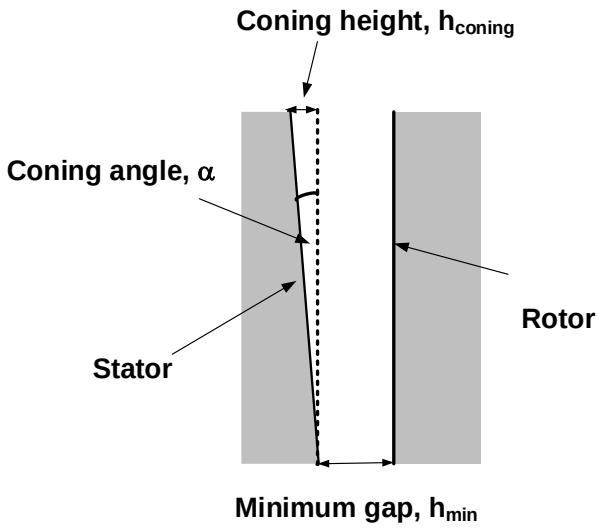

Figure 5-38: Geometry notation for diverging gaps, upstream gap.

Coning angle (deg.)	Coning Height h_{coning} (μm)	Minimum Gap h_{min} (μm)
+1	-270	50,100, 200, 300
+2	-540	50,100, 200, 300

Table 5.4: Range of minimum gap heights, diverging coning angles and coning heights.

Two diverging angles were considered $\alpha = +1.0^{o}$ and $\alpha = +2.0^{o}$. The experimental procedure remained the same as before but in contrary to the converging case, the touch-down occurred at the inlet to the gap where the primary face was in closest proximity to the rotor. Figures 44 to 52 show the circumferentially averaged radial pressure distributions for both diverging angles considered at a range of minimum gap heights (50 μm to 200 μm) and inlet pressures (0.69 barg up to 3.45 barg). For comparison, the corresponding parallel case with the same minimum gap height is also plotted in blue and denoted by $\alpha = 0^{o}$.

Upon inspection of the radial pressure profiles in Figure 5-39 to Figure 5-47, it is evident that a diverging gap causes the air-film to behave very differently compared to both previous configurations. The flow loses most of the pressure coming into the gap and pressure continues dropping before suddenly rising again prior to exiting the gap. One might then expect that the normalised pressure is fixed and independent of the divergent angle at the geometric throat of the system where sonic conditions should be expected. However, as also observed by Al-Bender and van Brussel (1992) the flow accelerates into the entrance of the channel and dependent on the geometry separation –heat transfer and friction, should the flow become

choked it will do so some distance downstream of the geometric vena contracta at the entrance, meaning that the pressure ratio at the inlet need not be 0.52 at this point to indicate choking within the passage. The flow is neither isentropic, nor classical Fanno flow in the passage as there are mixing losses, heat transfer and friction present, but the passage is short and there is limited possibility for heat transfer to occur. In fact provided there is sufficient pressure drop, at small angles the flow will continue to accelerate until a pressure rise is required to satisfy the exit pressure conditions. In this highly viscous flow regime, this appears to occur through a series of weak shock waves leading to gradual pressure recovery in the channel.

The only case where no abrupt pressure recovery was observed for h_{min} = 50 μm at $\alpha = 2.0^{o}$ and P_{in} =0.69 barg, Figure 5-39, where the flow loses pressure at the inlet before immediately dropping to atmospheric conditions – here we have a classic restricting sharp edged orifice. For the smaller angle ($\alpha = +1.0^{o}$) and the same configuration a pressure drop followed by an abrupt recovery to atmospheric levels, is seen similar to all other cases. The inlet loss associated with the larger diverging angle was lower than the smaller angle for most cases and increased with larger minimum gap heights. Only the case with a minimum gap height of h_{min} = 200 μm at P_{in} =0.69 barg, Figure 5-41, did not exhibit the aforementioned trend.

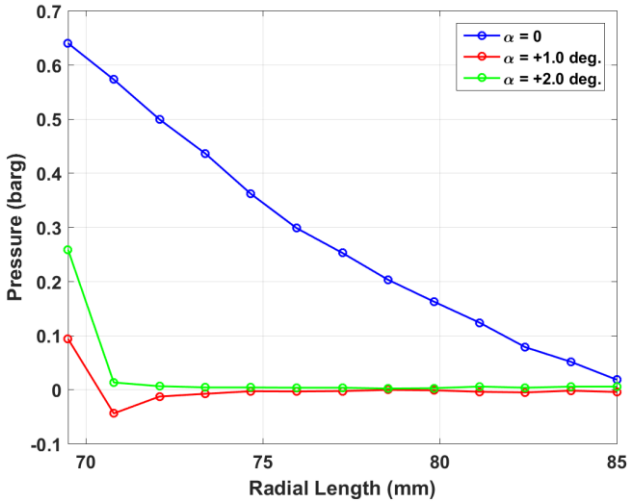

Figure 5-39: Experiments, Diverging coning, Radial pressure distribution, h_{min}=50µm, P_{in}=0.69 barg.

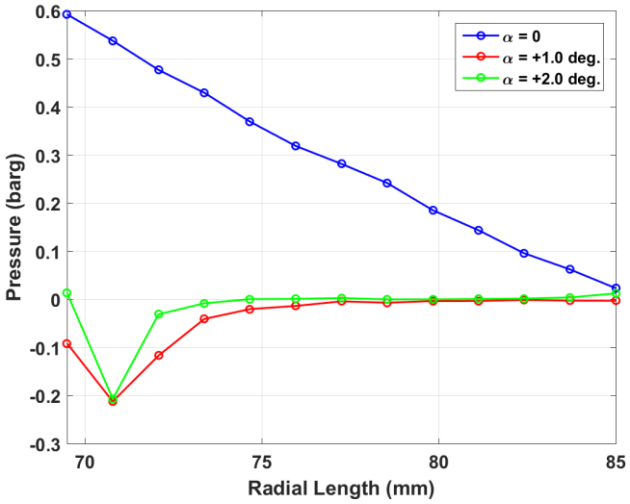

Figure 5-40: Experiments, Diverging coning, Radial pressure distribution, h_{min}=100µm, P_{in}=0.69 barg.

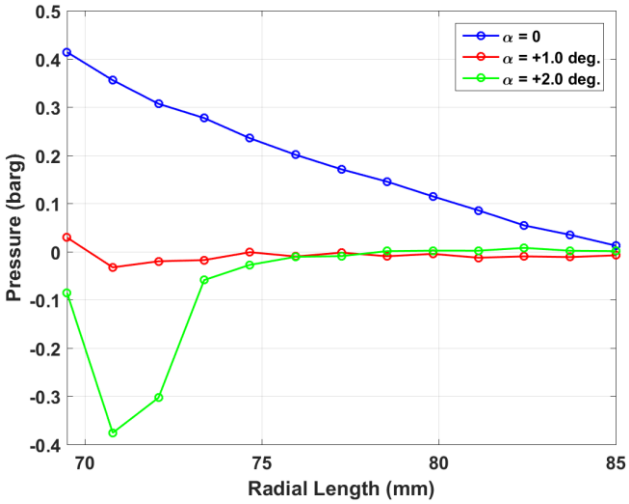

Figure 5-41: Experiments, Diverging coning, Radial pressure distribution, h_{min}=200µm, P_{in}=0.69 barg.

The pressure recovery region for the largest minimum gaps (h_{min} = 200 µm) at highest inlet pressure (P_{in} = 3.45 barg), Figure 5-47, showed that the pressure did not recover to atmospheric levels within the gap, unlike cases with lower inlet pressures – suggesting that a shock train must exist downstream of the exit. Furthermore, the pressure drop downstream of the inlet to

the gap in cases with the higher diverging angle was more severe compared to that of the smaller angle for a given minimum gap and operating pressure. However, the radial location of the abrupt pressure recovery showed little variation between both coning angles tested.

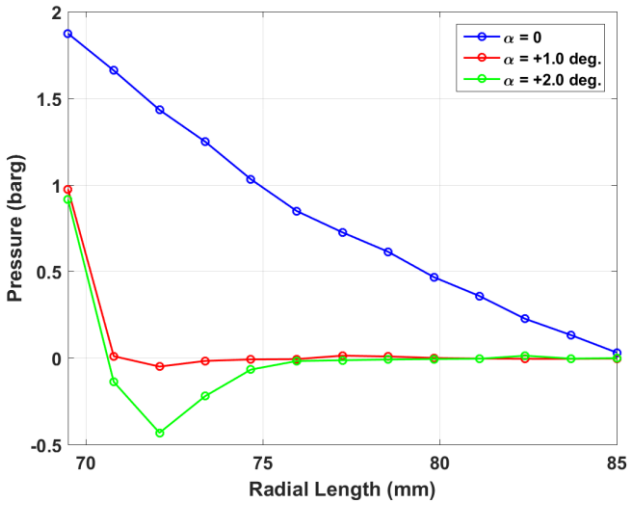

Figure 5-42: Experiments, Diverging coning, Radial pressure distribution, h_{min}=50µm, P_{in}=2.07 barg.

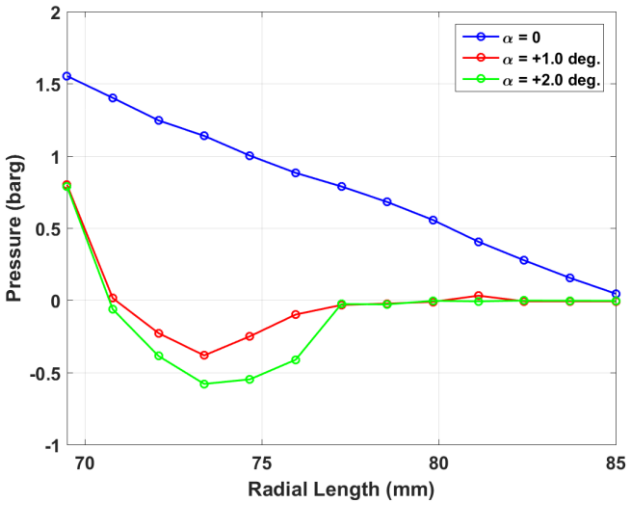

Figure 5-43: Experiments, Diverging coning, Radial pressure distribution, h_{min}=100µm, P_{in}=2.07 barg.

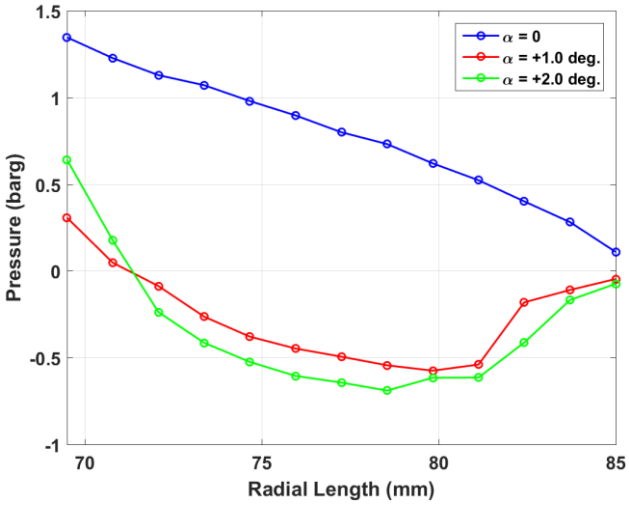

Figure 5-44: Experiments, Diverging coning, Radial pressure distribution, h_{min}=200µm, P_{in}=2.07 barg.

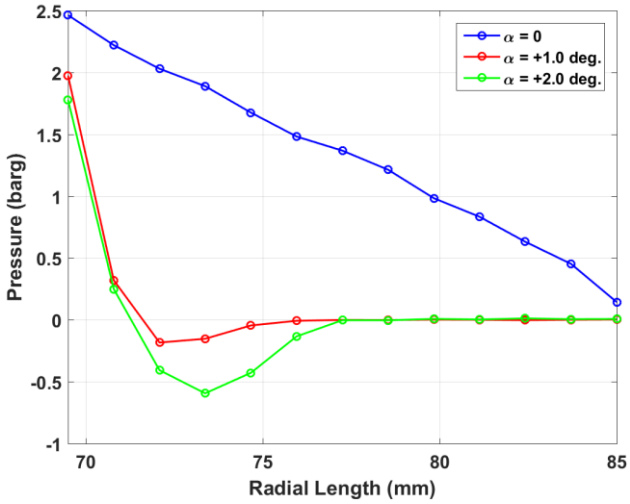

Figure 5-45: Experiments, Diverging coning, Radial pressure distribution, h_{min}=50µm, P_{in}=3.45 barg.

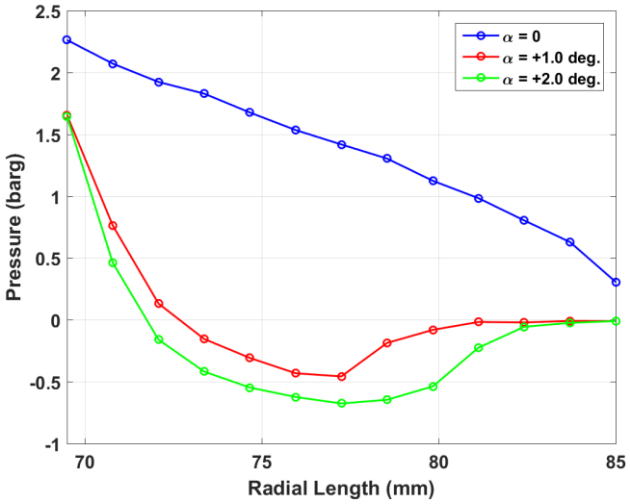

Figure 5-46: Experiments, Diverging coning, Radial pressure distribution, h_{min}=100µm, P_{in}=3.45 barg.

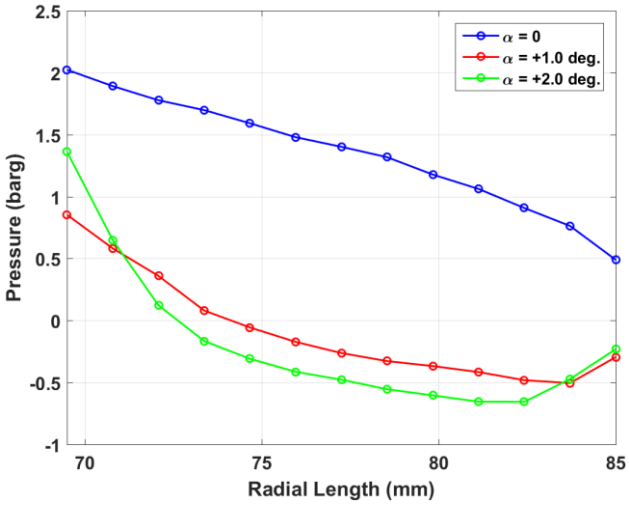

Figure 5-47: Experiments, Diverging coning, Radial pressure distribution, h_{min}=200µm, P_{in}=3.45 barg.

Figure 5-48 to Figure 5-51 illustrate the effect of changing the inlet pressure for a given minimum gap and coning angle. The main observation was that increasing the inlet pressure extended the low pressure region further into the gap and moved the location of abrupt pressure recovery further downstream.

Contrary to the previous two configurations (parallel and converging coning) where increasing the inlet pressure resulted in a desirable higher film pressure, it has proven to be detrimental to the film pressure where a diverging gap was present. Moreover, the drop in air-film pressure was further worsened at larger gap heights and coning angles.

The abrupt pressure recovery characteristic is believed due to choked flow conditions near the gap inlet, *i.e*. where the minimum gap exists (throat). At the inlet pressures considered, the flow reached supersonic speeds within the gap. Hence, as the flow chokes at the inlet a region of supersonic flow will exist where the flow accelerates as the area increases further in the radial direction. The supersonic region is eventually terminated by a shockwave or series of shocks that causes progressive deceleration of the flow towards subsonic conditions at the gap exit, marked by the sudden pressure rise. The smaller the initial gap the faster the increase in area ratio for a given diverging angle and so if the flow were isentropic the more rapid rise in Mach number and decrease in pressure, hence for the same inlet pressure we expect the pressure recovery to happen earlier within the smaller gap. For increasing pressure inlet the flow can accelerate to lower pressure before recovering as the flow has higher momentum at the same static pressure in the channel. This can be seen in the downstream-shifting of the recovery region at higher pressures. A more detailed insight is gained from the 3D CFD results.

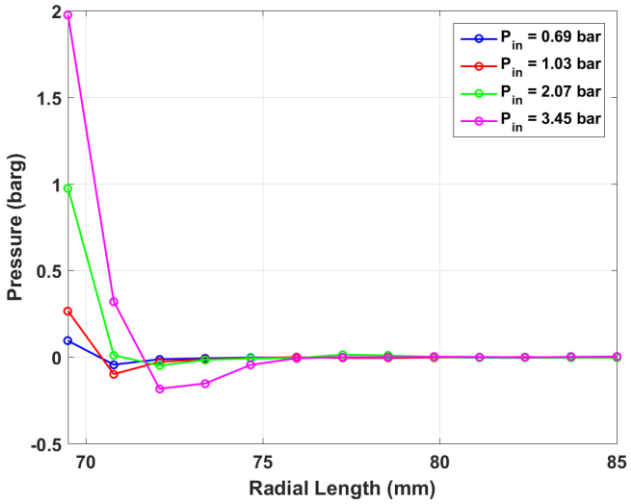

Figure 5-48: Experiments, Diverging coning, Radial pressure distribution, h_{min}=50μm, α = +1.0°.

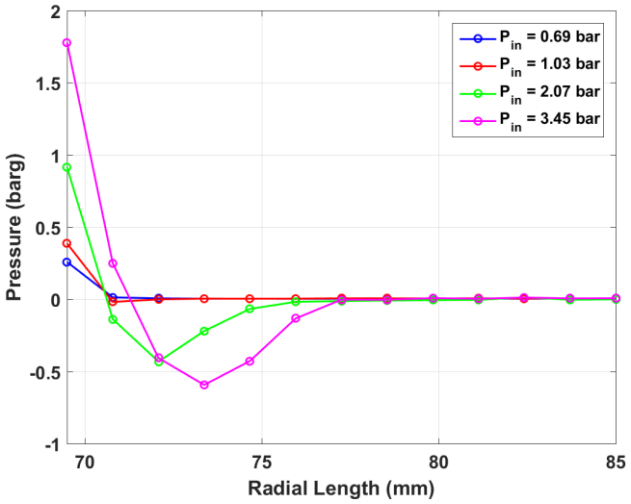

Figure 5-49: Experiments, Diverging coning, Radial pressure distribution, h_{min}=50μm, α = +2.0°.

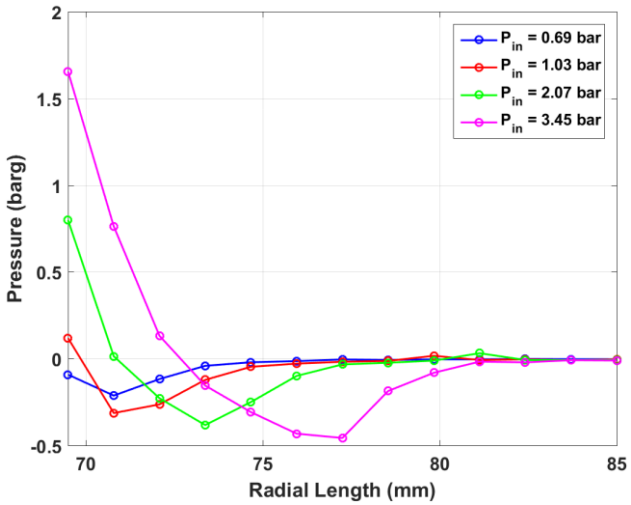

Figure 5-50: Experiments, Diverging coning, Radial pressure distribution, h_{min}=100μm, α = +1.0°.

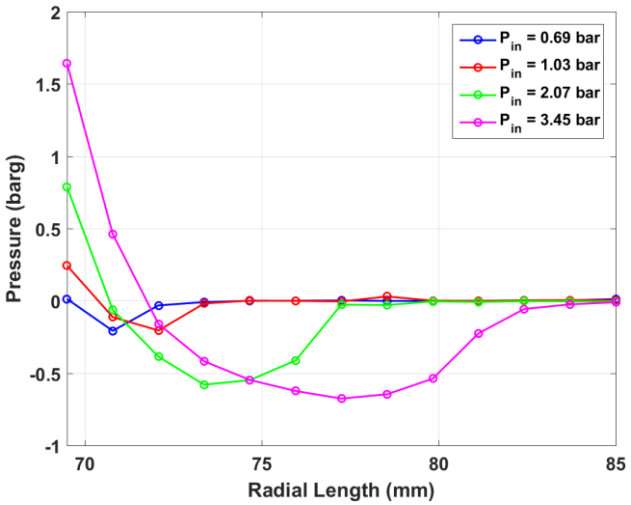

Figure 5-51: Experiments, Diverging coning, Radial pressure distribution, h_{min}=100μm, α = +1.0°.

5.3.2 Diverging Gaps: 3D CFD Radial Pressure Distributions

Figure 5-52 to Figure 5-59 show predictions from CFD against experimental results for both diverging angles at two different minimum gaps (50 μm and 100 μm) and four inlet pressures

ranging from 0.69 barg up to 3.45 barg. Each graph shows the results for both diverging angles at a given minimum gap and inlet pressure. The CFD predictions are represented by the dotted lines while the solid lines correspond to experimental data.

Across all the data presented, the inlet loss from the CFD was consistently more severe than the corresponding experimental case. As expected, the inlet loss increased with increasing the minimum gap. However, apart from the first case shown in Figure 5-52, the inlet loss predicted by the CFD was persistently lower for the largest angle. Although the inlet loss magnitude did not match the experimental data, the trend largely agreed with what has been shown experimentally.

The cases for the two lowest inlet pressures (0.69 barg and 1.03 barg), Figure 5-52 to Figure 5-55, showed good agreement between the CFD and experimental results in terms of the radial position of the abrupt pressure recovery. As seen previously, the pressure recovery radial location moved further downstream as the pressure increased. The pressure levels predicted by the CFD were lower than experiments which is mainly due to the higher inlet loss exhibited by the CFD. The match between both data sets converged towards the gap exit.

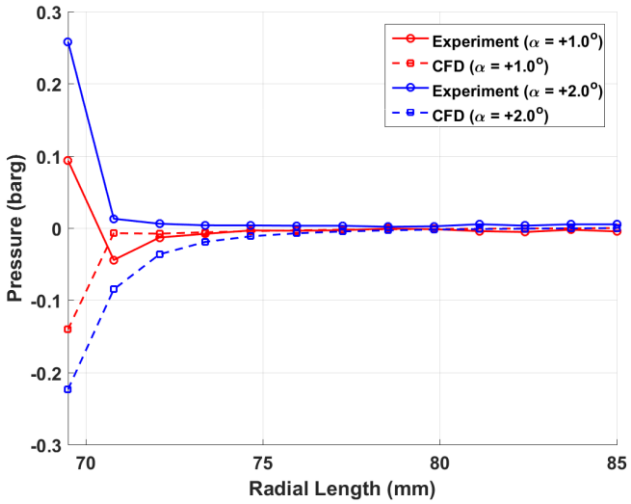

Figure 5-52: CFD, Radial pressure distribution, Diverging Coning, h_{min}=50µm, P_{in} = 0.69 barg.

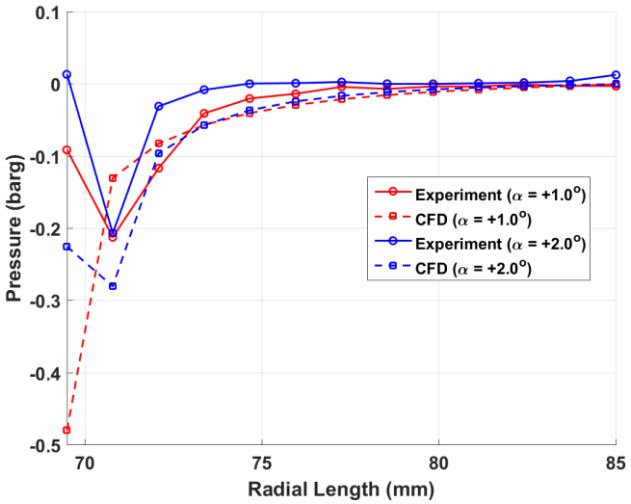

Figure 5-53: CFD, Radial pressure distribution, Diverging Coning, h_{min}=100µm, P_{in} = 0.69 barg.

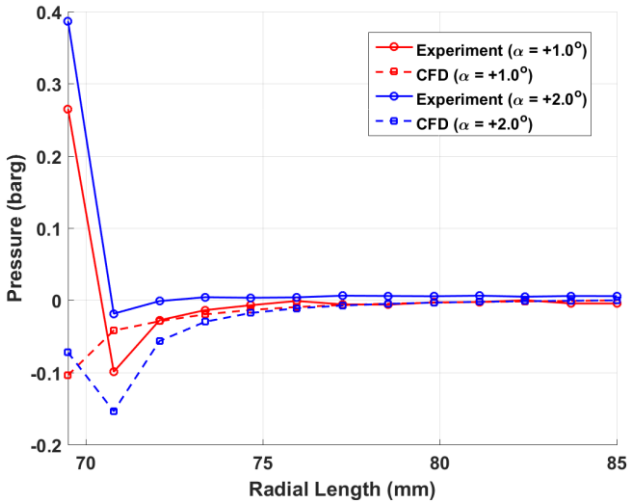

Figure 5-54: CFD, Radial pressure distribution, Diverging Coning, h_{min}=50µm, P_{in} = 1.03 barg.

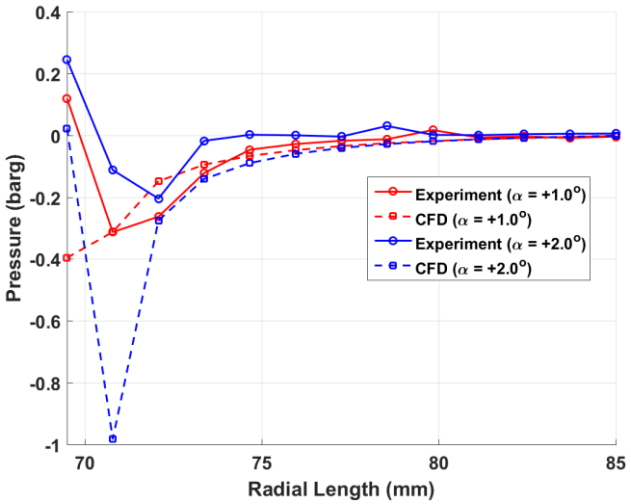

Figure 5-55: CFD, Radial pressure distribution, Diverging Coning, h_{min}=100µm, P_{in} = 1.03 barg.

At higher inlet pressures (2.07 barg and 3.45 barg), Figure 5-56 to Figure 5-59, the CFD prediction of the abrupt pressure recovery occurred at a slightly larger radial location for the smaller angle (α = +1.0°). Although both data showed good agreement at locations towards the

gap exit, pressure recovery from experiments was quicker. For the larger angle (α =+ 2.0^o) case, recovery was predicted to occur earlier in CFD than experiment.

Furthermore, the larger angle cases from the CFD model showed the abrupt pressure recovery region to occur at a more upstream radial location compared to the smaller angle cases and recovery to gap exit pressure was achieved earlier. Both trends point towards the presence of a stronger shock wave. Experiments only showed the same trend at low inlet pressures (0.69 barg and 1.03 barg), and the radial location of the abrupt pressure recovery showed little variation with coning angle for a given minimum gap. As the inlet pressure increased, experiments showed the smaller angle cases to exhibit a less severe pressure drop.

In general, predictions from the 3D CFD model were in reasonably good agreement with experiments, particularly in terms of capturing the correct trends. Although the magnitudes were not a complete match they were in a much better agreement compared to CFD predictions for the converging cases. This supports the idea that the due to the very low the air-film pressures in a diverging configuration, the load on the disc will not be significant and the structural aspect can be ignored. The main mismatch between the CFD predictions and experiments for diverging cases was the shifting of the location of the abrupt pressure recovery. This is thought to be due machining inaccuracies which will become amplified at higher pressures. The *Knudsen number* of the flow through the gap was calculated from the CFD solutions and found to lie in the range 7.78e-05 - 5.49e-04. Thus, it is appropriate to consider the fluid as a continuum in all calculations, and no correction for rarified effects need be considered.

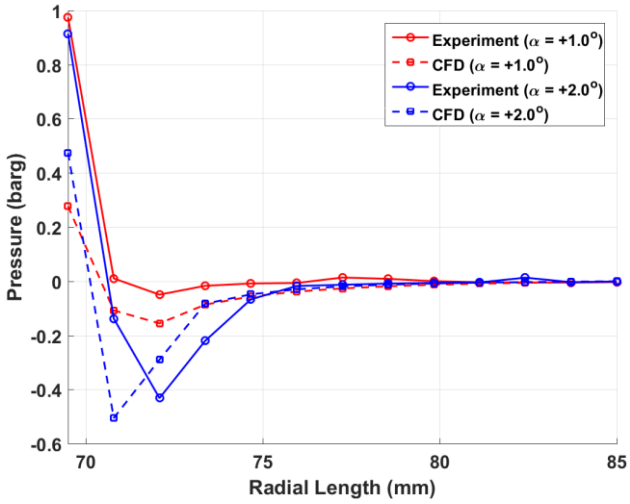

Figure 5-56: CFD, Radial pressure distribution, Diverging Coning, h_{min}=50µm, P_{in} = 2.07 barg.

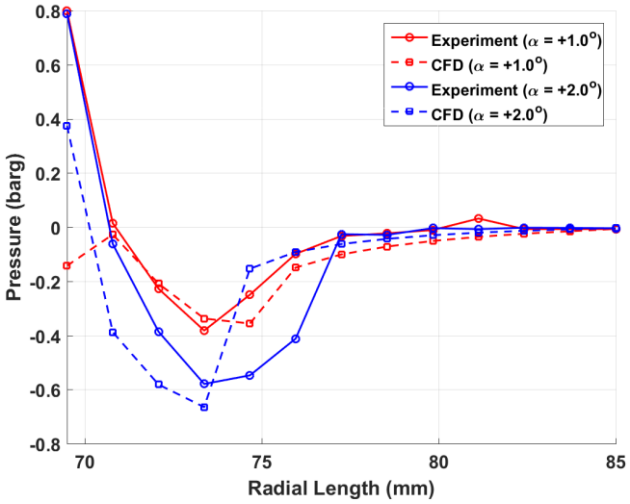

Figure 5-57: CFD, Radial pressure distribution, Diverging Coning, h_{min}=100µm, P_{in} = 2.07 barg.

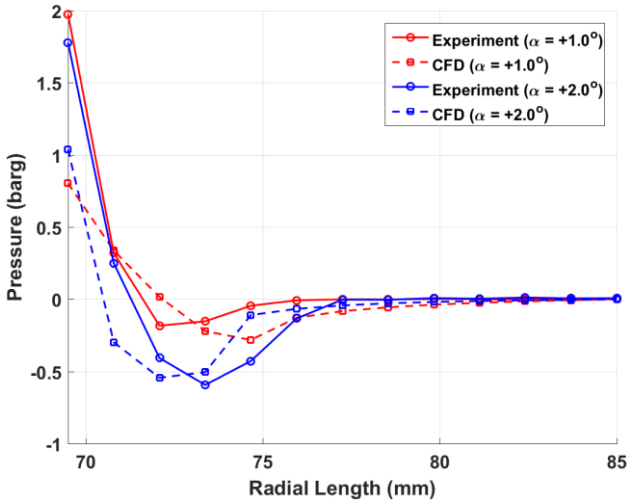

Figure 5-58: CFD, Radial pressure distribution, Diverging Coning, h_{min}=50µm, P_{in} = 3.45 barg.

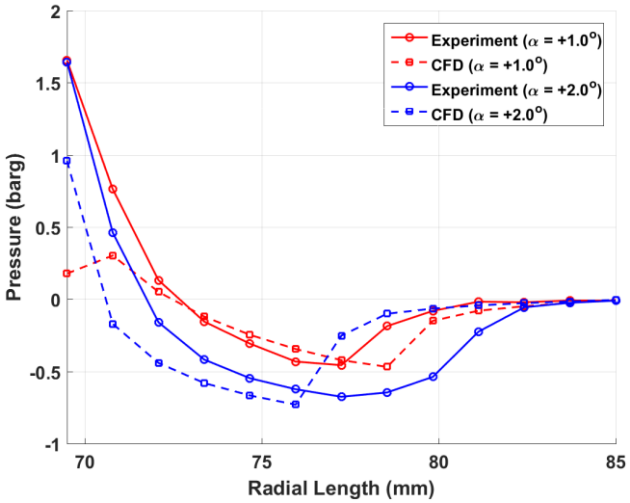

Figure 5-59: CFD, Radial pressure distribution, Diverging Coning, h_{min}=100µm, P_{in} = 3.45 barg.

Figure 5-60 to Figure 5-63 show the radial average Mach number distribution within the gap obtained from CFD at four different inlet pressures (0.69 barg to 3.45 barg) for two minimum gaps (50 µm and 100 µm) and both diverging coning angles considered. As illustrated in Figure 5-60, which corresponds to the radial pressure distribution for the α = +1.0° case in Figure 5-52,

the two lowest inlet pressures show that Mach number initially increases due to the inlet pressure loss but does not fully reach sonic conditions. Subsequently, the Mach number starts dropping as the pressure recovers. However, no shockwaves were evident, as also suggested by the CFD pressure distribution where the abrupt pressure recovery region was absent. On the other hand, as the inlet pressure increased the Mach number approached sonic conditions close to the inlet and continued increasing to supersonic speeds further downstream. The supersonic region was then terminated by a shockwave marked by the sudden drop in Mach number and abrupt pressure recovery.

As both the minimum gap height and coning angle are increased, figures 66, 67 and 68, the flow reached sonic conditions close to the gap entrance, including the low inlet pressure cases. The same trends described before apply to the rest of the cases shown. Additionally, the shock wave was significantly more pronounced as the coning angle increased, and to a lesser extent as the minimum gap increased. Moreover, higher Mach numbers were seen at higher inlet pressures along with the downstream-shifting of the radial location at which the shock occurs. Furthermore, the Mach number distributions confirm that at larger angles, a stronger shock wave causes the abrupt pressure recovery to occur earlier than in smaller angle cases.

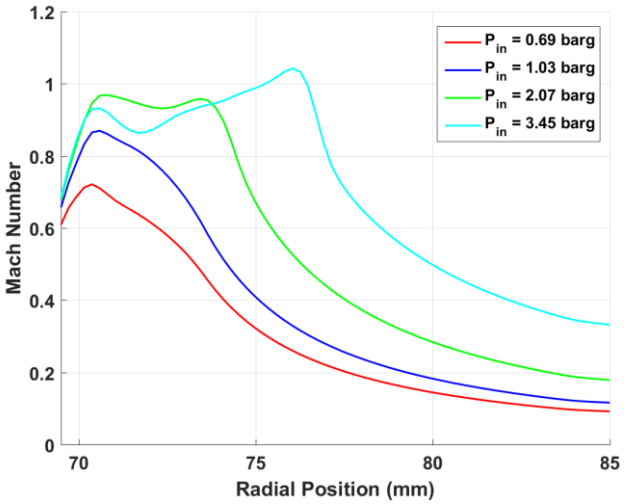

Figure 5-60: CFD, Radial Average Mach number distribution, Diverging Coning, h_{min}=50µm, α = +1.0º.

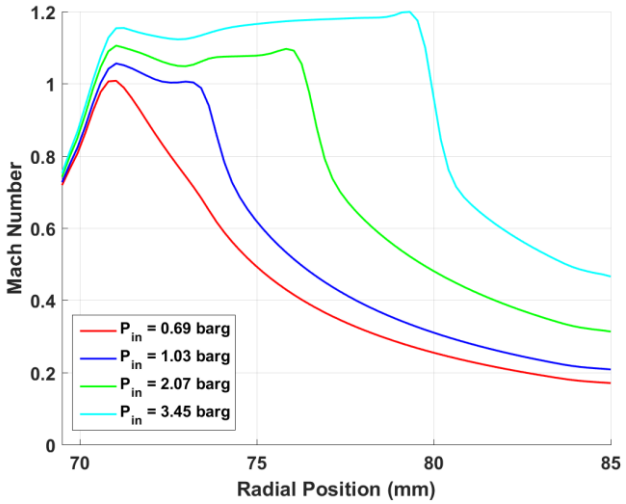

Figure 5-61: CFD, Radial Average Mach number distribution, Diverging Coning, h_{min}=100µm, α = +1.0º.

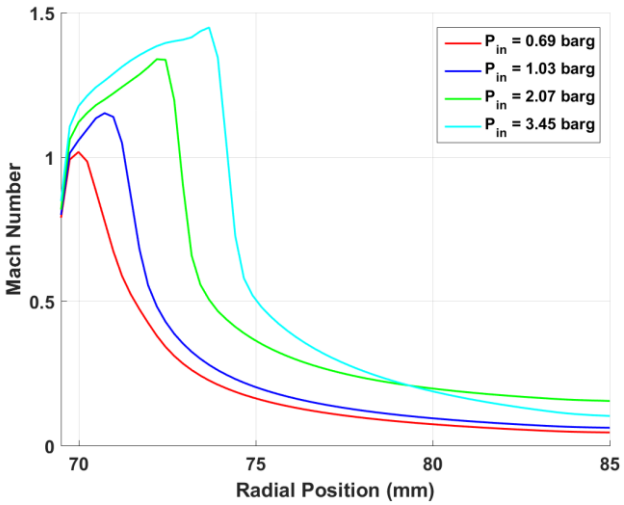

Figure 5-62: CFD, Radial Average Mach number distribution, Diverging Coning, h_{min}=50µm, α = +2.0º.

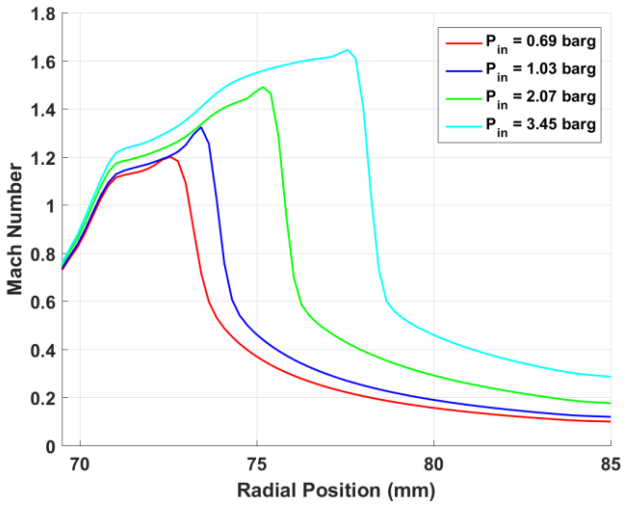

Figure 5-63: CFD, Radial Average Mach number distribution, Diverging Coning, h_{min}=100µm, α = +2.0º.

To confirm that choked flow conditions exist in the diverging configurations considered, the mass flow rates through the primary gap were plotted against inlet pressures in Figure 5-64. The red markers represent the α = +1.0º case while the green marker denotes the α = +2.0º case. Different marker shapes correspond to different gap heights. The results confirm that the

flow chokes as long as the same minimum gap height (throat area) is maintained at a given inlet pressure, regardless of the diverging angle. This ties in well with the behaviours seen in the radial pressure and average Mach number distributions shown earlier.

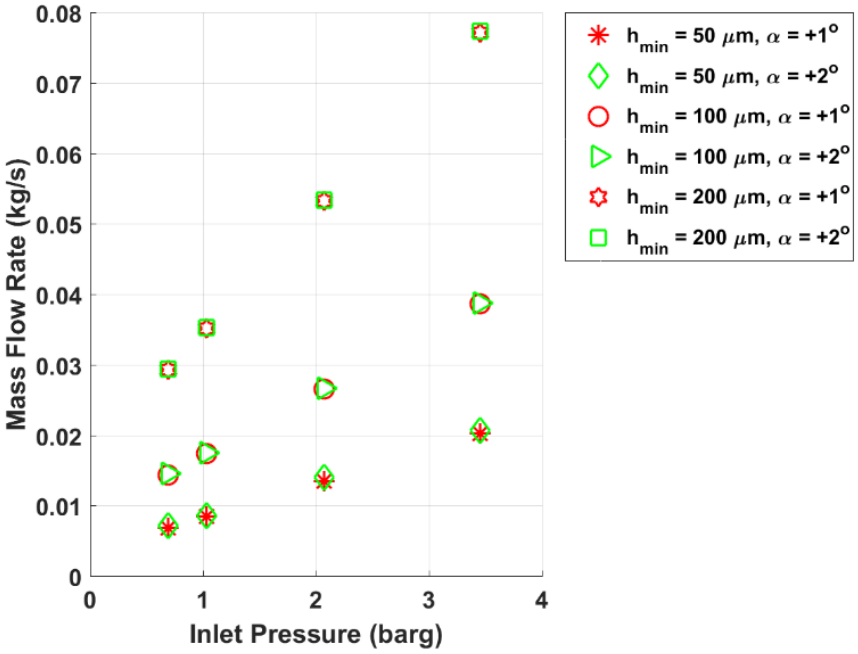

Figure 5-64: CFD, Mass flow rate through primary gap, Diverging Coning, h_{min}=50μm and 100μm, α = +1.0° and +2.0°.

5.4 Air-film force behaviour in coned and parallel gaps

This section builds on the data gathered from the results shown before to draw a more complete picture of how changing the minimum gap, coning angle and operating pressure will affect the load capacity of the seal. Having obtained the pressure distributions for all the configurations tested and knowing the area of seal face, the radial pressure distribution was numerically integrated over the area of the front face to obtain the air-film force.

Figure 5-65 shows the change in force with coning angle at four minimum gap heights (50 μm, 100 μm, 200 μm and 300 μm) and two inlet pressures (0.69 barg and 2.07 barg). The zero on the *x*-axis denotes the parallel case while negative values correspond to converging angles and

positive values represent diverging angles. The plot shows that moving towards the left (more converging coning) increases the air-film force while shifting to the right (more diverging coning) diminishes the load capacity of the air-film. As suggested previously by the radial pressure distributions, the smaller the gap the higher the force is and vice versa. Diverging coning cases, particularly those with a gap bigger than or equal to a 100 μm, resulted in a negative net force which indicates that in operation the seal will not be able to maintain a clearance and will rub against the rotating face. Additionally, higher inlet pressures increased the air-film force for a given configuration.

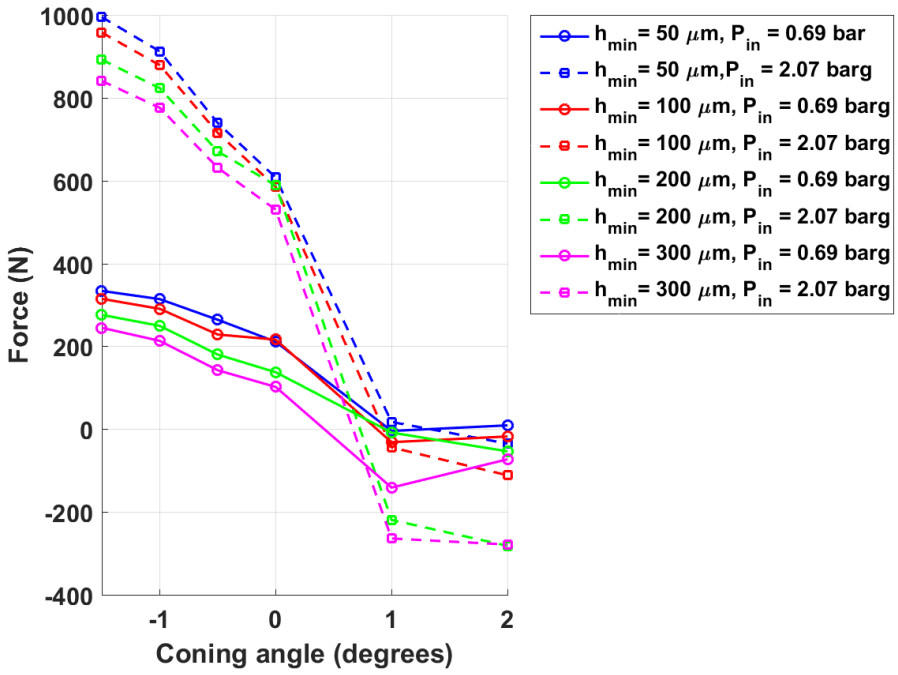

Figure 5-65: Experiments, Change of air-film force with coning angle, minimum gap height and inlet pressure.

Figure 5-66 to Figure 5-69 show contour plots of force (N) plotted against minimum gap height (μm) and coning angle (degrees) and cover the entire set of data produced. The colour bar is given the same range (-200 N to 1500 N) to enable comparison of the generated maps at all inlet pressures considered. The contour plots progress from the lowest inlet pressure (0.69 barg) to the highest inlet pressure (3.45 barg).

Starting from the zero angle case and moving leftwards shows an increase in the air-film force, however moving from there upwards shows a decrease in force as larger minimum gap heights are approached. The region with the highest force is found within the bottom left corner of the contour corresponding to the largest converging angle and smallest minimum gap. On the other hand, moving from the zero coning angle case rightwards shows a progressive decrease in air-film force which worsens when moving towards larger gaps. The region with the lowest air-film force is at the top right hand corner of the contour map which corresponds to larger gaps and larger diverging coning angles. As the inlet pressure increases, the aforementioned trend holds true with the force increasing with increasing the converging angle. However, as the inlet pressure increases the air-film force for the diverging cases (towards the right hand side) goes more negative which indicates that the seal is not able to generate an opening force to maintain a gap. The contour plots clearly suggest that for an increased load capacity it would be favourable to maintain a smaller gap with a converging coning while avoiding any scenario that would result in a diverging coning and/or large gaps.

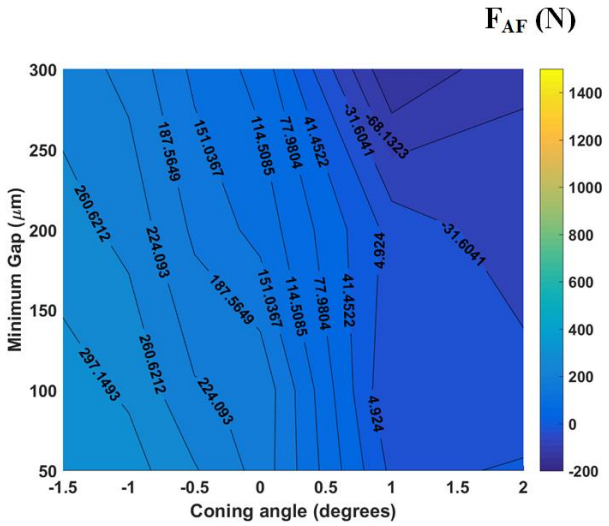

Figure 5-66: Contour map illustrating the change in air-film force F_{AF} with the full range of coning angles and minimum gap heights tested at P_{in}= 0.69 barg.

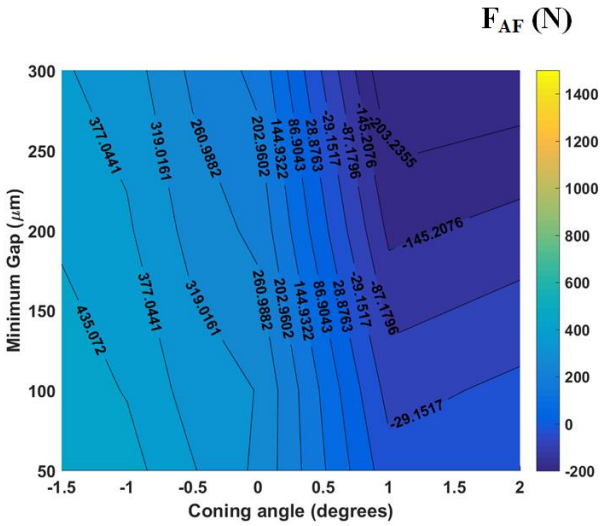

Figure 5-67: Contour map illustrating the change in air-film force F_{AF} with the full range of coning angles and minimum gap heights tested at P_{in}= 1.03 barg.

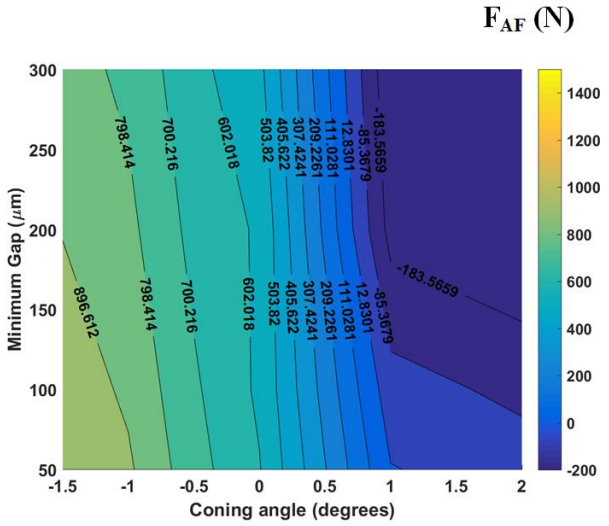

Figure 5-68: Contour map illustrating the change in air-film force F_{AF} with the full range of coning angles and minimum gap heights tested at P_{in}= 2.07 barg.

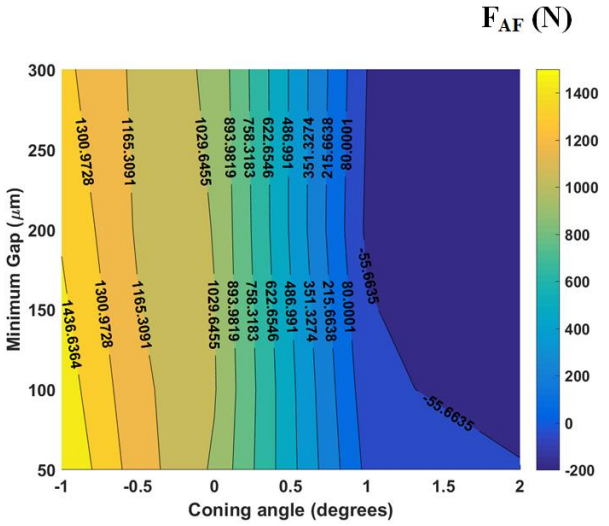

Figure 5-69: Contour map illustrating the change in air-film force F_{AF} with the full range of coning angles and minimum gap heights tested at P_{in}= 3.45 barg.

5.5 Effect of coning on leakage rate

Another important parameter to consider for the operation of a face seal is the leakage rate.

This section studies the effect the effect introducing coning angles would have on the leakage

through the primary sealing gap. The total mass flow rate is comprised of the mass flow rate through the primary gap in addition to the mass flow rate through the secondary seal, Eq. 4.3.

$$\dot{m}_{Total} = \dot{m}_{Primary\ Gap} + \dot{m}_{Secondary\ Seal} \qquad \textbf{Eq. 5.3}$$

To arrive at the flow rate through the primary seal gap only, the housing was displaced axially until the static face was in complete contact with the disc, thus blocking the flow path through the primary gap. Locking the actuator in that position ensured the housing remained in its assigned location. Any change in position upon pressurisation was picked up by the dial gauges and compensated for taking into account the axial displacement of the disc. Figure 5-70 illustrates the method described with the green arrows highlighting the leakage path through the secondary seal which is a tight-fit brass ring. The red arrow shows the blocked-off primary gap. The rig was then pressurised and the mass flow rate through the secondary seal was recorded for a range of operating pressures. By subtracting the secondary seal leakage rate for a given inlet pressure from the total mass flow rate for a set gap at the same pressure the leakage rate through the primary gap could be characterized.

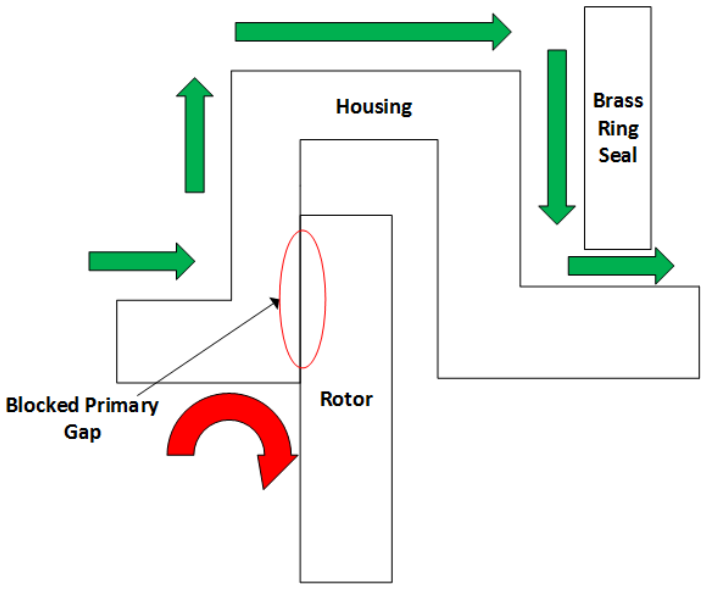

Figure 5-70: Method of blocking primary seal gap to characterize leakage through secondary seal.

Figure 5-71 to Figure 5-73 show the mass flow rates through the primary gap plotted against the coning angle for a given inlet pressure. The plots show that parallel gaps exhibited the lowest leakage rate compared to both coning configurations. Leakage rate was highest for the converging configuration and increased with increasing the coning angle. Interestingly, at higher pressures, Figure 5-73, the leakage rate appeared to taper off which could indicate that flow is approaching choked conditions as the converging angle increases while the minimum gap and inlet pressure remain unchanged. This effect could be beneficial as it would allow for having a larger coning angle to augment the opening force while keeping the leakage rate at acceptable levels. Diverging coning cases showed a lower rate of increase in leakage rate with an increase in coning angle compared to the converging cases. For the 0.69 barg inlet pressure case, Figure 5-71, increasing the diverging angle from $\alpha = +1.0^{o}$ to $\alpha = +2.0^{o}$ had little effect on the leakage rate, although for the smallest gaps it showed a minor drop. However, as the inlet pressure increased this behaviour disappeared and the leakage rate increased steadily for an increase in diverging angle.

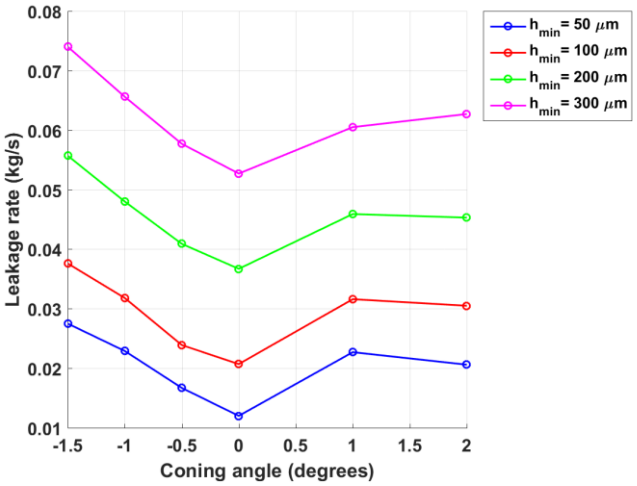

Figure 5-71: Experiments, Change of leakage rate with coning angle and minimum gap height, P_{in}=0.69 barg.

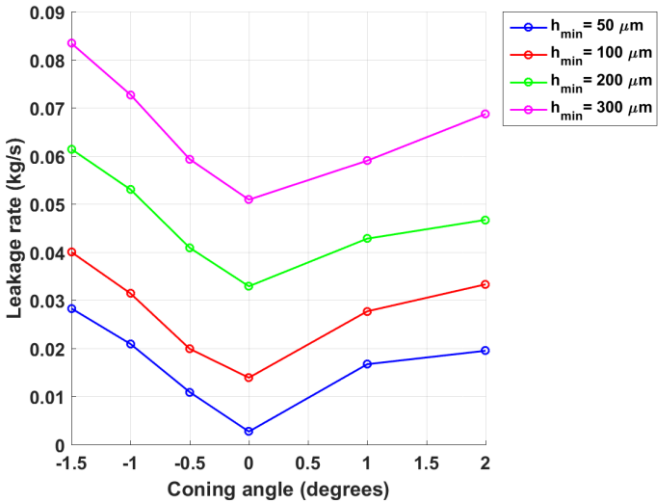

Figure 5-72: Experiments, Change of leakage rate with coning angle and minimum gap height, P_{in}=1.03 barg.

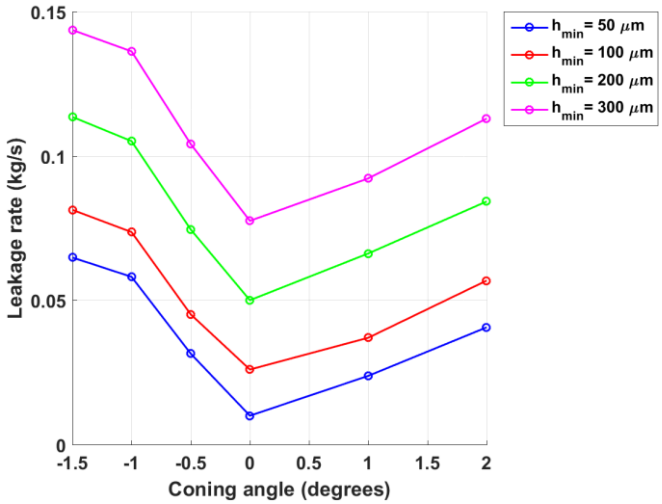

Figure 5-73: Experiments, Change of leakage rate with coning angle and minimum gap height, P_{in}=2.07 barg.

Figure 5-74 to Figure 5-77 show contour maps for the complete set of performance data produced for leakage rates against both the minimum gap and coning angle as the inlet pressure is increased from 0.69 barg to 3.45 barg. The colour bar represents the leakage rates and the range is kept constant for all contour maps to enable direct comparison.

Results show that the leakage rate increases with increasing the minimum gap, coning angle and inlet pressure. The lowest leakage rate region is dominated by the parallel configurations and increases moving towards the bottom left of the map (more converging) and with moving upwards (larger gaps). A similar trend is seen when moving towards the right portion of the maps, however the increase remains less severe across all operating conditions. The contour map for the highest inlet pressure, Figure 5-77, shows that most of the increase in leakage rate moves towards the left hand side of the plot as the converging angle and minimum gap increase.

The data shown suggests that in terms of leakage rate, it would be best to operate with a parallel gap. Nonetheless, in operation it is not possible to maintain a parallel gap as due mechanical and thermal loads the gap is more likely to take up a diverging path which would quickly diminish the seal's ability to lift-off. Although forcing a converging angle by machining it on the face of the seal would appear to increase the leakage rate, the amount of extra opening force it generates should not be ignored. Hence, a trade-off should be made to assess what level of coning would be optimal.

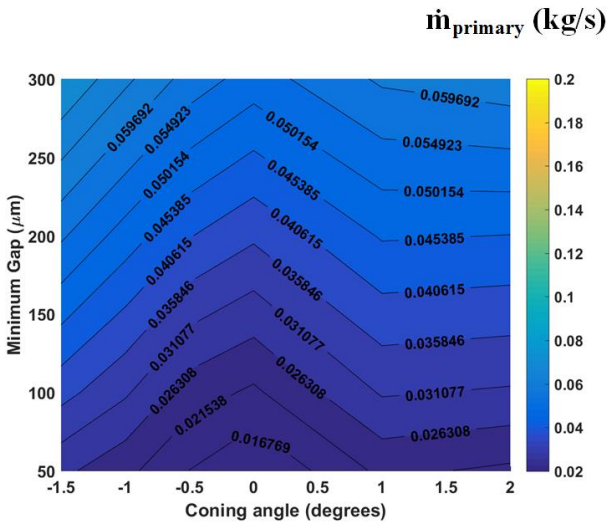

Figure 5-74: Contour map illustrating the change in leakage rate $\dot{m}_{primary}$ with the full range of coning angles and minimum gap heights tested at P_{in}=0.69 barg.

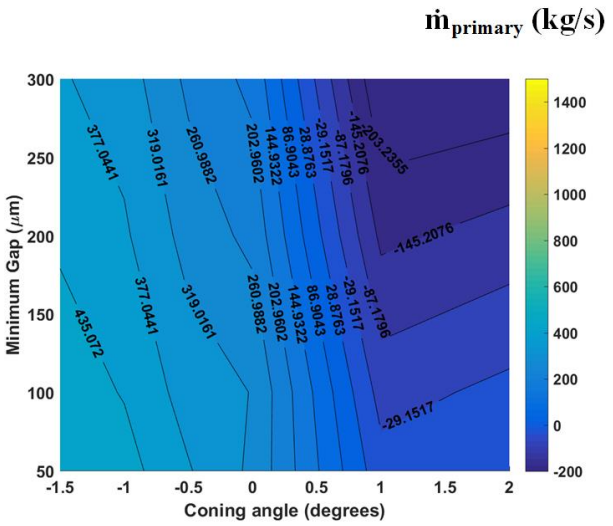

Figure 5-75: Contour map illustrating the change in leakage rate $\dot{m}_{primary}$ with the full range of coning angles and minimum gap heights tested at P_{in}=1.03 barg.

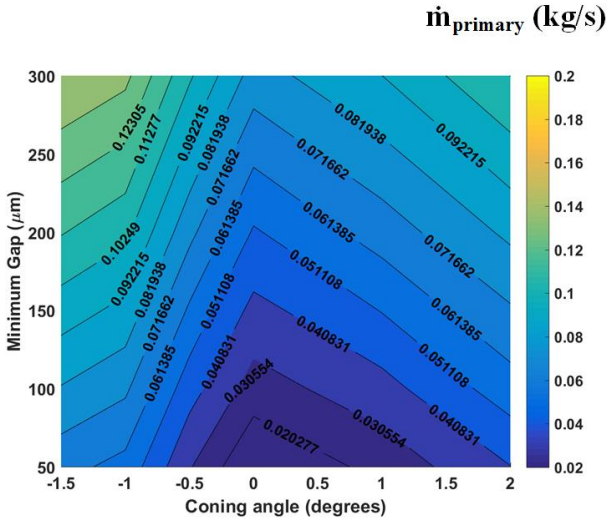

Figure 5-76: Contour map illustrating the change in leakage rate $\dot{m}_{primary}$ with the full range of coning angles and minimum gap heights tested at P_{in}=2.07 barg.

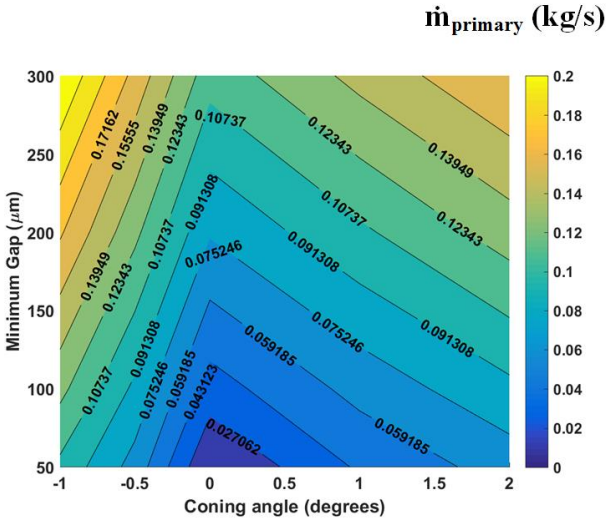

Figure 5-77: Contour map illustrating the change in leakage rate $\dot{m}_{primary}$ with the full range of coning angles and minimum gap heights tested at P_{in}=3.45 barg.

5.6 Two-way Fluid-Structure Interaction

In *section 5.2.2* absolute error representations comparing 3D CFD predictions against experimental pressure data for converging gaps revealed that a considerable increase in error towards the outer radius of the sealing gap was evident. This implied that the structural

deformation of the disc could be of sufficient significance to cause the discrepancy in film pressure between both data sets. It has been shown before, Figure 5-12, that the effects of adding surface roughness with and without rotation did not improve the CFD predictions. To account for the interplay of fluid forces and structural loads, a two-way Fluid-Structure Interaction (FSI) model was setup to solve the multi-physics problem. In a FSI simulation, the fluid model is solved as well as the structural model where at the boundary between the solid and the fluid (*i.e.* fluid structure interface) information is exchanged between both solvers. Note that, two methods can be used to discretize the fluid and solid models in a FSI simulation: 1- *Monolithic* approach (fully coupled) where the governing equations for both domains are solved simultaneously. This method requires a conformal mesh with matching nodal positions on both the fluid and solid domains. Although this fully coupled technique is robust it can be computationally expensive. 2- *Partitioned* approach (Staggered) where the governing equations for each domain are solved separately depending on the sequential order prescribed. Hence, it does not require a conformal mesh and the nodal positions need not be a complete match on either meshes. This is the method applied in the solver used in this study. Although more computationally efficient, it can be more difficult to reach convergence compared to the monolithic approach. A staggered FSI model can be classed as either a one-way coupling or a two-way coupling. In a one-way coupling the calculations are exchanged once. For instance, a pressure loading on a solid surface is calculated and then the forces transferred to the structural solver concluding the simulation when a converged solution for the resultant displacements is obtained. In a two-way coupling interaction the displacements from the solid surface are transferred back to the fluid solver where coupling steps are executed iteratively till convergence is reached, refer to Figure 5-78 for a flowchart highlighting the algorithms for (a) one-way and (b) two-way FSI models. In a FSI simulation the solution is said to have

converged when the convergence criteria are satisfied such that the change in a data transfer variable from one iteration to the next is less than the value prescribed for convergence and the total time duration is reached in case of a transient analysis.

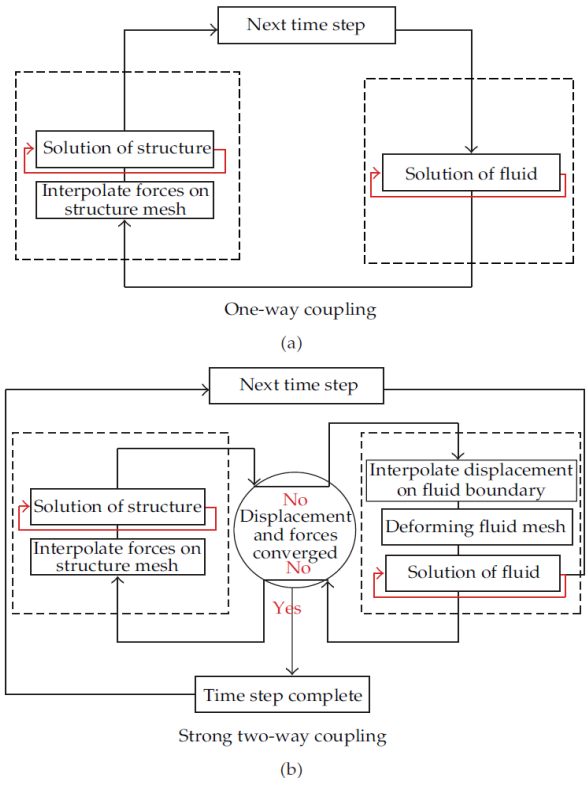

Figure 5-78: Solution algorithm for one and two coupling FSI, Benra *et.al.* 2011.

The FSI model applied in the case of the rigid seal considered in this chapter was a two-way interaction. As the coning of the disc under load is expected to be in the order of magnitude of the minimum gap height, it would not make physical sense to apply a one-way interaction model as the changes in gap height due to the coning of the runner under are significant, which is what prompted the development of this model. *ANSYS CFX 18.1* was used to solve the flow domain, *ANSYS Mechanical* for the structural domain and the *System Coupling* tool in *ANSYS Workbench* was used to manage the coupled simulation. Both the fluid and solid meshes were constructed in *ICEM*. A Flowchart is shown in Figure 5-79 outlining the algorithm used in the staggered two-way coupling FSI model introduced in this study.

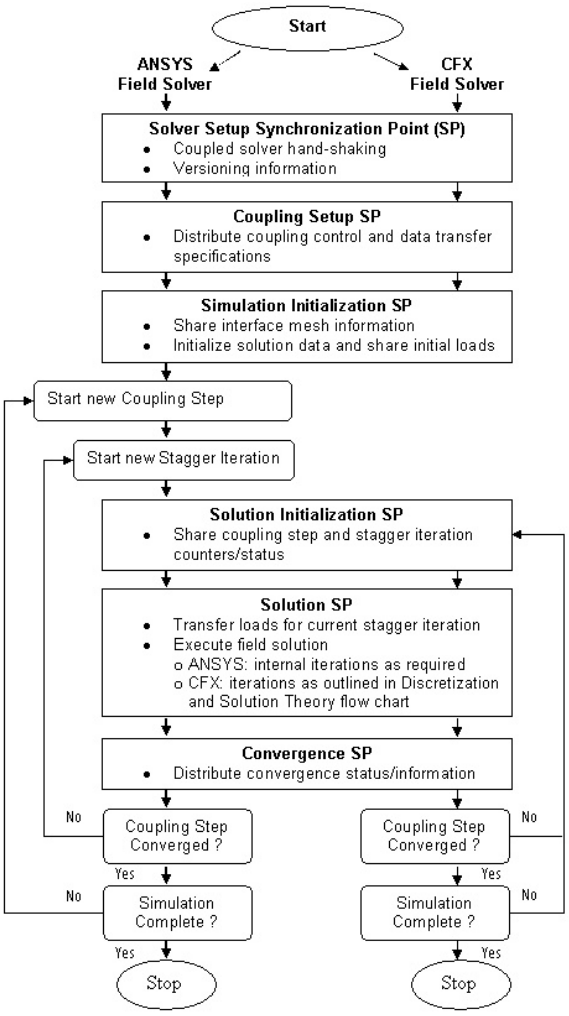

Figure 5-79: Flowchart of ANSYS staggered two-way coupling algorithm.

5.6.1 Two-way FSI: Model Setup

5.6.1.1 Fluid Domain Setup

Figure 5-80 shows a 36-degree sector of the fluid domain. However due issues with the software capabilities in applying cyclic boundary conditions to this type of problem, the entire annulus had to be modelled. Note that in this domain the radial extent of the rotor is fully modelled to account for the pressure loading from the bulk flow on the portion of the disc not covered by the radial extent of the seal.

The same blocking methodology used in the CFD model presented in *chapter 3* was used to mesh the current fluid domain. As mentioned before, it was not possible to apply cyclic boundary conditions so a sector of the mesh was modelled and then extruded around the axial axis. The total number of hexahedral elements used to build the structured mesh for the fluid domain was 6,565650. The pressure inlet and outlets were defined as an 'Opening': a type of boundary condition in *CFX* that differs from the conventional 'Inlet' boundary condition in the same solver in allowing for reverse flow to occur. Turbulence modelling and material properties remain the same as the previously setup CFD model, refer to sections *3.3.2* and *3.3.3*.

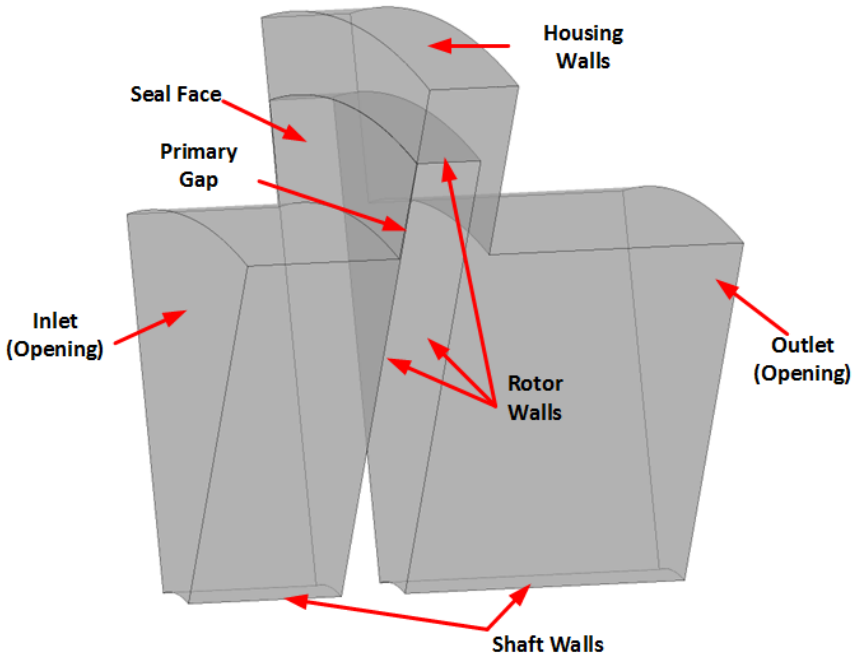

Figure 5-80: FSI model domain.

As part of the fluid setup, the walls taking part in the FSI interaction have to be defined and setup for data transfers to and from the structural solver through the *System Coupling* tool. In this case the upstream, top and downstream rotor walls were set to exchange data with the structural solver.

5.6.1.2 Structural Domain Setup

Figure 5-81 shows a model of the rotor disc used in this study. The region denoted by the '***A***' was set to a be fixed a support and motion was constrained in all degrees of freedom to mimic the disc support under static conditions. Surfaces ***D***, ***C*** and ***B*** are the upstream, top and downstream rotor walls and were set to be 'Fluid-Solid interfaces'. The 'Fluid-Solid interface' boundary condition defines the interfaces that the structural solver uses to exchange information with the fluid solver. It would have been sufficient to exchange data to and from the upstream face of the rotor where the load would be highest as the pressure on the downstream portion is largely at atmospheric conditions. However, in this study all rotor faces were included in the coupling process to account for the full deformation of the disc under the net forces from the fluid. The disc material properties are listed in Table 5.5. A structured mesh was used to discretize the structural domain and the total number of elements was 111,428. Note that, in the case of a steady state coupled analysis each coupling step represents one second of *Mechanical* solver time. To ensure the load was ramped linearly, the step end time for mechanical was set to be equal to the number of coupling steps in *System Coupling*, this was done to speed up convergence.

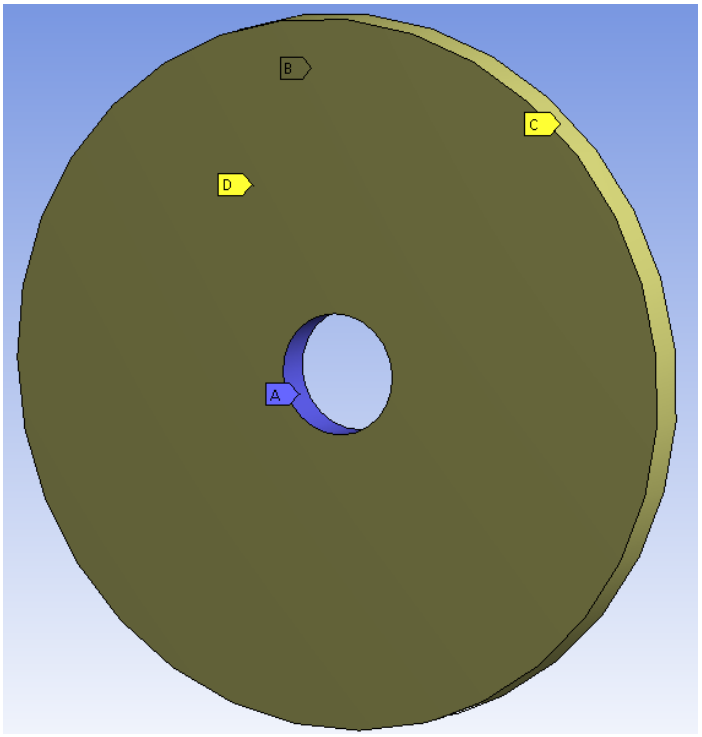

Figure 5-81:FSI, rotor disc with boundary conditions highlighted.

Table 5.5: Disc Material Properties

Disc Material	**Super CMV**
Elastic Modulus (E)	206.8 GPa
Poisson's ratio (ν)	0.28
Yield Stress, (σ_y)	1241 MPa
Ultimate Strength (σ_{uts})	1697 MPa

5.6.1.3 Coupling Setup

The coupling process was managed and executed using the *System Coupling* tool in *ANSYS Workbench*. As both solvers were set to execute steady and static analyses, the analysis type was set to general in the coupling manager. Next, the data transfers between the fluid solver and the structural solver were defined. Sequentially, the fluid solver was set to run first and as a converged solution was reached the force data were transferred to the structural solver and applied onto the rotor disc. The mesh displacements were then evaluated and fed back to the fluid solver and an updated solution was then obtained based on the deformed mesh. Table 5.6 tabulates the data transfers created for this simulation. The number of coupling steps was set to 40, which was found to be sufficient to yield converged solutions. The minimum number of iterations per coupling step was set to 1 and the maximum to 7. The solver proceeded to the next coupling step if all convergence criteria were met prior to reaching the maximum number of iterations. The coupling service terminated when the maximum number of coupling steps was reached.

Table 5.6: Definition of Data Transfers for Coupled Analysis

	Source			Target		
Data Transfers	**Participant**	**Region**	**Variable**	**Participant**	**Region**	**Variable**
Data Transfer 1	*CFX* (Fluid Solver)	Rotor Downstream Wall	Force	*ANSYS Mechanical* (Structural Solver)	Rotor Downstream Surface	Force
Data Transfer 2	*ANSYS Mechanical* (Structural Solver)	Rotor Downstream Surface	Incremental Displacement	*CFX* (Fluid Solver)	Rotor Downstream Wall	Mesh Displacement
Data Transfer 3	*CFX* (Fluid Solver)	Rotor Top Wall	Force	*ANSYS Mechanical* (Structural Solver)	Rotor Downstream Surface	Force

Data Transfer 4	*ANSYS Mechanical (Structural* Solver)	Rotor Top Surface	Incremental Displacement	*CFX* (Fluid Solver)	Rotor Top Wall	Mesh Displacement
Data Transfer 5	*CFX* (Fluid Solver)	Rotor Upstream Wall	Force	*ANSYS Mechanical* (Structural Solver)	Rotor Upstream Surface	Force
Data Transfer 6	*ANSYS Mechanical* (Structural Solver)	Rotor Top Surface	Incremental Displacement	*CFX* (Fluid Solver)	Rotor Downstream Wall	Mesh Displacement

5.6.1.4 Convergence Criteria

CFD solver convergence was monitored in the same manner as previously described in section *3.3.5*. For the mechanical solver, the solution was said to be have converged when force and displacement residuals fell below *1e-6*. By default the *System Coupling* manager outputs Root Mean Square (RMS) convergence for the data transfers defined above for both the source and target sides of the exchange. At the end of each coupling iteration within a coupling step, convergence is assessed and if convergence criteria are met and the minimum number of coupling iterations are satisfied, the solver moves to the next coupling step. The residual RMS value defined as a convergence criterion for all data transfers was *1e-3*. The CFD part of the coupling was given an initial solution of the same CFD model run prior to coupling it with the structural solver as this was found to aid with convergence.

5.6.2 Two-way FSI: Results

The model was applied to the case of a 0.5 degree converging angle with a minimum gap height of 50 μm. Figure 5-82 to Figure 5-85 show the radial pressure distributions as predicted by the FSI and the CFD models against those obtained experimentally at four inlet pressures (1.03 barg to 3.45 barg). The resultant mesh displacement in the axial direction is plotted against radial position in Figure 5-86. Displacements are shown only for the region of the disc covered by the radial extent of the seal, *i.e.* r = 69.5 mm to 85 mm.

The pressure distributions predicted by the FSI model show an improved agreement with experiments compared to the CFD model. The film pressure is seen to drop as the air-film load causes the disc to bend thus increasing the minimum gap height, as postulated earlier in this chapter. Although, the resulting drop in film pressure from the FSI model provides a better representation of the physics of the system, there is still a considerable discrepancy when compared to experiments. Nonetheless, it is apparent that the structural deformation of the disc was a contributing factor in the mismatch previously seen between experiments and the CFD model. In terms of the characteristics of the pressure distribution curve, the FSI model showed the typical entry loss which was higher than that predicted by the CFD due to the gap opening up as the disc cones. Additionally, the CFD model predicted an entry loss followed by region of pressure recovery. This region was not present experimentally for the minimum gap height and coning angle considered here. On the other hand, the FSI model predictions did not feature any pressure recovery zones after the initial entry loss. In fact the FSI model suggests that increase in gap height along the radius the caused the film pressure to drop further after the initial entry loss and showed no recovery at any point along the gap. In addition to structural deformation of the disc, the failure of both models in correctly capturing the extent of the entry

loss obtained experimentally lead to further disparities between both data sets. Furthermore, the gradients of the profiles along the gap predicted by the FSI are closer to experiments.

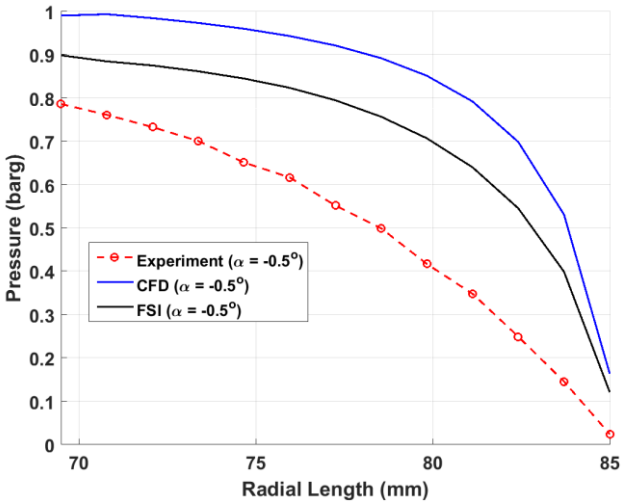

Figure 5-82: Radial pressure distribution, Converging Coning, h_{min}=50µm, P_{in} = 1.03 barg.

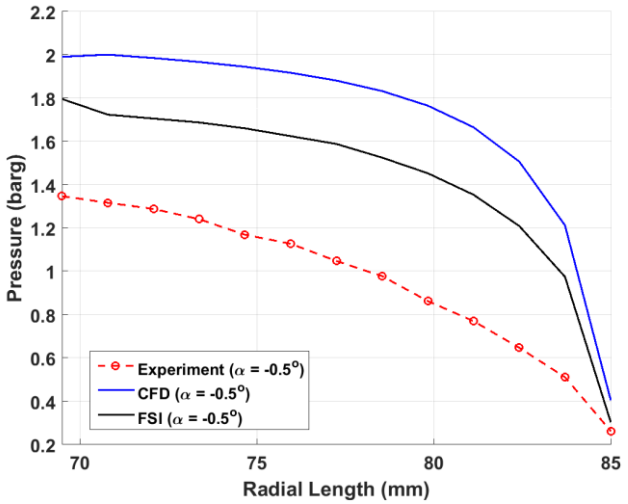

Figure 5-83: Radial pressure distribution, Converging Coning, h_{min}=50µm, P_{in} = 2.07 barg.

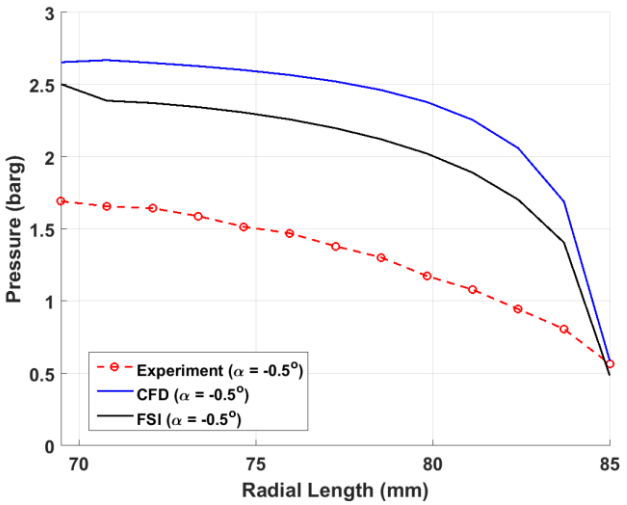

Figure 5-84: Radial pressure distribution, Converging Coning, h_{min}=50µm, P_{in} = 2.76 barg.

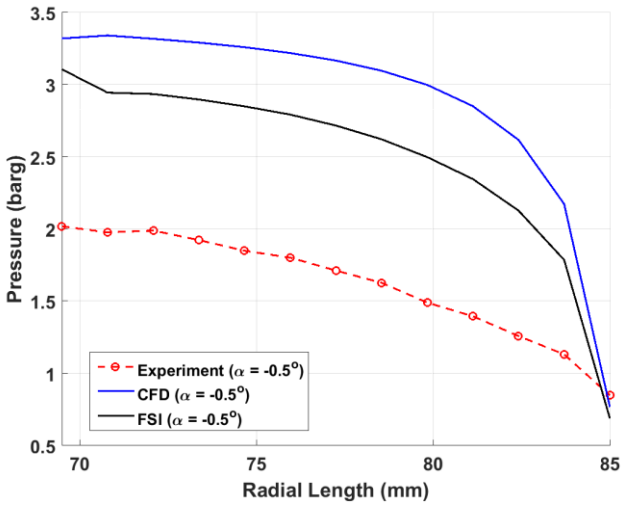

Figure 5-85: Radial pressure distribution, Converging Coning, h_{min}=50µm, P_{in} = 3.45 barg.

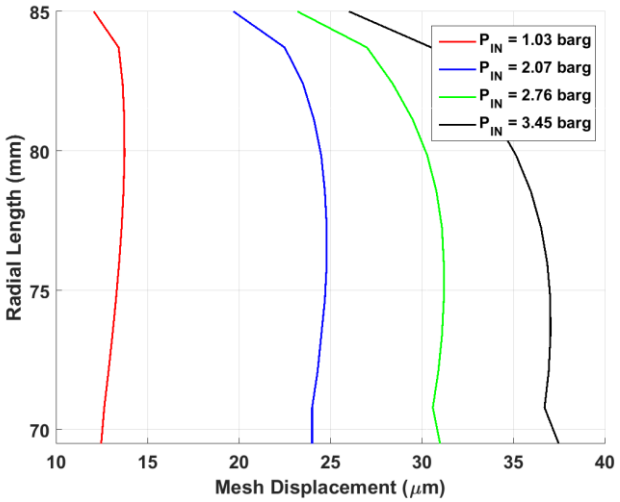

Figure 5-86: FSI, Mesh displacement, Converging Coning, h_{min}=50μm, α = -0.5°.

The improvement in numerical prediction in case of FSI over CFD can be seen in the absolute error plot shown in Figure 5-87. The pressure for all cases was normalised before calculating the absolute error, as previously shown in Figure 5-36 and Figure 5-37 using equation 5.1. Although the FSI model predictions are not entirely representative of the magnitudes of film pressures obtained experimentally, it serves as strong evidence that structural deformation due to pressure loading on the sealing faces can be significant and needs to be accounted for when modelling face seals under high pressure loads. This result of particular significance to large diameter face seals where structural deformation is more likely to alter the seal's flow domain.

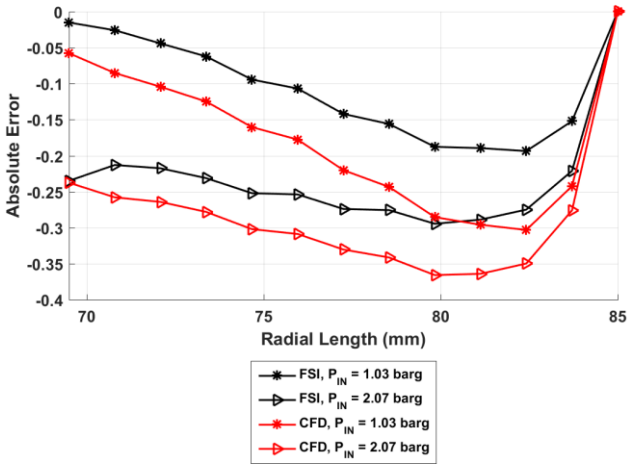

Figure 5-87: Absolute error in normalised radial pressures in CFD and FSI predictions, h_{min}=50μm, α = -0.5,° , P_{in} = 1.03 and 2.07 barg.

5.7 Chapter Summary

An extensive investigation has been carried out on the behaviour of the air-film under three different gap configurations; parallel, converging and diverging. Radial pressure distributions, load capacity and leakage rates have been assessed for all three configurations at multiple operating conditions. All cases showed an inertia-driven entry pressure loss which decreased with smaller gaps. For converging gaps, entry loss was more sensitive to the minimum gap height rather than the coning angle. Radial pressure distributions for converging configurations showed the highest air-film pressures, which increased with an increase in converging angle. On the other hand, diverging gaps maintained the lowest air-film pressure out of all configurations. Additionally, radial pressure distributions from diverging cases uncovered a highly compressible behaviour involving choked flow conditions at the gap inlet and a supersonic flow region that was terminated by a shockwave. The radial location of the shockwave occurrence moved further downstream at higher inlet pressures as higher Mach numbers were reached. The shockwave location showed little variation between both diverging angles tested for the same minimum gap. It was found to be more a function of inlet pressure

and minimum gap height. For diverging gaps, entry loss increased as the minimum gap height increased, however, larger angles incurred a less severe loss in most cases.

The experimental data generated allowed for the air-film force behaviour to be assessed in addition to the leakage rate through the primary gap. The air-film opening force was highest for the converging coning cases and increased with increasing the coning angle. The same trend applies for leakage rates, although the rate at which the leakage rate increased with converging coning angle showed a drop at higher pressures. Diverging coning cases showed the least air-film force. The lowest leakage rates were exhibited by the parallel cases.

The 3D CFD model compared well with parallel cases at larger minimum gaps and lower inlet pressures. Mismatch observed at high inlet pressures and small angles was due to coning of the disc. Discrepancies at larger gaps were due to the assumption of laminar flow in the gap, once turbulence effects were considered, the agreement improved significantly. Comparison between CFD predictions and experiments for converging cases showed large discrepancies which worsened at higher inlet pressures. A trend in absolute error between both sets of data suggested that the discrepancy was sensitive to inlet pressure and air-film force which points towards significant structural deformation of the disc under higher loads. This prompted the development of a two-way FSI which improved the comparison with experiments. The structural deformation of the disc, however, was not the only contributing factor to the discrepancy as both numerical predictions under-predicted the initial entry loss leading to over-predicted film pressures. For diverging cases, CFD predictions were in reasonably good agreement with experiments, particularly in capturing the correct trends. Main areas of mismatch were the magnitude of entry loss and the location of shockwave occurrence; CFD model predicted higher entry losses and the shockwave to occur earlier than experiments. Average Mach number in the sealing gap showed stronger shockwaves occurring earlier for

the larger angle case, particularly at high pressures. Furthermore, mass flow rates obtained from CFD confirmed that choked flow conditions were present. With regard to a face seal design, the work is an enabler to allow the positioning of a secondary seal on the rear of the face seal such that the seal is nearly hydrostatically balanced throughout its range of operating conditions. The pressure distributions allow local deformations of flexible faces to be accurately predicted. The surprizing result of some pressure recovery in the case of a diverging gap has defined a larger acceptable design envelop for the seal, and enables a seal with large starting offset to be defined which will under all conditions come into close proximity to the rotor at engine start-up.

6 Design and Testing of Prototype Seal

This chapter outlines the main components of a new design of a prototype seal. In previous chapters only one element of the seal has been fully modelled – namely the front face of the seal. The prototype is intended to operate at very small face seal displacement but over a wide range of axial displacements, and to test this behaviour a more realistic seal configuration where the primary face is mounted on a movable carrier restrained by sprung elements is employed. This allows the seal to move axially in response to the load from the air-film and the sealed pressure, and in the engine to follow large axial relative movements between the rotor and the casing, typically caused by thermal soaking and transients. Figure 6-1 outlines the main components of the new setup; the primary leakage path is highlighted by the coloured arrows: Red arrows show the flow the primary gap while yellow and orange arrows highlight the flow through the secondary seal. Table 6.1 and Table 6.2 report the geometric specifications and the operating conditions of the new setup, respectively. The main objective of testing this prototype seal is (*i*) to assess whether it is capable of successfully maintaining a non-contacting mode of operation under engine representative pressure differentials while (*ii*) withstanding significant runner distortions (*i.e.* swash), (*iii*) allowing for large axial movements (10 mm) and (*iv*) providing a competitive level of leakage. An axial extension of the existing test rig was necessary to accommodate the prototype seal and allow a very large range of axial movement. Instrumentation, data acquisition, calibration, experimental procedure and uncertainty data remain as described in *chapter 4* for the 'rigid' seal, however, in the revised setup, one of the digital dial gauges was used to measure the axial displacement of the housing relative to the baseplate and the other to measure the displacement of the front face, also relative to the baseplate. Three front faces with uniform inner radius and varying outer radii were tested. Changing the outer radius changes the area the air-film pressure acts over, thereby augmenting

or reducing the opening force. Based on the knowledge acquired from the previous study in *chapter 5*, all three faces had a converging angle of 0.5 degree and a radial step at 90% of the front face's radial extent. This is expected to provide an augmented load capacity to ensure the seal operates in a non-contacting mode throughout the test campaign. The initial set of tests

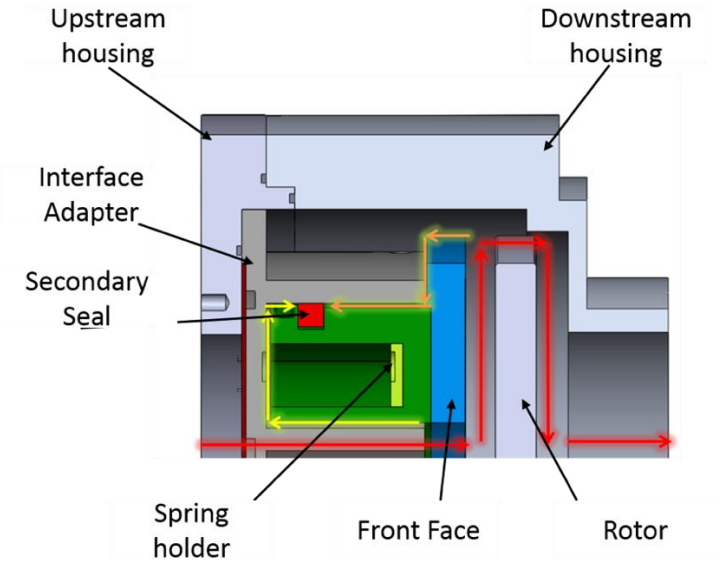

Figure 6-1: Embodiment of the prototype seal showing its primary and secondary leakage paths.

were conducted on all three faces without rotation. Sets of 3D-printed blocks of pressure tappings were used to monitor the local pressure distributions on the primary seal faces. The effects of changing the front face radial extent on the achieved balance gap height, mass flow leakage rate, film force behaviour are reported. Subsequently, the 'best' performing face was chosen for rotational swash tests. The effect of adding swash to the rotor on the seal's performance was then assessed. A 3D CFD model of the updated flow domain is presented at the end of the chapter.

Geometric specifications	
Seal inner diameter (ϕ_{inner})	139 mm
Seal outer diameter (ϕ_{outer})	170 mm, 162 mm and 157 mm

Front face thickness	9.5 mm
Rotating disc diameter	170 mm
Rotating disc thickness	10 mm
Total available axial space	14.8 mm

Table 6.1: Geometric specifications of prototype seal

Rig operating conditions	
Differential Pressure	Up to 3.45 barg
Downstream Pressure	Atmospheric
Axial movement	14.8 mm
Axial movement rate	18 mm/s
Speed	Up to 15 kRPM (133.5 m/s surface speed @ 170 mm diameter)
Temperature	Ambient temperature

Table 6.2: Rig operating conditions.

6.1 Key Components

6.1.1 Carrier Module

The transferrable technology being investigating in the seal (as opposed to rig specific embodiments) are all contained within the carrier module, Figure 6-2. The figure highlights all the constituent components of the new prototype seal. The system consists of the primary sealing face, mounted on a carrier ring which sits in a static mount (the interface adaptor). Rotation of the carrier ring is stopped by 4 cross keys, and leakage past the carrier ring is prevented by a secondary seal which operates in a near static environment. Details of the components are provided below.

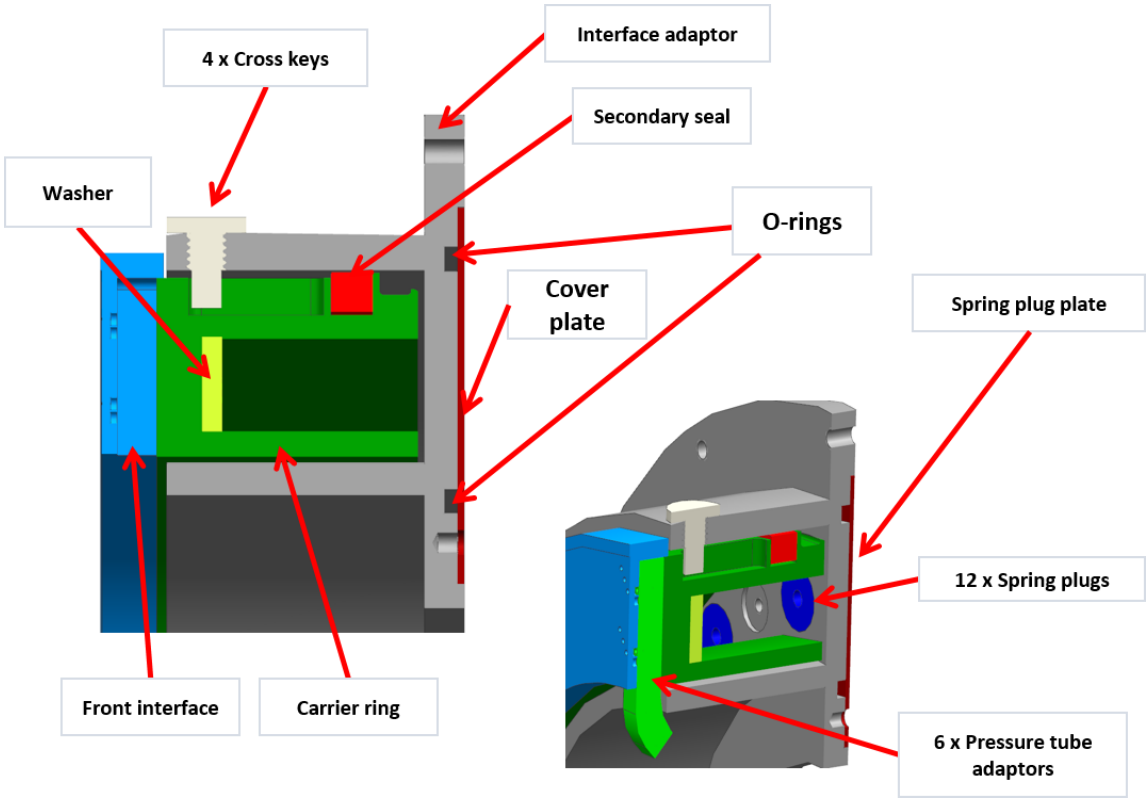

Figure 6-2: Carrier Module.

6.1.2 Interface Adaptor

Figure 6-3 shows the interface adaptor which fits onto the existing upstream housing using 12 M4 bolts. The adaptor is made of mild steel and features 4 cross key holes where anti-rotation pins are placed. 12 counter bored holes are included for compressive spring pins (not used), Figure 6-4 and, additionally, there are 12 holes that allow spring plug to be included with an anchor for use with tension springs, Figure 6-5 which were used in the current tests. A cover plate attaches to the back of the adaptor, shown in Figure 6-2, where two O-rings grooves are used to provide sealing.

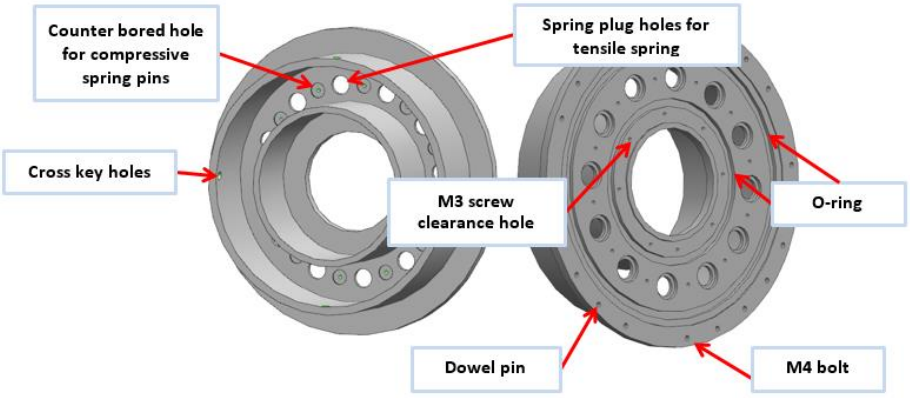

Figure 6-3: Interface adaptor.



Figure 6-4: Compressive spring pins.



Figure 6-5: Spring Plug with anchor for using tension springs

6.1.3 Front face

Three front faces with three different outer radii were manufactured, from aluminium alloy, as detailed in Table 6.1. The front face acts as the primary sealing face and is assembled onto the carrier module using a set of M3 bolts. All three faces have 6 radial grooves machined into the rear face at angular intervals (0^0,15^0, 49^0, 90^0, 180^0 and 270^0) with pressure tappings drilled through the seal face to allow static pressure distribution measurements to be made in the primary gap. As seen in the final seal assembly Figure 6-8.

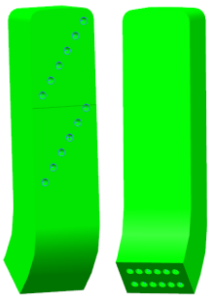

Figure 6-6: 3D Printed pressure tube adaptors.



Figure 6-7: Rear face of the sealing face with 3D printed pressure adaptors in place.

Each of the grooves holds a 3D-printed pressure tube adaptor, as shown in Figure 6-6 which connects 12 tappings on the face to *Scanivalve* metal pressure tubulations at the back of the adaptors as shown in Figure 6-7. At the front face a set of 1mm O-rings sits at the interface between the pressure adaptors and the slot. Short 1 mm stainless steel tubes are inserted to seal this final connection to the front face. Figure 6-8 shows schematic and photograph of the complete prototype seal assembly. The assembly is fitted into the test rig and its operation is very similar to that described in *chapters 4 and 5*.

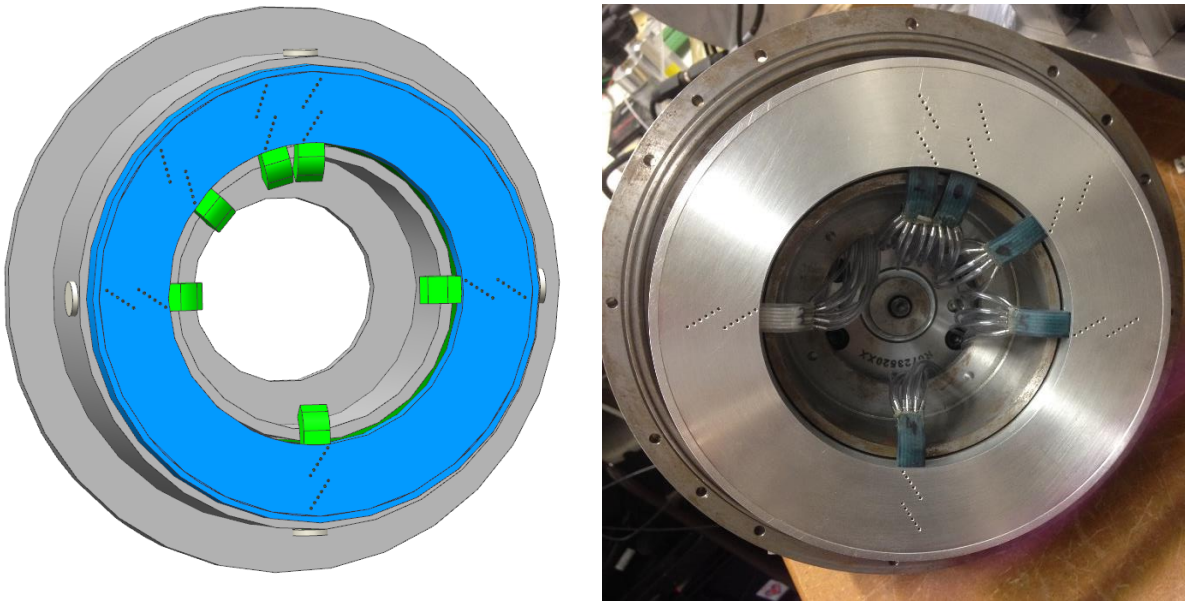

Figure 6-8: Complete prototype seal assembly Front face shown in blue and pressure tapping blocks in green.

6.2 Experimental Test Matrix

There are a wide range of test parameters which need to be considered when testing the seal assembly in order to determine its performance and robustness over the full range of operating parameters. At these conditions the primary results are once again the pressure distribution across the faces, the resulting force on the primary face, the leakage *and in the case of this free*

floating assembly the balance gap achieved by the seal assembly. Some parameters, however, were not and could not be widely varied during the collection of the data reported below.

One aim of the seal design was to provide a self-starting seal which would either pull itself in, towards the rotor on start-up or push itself away from the rotor as soon as rotation commenced. The former is more desirable, and as this was achieved in initial testing with a set of 12 tensile springs giving a total stiffness of 0.53 of N/mm was used in all subsequent tests. Their chief purpose is to restrain the seal at start up rather than provide a restoring force, however as the final operating condition relies on a balance of the forces on the front element of the seal they are moderately significant in the steady state gap achieved. From a business case point of view it could be argued that having a seal that is touching to begin with would perform better at low power or idle conditions. However, in the event of seal failure, this type of arrangement will result in both sealing faces rubbing which could happen at high temperatures and/or speeds leading to excessive wear that can be detrimental not only to the seal but to its surrounding environment. On the other hand, a seal that in event of loss of pressurisation pulls itself back away from the rotor alleviates this issue. More insight is given in the presented data regarding the seal's leakage behaviour under a range of pre-defined axial offsets.

Likewise the choice of secondary seal needs to be adequate to provide sealing without introducing a large hysteresis force to overcome when the seal is moved within its housing, and a sprung PTFE ring seal was used as for this purpose (between the carrier ring and the front face adaptor) in all test cases. The PTFE ring seal clearance was ~100 μm. The static and dynamic force induced by the seal is unknown, but is small in comparison to the force on the primary seal faces.

Inducing a high force on the primary sealing face allows a seal to be stiffer and theoretically more resilient to touchdown through small changes in pressure conditions than for a smaller force on the primary face. Therefore, using the knowledge from *chapters 3 and 5* it was decided that the primary sealing face would include a radial step, at 90% radial extent, as well as an α = -0.5^o (converging) angle on its front face. The notation used to describe the converging gap remains as before, refer to Figure 5-20.

In early design stages, what was known was the area upon which the sealed pressure acts. Due to geometry constraints concerning rig build the pressure balancing could only feasibly be altered by changing the outer radius of the primary static face thus changing the balance ratio, ***B***. For instance, to determine the level coning required to balance the opening force consider the force-coning angle diagram in Figure 5-65. Now at 0.69 barg a closing force of ~ 600N can be estimated based on the surface area of the sealed region, assuming no losses. As this force is constant a straight line can be drawn parallel to the *x*-axis which then intersects the opening force curves at the smallest and largest minimum gap at a given inlet pressure. This in turn gives the required range of coning necessary so that the air-film force can balance the closing pressure forces. Similarly, at higher pressures the same procedure can be performed to obtain initial predictions of the coning range required. Not knowing the balance gap heights *a priori* made it difficult to accurately pinpoint a coning angle to cover the entire envelope of pressures. However, coning angles of α = -0.4^o to -0.7^o were roughly estimated to pressure balance the seal. Based on this and to account for losses associated with both the air-film and the sealed pressure region each of the three front faces considered here was manufactured first with a coning angle of α = -0.5^o and another with α = -1.0^o. Experiments were initially run using the α = -0.5^o which was found to be sufficient to balance the seal using all three faces, although initial estimations assumed an outer diameter of 170 mm (as in the rigid seal outlined in *chapter*

5). Testing the larger coning angle was not performed as it would have increased leakage and decreased film stiffness, it was mainly a backup had the smaller converging angle not sufficed.

With these values fixed, the primary matrix of experimental running parameters is then: the outer radius of the primary sealing faces, the initial offset of the assembly from the rotor, pressure difference across the seal, the rotational speed of the rotor, the flatness of the rotor as described by swash on the rotor surface. Table 6.3 and Figure 6-9 list the geometric specifications of the seal along with the notation used. Note that, the cross-section of all three faces are shown in Figure 6-9.

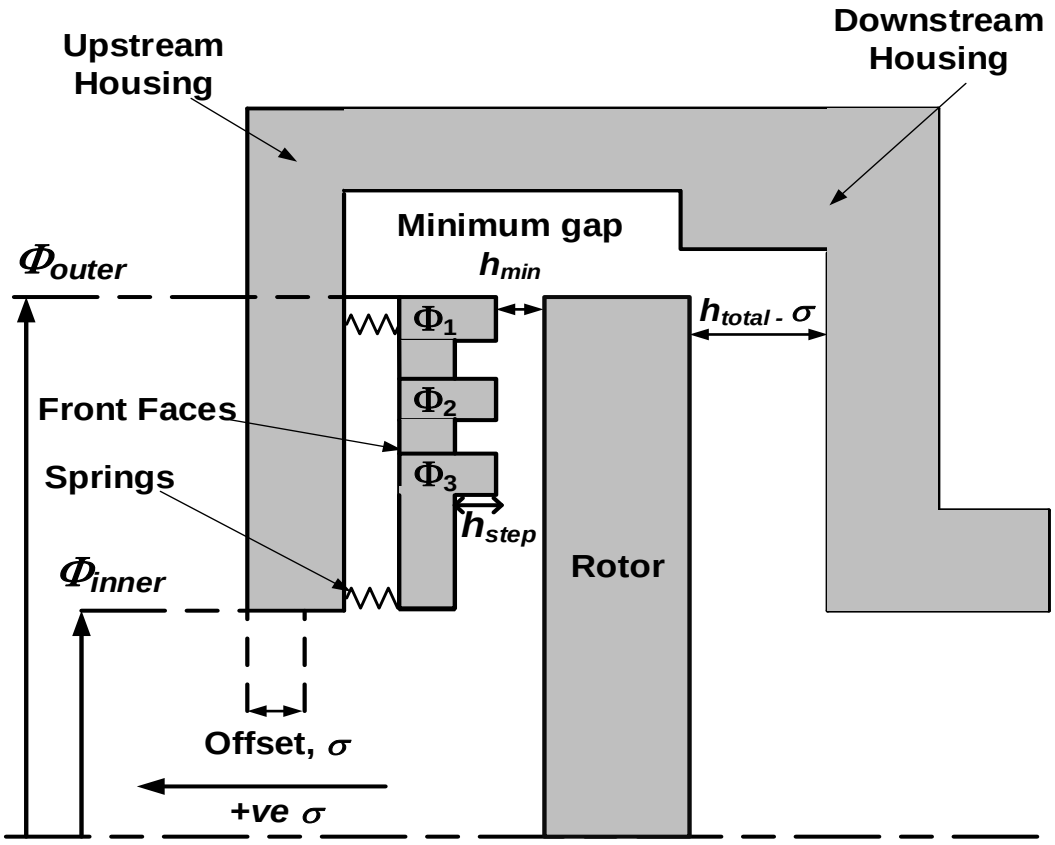

Figure 6-9: Geometry notation of prototype seal.

Front Face (Primary Sealing Face) Geometric Specifications	
Front face inner diameter (ϕ_{inner})	139 mm
Front face outer diameter (ϕ_{outer})	φ_1 = 170 mm, φ_2 = 162 mm and φ_3 = 157 mm
Step location	90% of radial extent
Step height (h_{step})	200 μm
Coning angle (α)	-0.5°
Total available axial space (h_{total})	14.8 mm

Table 6.3: Front face geometric specifications.

The mechanism for balancing a seal such that it operates over a wide range of conditions and maintains a sensible equilibrium position is set out in *chapter 1*. To investigate the effect of changing the balance ratio, ***B***, in this study the outer diameter of the primary sealing face was changed while the position of the secondary PTFE seal remained unchanged, both radially and axially. To operate the seal in a non-contacting mode for the entire operational envelope defined, balance ratios of less than ***B*** = 1 were required, however in an engine environment the precise spring constant used may vary over the life of the engine through mechanical aging and so a very small balance ratio is undesirable. Thus three faces (φ_1, φ_2 & φ_3) were chosen to provide balance ratios of 0.7, 0.8 and 0.9, respectively.

Close to bearings in a jet engine, static and rotating components suffer little relative axial movement. In those positions a close fitting filament seal may be suitable to generate a very low effective clearance seal. Thus for the current testing the largest possible range of initial axial clearances, i.e. the initial offsets σ, was considered to be representative of suitable locations for this seal. The range of starting offset conditions considered was chosen to be between 2 – 12 mm offset from the rotor face. Under non-pressurised conditions this is

equivalent to the minimum gap, $\boldsymbol{h_{min}}$, note the positive direction of σ in Figure 6-9. When the pressure loading is instigated on the seal, the front face can move forwards to close the minimum gap, while the offset and gap between the rotor and the downstream housing remain constant. For the seal to be feasible for implementation it needs to *pull in* and onto the rotor, without touchdown, but creating a tolerable level of leakage at the end of the process.

Most of the tests conducted in this section of the report use a flat rotor, however, both machining and thermal gradients in the system mean that there is likely to be swash on the radial upstand which forms the rotor surface of the seal. The term *swash* refers to a periodic change in circumferential gap height of a known amplitude and period length. Industrial experience suggests that this is typically 3 or 5 wave in order around the circumference of the rotor, and these were used as experimental parameters for testing reported later in this chapter. To introduce swash onto the rotor face, *kapton* sheets with double sided glue were used. The *kapton* sheet was cut into equal sectors and placed around the rotor face as shown in Figure 6-32. The thickness of each of the *kapton* sectors was $\boldsymbol{h_w}$ = 221 μm. This level was considered high enough to induce hydrodynamic effects even at the relatively low rotor radii used in this test rig. As previously illustrated in section 2.1.2, swash typically takes up a near-sinusoidal profile. However, in this campaign the swash profile differed than those shown in Figure 2-10 and Figure 2-11 in the fact that it was represented as a square wave rather than a near-sinusoidal wave. This, in principal, was done for two reasons: 1- The square wave will introduce a once per revolution forcing which will not be as smooth of a transition compared to a sinusoidal wave. However, this is bound to introduce additional mixing losses that are greater than a sinusoidal profile and whether the seal will withstand this level of swash without failing was one of the objectives behind this experimental campaign. 2- Due to the larger gaps inherent to the seal introduced in this thesis, potential hydrodynamic augmentation due to swash will be

insignificant compared to the hydrostatic component. Therefore, it was simpler to introduce swash on the rotor disc as a square wave.

As for the constrained primary leakage face testing, *chapter 5*, the range of pressure differences considered was moderate Δp = 0.69 bar to 3.45 bar with exit conditions from the test rig remaining atmospheric as before.

6.2.1 Radial Pressure Distributions

Figure 6-10 to Figure 6-13 show the circumferentially averaged radial pressure distributions at four different inlet pressures (0.69, 1.03, 2.07 and 2.76 barg) for the largest of the front faces used, φ_1. The radial pressure readings from the 3D printed pressure blocks were averaged at four circumferential locations; 0^0, 90^0, 180^0 and 270^0. The face has an outer diameter of 170 mm, an inner diameter of 103.6 mm and a balance ratio of B = 0.7. The offset was increased gradually from σ = 2 mm up to σ =12 mm in five steps (2, 5, 7, 10 and 12 mm). The achieved balance gap height for each offset is reported in each figure label. Note that, the balance gap height here is defined as the minimum axial gap height between both sealing rings which in this study will always be the axial distance between the edge of the radial step and the rotor face. i.e. $h_{min} = h_{bal}$. The displacement of the front face relative to the baseplate was measured using a dial gauge that pierces through the back of the cover plate through to the backside of the front face. While a dial gauge sitting on the back of the seal housing measured the displacement (offset) of the entire seal assembly, also relative to the baseplate. The touch-down location was determined in an identical manner to the method outlined in *section 4.3.1.2*.

As seen in the radial pressure distributions for the rigid face seal tested previously, an entry loss was evident for all cases. The lowest entry loss was for the σ = 2 case and increased as

σ increased. This is because the balance gap height, h_{bal}, increases slightly with increasing σ at the same inlet pressure. Consequently, the highest film pressures were consistently achieved in the σ = 2 mm cases and dropped as σ increased. This agrees well with the trends highlighted before in *chapter 5* where the inlet pressure loss increased with increasing the gap size as inertial forces become dominant. Increasing the offset results in an increased spring force which due to the use of tensile springs acts as an opening force component in addition to the air-film force. The increased total opening force resulted in larger balance gap heights which explains the increase in h_{bal} values with increasing offset. Additionally, the balance gap height for a given σ increased with increasing inlet pressure due to the increased film pressure. Moreover, the change in balance gap height was less sensitive at higher pressures compared to lower pressures where the change in balance gap height with available axial space was more pronounced. For instance, the balance gap for φ_1 at P_{in}=0.69 barg increased by 26% as the offset was increased from σ = 2 mm to σ = 12 mm, while at P_{in}= 2.76 barg it only increased by 3.67%. This is entirely unsurprising as a smaller change in gap height is required across the primary sealing face to affect the same change in force with offset when the inlet pressure is higher – compare this to the very nearly constant change in the spring force with changing offset.

Note that due to space restrictions on the front face of the seal, the pressure distribution could only be measured to an outer diameter of 148 mm. Thus, the pressure distributions as plotted show only the film pressure upstream of the radial step. This explains the apparently higher gap exit pressures compared to the rigid face setup as most of the pressure drop occurs across the step located at 90% - 100% of the radial extent. As this step is only 10% of the radial extent of the seal the drop is considered to be linear over this length.

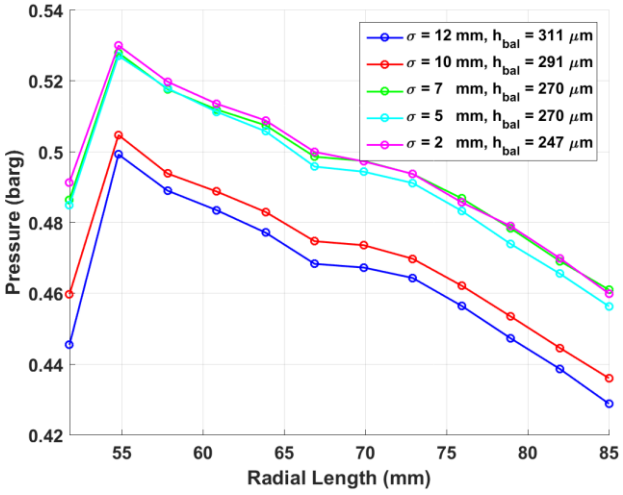

Figure 6-10: Radial Pressure Distribution, φ_1, P_{in}=0.69 barg.

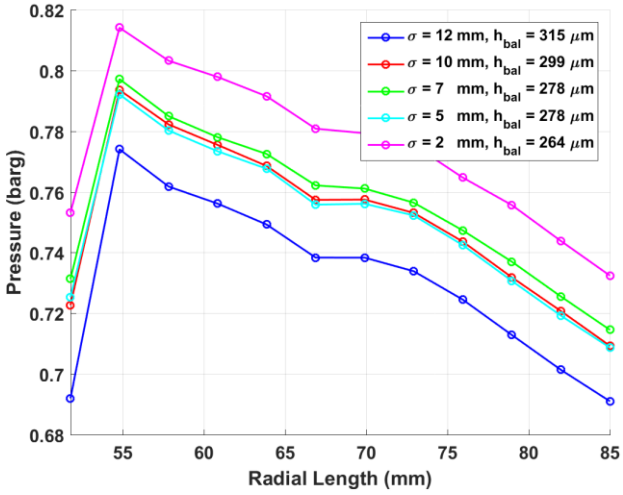

Figure 6-11: Radial Pressure Distribution, φ_1, P_{in}=1.03 barg.

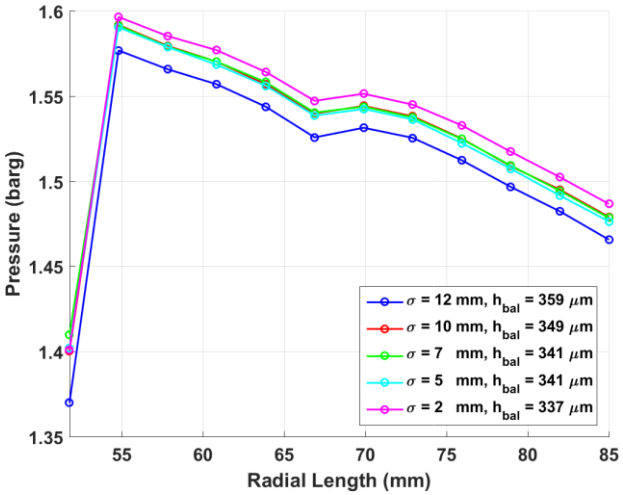

Figure 6-12: Radial Pressure Distribution, φ_1, P_{in}=2.07 barg.

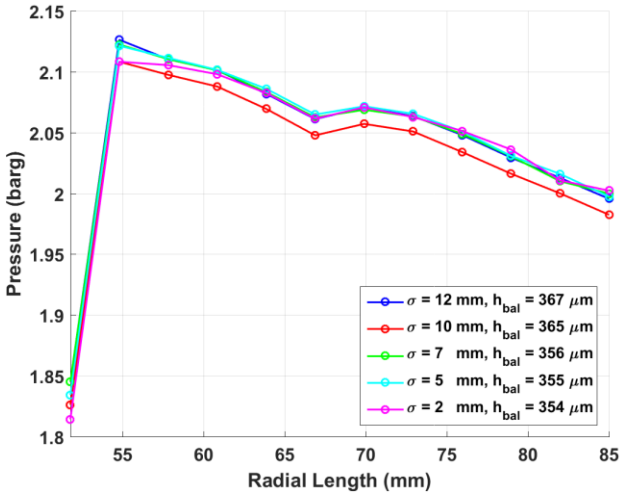

Figure 6-13: : Radial Pressure Distribution, φ_1, P_{in}=2.76 barg.

Figure 6-14 to Figure 6-17 show the same radial pressure distributions for front face, φ_2, outer diameter = 162 mm ($\boldsymbol{B}$ = 0.8). The inner radius, step location and converging angle remain the same as the larger face, φ_1. Similar to the previous configuration, an entry loss followed by a recovery region was evident across all test cases which increased with an increase in balance gap height. Compared to the larger face, the inlet pressure loss was less

severe as the balance gap height is reduced in all cases. The reduction in balance gap height is due to the smaller surface area on the primary sealing face, φ_2 which provides a smaller opening force, while the surface area over which the seal upstream pressure acts remained unchanged. Apart from σ = 2 and 5 mm cases, the film pressure dropped consistently as σ increased. For the σ = 2 and 5 mm cases, a very similar entry loss was observed while the σ = 5 case maintained a higher film pressure compared to σ = 2 case, unlike what had been seen with the larger face. The balance gap height increased with increasing pressure and increasing σ, and in line with φ_1, the balance gap height was observed to be more sensitive to a change in σ at low pressures where h_{bal} increased by 62.3% as σ increased from 2 to 12 mm at P_{in} = 0.69 barg while a 16.4% increase was realised at P_{in}= 2.76 barg. It is unsurprising that φ_2 is more sensitive to changes in offset as the smaller face will require a larger change in height to affect the same change in force as φ_1 at any given inlet pressure.

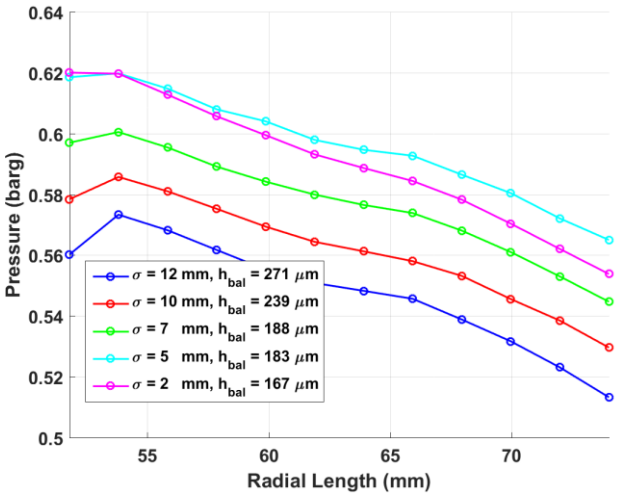

Figure 6-14: Radial Pressure Distribution, φ_2, P_{in}=0.69 barg.

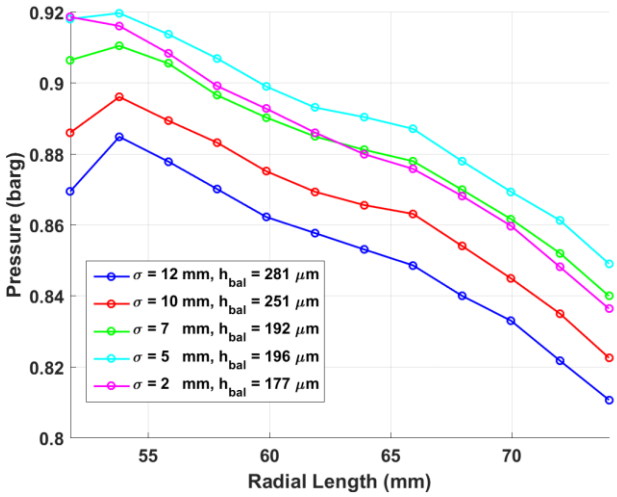

Figure 6-15: Radial Pressure Distribution, φ_2, P_{in}=1.03 barg.

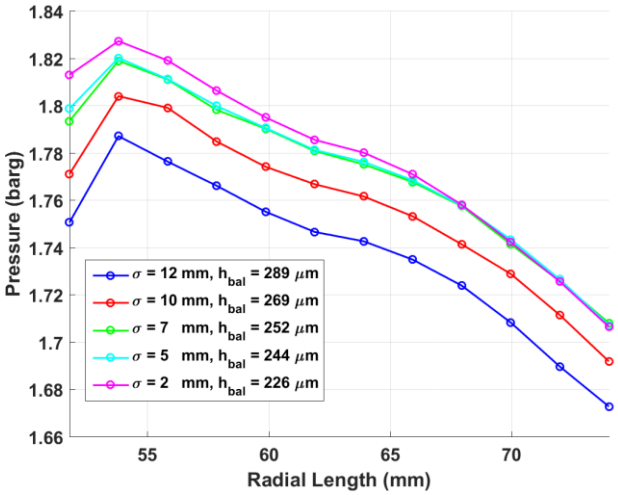

Figure 6-16: Radial Pressure Distribution, φ_2, P_{in}=2.07 barg

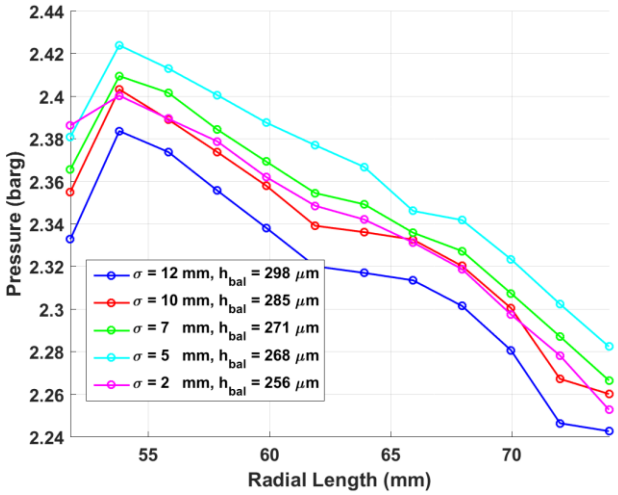

Figure 6-17: Radial Pressure Distribution, φ_2, P_{in}=2.76 barg

Figure 6-18 to Figure 6-22 show the radial pressure distributions for the smallest and final front face tested, φ_3. The face has an outer diameter of 157 mm and a balance ratio of B = 0.9. In line with the previous results the entry loss was reduced compared to the larger faces as the balance gap is reduced for each equivalent case. The change in balance gap height was very subtle with increasing inlet pressure, indicating a passively balanced seal. For instance, at σ = 12 mm and P_{in} = 0.69 barg the balance gap height was, h_{bal} = 240 μm which dropped to h_{bal} = 217 μm at P_{in} = 1.03 barg and then settled at h_{bal} ~210 μm for P_{in} = 2.07, 2.76 and 3.45 barg.

Similarly, at σ = 10 mm, the balance gap height lies between h_{bal} = 195 to 206 μm across the entire range of operating pressures. The balance gap height, however increases with increasing σ and for this smallest primary face the change in balance gap with offset is higher at all pressures compared to φ_1 and φ_2.

Note that, at higher pressures (P_{in} = 2.76 and 3.45 barg, Figure 6-21 and Figure 6-22) the pressure distributions show some abrupt changes which are believed to be due to some blockage/leakage issues with pressure tubes adaptor. In general, the 3D printed pressure tube

adaptors performed well and allowed for assessing the pressure field in the primary sealing gap without constraining the axial flexibility of the front face. The limitations of those adaptors are mainly tied to the maximum pressure the inner channels of the adaptors can withstand without breaking, which in the work presented here became evident at pressures greater than 2.07 barg.

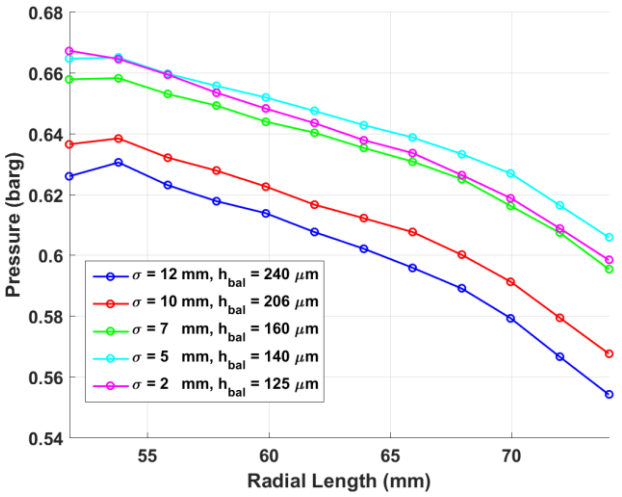

Figure 6-18: Radial Pressure Distribution, φ_3, P_{in}=0.69 barg

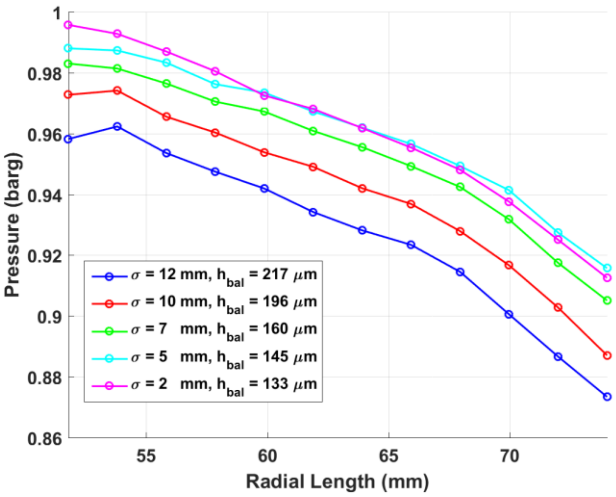

Figure 6-19: Radial Pressure Distribution, φ_3, P_{in}=1.03 barg

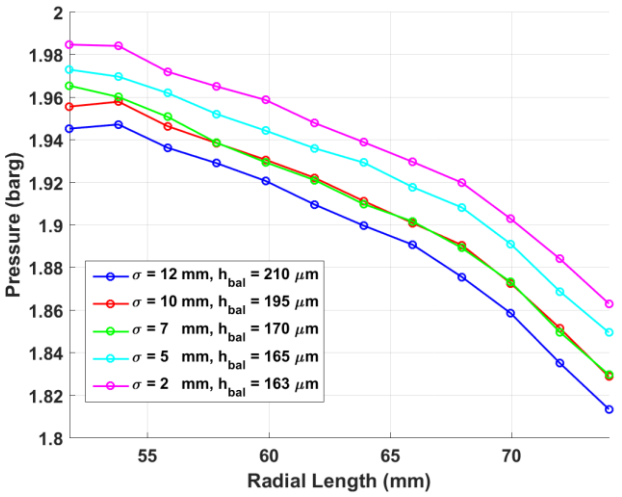

Figure 6-20: Radial Pressure Distribution, φ_3, P_{in}=2.07 barg

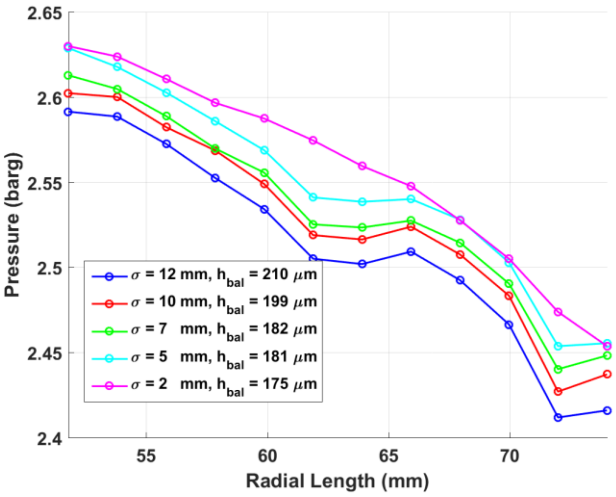

Figure 6-21: Radial Pressure Distribution, φ_3, P_{in}=2.76 barg

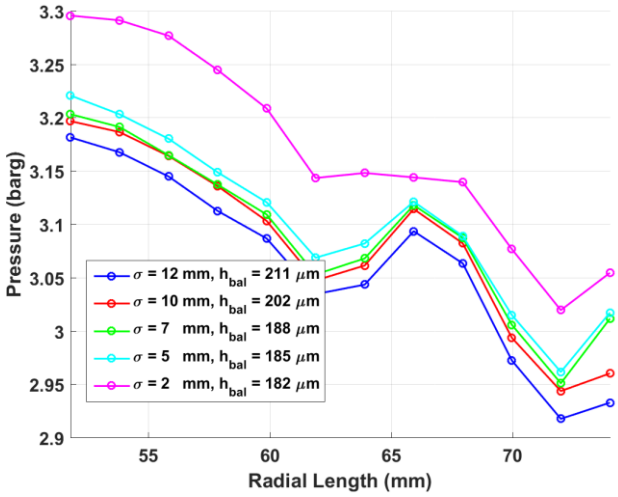

Figure 6-22: Radial Pressure Distribution, φ_3, P_{in}=3.45 barg

6.2.2 Air-film opening force

Figure 6-23 shows the change in air-film opening force against offset, **σ**, at four different inlet pressures for the largest and the smallest faces tested, $\boldsymbol{\varphi_1}$ and $\boldsymbol{\varphi_3}$ as the offset increased from 2 to 12 mm. The film forces were computed by numerically integrating the circumferentially averaged radial pressures acting on the front face as read by the pressure tappings. For all faces, a general trend of a decreased film force is evident with increasing offset. The reason for this subtle decrease is the drop in balance gap height at smaller offsets resulting in a slightly higher film pressure. As expected, the largest air-film force is provided by the largest face, φ_1, and the lowest film force provided by φ_3. The difference in the resulting film force is more significant at higher pressures. Changing the outer radius from a large face to a smaller one ($\boldsymbol{\varphi_1}$ and $\boldsymbol{\varphi_3}$) reduces the achieved balance gap height. Although the opening force has dropped compared to the larger face, the drop was not significant enough to compromise the seal's ability to maintain a non-contacting mode of operation across the entire operational envelope with a plane rotor and no rotation. Also, note the slight decrease in film-force for both faces considered as the

balance gap height increases with increasing offset. Ideally, the primary driving factor in changing the pre-defined offset is the spring constant. Increasing the offset augments the spring force which in the case of the tensile springs used here acts as an opening force. This results in an increased total opening force.

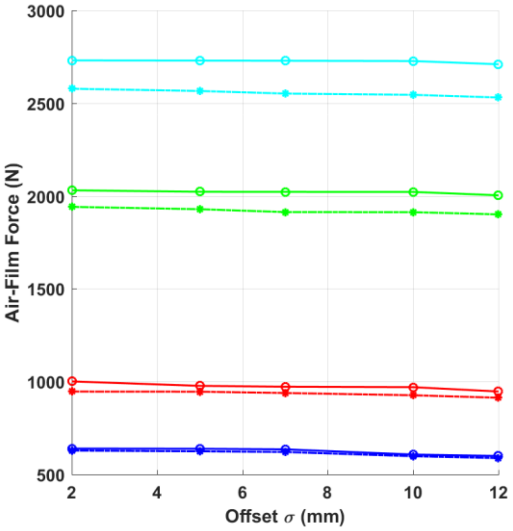

Figure 6-23: Change of air-film force with offset.

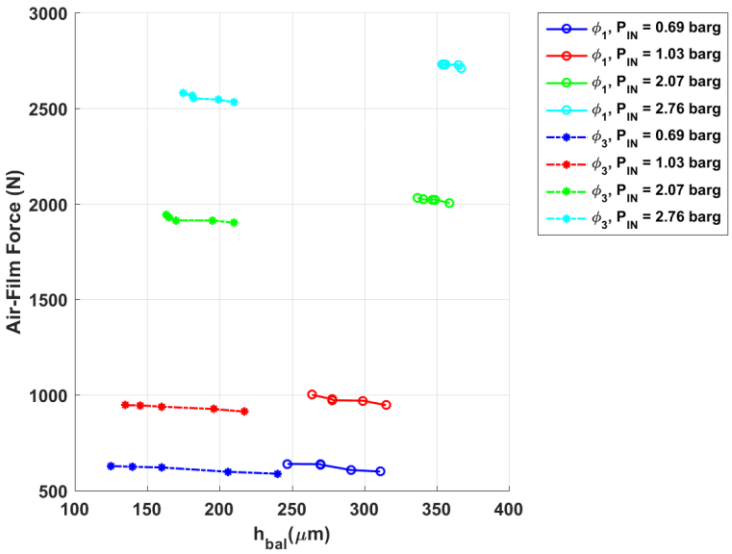

Figure 6-24: Change of air-film force with balance gap height.

The opening force, closing force and net force on the seal at four inlet pressures for φ_1 and φ_3 are shown in Figure 6-25 and Figure 6-26 respectively. The opening force constitutes the total contribution from the air-film force, F_{AF}, plus the spring force F_{SP},

$$F_{OPEN} = F_{AF} + F_{SP} \quad \text{Eq. 6.1}$$

$$F_{CLOSE} = P_{Sealed} * A_{Sealed} \quad \text{Eq. 6.2}$$

$$F_{NET} = F_{CLOSE} - F_{OPEN} \quad \text{Eq. 6.3}$$

The tension springs contribute to the opening force. The air-film force is obtained by integrating the pressure field acting on the area of the front face. The sealed pressure is

monitored through a pressure tapping drilled through the adaptor and located inside the sealed pressure cavity and used to calculate the closing force, see Figure 1-12.

For both Figure 6-25 and Figure 6-26, different inlet pressures are marked by different colours, the opening force is represented by the solid line, the closing force by the dashed line and the net force by the dash-dot line. Inspection of aforementioned figures confirms that the seal was balanced for the operational envelope covered here. Both the opening forces and closing forces are in good agreement as also shown by the net force residual for each case. Note that, unlike the air-film force, a slight increase in the total opening force with increasing offset is evident. This is due to the spring force contribution which increasing with increasing offset. The positive direction of σ is indicated in Figure 6-9.

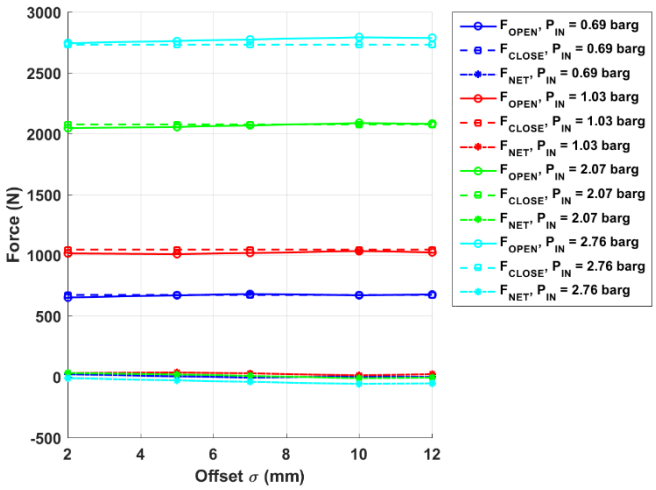

Figure 6-25: Force on Seal, φ_1

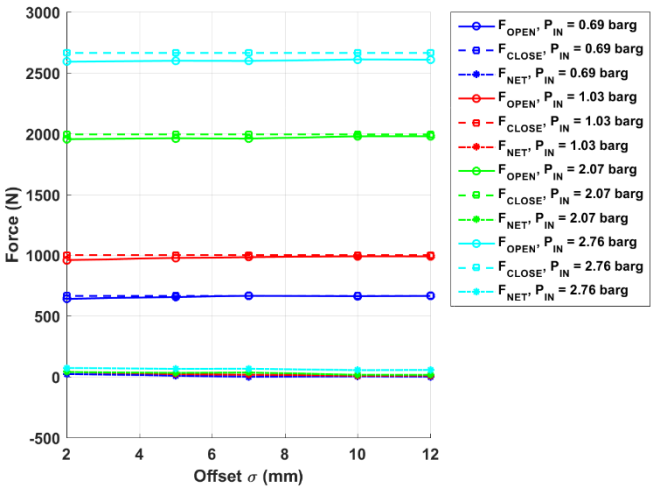

Figure 6-26: Force on Seal, φ_3

6.2.3 Change in Steady-state Balance Gap Height

Figure 6-27 shows the change in balance gap height with offset for all three faces tested at four inlet pressures (P_{in} =0.69, 1.03, 2.07 and 2.76 barg). The largest face, φ_1 , is represented by the solid lines, φ_2 is represented by the dotted lines and φ_3 is represented by the dashed lines.

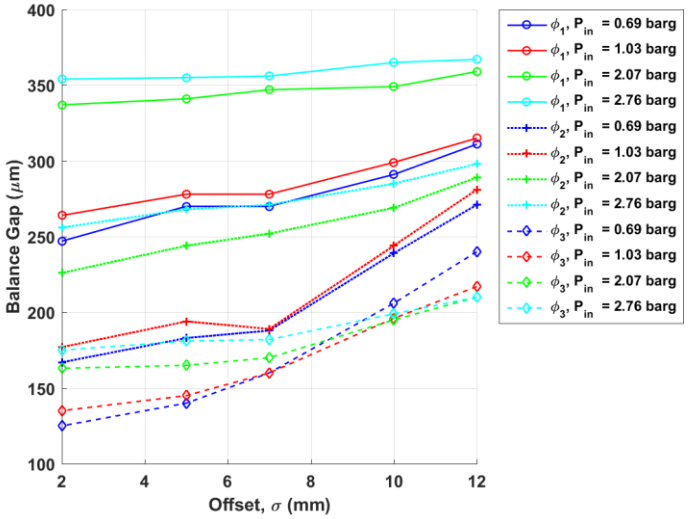

Figure 6-27: Change of balance gap height with offset.

All faces show an increase in balance gap height both with increasing pressure and offset which is associated with a rise in the opening force. The smallest face, $\boldsymbol{\varphi_3}$, also showed an increase in balance gap heights with increasing pressure. For $\boldsymbol{\sigma}$ > 7 mm a balance gap heights cross over was seen between the curves at the three highest inlet pressures (P_{in} =1.03, 2.07 and 2.76 barg) indicating that the seal's tendency to open up has decreased and the seal maintained almost the same gap height across most of the operating pressures.

The maximum balance gap height dropped by almost 40% moving from the largest face $\boldsymbol{\varphi_1}$ to the smallest face $\boldsymbol{\varphi_3}$. Furthermore, the gap heights for the two larger faces were strongly coupled to a change in pressure as well as offset. The smallest face, on the other hand, showed the balance gap height to be significantly less dependent on inlet pressure and mainly a function of offset, particularly for values of $\boldsymbol{\sigma} \geq 7$ mm.

6.2.4 Air-film Stiffness

Having obtained sufficient air-film force data along with the respective balance gap heights, it was then possible to compute the rate of change of air-film force with gap height using a central

differencing numerical scheme applied to all data points apart from those at the boundaries where forward and backward differences were used. Investigating the air-film stiffness is of interest as it provides an indication of the resilience of the seal to transient loading during its operation. Caution must be taken in over interpreting the results as the relative sparsity of the data and the differentiation involved means that some data are severely discontinuous. Figure 6-28 shows the offset average stiffness of each of the faces plotted against inlet pressure to the system.

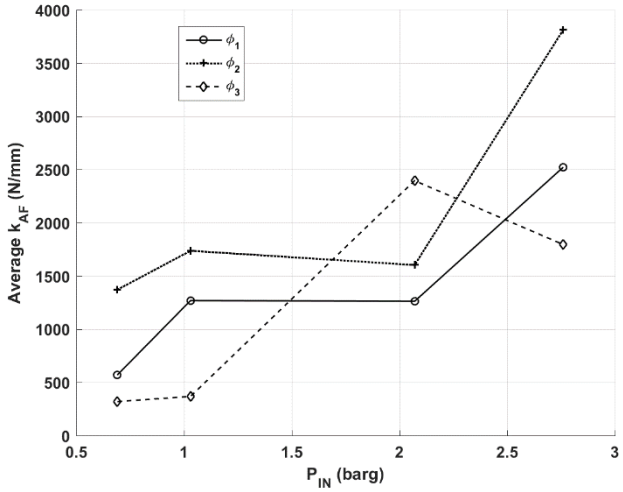

Figure 6-28: Average Seal stiffness vs inlet pressure

For all three faces, the air-film stiffness shows a marked increase with pressure by a factor of between 3 and 5 times over the range 0.69 bar to 3.45 bar. The stiffness result shown here is based on the change in the offset position of the entire seal and not on the position of the seal face itself. So for a change of 10 mm in the relative axial position of the interface adapter relative to the rotor there is only a change of ~100 μm (low pressure) or 10 μm (high pressure). The stiffness after the initial deflection will quickly increase in response to the decrease in the seal gap, for the case of reducing offset, but cannot be quantified through steady-state testing

of the seal assembly. To map the full transient operating stiffness a surrogate CFD model may be best employed – this is beyond the scope of the current work.

6.2.5 Leakage rates

The mass flow rate entering the system upstream of the seal was measured as described in *chapter 4* for all test cases. The leakage of parasitic flow through the rig was calculated by blocking the primary gap using a rubber seal on the front face and measuring the remaining leakage over the full range of pressure difference. Thus the leakage through the secondary PTFE and brass ring seals were characterized. The raw mass flow rates could then corrected for the flow through the gap around the seal housing.

Figure 6-29 shows the change in leakage rate through the primary gap as the offset was increased from σ = 2 mm to σ = 12 mm for φ_1, φ_2 and φ_3 at four inlet pressures. All faces showed a slight increase in leakage rate with increasing σ due to the larger balance gap heights attained by the seal at larger offsets. The lowest leakage rates were exhibited by φ_3 as the balance gap heights were the smallest at any given pressure across the full test envelop.

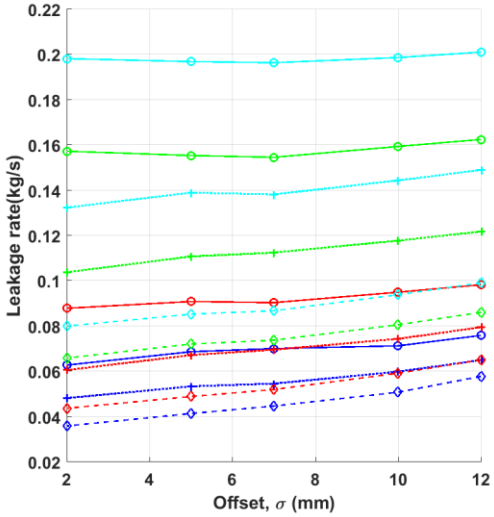

Figure 6-29: Effect of offset on leakage rate.

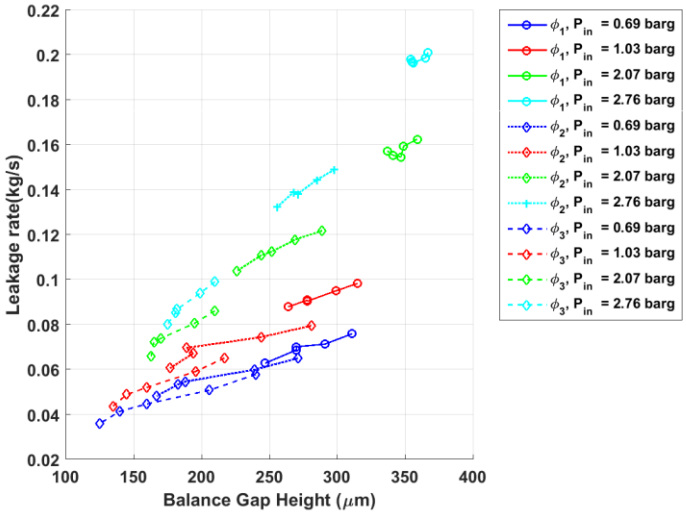

Figure 6-30: Effect of offset on leakage rate.

Figure 6-31 shows the effective clearance (*ec*), as defined in *chapter 3*. For a radial seal the definition of the operating diameter is somewhat problematic and an average diameter (D = 153.6 mm) taken here at the midpoint of the radial step to approximate the effective flow area through seal. Perhaps because of this, the effective clearance appears to be higher than the balance gap for some cases. Additionally, the errors associated with *ec* are typically large compared to flow rate as this is a derived quantity from another derived quantity. Nonetheless, The *ec* values shown above for this seal are considered competitive relative to labyrinth and brush seals. The trend line of *ec* versus h_{bal} can be shifted downwards by design by placing the secondary seal at a higher radial location to provide a larger closing force, by using less stiff springs (for tensile springs) or by adjusting the level of coning to provide a smaller opening force thus reducing leakage.

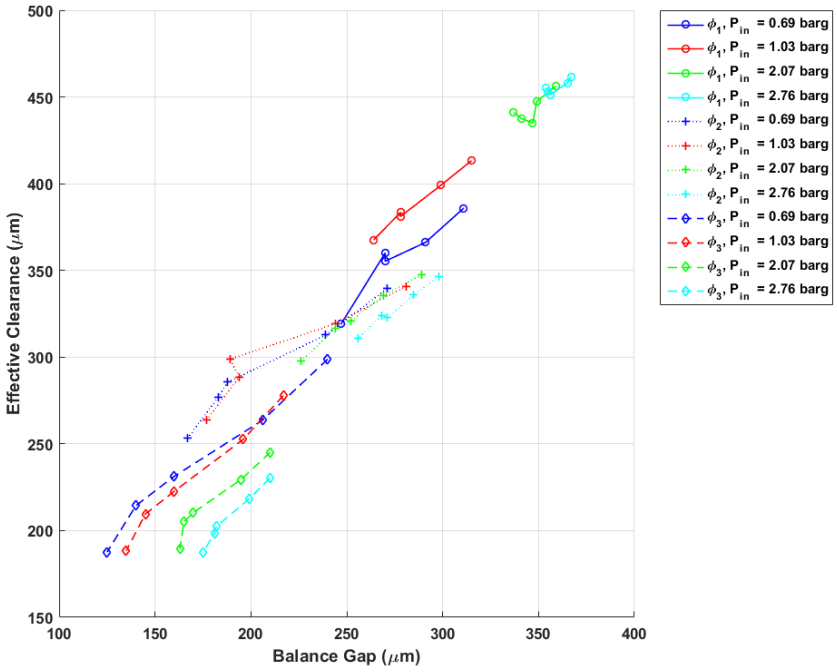

Figure 6-31: Effective clearance calculated at an average radius of *r* = 77.1 mm.

6.2.6 Swash: Radial pressure distributions

Experiments were performed on the prototype seal to investigate the effect of adding 3 wave and 5 wave swash on the rotor face. Front face φ_3, was used for all experiments as it had the best sealing performance when used on the plane rotor. A photograph of three wave swash installed on the rotor is included as Figure 6-32 while Figure 6-33 shows a representation of the surface profiles of the introduced swash for the 3-wave and 5-wave cases. While swash is usually sinusoidal in nature, a square wave will excite the same fundamental behaviour and is easier to implement.



Figure 6-32: Rotor with kapton tape sectors to introduce swash.

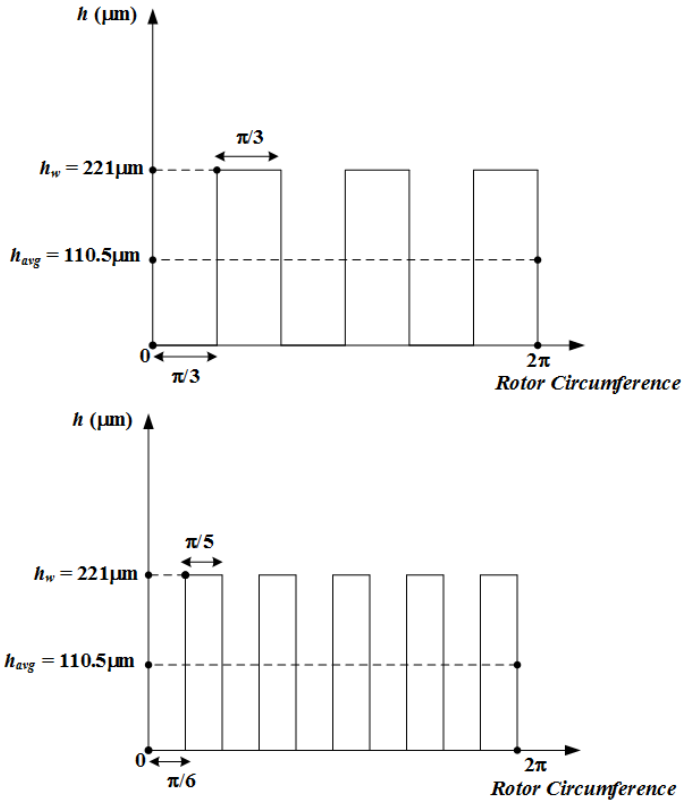

Figure 6-33: Amplitude and period length of swash using kapton tape sectors on rotor.

6.2.6.1 No –added Swash with rotation

Figure 6-34 to Figure 6-36 show the radial pressure distributions for the no-added swash case for two offsets σ = 2 and 12 mm represented by the dashed and solid line, respectively. The data are shown for three different inlet pressures, P_{in} = 0.69, 1.03, and 2.07. For each offset and inlet pressure combination, data were captured with no rotation and at 5 different rotational speeds (ω = 500, 2500, 5000, 10,000 and 15,000 RPM). The rotational speeds and balance gap heights are reported on all plots.

For all radial distributions shown, the typical trend of pressure loss followed by recovery is again seen. It is also evident that the smaller offset, σ = 2 mm, configurations maintain a higher film pressure than the larger offset, σ = 12 mm. At the two lowest inlet pressures P_{in} = 0.69 and

1.03 barg , Figure 6-34 and Figure 6-35, the lowest film pressure was seen with the disc at rest and σ = 12 mm. A sudden but very slight (note the non-zero origin) increase in film pressure is seen at ω = 500 RPM, for a small gap with rotation causing pumping this may be appropriate. This was followed by a drop in film pressure as the speed increased to ω = 5 kRPM. The differences in pressure and balance gap here between all cases at the same offset are very small, and may simply be caused by vibration in the rig overcoming stiction as the seal pulls in at low pressures. Nevertheless, the film pressure remained higher than for the stationary case.

As the operating pressure increased to P_{in} = 2.07 barg, the film pressure for σ = 12 mm cases increased with speed till ω = 15 kRPM suggesting some slight hydrodynamic effect, with no intermittent decrease in film pressure during the process. Moreover, the balance gap heights obtained by both offsets were significantly closer in magnitude compared to those obtained at lower pressures. Unfortunately when the pressure was further increased (P_{in} = 2.76 and 3.45 barg) the tubing in the tunnel was found to have detached from the pressure tappings and further pressure data were not available. These data have been omitted.

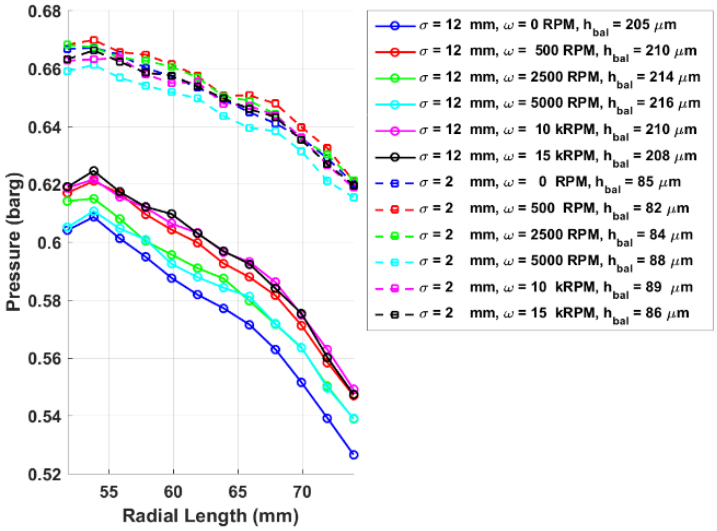

Figure 6-34: No -added Swash, Radial Pressure Distribution, φ_3, P_{in}=0.69 barg

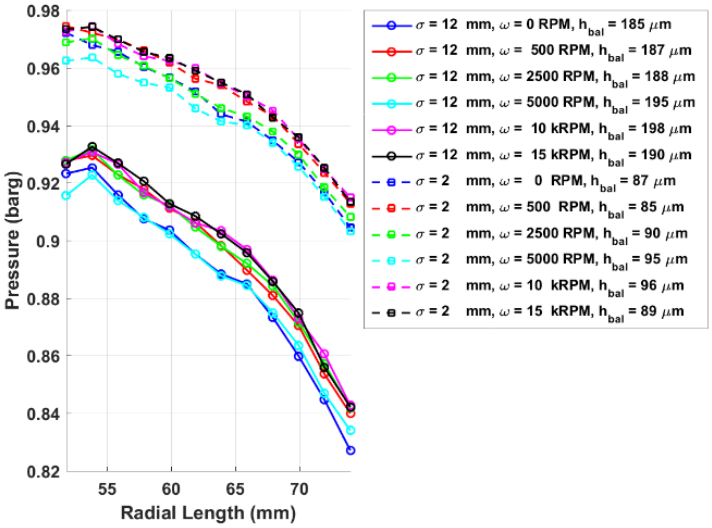

Figure 6-35: No -added Swash, Radial Pressure Distribution, φ_3, P_{in}=1.03 barg

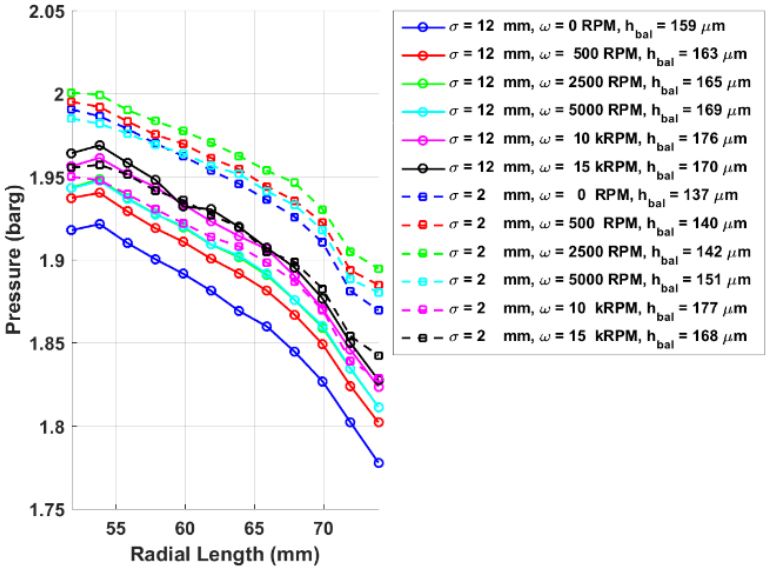

Figure 6-36: No -added Swash, Radial Pressure Distribution, φ_3, P_{in}=2.07 barg

6.2.6.2 3-Wave Swash with rotation

Figure 6-37 to Figure 6-39 show the radial pressure distribution for the 3-wave swash tests. In this case, for both σ = 2 and 12 mm cases, the highest film pressure was maintained at ω = 0 RPM at all operating pressures, it is unclear if that is significant. The 0 rpm data are problematic with swash as the distribution of the faces relative to the pressure tappings is unknown. Whereas the large and small gaps are periodically averaged across the face of the seal during rotational operation this is not the case with no rotation. Thus the measured pressure may reflect a narrow gap at some tappings and a wide gap at others. It is clear that the effect of averaging without knowing the bias on the tappings will yield a biased result at 0 rpm. Therefore it is appropriate only to compare the rotational cases. One might also note that the balance gap height here is based on the minimum gap measured in the system. of course for 50% of the disc the balance gap is increased by the height of the Kapton steps so a better comparator for balance height might be $h_{bal} + 221\mu m/2$, but if $h_{bal} \rightarrow 0$ then there will be seal touchdown. Thus quite different forces may be expected for cases with and without swash at the same balance gap.

At low pressures with rotation the film pressure is steady and low with little change in h_{bal}. A significant rise in pressure across the entire face is seen at ω = 15 kRPM. particularly for the σ = 12 mm case. Here, at low speeds, the steps on the shaft may turbulate the flow causing additional loss which balances the pumping work and hydrodynamic force from rotation. At higher speeds these latter terms appear to become more significant. Increasing the pressure to P_{in} = 2.07 barg, Figure 6-39, causes the balance gap heights for σ = 12 mm to decrease by a very small amount but for the σ = 2 mm case these are increased significantly. This suggests

the hydrodynamic force which scales with density and inversely with gap becomes more significant here.

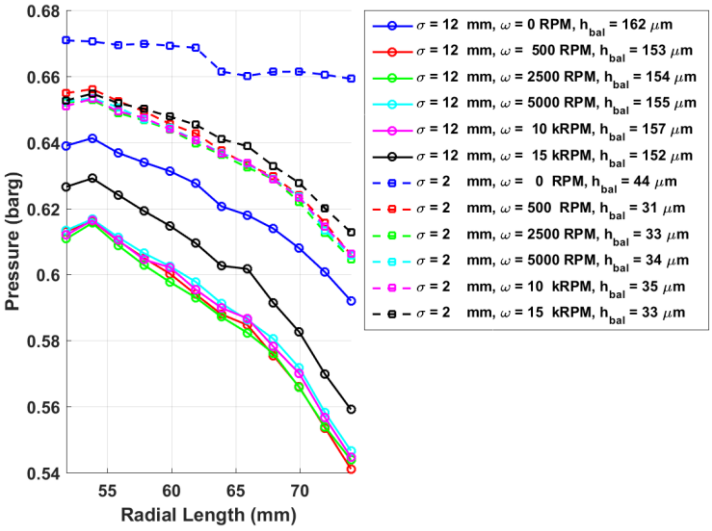

Figure 6-37: 3-wave Swash, Radial Pressure Distribution, φ_3, P_{in}=0.69 barg

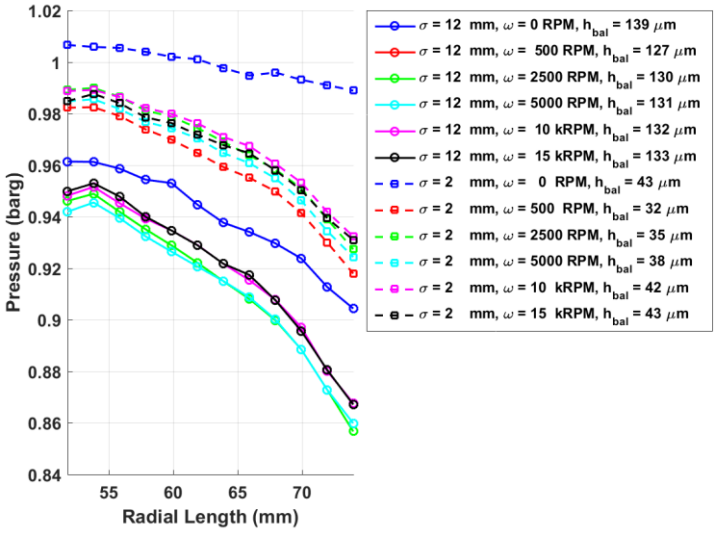

Figure 6-38: 3-wave Swash, Radial Pressure Distribution, φ_3, P_{in}=1.03 barg

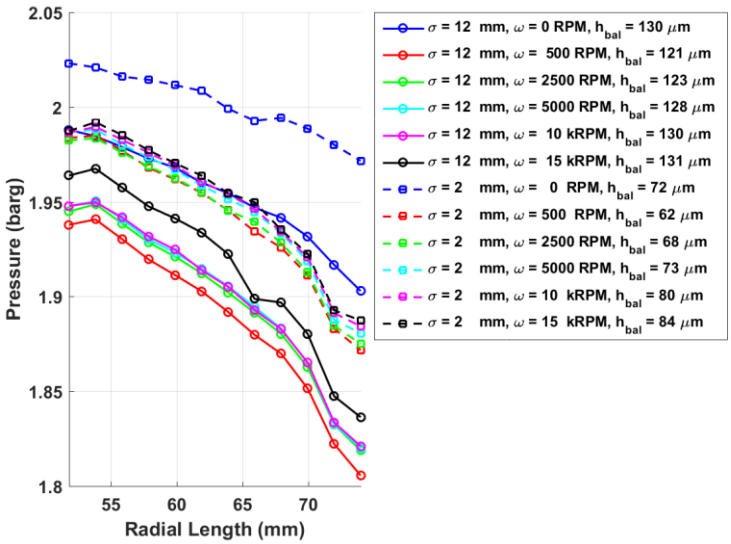

Figure 6-39: 3-wave Swash, Radial Pressure Distribution, φ_3, P_{in}=2.07 barg

6.2.6.3 5-Wave Swash with rotation

Figure 6-40 to Figure 6-42 show the radial pressure distributions for the 5-wave swash configurations. The film pressure for the 5-wave case, at both offsets, increases with speed and, as before, smaller offset cases maintain a smaller balance gap However, the film pressure dropped with increasing speed at P_{in} = 2.07 barg when spinning the disc from ω = 10 kRPM to 15 kRPM. Indeed, at P_{in} = 2.07 barg only two σ = 2 mm pressure profiles could be plotted at ω = 0 and 500 RPM as beyond this speed a significant increase in torque was observed indicating that touch-down occurs. No higher pressure cases could be run with the 5-wave swash at σ = 2 mm. Therefore, as might be expected, the balance gap heights measured at P_{in} = 1.03 barg and σ = 2 mm, Figure 6-41, were the smallest encountered throughout the experimental campaign. The collapse of the film pressure here is a significant finding, as with significant surface swash amplitude and reduced wavelength it is clear that the hydrodynamic lift effects, intuitively imagined, are absent from the system unlike in the high pressure 3 wave case. This is could also be due to the additional mixing losses associated with having a sharp edged square wave swash profile as opposed to a sinusoidal wave profile. Further work is required to fully characterise this process and more testing with changed swash profile and amplitude would improve understanding further.

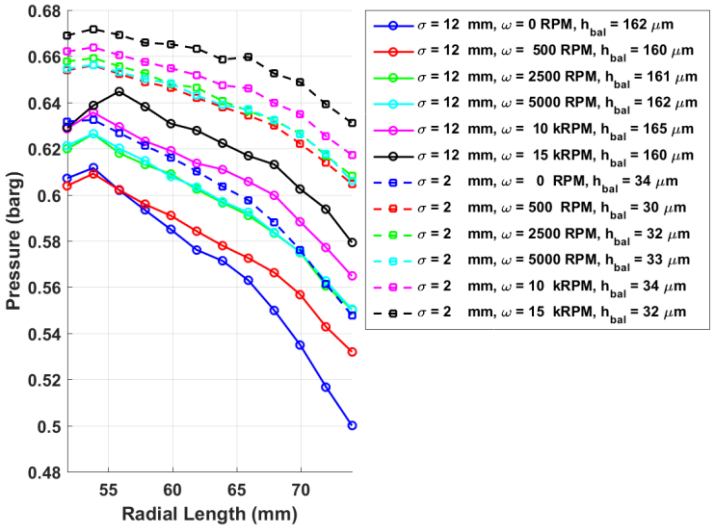

Figure 6-40: 5-wave Swash, Radial Pressure Distribution, φ_3, P_{in}=0.69 barg

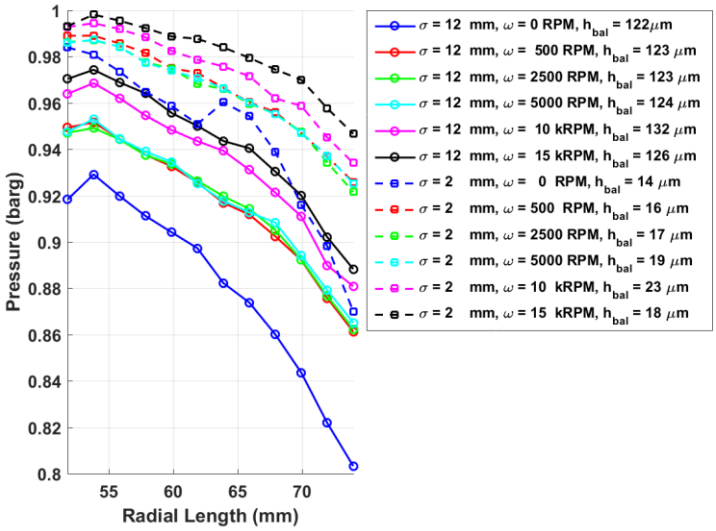

Figure 6-41: 5-waveSwash, Radial Pressure Distribution, φ_3, P_{in}=1.03 barg

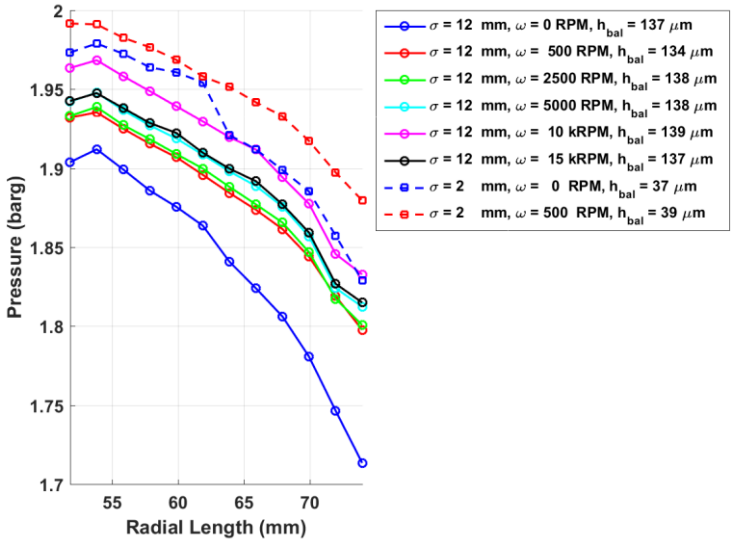

Figure 6-42: 5-wave Swash, Radial Pressure Distribution, φ_3, P_{in}=2.07 barg

6.2.7 Swash: Effect on Air-film Opening Force

Air-film opening forces are reported in this section for an offset of 12 mm. They are in effect integrated pressure distribution plots. The film force shows a consistent increase with speed, excepting some anomalous static data, and while the highest film force is that of the 3-wave

swash case without rotation this is likely due to the unknown measurement bias noted above. At P_{in} = 1.03 barg, as the rotational speed increases, the 5-wave swash provides the largest film force followed by the 3-wave case. At 2.07 barg, there is little difference between all geometries (and it is worth remembering here that the average gap height is increased for the cases with added swash). At the highest inlet pressure, the no-swash cases provided the highest film force followed by the 3-wave swash case. There is little augmentation in film force with rotation and the force for faces with swash is substantially less than for a nominally flat surface. In short, increasing the number of waves had a detrimental effect on the film force at higher operating pressures. As noted above when the opening force provided by the spring was reduced – i.e. for the offset = 2mm case, touchdown occurred at high pressure.

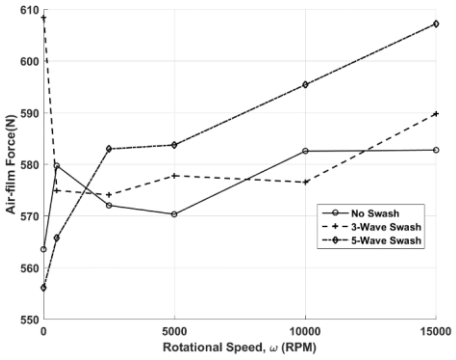

Figure 6-43: Effect of rotational speed on air-film force, σ = 12 mm, P_{in} = 0.69 barg

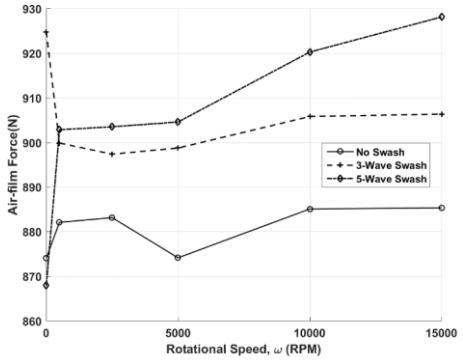

Figure 6-44: Effect of rotational speed on air-film force, σ = 12 mm, P_{in} = 1.03 barg

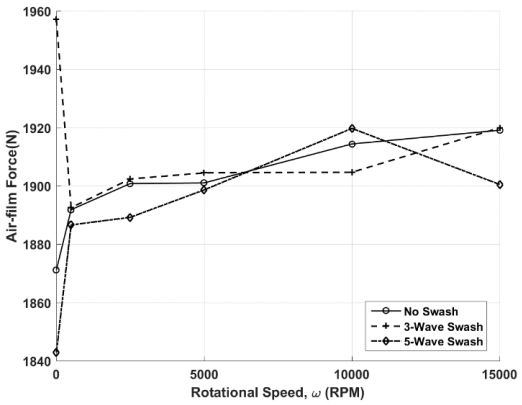

Figure 6-45: Effect of rotational speed on air-film force, σ = 12 mm, P_{in} = 2.07 barg

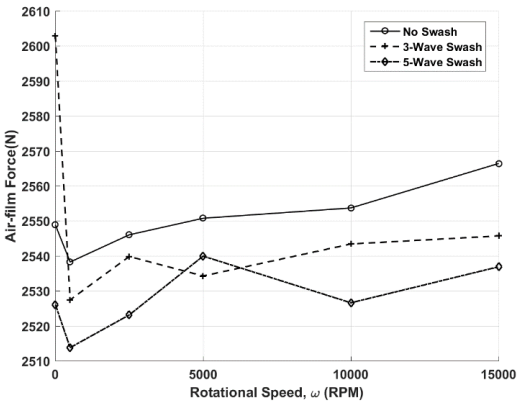

Figure 6-46: Effect of rotational speed on air-film force, σ = 12 mm, P_{in} = 2.76 barg

Finally regarding forces on the system, **Figure 6-47** shows the opening force, closing force and the resultant net force for the three-wave swash configurations at a range of inlet pressures and rotational speeds. The plot serves to confirm that the data collected show the seal to be successfully pressure balanced state across the most of the operational envelope. Thus, we can consider the axial friction force provided by the secondary seal to be negligible on the system.

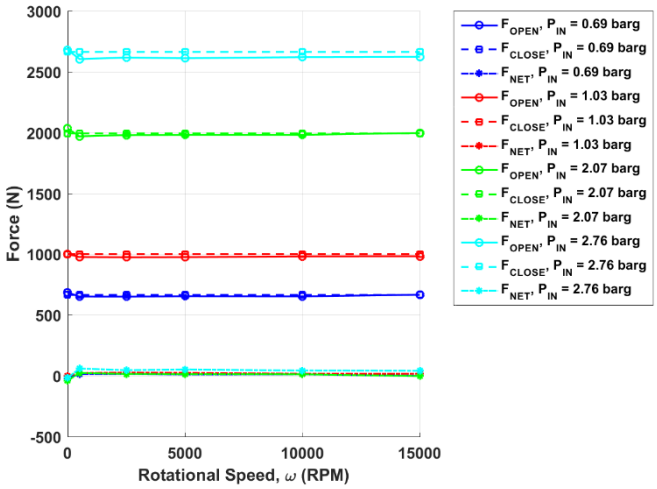

Figure 6-47 Opening, closing and net forces on seal, 3-wave swash, σ = 12 mm.

The force data seen have confirmed that the seal, using ϕ3, could tolerate the levels of swash introduced to the disc without touching down when running at the maximum offset, σ = 12 mm. Issues with touch down were reported only when running the 5-wave swash cases

at an offset of σ = 2 mm. Swash offered hydrodynamic gains in film force at low operating pressures (up to 1.03 barg) and a wide range of speeds while its effect was detrimental to film force at higher pressures and with an increase in the number of waves on the rotor face. The abovementioned trends agree qualitatively with work conducted by Lebeck *et.al.* (1978). Their work resulted in a 1-D model for a wavy contacting face seal that accounts for surface roughness, waviness, asperity load support, elastic deflection and wear. The problem was solved numerically and yielded 1-D hydrodynamic and asperity pressure distributions in addition to mean film thickness and friction for a given load. The model was applied to the baseline case of a hot water carbon contacting face seal The seal was tested with 3-wave swash of amplitude of 4.06 μm and a period length of 106.43 mm at 3.21 bar, 148.85 ^{o}C and a shaft speed of 2500 RPM. By changing the design they determined the percentage of the total load capacity generated by hydrodynamic effects. They also showed that for a balanced seal, the hydrodynamic load is not always always sufficient to achieve complete lift-off of the seal and an optimum number of periodic waves leading to the maximum amount of hydrodynamic load. Further work (Lebeck, 1981) showed the effect of varying the operating pressure: an increase in operating pressure caused the percentage hydrodynamic film load support to drop. This is in line with the current tests, despite differences in scale and operating fluid. Referring back to the ratio of hydrodynamic load to the hydrostatic load, ϕ, in *section 2.1.2*, the effect of a reduced gap height in improving the hydrodynamic action was established to be significant. A greater gain in hydrodynamic action would also be realised under reduced pressure differentials. This explains the weaker hydrodynamic action achieved in this study compared to the literature discussed above.

Figure 6-48 and Figure 6-49: show the effect of changing the rotational speed and offset on film force at the lowest and highest pressures for the no-swash and the 3-wave swash

configurations at offsets of σ = 2 and 12 mm. For the σ = 2 mm cases 3 wave swash is seen to more effective at maintaining a pressure distribution higher than the no swash case at the highest pressure, at the lowest pressure the distribution is more expected as the average gap for the swash cases is much larger (>100 μm) compared to the no swash case. On the other hand where σ = 12 mm., the additional pressure generated by the rotation merely compensates for the increased offset at low pressures, but this compensation is also maintained for the highest pressure case.

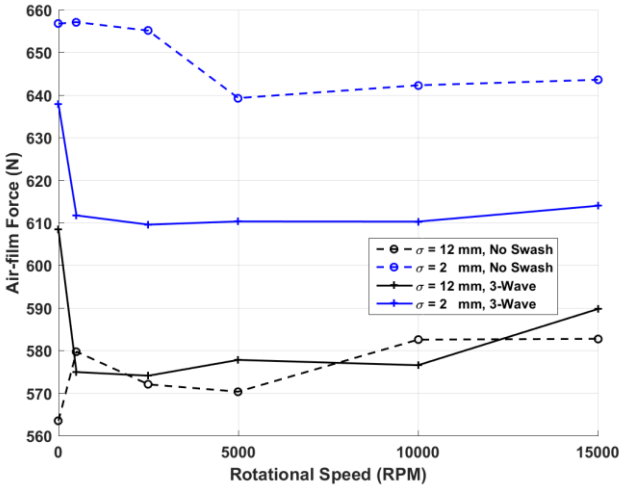

Figure 6-48: Effect of rotational speed and varying offset on air-film force, P_{in} = 0.69 barg

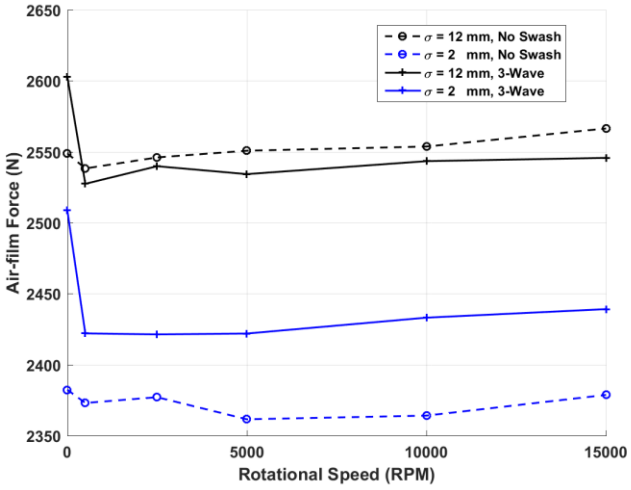

Figure 6-49: Effect of rotational speed and varying offset on air-film force, Pin = 2.76

6.2.8 Swash: Effect on Steady-state Balance Gap Height

This section illustrates the effect of swash on the measured balance gap height. Both swash configurations were included and compared to a no-added swash case at the same range of speeds and operating pressures. Figure 6-50 to Figure 6-53 show the change in balance gap height for the aforementioned cases with rotational speed at four inlet pressures. All cases shown here are for the smallest face, φ_3, at a predefined offset of σ = 12 mm.

Initial inspection reveals that for all cases, the introduced swash resulted in a drop in the *measured* balance gap height compared to the no-added swash case. All swash cases showed a characteristic drop in gap height as the disc was spun from rest to ω = 500 RPM at all inlet pressures. This drop was absent in the no-added swash cases, in fact a slight and fairly consistent increase in measured balance gap height was recorded at all inlet pressures apart from the highest one across the full speed range. It is assumed that this is mainly due to the increased hydrodynamic load resulting in larger opening forces.

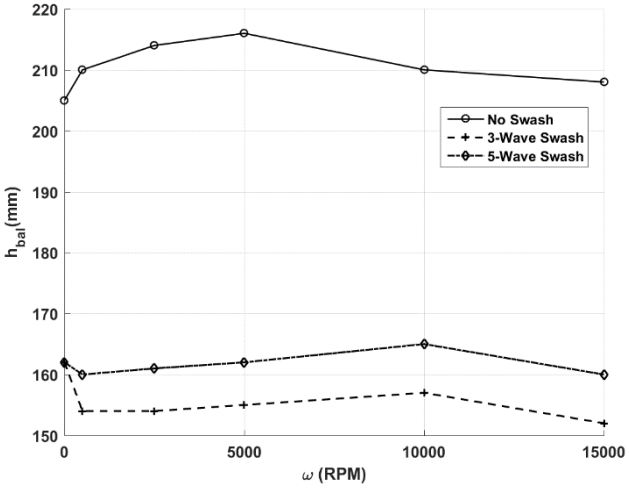

Figure 6-50: : Effect of rotational speed on measured h_{bal}, σ= 12 mm, P_{in} = 0.69 barg

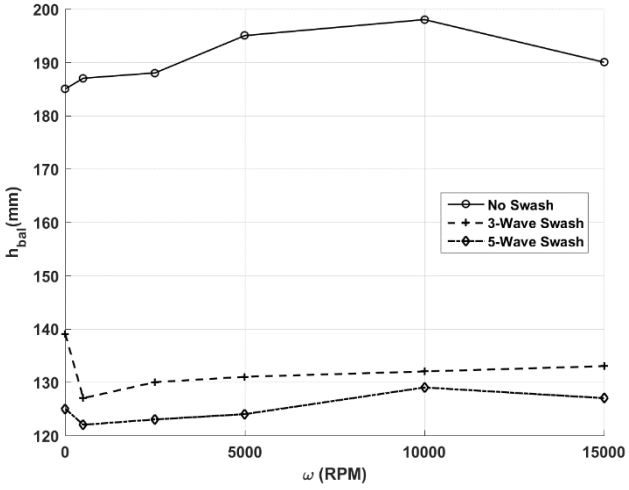

Figure 6-51: Effect of rotational speed on measured h_{bal}, σ= 12 mm, P_{in} = 1.03 barg

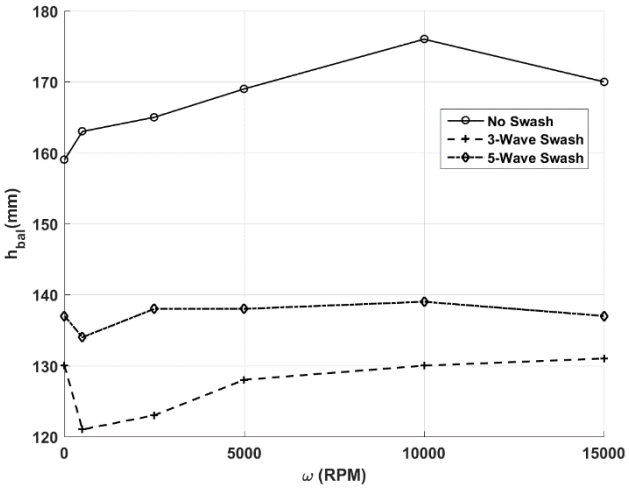

Figure 6-52: Effect of rotational speed on measured h_{bal}, σ = 12 mm, P_{in} = 2.07 barg

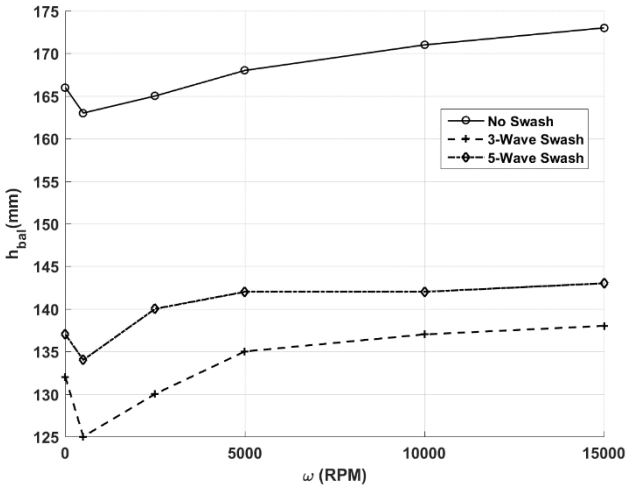

Figure 6-53: Effect of rotational speed on measured h_{bal}, σ = 12 mm, P_{in} = 2.76 barg

Figure 6-54 to Figure 6-56 show contour maps highlighting the achieved gap height for each of the swash cases tested with an offset of $\boldsymbol{\sigma}$ = 12 mm. For the no-swash case, Figure 6-54, the achieved balance gap height is closely coupled to increasing pressure and less so to rotational speed for inlet pressures < 1 barg. The initial increase in $\boldsymbol{h_{bal}}$ as the disc is spun from rest to 500 RPM is evident in all cases as well as the decrease in gap height with increasing inlet pressure. Interestingly, the region encompassing inlet pressures greater than 2 barg show the balance gap heights to be almost independent of rotational speeds within the range of 0-2500 RPM. Beyond this region, balance gap heights show a slight increase with speed. The region enveloping inlet pressures between 1.4 and 1.8 barg showed a larger area where $\boldsymbol{h_{bal}}$ was also less dependent on rotational speed.

Regarding the 3-wave swash, Figure 6-55, the contour map shows $\boldsymbol{h_{bal}}$ to be more dependent on operating pressure rather than speed for inlet pressures < 1 barg. At higher pressures, the achieved $\boldsymbol{h_{bal}}$ was found to be more a function of speed than increasing pressure and the rate of change of balance gap height with operating pressure dropped significantly. Three distinct regions showed more dependence on speed, one ranging from 500-2500 RPM and inlet

pressures between 1.4 and 2.76 barg, another is enclosed within pressures of 1 barg to 2.76 barg and speeds of 500-10000 RPM and finally the region covering speeds from 10 - 15 kRPM for the same pressure range. Across the aforementioned regions, increasing speed resulted in a decrease in h_{bal}. Similar to before, balance gap heights were smaller for higher pressures. Additionally, the resulting balance gap heights were smaller than those of the no-swash case.

The 5-wave swash contour map also showed little change in h_{bal} with speed for inlet pressures of less than 1 barg. Similar to the 3-wave swash cases, the rate of change of balance gap height with pressure decreased at higher inlet pressures. A smaller region showed a more significant dependence on speed for pressures ranging from 1 to 1.3 barg and speeds spanning from 0 to 5000 RPM. Such region did not exist in either of the former setups at such low pressures. The balance gap heights beyond the previously stated ranges continued to drop with increasing pressure while also showing a very slight increase with rotational speed in most cases.

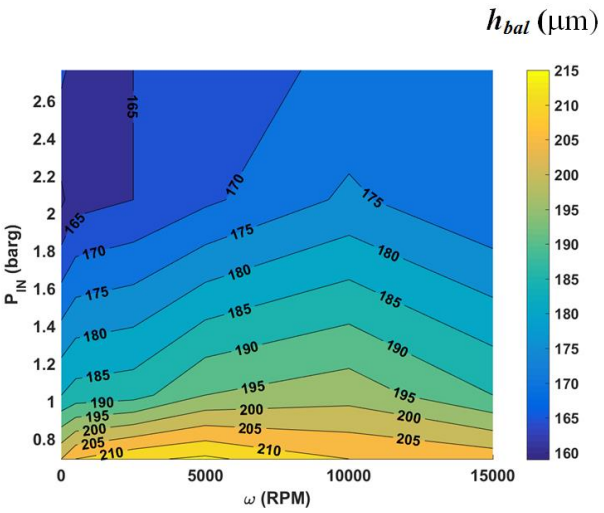

Figure 6-54: No-added swash, Contour map illustrating the change in measured h_{bal} rate at the full range of operating pressures and speeds.

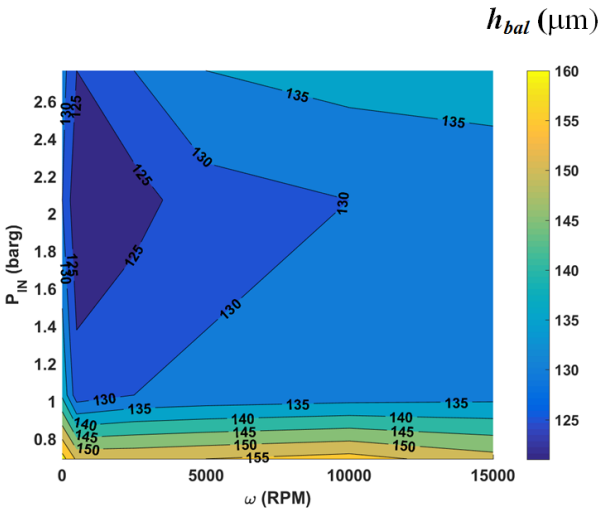

Figure 6-55: 3-wave swash, Contour map illustrating the change in measured h_{bal} rate at the full range of operating pressures and speeds.

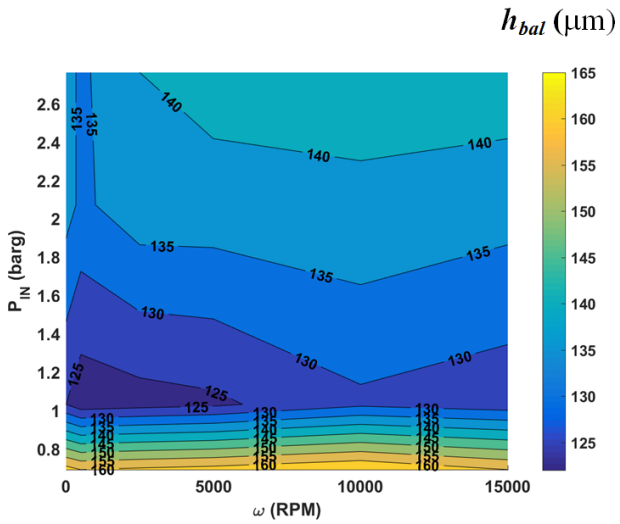

Figure 6-56: 5-wave swash, Contour map illustrating the change in measured h_{bal} rate at the full range of operating pressures and speed.

In the highest pressure low offset cases a new and undesirable phenomenon was observed. Here the diminution of the lift force on the front face with rotation caused touchdown of the seal face at speeds above 500 RPM. The lower offset of 2 mm is associated with a smaller spring force, however the pressure force on the upstream side of the seal will otherwise remain constant. The displacement was seen reduced from 111 μm to 109 μm between 0 and 500 RPM with touchdown during acceleration from this speed. Unfortunately the presence of this negative force at a low rotational speed, and very low offset makes the datum value for the seal under these conditions unreliable, and a sudden jump in balance gap from 109 μm to zero seems unlikely. As the force for all other conditions tested always forms an equilibrium with a non-zero gap, this artifice will not affect the other results presented. Thus, for the 2 mm offset the seal is not a viable solution if the level of swash is high, but the equilibrium limit can be adjusted by increasing the stiffness or the preloading of the springs in the seal holder. For a given axial range of required movement then, the spring constant should be chosen to allow the seal to start from a given maximum offset, and not to touch from the minimum offset. Knowledge of the axial position of the seal throughout the cycle may allow these parameters

to be relaxed, as the lowest film-face force in the presence of swash is found at very low rotational speeds.

In terms of face seal design, the aforementioned observation suggests that knowing the level of swash the seal would be expected to experience is of paramount importance as it will dictate the placement and arrangement of the secondary sealing element to ensure a restoring force can still be maintained thus avoiding touch-down. Additionally, it is crucially important to ensure that the stator (primary face) is able to track the rotor's axial movements, which requires the air-film to have sufficient stiffness to enable it to displace the primary face by itself in response to perturbations in film force. The secondary sealing arrangement also supports and guides the primary seal ring along its axial and radial movements.

As previously mentioned, the plots shown above were for a predefined offset of σ = 12 mm. Figure 6-57 to Figure 6-60 show the change in balance gap height with a change in offset (σ = 2 and 12 mm) at the range of rotational speeds and inlet pressures covered here. As mentioned in the previous section, no data were available for the 5-wave swash case at σ = 2 mm as rubbing contact between the sealing faces became an issue at inlet pressures of 2.07 barg and above. It has been demonstrated before that the most noticeable implication of reducing the pre-set offset was the significant drop in the achieved balance gap height which led to decreased leakage rates and increased film pressures. However, it also made the seal more susceptible to rubbing contact in swash cases as reported previously on the 5-wave swash case running with an offset of 2 mm. After the introduction of swash and rotation σ = 2 mm cases continued to maintain much smaller gap heights at all inlet pressures apart from P_{in} = 2.76 barg, Figure 6-60.

For both the no-swash and swash configurations the h_{bal} values maintained by the σ = 2 mm configurations were smaller than those attained by the largest offset for the two lowest

pressures, (P_{in} = 0.69 and 1.03 barg, Figure 6-57 and Figure 6-58). This, as previously discussed, is predominantly due to the rise in opening forces associated with larger offsets. Interestingly, however, this behaviour was reversed in the case of no-added swash at the two highest inlet pressures. At P_{in} = 2.07 barg, Figure 6-59, a jump in h_{bal} values as the disc was spun from ω = 5 kRPM to ω = 10 kRPM brought the h_{bal} values of the σ = 2 mm cases much closer to those of the largest offset. This behaviour subsisted at the highest inlet pressures where at speeds ω > 500 RPM the h_{bal} values maintained by the σ = 2 mm cases were consistently larger than those of the largest offset. The measured balance gap heights for the 3-wave swash cases showed the h_{bal} values achieved by the σ = 2 mm cases to remain below those of the larger offset throughout the operational envelope. Furthermore, the effect of increased hydrodynamic load resulting in larger balance gap heights remained evident in the σ = 2 mm cases, with and without swash.

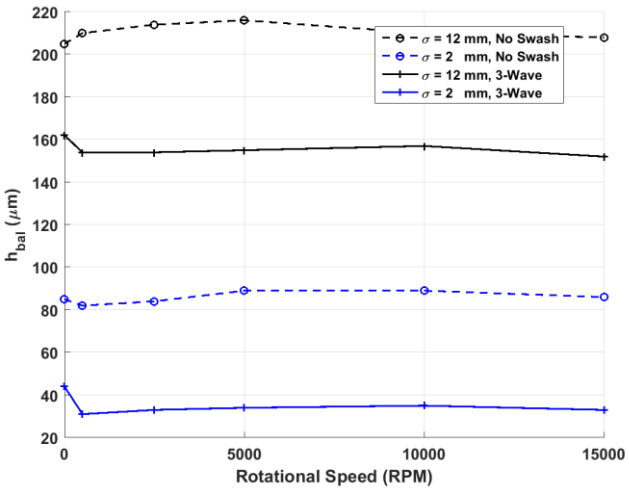

Figure 6-57: Effect of rotational speed and varying offset on measured h_{bal}, P_{in} = 0.69 barg

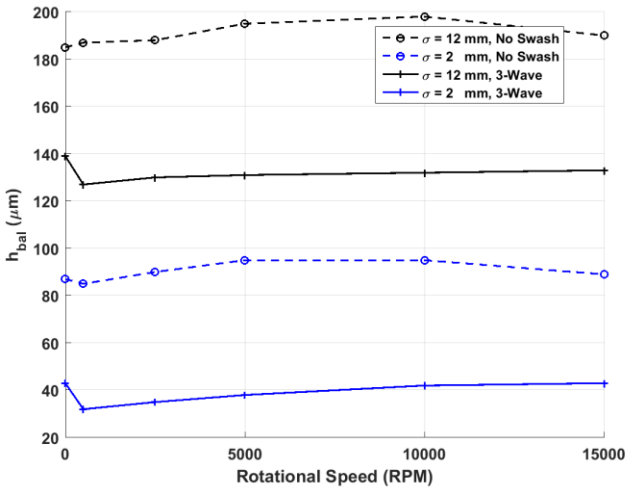

Figure 6-58: Effect of rotational speed and varying offset on measured h_{bal}, P_{in} = 1.03 barg

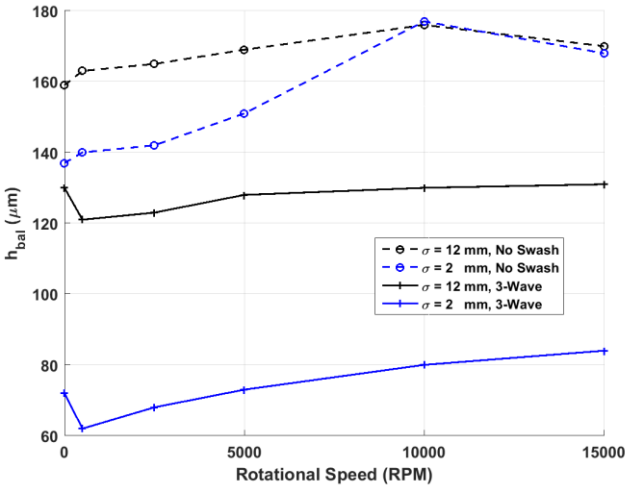

Figure 6-59: Effect of rotational speed and varying offset on measured h_{bal}, P_{in} = 2.07 barg

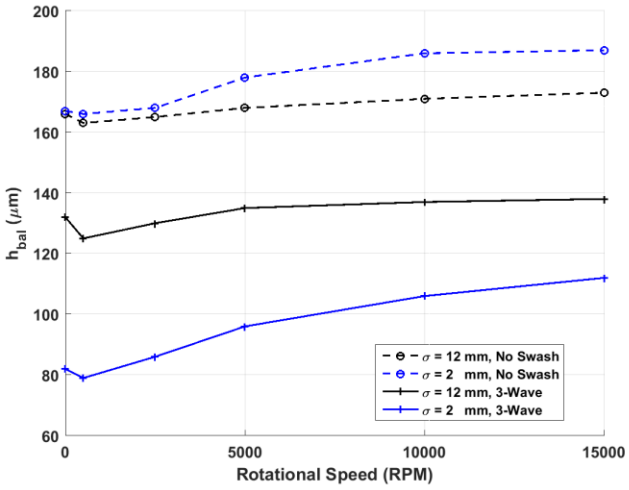

Figure 6-60: Effect of rotational speed and varying offset on measured h_{bal}, P_{in} = 2.76 barg

6.2.9 Swash: Effect on leakage rate

Figure 6-61 to Figure 6-64 illustrate the effect of swash on leakage rate at a range of rotational speeds and inlet pressures. Across the data presented, a consistent decrease in leakage rate with speed was evident, apart from regions of low pressures (0.69 barg to 1.03 barg) and low speeds (0 – 500 RPM). It should be noted that the drop in leakage is subtle – the axis are all non-zero but consistently apparent. The no-swash cases exhibited the lowest leakage rates compared to both swash configurations. This is expected as the mean gap height for the swash cases is larger. It has been previously shown that the measured balance gap heights showed a tendency, albeit subtle, to increase with speed. This implies that a slight increase in leakage rate should be expected. This, however, has not been the case which suggests that there is another driving factor affecting the leakage rate through the system in addition to the minimum clearance. Additionally, given that the aforementioned trend applied to both the no-added swash and the swash cases it is most likely to be induced by the rotation of the disc, a change in the approach angle to the gap, and possibly the downstream pressure because of pumping in the downstream cavities not associated with the seal

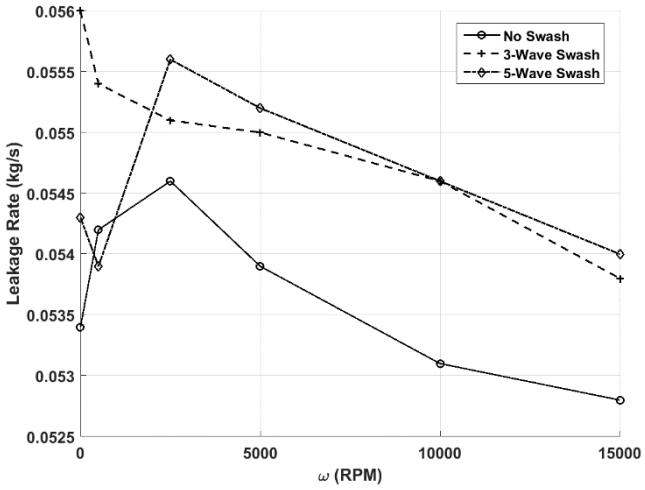

Figure 6-61: Effect of rotational speed and varying offset on leakage rate with and without added swash, σ = 12 mm, P_{in} = 0.69 barg

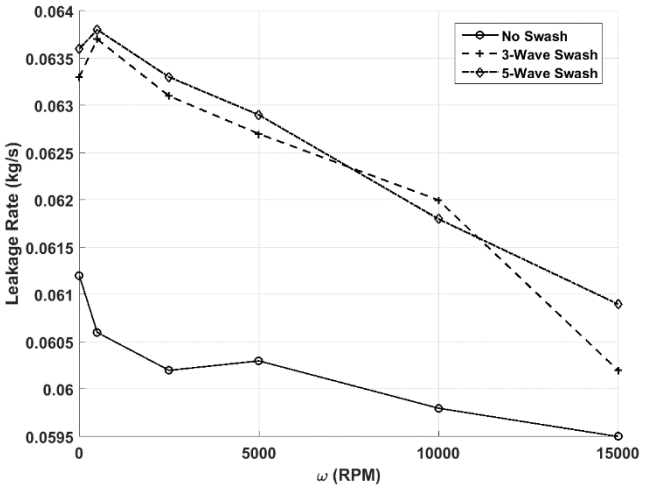

Figure 6-62: Effect of rotational speed and varying offset on leakage rate with and without added swash, σ = 12 mm, P_{in} = 1.03 barg

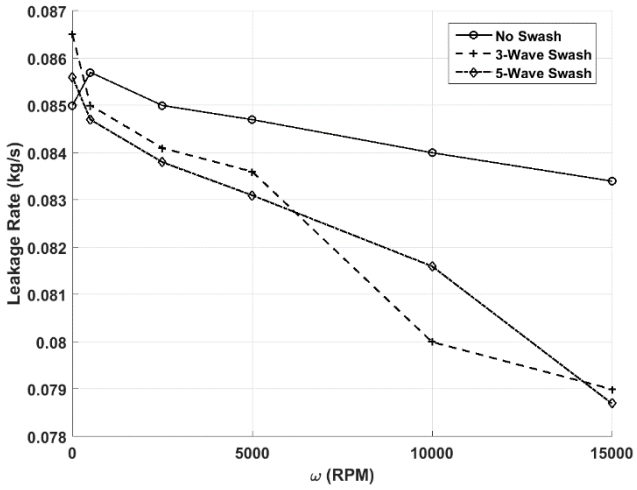

Figure 6-63: Effect of rotational speed and varying offset on leakage rate with and without added swash, σ = 12 mm, P_{in} = 2.07 barg

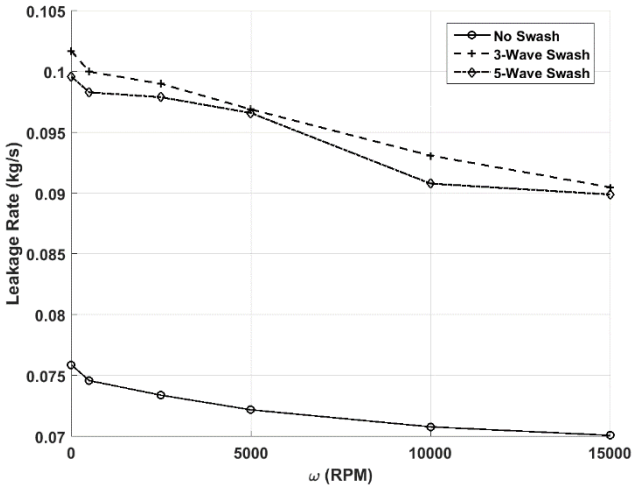

Figure 6-64: Effect of rotational speed and varying offset on leakage rate with and without added swash, σ = 12 mm, P_{in} = 2.76 barg

The leakage, re-expressed as effective clearance (*ec*), was computed for the no-added swash and the 3-wave swash cases at both predefined offsets ($\boldsymbol{\sigma}$ = 2 mm and 12 mm) and the full the range of inlet pressures considered. The data are shown in the scatter plots in Figure 6-65 and Figure 6-66 for the no-added swash and 3-wave swash cases, respectively. Each row of scatter data at each pressure point represents either the balance gap height ($\boldsymbol{h_{bal}}$) or the effective clearce

(*ec*) *vs*. rotational speed. Black markers are used to denote the σ = 12 mm cases while blue markers represent the σ = 2 mm cases.

The data show that starting the seal from a smaller offset location is particularly beneficial at low operating pressures where low values of h_{bal} and *ec* are seen. Unsurprisingly this advantage all but disappears as the operating pressure increases which can be seen in the convergence of the scatter data points for both offsets of both type at higher pressures. In terms of seal operability this could have a significant implication as it suggests that although starting the seal at a large offset might initially cause an increase in leakage, this increase will taper off with increasing pressure. As previously reported in this study, when the seal was run against the 5-wave swash rotor at the smallest offset (σ = 2 mm), the seal touched-down and failed to lift-off at inlet pressures of 2.07 barg and higher. On the other hand, for the same configuration run with the largest offset (σ = 12 mm), the seal successfully lifted-off and maintained a non-contacting mode of operation for the entire operational envelope. Hence, starting the seal at larger offsets can potentially help extend the seal's ability to withstand swash distortions without having to concede an excessive amount of leakage, if run at sufficiently high differential pressures.

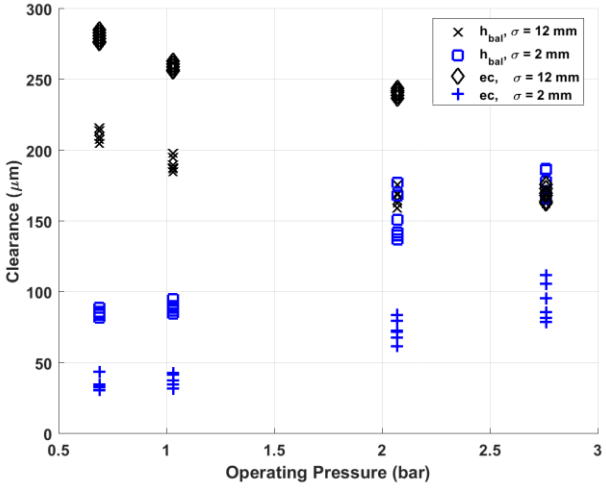

Figure 6-65: No-added swash, change in balance gap heights and effective clearances at the full range of inlet pressurs.

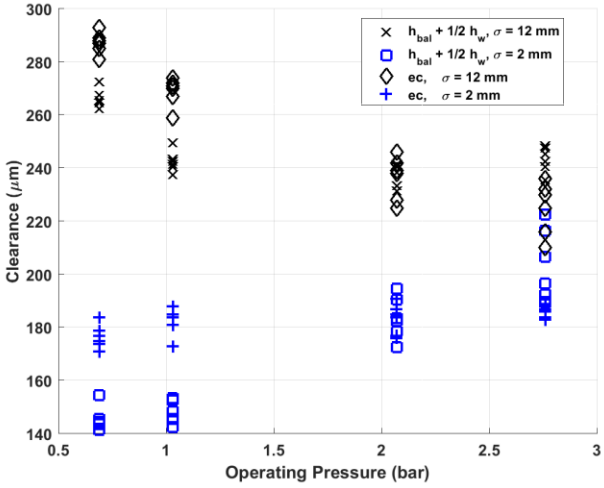

Figure 6-66: 3-wave swash, change in balance gap heights and effective clearances at the full range of inlet pressures.

6.3 3D CFD Model for Prototype Seal

A 3D CFD model was created based on the leakage paths for the prototype seal. The model was setup to assess the capability of 3D CFD in predicting the seal's primary gap pressure field and leakage characteristics. A schematic outlining the main features of both the solid (in grey) and fluid (in red) domains is shown in Figure 6-67. The housing and the adaptor carrying the front interface along with the rotor constitute the solid walls of the fluid domain. The PTFE secondary seal was designed to give a clearance of 100 μm which was also maintained in the CFD model. The schematic shown in Figure 6-67 is for the largest face tested, ϕ_1, however the model was also extended to include the smallest face tested, ϕ_3. The first set of results compare radial pressure distributions and leakage rates predicted by the CFD model against experimental data for ϕ_1 and ϕ_3 at stationary conditions. Secondly, a model was formulated to investigate the effect of the rotation-induced leakage drop with speed discussed in the previous section. The predicted leakage rates were compared with those obtained experimentally and velocity contour maps were presented to highlight driving force behind this phenomenon.

6.3.1 Models Parameters and Boundary Conditions

Similar to the CFD used in *chapter 3*, rotational periodicity was applied and a 30-degree sector of the fluid domain was modelled, representing one-twelfth of the total annulus. As mentioned previously, the front face was attached to a set of 12 tensile springs (located in the sealed pressure cavity) and was free to displace axially in response to loads from the sealed pressure and the air-film. This meant that a new mesh was required for each run to account for the changing balance gap height depending on the operating conditions. Note that, swash is not modelled in this setup and where rotational cases are presented, the rotor walls were set as rotating walls about the global *x*-axis (axial) direction. Structured meshes were created using *Pointwise 17.3*. The total number of cells was 3 million and a mesh independent solution was obtained with 32 nodes across the minimum gap height.

ANSYS CFX was used as the solver for this analysis. The inlets and outlet to the domain were defined as pressure 'Opening' in *CFX* to allow for reverse flow. The values used for upstream and downstream pressures were those obtained experimentally for each respective case. Unlike the previous CFD model, the two-equation *Shear Stress Transport* turbulence model (SST *k*-ω (Menter, 1993, 1994)) was used instead of realizable *k*-ε as this was found to aid in convergence. The aforementioned turbulence model uses the *k*-ω formulation to resolve the boundary layer all the way to the domain wall, as opposed to using wall functions in the *k*-ε models, and switches to the *k*-ε formulation in the free stream. Material properties and convergence criteria remain the same as those outlined in sections *3.3.3* and *3.3.5*, respectively. The advection scheme selected for this model was the '*High resolution*' scheme in *ANSYS CFX*. This scheme attempts to maintain as high an order of scheme as possible while keeping the solution bounded (ANSYS CFX 18 Theory Guide, 2017).

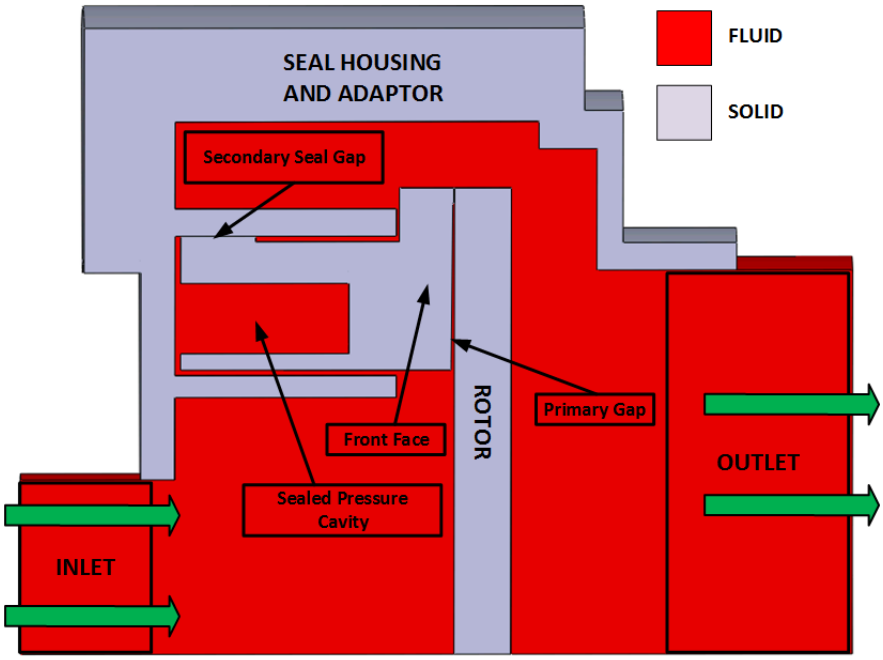

Figure 6-67: Schematic of the solid and fluid domains for the prototype seal.

6.3.2 CFD Model Results: Radial pressure distributions and leakage rates

Figure 6-68 shows the radial pressure distributions predicted by the CFD against those obtained experimentally for the largest face, ϕ_1, at inlet pressures ranging from 0.69 barg to 2.76 barg. Similarly, Figure 6-69 reports the same comparison for the smallest face tested, ϕ_3. Note that experimental pressure distributions only extend to r = 74 mm which is upstream of the radial step for both faces considered. Film pressures predicted by the CFD shown here cover the entire radial length of the seal.

In general, the CFD model predictions compared very well with experimental data. The inclusion of the radial step resulted in most of the film pressure being maintained till the step location. The sudden decrease in gap height at the step location resulted in a significant inertial loss after which the film pressure showed some recovery followed by a viscous drop till the gap exit. Figure 6-70 shows the force on the portion of the seal downstream of the step as a *percentage* of the total air-film force F_{AF} at the range of inlet pressures considered here. A

maximum of 3.4% was contributed by the portion of the seal downstream of the step to F_{AF} for ϕ_1 at the highest inlet pressure, whereas a maximum contribution of 5% was obtained in the case of ϕ_3. This demonstrates the effectiveness in terms of hydrostatic augmentation resulting from imposing a converging angle and a radial step at a far downstream location on the front interface.

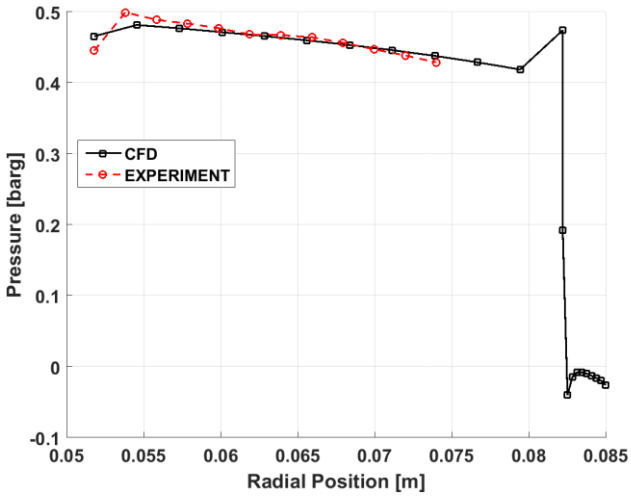

(a) P_{in}=0.69 barg.

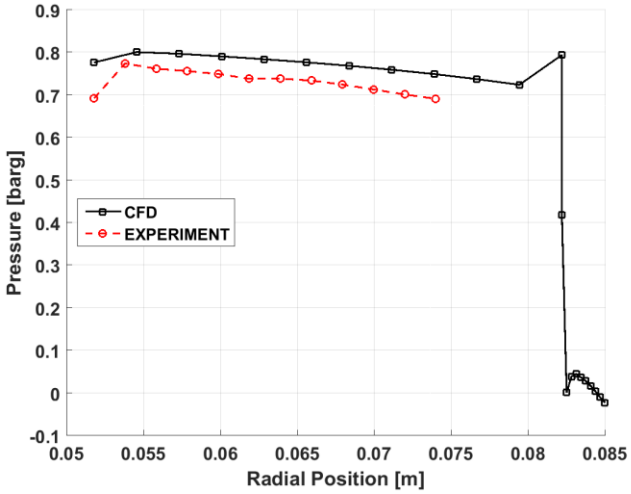

(b) P_{in}=1.03 barg

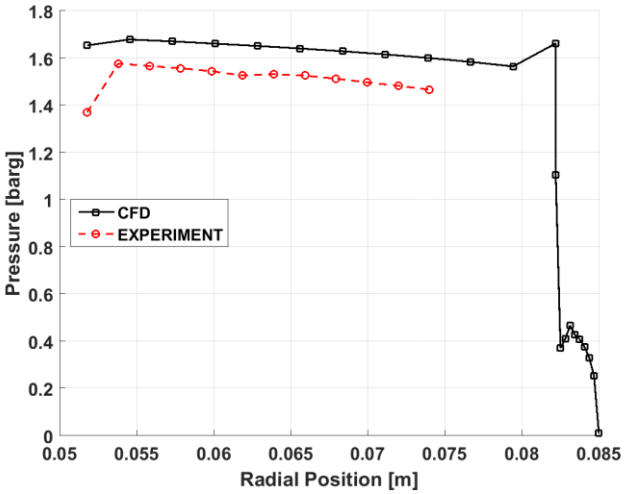

(c) Pin=2.07 barg

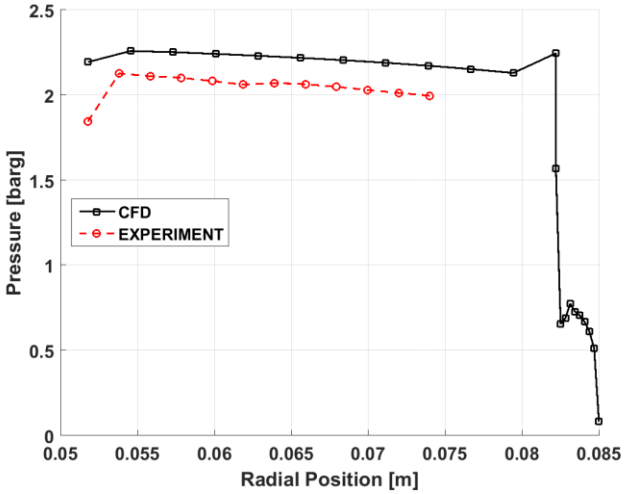

(d) Pin=2.76 barg

Figure 6-68: Radial Pressure Distribution, CFD vs Experiment, φ_1, σ = 12 mm,

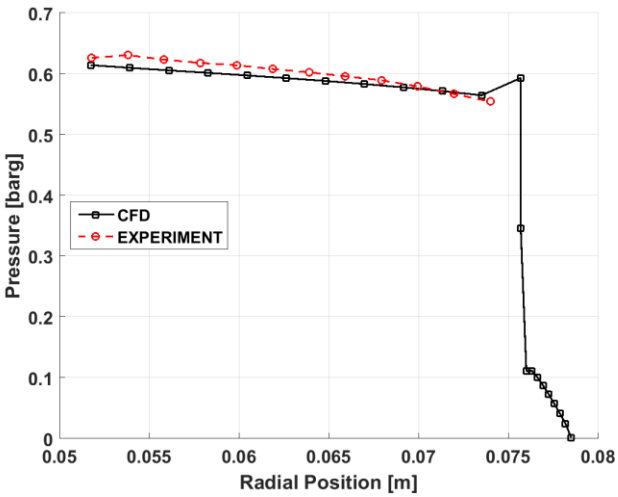

(c) P_{in}=0.69 barg.

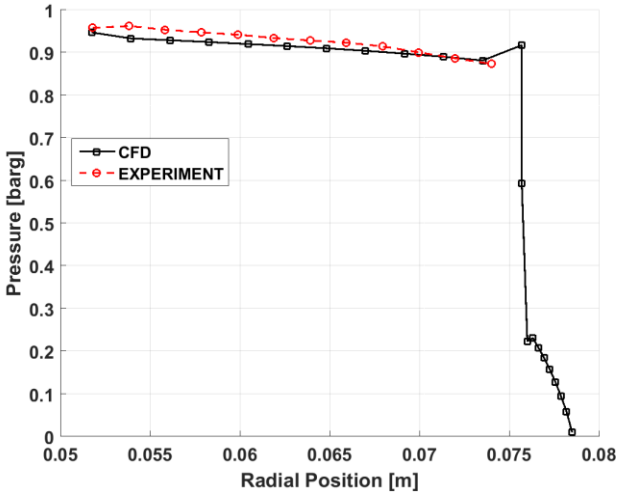

(d) P_{in}=1.03 barg

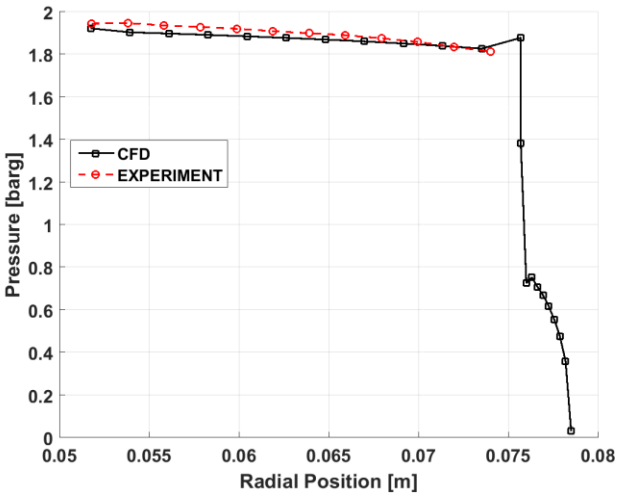

(c) Pin=2.07 barg

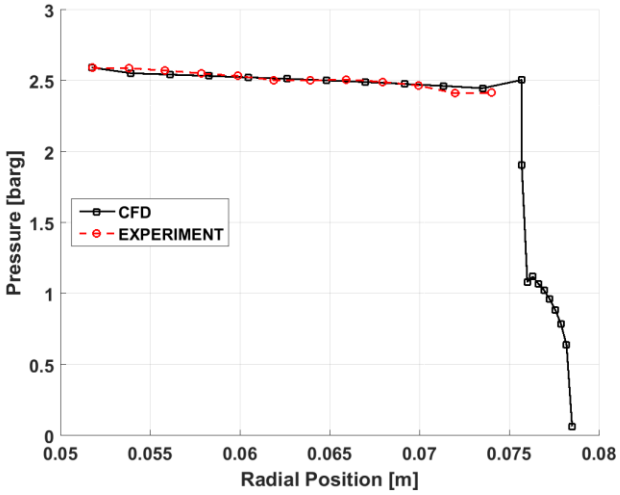

(e) Pin=2.76 barg

Figure 6-69: Radial Pressure Distribution, CFD vs Experiment, φ_3, σ = 12 mm,

The radial film pressures predicted by the CFD model for the largest face ϕ_1 compared well to experiments at the lowest inlet pressure, Figure 6-68 (a), resulting a maximum relative error of 10% at the last radial location covered by the pressure tappings. This value increased to almost 20% at the highest inlet pressure, Figure 6-68 (d). Once more, the direct increase in error with operating pressure indicates that the coning of the disc under film load might significantly alter the gap profile. This trend disappeared in the case of the smallest face ϕ_3 where both data sets

showed excellent agreement giving a maximum relative error of 7% at both the lowest and highest inlet pressures, Figure 6-69. From a structural point of view, the radial extent of the smallest face ϕ_3 covers a smaller portion of the disc. Hence, the air-film force acts on a reduced area that is closer to the disc's fixed support resulting in a lessened level of disc bending in the experimental case.

The leakage rates predicted by the CFD model for both faces are compared to the experimental values and shown in Figure 6-71 and Figure 6-72. The model showed better agreement compared to experiments for ϕ_3 cases with a maximum relative error of 6%, as opposed to 17% for the largest face, ϕ_1. The excellent agreement between the CFD model predictions, particularly for ϕ_3, gives confidence in the experimental method described in this thesis.

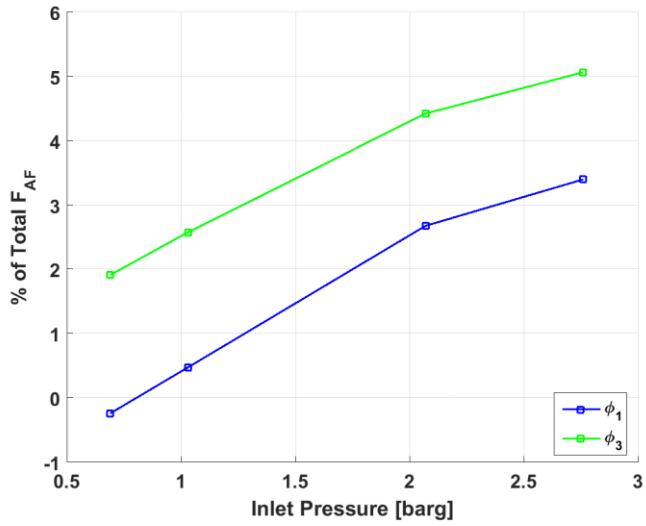

Figure 6-70: Total contribution to air-film force by the portion of the seal length downstream of the radial step, σ = 12 mm.

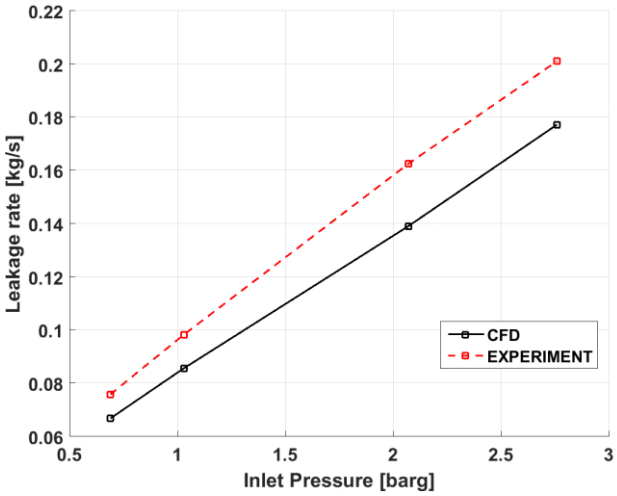

Figure 6-71: Leakage rate, CFD vs Experiment,φ_1, σ = 12 mm.

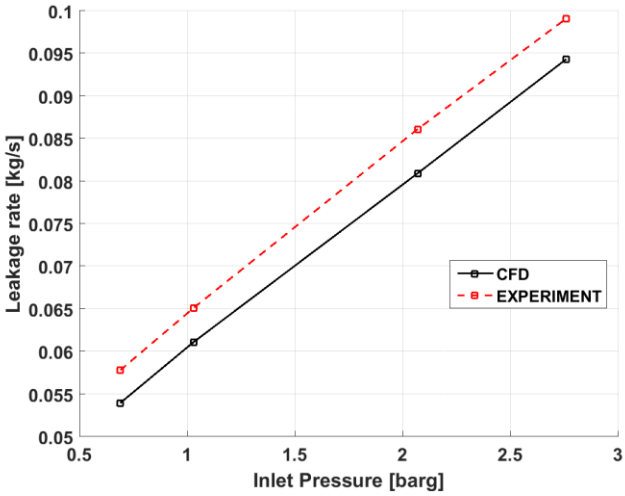

Figure 6-72: Leakage rate, CFD vs Experiment,φ_3, σ = 12 mm.

6.3.3 CFD Model Results: Rotation-induced Drop in Leakage Rate

It was previously demonstrated in section *6.2.5* that there was a consistent, albeit not significant, drop in leakage rate with increasing rotational speed. This phenomenon was observed experimentally, however the driving mechanism behind it was not clear. The CFD model described above was applied to investigate the effect of rotating the disc on the leakage rate. The model was setup based on the operating conditions for the no-added swash cases with and without rotation. An updated mesh was constructed to account for changes in steady state balance gap height due to varying operating pressures and speeds.

Figure 6-73 compares the leakage rates predicted by the CFD model against those obtained experimentally at the full range of operational speeds and operating pressures up to 2.07 barg. The CFD model predictions showed excellent agreement with experimental data in terms of both the trends observed and the magnitudes of leakage rates predicted. The maximum relative error at the lowest (0.69 barg) and highest inlet pressure (2.07 barg) cases was calculated to be 10% and 6%, respectively. As encountered before, leakage rates predicted by the CFD model

were lower than experiment. The CFD model was able to accurately capture the trend of the consistent drop in leakage rate with increasing rotational, particularly for speeds of 5 kRPM and higher.

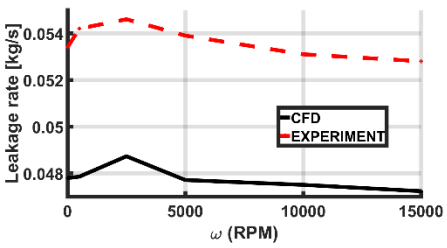

(a) Pin = 0.69 barg

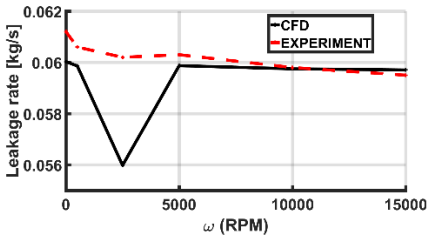

(b) Pin = 1.03 barg. The value at ω = 2500 RPM appears to be an outlier.

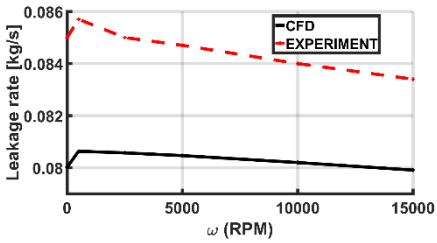

(c) Pin = 2.07 barg.

Figure 6-73: Effect of rotational speed on leakage rate, CFD vs EXP, φ3, σ = 12 mm

Contour maps in Figure 6-74 show velocity fields of the flow through the seal for the full range of operating speeds at an inlet pressure of 0.69 barg. Each contour map contains information for a given rotational speed. Velocity vectors indicating the direction of the flow are also plotted for each case. At stationary conditions, Figure 6-74 (a), the flow enters the domain where a portion of the bulk flow fills in the sealed pressure cavity and another flows through the primary sealing gap. The pressure drops within the sealing gap and the velocity increases, which is marked by the very high-speed jet of air exiting the primary gap. The flow then recovers some pressure and slows down as it goes through the downstream gap. Some of the air continues flowing along the rotor walls where the flow can be seen exiting the domain along the bottom edge of domain outlet. Two higher pressure zones showing the flow speed to be very low existed in regions above and below the higher speed jet exiting the domain. As the speed was increased to 500 RPM, the higher pressure region below the exiting jet exhibited a subtle amount of reverse flow.

Moreover, the cavity enclosed by the upstream housing showed an elevated level of recirculation compared to the stationary case. In the region above the downstream exiting jet,

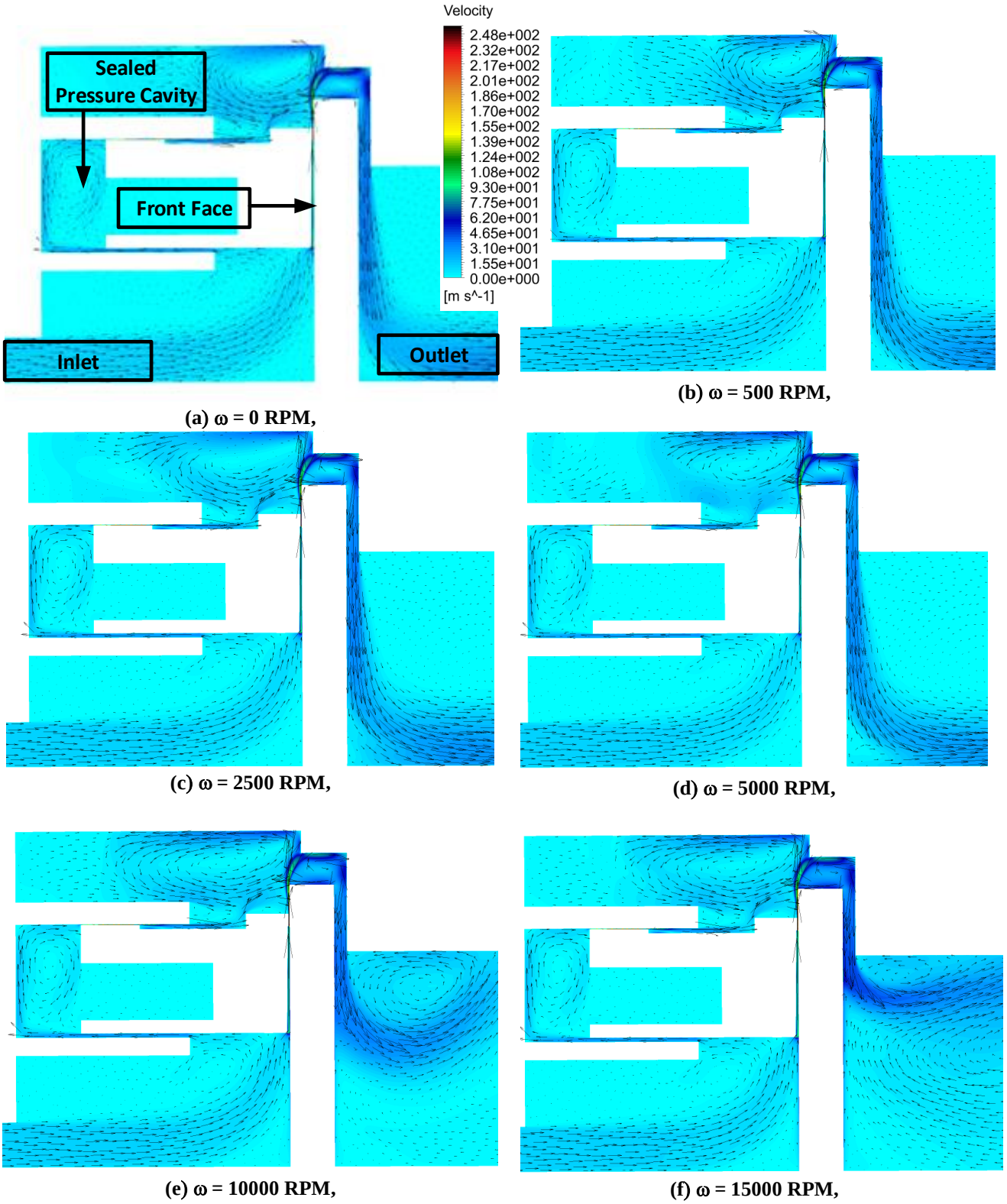

(a) ω = 0 RPM, (b) ω = 500 RPM,

(c) ω = 2500 RPM, (d) ω = 5000 RPM,

(e) ω = 10000 RPM, (f) ω = 15000 RPM,

Figure 6-74: Velocity contour and velocity vectors highlighting the effect of rotation on the flow field, ϕ3, σ = 12 mm, PIN = 0.69 barg.

the velocity vectors indicate reverse flow, albeit initially less significant at lower speeds. Furthermore, the velocity vectors show the air in the higher pressure region at the far end of

the housing cavity being pulled towards the lower pressure recirculation zone. Driving the disc at higher speeds increased the flow velocity and the levels of recirculation in the aforementioned zones. This persisted till a speed of ω = 10 kRPM was reached where the exiting jet downstream of the disc met the reverse flow in the higher pressure zone where the pressure was high enough to separate the jet from the surface. The jet then 'rolls up' and a recirculation zone is formed in the region above. Increasing the speed further resulted in straightening of the exiting jet and encountering higher levels of reverse flow at ω = 15 kRPM. Although the size and strength of the recirculation zone at the exit would be expected to interfere with the exit jet, the aforementioned behaviour persisted at higher inlet pressures and the exiting-jet 'roll up' constantly occurred at ω = 10 kRPM. The flowfield clearly shows that there is a flow pumping effect from the disc rotation, and this is very evident on the low pressure side of the disc.

The increased levels of reverse flow resulting from rotating the disc appeared to be a possible means of blocking the flow exiting the system and a contributing factor to the mechanism driving the consistent drop in leakage rate with speed. However, the effective clearance (*ec*), calculated based on CFD predictions of leakage mass flow rate for an upstream pressure of 0.69 barg and at an average radius of r = 77. 1 mm, suggests otherwise. Three different curves are plotted in Figure 6-75 each show *ec* computed for three different outlet pressures. First, *ec* was computed for the whole seal leakage path based on the mass flow rate predicted by the CFD model followed by the upstream primary gap exit pressure taken at the axial midpoint between the two sealing faces.

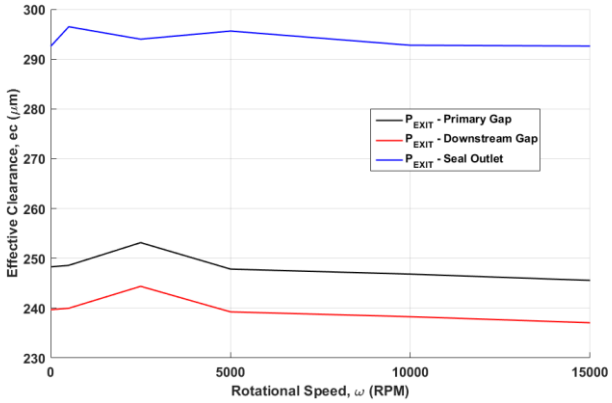

Figure 6-75: Change in effective clearance, calculated for three different exit pressures, with rotational speed, φ_3, σ= 12 mm P_{in} = 0.69 barg.

Finally, the downstream gap exit pressure taken at the axial midpoint between the rotor downstream face and the downstream housing wall was used to calculate *ec* at the full range of speeds. The result demonstrates that the primary gap is the dominant gap in the system and hence it would be unlikely for the rotation-induced recirculation zones in the downstream region to be the primary cause of leakage drop with speed. This prompted a closer look at effect of rotation on the pressure field of the system as a whole. Figure 6-76 shows a contour plot of the pressure difference between the stationary case and the highest speed case, ω = 15 kRPM - ω = 0 kRPM. The contour map range was limited to -500 Pa to 500 Pa to better visualize rotation-induced effects on the pressure field that are likely to be of a similar magnitude. It is immediately evident that there is a slight increase in pressure with rotation on the system, excluding the previously mentioned low pressure zones in the downstream region. Regions of increased pressure can be seen acting on the axially-flexible front face both on the air-film side and the sealed pressure side, associated with the closing forces. This implies that the seal should tend to open up in response to the increased film pressure while also facing an augmented, but smaller restoring force due to increased pressure in the sealed cavity. But the dominant effect can be seen near the exit of the primary sealing face where a large increase in pressure is seen. Increasing the pressure difference across the inlet and outlet of the gap by a

similar amount would tend to decrease, slightly the pressure ratio across the gap, and this would tend to reduce the isentropic ideal velocity across the gap. This is balanced by a small increase in the density of the flow in the gap but overall, it appears that this must be the root cause of the decrease in mass flow in this region. The CFD model was run for the full range of pressures (up to 2.76 barg) at the largest offset σ = 12 mm with this behaviour being consistently present.

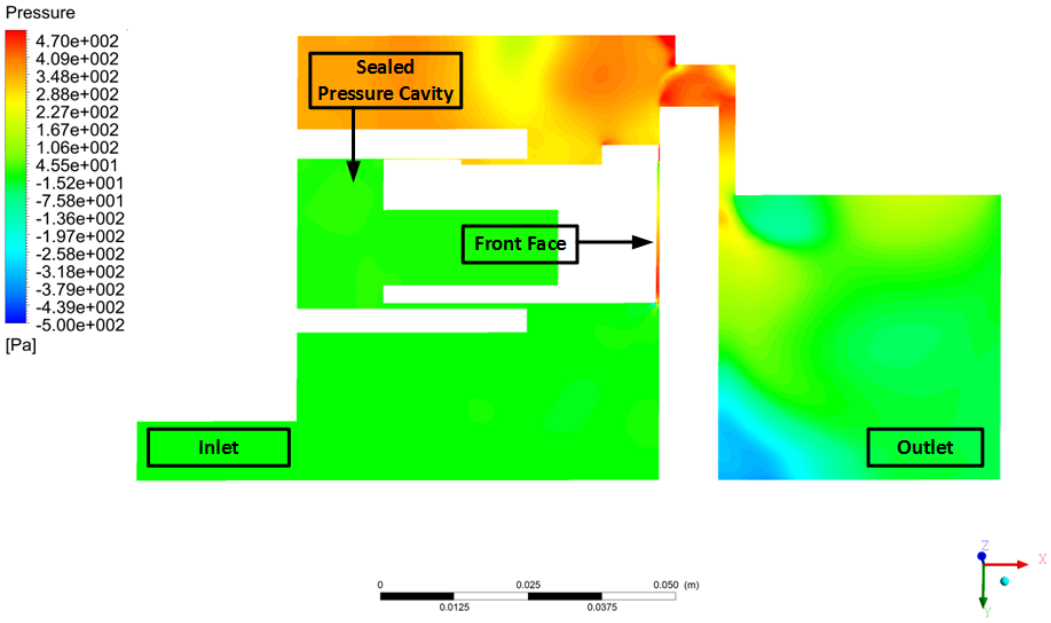

Figure 6-76: Pressure difference contour between ω = 0 RPM and ω = 15 kRPM cases, φ_3, σ = 12 mm P_{in} = 0.69 barg.

As it is not possible to perfectly match experimental conditions: this is not a fluid structure interaction numerical CFD model, it is not possible to fully test this and to accurately predict and compare the level of balancing between both forces. It is, however, appreciated that this very subtle, albeit consistent, pressure increase will cause very subtle changes in the actual minimum clearance that could be difficult to pick up with sufficient experimental certainty using the equipment used in the tests conducted for this thesis. The closing and air-film forces acting on the flexible face as predicted by the CFD are plotted against speed and are shown in

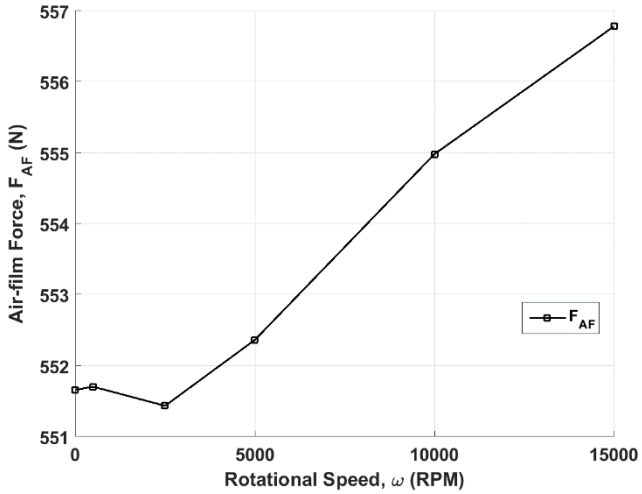

Figure 6-77: CFD, effect of rotational speed on air-film force, φ_3, σ = 12 mm, P_{in} = 0.69 barg.

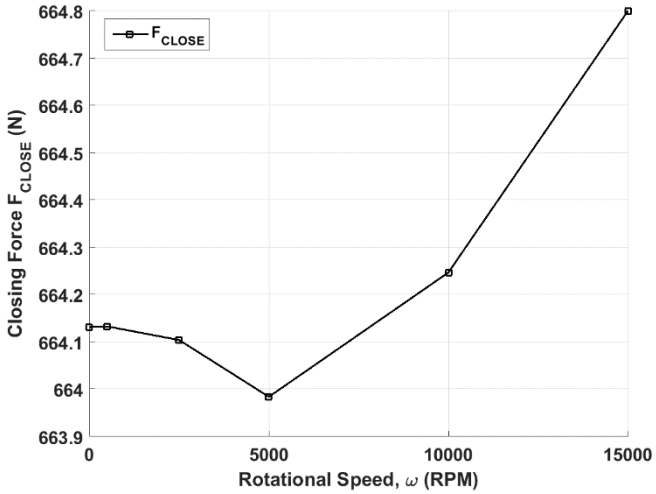

Figure 6-78: CFD, effect of rotational speed on closing force, φ_3, σ = 12 mm, P_{in} = 0.69 barg.

Figure 6-77 and Figure 6-78 respectively. The closing force is seen to increase only by 0.4 N with rotation from 0 – 15 kRPM, while the opening force increases by 5 N. The offset in values merely in the graphs merely suggests that the system is not fully balanced, but the change in offset suggests that the gap is likely to open slightly with increasing rotational speed. This points to the changing pressure boundary conditions being the principal causes of the change in the flow regime.

Overall the CFD study has shown that it is possible to capture the performance of the seal accurately with RANS steady CFD. Results from previous chapters show that inclusion of FSI features would be likely to improve the fidelity of the CFD further, but at a cost of solution time. Assuming a constant gap through the seal, allowed subtle changes in leakage flow to be detected for a given upstream pressure, suggesting that a surrogate CFD model populated only at static conditions could be used to specify the operating gap of the seal in simulations designed to capture dynamic behaviour in transient running.

6.4 Chapter Summary

This chapter outlined the design of a prototype seal and reported on a set of tests the seal underwent. The first set of tests considered the effect of changing the balance ratio, achieved by altering the outer radius of primary seal face, on the sealing performance in terms of the pressure distribution in the primary gap, load capacity and leakage rate. All three faces tested had a radial step at 90% of the radial extent and a converging angle, features that the previous investigation into air-film behaviour on the solid seal has shown to augment the opening force. The largest of the faces, φ_1, resulted in the largest balance gap heights, leakage rates and opening forces. While the smallest face, φ_3, resulted in the smallest balance gap heights and consequently the lowest leakage rates. Although the opening force saw a drop, the seal successfully maintained non-contacting operation throughout all test conditions. Moreover, the average seal axial stiffness showed a considerable increase with operating pressure as balance gap heights were shown to less sensitive to a change in offset. Overall, face φ_3 provided the best sealing performance. Having decided on the face providing the best sealing capabilities, the seal underwent a set of tests to investigate the effect of swash on the seal's performance. The key findings were that swash can improve the hydrodynamic load capacity of the seal given that the number of waves is limited. Increasing the number of waves further caused a depreciation in film force and resulted in touch-down at small offsets. Furthermore, for both the no-added swash and swash cases increasing the offset did result in larger balance gap heights and higher leakage rates, at low pressures (< 1.03 barg). However, this trend diminished at higher inlet pressures as balance gap heights and effective clearances for both offsets converged. The 3D CFD model showed excellent agreement with experiments for this type of seal and was used to investigate the rotation-induced drop in leakage rate with rotational speed. The improvement of 3D CFD predictions in this chapter over what was achieved in

chapter 5 is thought to be largely due to the flow physics in the primary being dominated by the presence of the radial step, previous CFD modelling done by Aubry on a stepped self-centring seal (2011) was found to be in agreement with the above statement.

In terms of the operational aims of this seal, summarised at the start of chapter, it can be said that the seal was able to successfully cover most of the operational envelope under which it was tested without touching down while providing the large axial movement required and acceptable levels of leakage. This was even achieved with the seal withstanding exaggerated swash profiles. Furthermore, the dimensional analysis presented in *chapter 4* shows that the seal's operational characteristics in terms of pressure differentials, gap height, level of coning and surface speeds are appropriately matched to engine conditions. However, further testing is required at higher temperatures to assess its effect on the seal's performance. Moreover, testing using near-sinusoidal swash profiles as opposed to the harsher square-wave representation used here with varying amplitudes and period lengths would be required to further comment on the seal's resilience against swash distortions.

7 Conclusions and Further Work

The primary motivation behind the work presented in this thesis was to develop an understanding of the operational characteristics of an air-riding face seal for aero-engine applications. This type of seal is expected to run at larger clearances than conventional contacting and non-contacting face seals. The work was two-fold in its approach: both numerical and experimental data were produced and assessed.

In *chapter 3*, the validity of applying the 2D Reynolds equation commonly used for the design of conventional face seals, in its compressible form, to model the problem was examined and assessed against of a set of experimental data and a newly developed surrogate 3D CFD model.

- The 2D Reynolds flow model was unsuitable for this purpose: it failed to capture the significant inertial effects at entry and step locations through the seal. The code performed well mainly for small gaps (<50 μm) where pressure entry losses and losses due to geometric discontinuities where insignificant. Inclusion of inertial terms and turbulence modelling need to be included for more accurate predictions.

Validation of the 3D CFD model was extended in *chapter 3* to include convergent and divergent gaps, with and without the addition of radial steps. Equivalent experiments were conducted to validate the results *chapter 4 & 5*. An inertia driven entry loss, increasing with increasing gap heights was observed in both experiments and modelling.

- A carefully executed 3D CFD model provides good agreement to experimental data capturing initial entry losses and pressure distributions well in a face seal with moderately large clearances, and is suitable for use in seal design.

- Pressure distributions are extremely sensitive to small angular changes in the primary seal face and coupled fluid and mechanical modelling of the sealing system vastly improves the quality of numerically modelled data where the displacements of components are not known *a priori*. This result is significant for large diameter face seals operating under large pressure differences as without accounting for structural deformation representative modelling of the seal pressure field is unlikely.
- The CFD model showed that
    - convergent coned gaps increase the film pressure for a given minimum gap height, at the expense of increased leakage,
    - divergent gaps exhibit a complex compressible flow behaviour involving acceleration and pressure recovery through a series of weak shockwaves which was shown to diminish the opening force. Again leakage is increased by coning.
    - Unexpected pressure recovery in divergent gaps allows some load capacity to be retained at low levels of divergent coning
    - An axial step on the seal face at 90% of the radial location augmented the levels of hydrostatic pressures generated in the gaps compared to a plain case for across all gap configurations, and made the divergent gap pressure distributions much more robust. It should be noted, however, that even with the axial step augmenting the opening force in diverging gaps the film pressure would be insufficient to maintain a non-contacting mode of operation, particularly at high pressure differentials.

Having gained an understanding of air-film behaviour in moderate gap heights (both experimentally and numerically), a proto-type large axial movement face seal was designed and tested in *chapter 6*. The prototype seal was hydrostatically augmented through forcing a

converging angle and a radial step at 90% of the radial extent. The effect of changing the balance ratio and running the seal at large pre-defined offsets were considered in this campaign.

- The best sealing leakage performance was obtained with the smallest face tested (***B*** = 0.9),
- Increasing the pre-defined offset mainly resulted in larger gap heights and more leakage at lower pressures, but at high pressure differences were insignificant.

Real engine rotors suffer from circumferential waviness – swash, and testing was conducted with elevated levels of swash on the rotor.

- The seal leakage behaviour was always degraded by the addition of swash compared to a flat rotor
- The seal was tolerant to swash under a limited envelope of conditions, a *fight* between pressure loss through additional flow mixing and pressure gain through hydrodynamic effects occurring.
- The seal needs to be designed for the highest order swash expected: shorter wavelength swash resulted in a deterioration in film forces and eventually led to touch-down for a seal which performed well at all other running conditions.
- Designing such that where engine swash is high the offset is high could extend the seal's tolerance to swash.
- Additional leakage caused by swash is less significant at higher pressures
- 3D CFD model captures the behaviour of the full seal assembly very well.

A key conclusion of all the work is that steady-state RANS 3D CFD is capable of providing accurate predictions of performance characteristics for this type of seal, and simple

surrogate models of steady conditions may be used to populate transient models in the future.

Further work

The initial entry loss and other losses driven by inertial effects, usually ignored when modelling conventional face seals, were seen to be consistently present throughout the work presented here, both experimentally and numerically. Hence, a characterisation of this loss is necessary would allow the development of a reduced order model to replace the need to use 3D CFD, at least in the early design stages.

From an experimental point of view, the method applied in measuring the minimum gap height in this thesis relied on the use of contacting dial gauges. Performing measurements using a non-contacting capacitance probe or an eddy current proximity sensor would allow for more accurate gap height measurements along with capturing high-speed data to assess the dynamic stability of the seal which was not possible with the dial gauges used in the work presented in this thesis. Moreover, to ensure that the distortions tested were not due thermal gradients, all tests were run at ambient temperatures. To further comment on the performance of this type of seal, running at higher temperatures would be necessary as further depreciation in sealing performance could result from thermally-induced distortions. Shear heating and associated temperature increase at the interface could have further contributed to the distortions in addition to those resulting from pressure loading. This process would require a set of thermocouples to characterise the temperature field at the sealing interface and the intermediate pressure cavity. Moreover, this could have contributed to the mismatch between experiments and numerical models.

The shock loading dynamics of the seal are still poorly understood, and the addition of a shaker table to the test rig would allow the operability of the seal under rapidly changing body loads to be assessed. Catastrophic failures of carbon face seals have provided a corporate memory of failure of face seals within jet engine OEMs and testing under dynamic conditions will be required before they are implemented in any engine demonstrator programme.

Future publications

"Radial Pressure Distributions in an Air-Riding Face Seal – Part II: CFD vs FSI"

Extension paper to Part I of this work, presented at ISROMAC 2017. This paper would extend the 3D CFD modelling applied to rigid seal presented in *chapter 5* of this thesis to include the effects of structural deformation on the accuracy of the predictions in a Two-Way Fluid-Structure Interaction model. It has been shown that the structural deformation can indeed alter the fluid domain by way of the air-film applying a significant pressure loading on the rotating face, particularly with a converging primary face.

"A Large Axial Movement Air-Riding Face seal: A proof of concept"

This publication would be based on the prototype seal designed, tested and modelled in *chapter 6* of this thesis. The prototype seal succeeded in providing its primary design objectives by running in a non-contacting mode throughout the majority of the test envelope while also running against a heavily distorted rotor. All this was achieved with the seal covering a large range of axial movement and providing a competitive level of leakage. The paper would cover the design rationale behind this concept, its operational characteristics derived from the experimental campaign along with showing that 3D CFD steady state with RANS turbulence modelling can provide accurate performance predictions for this type of seal.

8 References

Agrawal, G., Patel, K. and Munson, J., *Hydrodynamic Foil Face Seal*, US Patent 7,261,300 B2, Aug.28, 2007.

Al-Bender, F., van Brussel, H., "*Symmetric Radial Laminar Channel Flow with Particular Reference to Aerostatic Bearings*", 1992, J. Tribology, 114, pp. 630 -636

Aubry, J., *Non-Contacting Shaft Seals for Gas and Steam Turbines*, D. Phil. Thesis, University of Oxford, 2011.

Aslan, F., Mammadov, V., Dohnal, F., "Brush Seals and Labyrinth Seals in Gas Turbine Applications", *Proceedings of IMechE Part A*, 2012.

Ausman, J. S., E. E. Bisson, and W. J. Anderson, *Gas Lubricated Bearing*, NASA SP-38, pp. 109-138, 1964.

Balducchi Franck, Arghir Mihaï, Gauthier Romain, "Experimental Analysis of the Start-Up Torque of a Mildly Loaded Foil Thrust Bearing," *ASME J. Tribology*, 135, 031702, 2013.

Balducchi Franck, Arghir Mihaï, Gauthier Romain, *"Experimental Analysis of the Dynamic Characteristics of a Foil Thrust Bearing," ASME Paper No., GT2014-25550*, 2014.

Basu, P., P. Datta, A. Johnson, R. Loewerithal, and J. Short, "Hysteresis and Bristle Stiffening Effects of Conventional Brush Seals," *Journal of Propulsion and Power*, no. 4, pp. 569-575, 1994.

Bill, R.C., *Wear of Seal Materials Used in Aircraft Propulsion Systems*, 59, no.1, pp. 165-189, 1980.

Bisson, E.E., and Anderson, W.J., eds., *Advanced Bearing Technology*, NASA SP-38, pp.63-138, 1964.

Brewe, D. R., D. P. Fleming, F. Dimote, and R. C. Hendricks, *Fluid Film Lubrication*, Chapter 8 *of Tribology for Aerospace Applications*, STLE Special Publications, 1997.

Brown, P.F., *Status of Understanding for Seal Materials Tribology in the 80's*, NASA CP−23000-Vol-2, pp. 811−829, 1984.

Bruckner, R. J., *Performance of Simple Gas Foil Thrust Bearings in Air*, NASA/TM 2012-217262, 2012.

Burcham R.E. and Keller R.B., *Liquid Rocket Engine Turbopump Rotating-Shaft Seals*, NASA SP-8121, Jr. 1979.

Caty, F., *Design of Secondary Air System And Thermal Models for Triple Spool Jet Engines*, MSc Thesis, KTH Industrial Engineering and Management, 2012.

Cheng HS, Chow CY, Wilcock DF. "Behavior of Hydrostatic and Hydrodynamic Noncontacting Face Seals", *ASME. J. of Lubrication Tech,* 1968 ;90(2):510-519.

Chupp, R. E., F. Ghrasripoor, N. A. Turnquist, and M., Aksit, M. F. Demiroglu. "Advanced Seals for Industrial Turbine Applications: Dynamic Seal Development," *Journal of Propulsion and Power*, 18, no. 6, 2002.

Chupp, R. E., R. C. Hendricks, S. C. Lattime, and B. M. Steinetz., *Sealing in Turbomachinery,* NASA/TM-20060214341, 2006.

Denny, D. F. "Some measurements of fluid pressures between plane parallel thrust surfaces with special reference to the balancing of radial face seals", *Wear, Lond.* 1961 4 (No. l), 64-83.

Dickman, J., *An Investigation of Gas Foil Thrust Bearing Performance and its Influencing Factors*, Master's thesis, Case Western Reserve University, OH, 2010.

Dykas, B., Bruckner, R., DellaCorte, C., Emonds, B., and Prahl, J., "Design, Fabrication, and Performance of Foil Gas Thrust Bearings for Microturbomachinery Applications," *Journal of Engineering for Gas Turbines and Power,* 131, no. 1, 12301, October, 2008.

Findlay JA., "Cavitation in Mechanical Face Seals", ASME. *J. of Lubrication Tech.* 1968 ;90(2):356-364. doi:10.1115/1.3601569.

Findlay JA., "Inward Pumping in Mechanical Face Seals" *ASME. J. of Lubrication Tech.* 1969 ;91(3):417-425. doi:10.1115/1.3554952.

Friedrich-Karl Benra, Hans Josef Dohmen, Ji Pei, Sebastian Schuster, and Bo Wan, "A Comparison of One-Way and Two-Way Coupling Methods for Numerical Analysis of Fluid-Structure Interactions," *Journal of Applied Mathematics*, vol. 2011, 2011.

Gross, W.A., Matsch, L.A., Castelli, V., Eshel, A., Vohr, J.H. and Wildmann, M., *Fluid Film Lubrication*, Wiley, New York, 1980.

Hendricks, R. C., T. A. Griffin, Kline T., Csavina K. R., Pancholi A., and D. Sood. *Relative Performance Comparison Between Baseline Labyrinth and Dual Brush Compressor Discharge Seals in a T-700 Engine Test*, NASA TM-106360, 1994.

Heshmat, H., Walowit, J., and Pinkus, O., "Analysis of Gas-Lubricated Compliant Thrust Bearings," *ASME J. Lubr. Technol.,* 105, No.4, pp. 638-646, 1983.

Heshmat, H., and W. Shapiro, "Advanced Development of Air-Lubricated Thrust Bearings," *ASLE Lubrication Engineering*, 40, no. 1, pp. 21-26, 1984.

Heshmat, H., "A Feasibility Study on the Use of Foil Bearing in Cryogenic Turbopumps," *Presented at AIAA/SAE/ASME/ASEE 27th Joint Propulsion Conference*, June 24–26, Sacramento, CA, AIAA Paper (1991-2103), 1991.

Heshmat, H., "Advancement In The Performance of Aerodynamic Foil Journal Bearings: High Speed and Load Capability," *ASME Paper No. 93-Trib-32, Accepted for Publication by ASME J. Tribol*., New Orleans, LA, 1993.

Heshmat, H., *High Load Capacity Compliant Foil Hydrodynamic Thrust Bearing*, US Patent 5,833,369, Nov. 10, 1998.

Heshmat Crystal A., Xu David S., Heshmat Hooshang, "Analysis of Gas Lubricated Foil Thrust Bearings Using Coupled Finite Element and Finite Difference Methods," *ASME J. Tribolog,*. 122, 199-204, 1999.

Heshmat, H., *Compliant Foil Seal*, U.S. Patent 6505837 B1 Jan., 2003.

Heshmat, H. and Tomaszewski, M., "Small Gas Turbine Engine Operating With High-Temperature Foil Bearings," *Proceedings of ASME Turbo Expo (GT2006-90971),* 2006.

Heshmat, H., Walton, J., Zhaohui, R., Hunsberger, A., Jahanmir, S., "The Emergence of Compliant Foil Bearing And Seal Technologies In Support of 21st Century Compressors and Turbine Engines," *Proceedings of ASME 2010 International Mechanical Engineering Congress and Exposition, ASME Paper No.(IMECE2010-40598)*, 2010.

Howard, S. A, and L. S. Andres., "A New Analysis Tool Assessment for Rotordynamic Modelling of Gas Foil Bearings*", Proceedings of ASME Turbo Expo (GT2010-22508),* 2010.

Hughes S., *A Study Of The Distribution Of Pressure And Flow In A Dynamic Gas Thrust Bearing*, Oxford University, DPhil Thesis, 1992.

Iny, E. H. 'The design of hydrodynamically lubricated seals with predictable operating characteristics', *Proc. 5th International Conference on Fluid Sealing*, 1971 (British Hydromechanics Research Association, Cranfield , Bedford).

Johnson, Robert L., and Ludwig, Lawrence P., *Shaft Face Seal with Self-Acting Lift Augmentation for Advanced Gas Turbine Engines*, NASA TN D-5170, 1969.

Kesti J., and Olsson S., *Fluid Structure interaction analysis on the aerodynamic performance of underbody panels,* MSc Thesis, Chalmers University of Technology, 2014.

Kim, T. H., and L. San Andres, "Heavily Loaded Gas Foil Bearings: A Model Anchored to Test Data," *ASME Paper No. GT2005-68486*, 2005.

Kim, D., and Lee, D., *"Design of Three-Pad Hybrid Air Foil Bearing and Experimental Investigation on Static Performance at Zero Running Speed," ASME J. Eng. Gas Turbines Power,* 132 (12), p. 122504, 2010.

Lebeck, A. O., *Waviness, distortion and wear in mechanical face seals*. Univ. of New Mexico technical report, ME-64(74)NSF-271–1, 1974.

Lebeck, A. O., "Mechanical Loading - A Primary Source of Waviness in Mechanical Face Seals", *A S L E Transactions*, 20:3, 195-208, 1977.

Lee, D., Kim, D., "Design and Performance Prediction of Hybrid Air Foil Thrust Bearings," *J. Eng. Gas Turbines Power* 133, 042501, 2010.

Lipschitz, A., "A zero-leakage film riding face seal", *American Society of Mechanical Engineers and American Society of Lubrication Engineers*, Joint Lubrication Conference, San Diego, CA; United States; 22-24 Oct., 1984.

Ludwig, L.P. and Johnson, R.L., *Design Study of Shaft Face Seal with Self-Acting Lift Augmentation- Mechanical Components,* IN D-6164, NASA, 1971.

Ludwig, L.P., *Gas Path Sealing in Turbine Engines,* NASA TM–73890, 1978a.

Ludwig L.P., "Self-Acting Shaft Seals", AGARD–CP–237, Paper 16, Aug., 1978; also AGARD–AR–123 and NASA TM-73856, 1978b.

Lynwander, P., *Development of Helicopter Engine Seals,* LYC-73-48, Nov. 1973, Avco Lycoming Div., Stratford, Conn.; also available as CR-134647, NASA, 1973.

Lynwander P., *Development of Self-Acting Seals For Helicopter Engines,* Avco Lycoming Report LYC 74-55, NASA CR-134739, 1974.

Mahler F.H., *Brushing Up On Technology: New Seal Design Cuts Leakage,* P&W Directions, September, 1993.

Menter, F. R., "Zonal Two Equation k-ω Turbulence Models for Aerodynamic Flows", AIAA Paper 93-2906, 1993.

Menter, F.R., "Two-Equation Eddy-Viscosity Turbulence Models for Engineering Applications", AIAA Journal, vol. 32, no 8. pp. 1598-1605, 1994.

Morgan, J.J., *Further Investigations into the Mechanics of Brush Seals,* D. Phil. Thesis, University of Oxford, 2004

Munson, J., and Pecht, G., "Development of Film Riding Face Seals for a Gas Turbine Engine," *Tribology Transactions* 35, no. 1, January, 1992a.

Munson, J. "Development of High Performance Compressor Discharge Seal." In *28th Joint Propulsion Conference and Exhibit*, Joint Propulsion Conferences, AIAA (1992-3714), 1992b.

Munson, J., “Testing of a High Performance Compressor Discharge Seal,” In *29th Joint Propulsion Conference and Exhibit*, Joint Propulsion Conferences, AIAA Paper (1993-1997), 1993.

Munson, J., Grant, D., and Agrawal, G., “Foil Face Seal Development,” In *37th AIAA/ASME/SAE/ASEE Joint Propulsion Conference & Exhibit*, AIAA Paper (2001-3483), 2001.

Munson, J., Grant, D., and Agrawal, G., “Foil Film Riding Face Seal Proof-of-Concept Testing,” In *38th AIAA/ASME/SAE/ASEE Joint Propulsion Conference & Exhibit*, AIAA Paper (2002-3791), 2002.

Munson, J., *Foil Face Seal Development/Testing,* Rolls-Royce Corporation Report No. AX.5204-010, 2009.

Nau, B. S., "Cavitation in Thin Films," The British Hydro- mechanics Research Association, TN832, Nov. 1964.

Nau, B. S., "Centripetal Flow in Face Seals," ASLE Paper No. 68 AM 4B-3, ASLE Annual Meeting, Cleveland, Ohio, May 6, 1968.

Salehi, M., H. Heshmat, J. F. Walton, and S. Cruszen, “The Application of Foil Seals to a Gas Turbine Engine,” AIAA Paper (99-2821), 1999.

Salehi, Mohsen, Erik Swanson, and Hooshang Heshmat. “Thermal Features of Compliant Foil Bearings—Theory and Experiments,” *Journal of Tribology* 123, no. 3, 2000a

Salehi, Mohsen, and Hooshang Heshmat, “High Temperature Performance Evaluation of a Compliant Foil Seal,” AIAA Paper (2000-3376), 2000b.

Salehi, M., and Heshmat, M., “Performance of a Compliant Foil Seal in a Small Gas Turbine Engine Simulator Employing a Hybrid Foil/Ball Bearing Support System,” Tribology Transactions, 44:3, 458-464, (2001).

Salehi, M., and Heshmat, H., “Evaluation of Large Compliant Foil Seals Under Engine Simulated Conditions,” AIAA Paper (2002-3792), 2002.

Salehi, M., H. Heshamt, and J. F. Walton, *Non-contacting Compliant Foil Seal for Gas Turbine Engine,* NASA Secondary Seal Workshop, 2002.

San Andres, L., and Kim. T. H., "Improvements to the Analysis of Gas Foil Bearings: Integration of Top Foil 1D and 2D Structural Models," *ASME Paper No. GT2007-27249,* 2007.

Smith, C. J., *Unique Propulsion Systems - Advanced Subsonic Technologies Evaluation and Analysis,* Task 14 Interim Report Document, Contract NAS3-25953, 1994.

Stanghan-Batch B. and Iny, E. H., 'A hydrodynamic theory of radial face mechanical seals', *J.mech. Eng Sci.,* 1973, 15,17-24.

Stanghan-Batch, B., Iny, E. H., Winney, P. E. 'Face lubrication in mechanical seals', Proc. 9th Tribology Conv. 1971 (Institution of Mechanical Engineers, London).

Steinetz B.M. and Hendricks R.C., *Engine Seals*, Chapter 9 of *Tribology for Aerospace Applications,* STLE Special Publication SP-37, 1997.

Steinetz, B.M., Hendricks, R.C., Munson, J., "Advanced Seal Technology Role in Meeting Next Generation Turbine Engine Goals," *Propulsion and Power Systems First Meeting on Design Principles and Methods for Aircraft Gas Turbine Engines, sponsored by the NATO Research and Technology Agency, Toulouse, France, May 11–15, 1998,* AVT-PPS Paper no. 11, NASA/TM-1998-206961, E-11109, May, 1998.

Stocker, B. M., D. M Cox, and G. F. Holle, *Aerodynamic Performance of Conventional and Advanced Design Labyrinth Seals with Solid, Smooth, Abradable and Honeycomb Lands - Gas Turbine Engines,* NASA CR-135307, 1977.

Vasco, V. M. B. I., *Development of a Cantilevered Floating Ring Seal,* D. Phil. Thesis, University of Oxford, 2009.

Walton, J. Heshmat, H. and Tomaszewski, M., "Testing of A Small Turbocharger/Turbojet Sized Simulator Rotor Supported on Foil Bearings," *Proceedings of ASME Turbo Expo (GT2004-53647),* 2004.

Whiteman K,.J. 'Pressure generation in radial face seals', *Br. Hydromech. Res. Ass. tech. Note T N 578,* 1958.

Young L.A. and Lebeck A.O. Experimental Evaluation of a Mixed Friction Hydrostatic Mechanical Face Seal Model Considering Radial Taper, Thermal Taper, and Wear. ASME. *J. of Lubrication Tech.* 1982;104(4):439-447. doi:10.1115/1.3253244.

Zheng, X., "Parametric Study of Hydrodynamic Seal Using 2D Design Code and Comparing with a 3D Model," *Proceedings of ASME Turbo Expo (GT2005-68915),* 2005.

Appendix A

Derivation of the Two-dimensional Compressible Reynolds Equation

To derive the Reynolds equation for thin film flows, consider the elemental volume of fluid shown in Figure A.1,

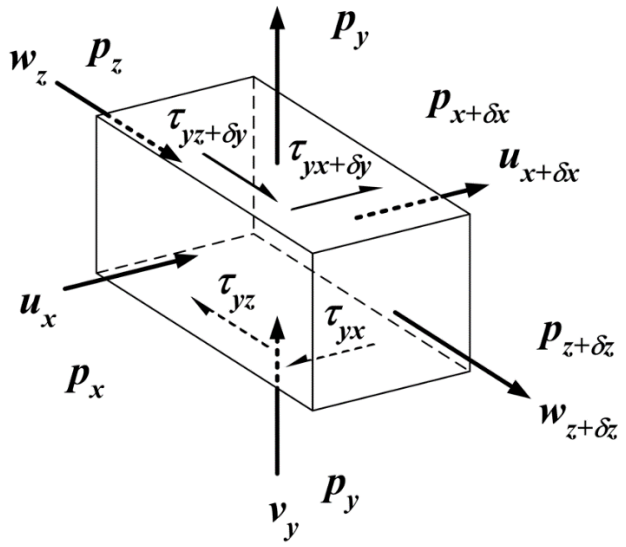

Figure A.1: Elemental volume of fluid (Franceschini, 2005).

The continuity equation from mass conservation yields,

$$\frac{\partial \rho}{\partial t} + \frac{\partial}{\partial x}(\rho u) + \frac{\partial}{\partial y}(\rho v) + \frac{\partial}{\partial z}(\rho w) = 0 \qquad \textbf{Eq. A.1}$$

And assuming steady-state conditions the time-derivative can be excluded to give,

$$\frac{\partial}{\partial x}(\rho u) + \frac{\partial}{\partial y}(\rho v) + \frac{\partial}{\partial z}(\rho w) = 0 \qquad \textbf{Eq. A.2}$$

The momentum equation in the *x*-direction for steady flow conditions and excluding body forces can be expressed as follows,

$$\frac{1}{\rho}\left(\frac{\partial \tau_{yx}}{\partial y} - \frac{\partial p}{\partial x}\right) = u\frac{\partial u}{\partial x} + v\frac{\partial u}{\partial y} + w\frac{\partial u}{\partial z} \qquad \textbf{Eq. A.3}$$

Treating the fluid as Newtonian, the following assumption can be made,

$$\tau_{yx} = \mu\frac{\partial u}{\partial y} \qquad \text{leading to} \qquad \frac{\partial \tau_{yx}}{\partial y} = \mu\frac{\partial^2 u}{\partial y^2} \qquad \textbf{Eq. A.4}$$

Applying the above yields the following momentum equation in the *x*-direction,

$$u\frac{\partial u}{\partial x} + v\frac{\partial u}{\partial y} + w\frac{\partial u}{\partial z} = -\frac{1}{\rho}\frac{\partial p}{\partial x} + \frac{\mu}{\rho}\frac{\partial^2 u}{\partial y^2} \qquad \textbf{Eq. A.5}$$

Similarly for momentum in the *z*-direction,

$$u\frac{\partial w}{\partial x} + v\frac{\partial w}{\partial y} + w\frac{\partial w}{\partial z} = -\frac{1}{\rho}\frac{\partial p}{\partial z} + \frac{\mu}{\rho}\frac{\partial^2 w}{\partial y^2} \qquad \textbf{Eq. A.6}$$

As the Reynolds equation deals with thin-films and the flow is assumed to be laminar, the convective acceleration terms are negligible compared to the pressure and viscous terms. Hence, equations A.5 and A.6 reduce to,

$$\frac{\partial p}{\partial x} = \mu\frac{\partial^2 u}{\partial y^2} \qquad \text{and} \qquad \frac{\partial p}{\partial z} = \mu\frac{\partial^2 w}{\partial y^2} \qquad \textbf{Eq.A.7, A.8}$$

Now integrating the above equations with respect to *y* and assuming that pressure does not vary across the film thickness *h* (i.e. $\frac{\partial p}{\partial x}$ and $\frac{\partial p}{\partial z}$ do not vary with *y*), the following is obtained,

$$\mu\, u = \frac{\partial p}{\partial x}\frac{y^2}{2} + Ay + B \qquad \text{and} \qquad \mu\, w = \frac{\partial p}{\partial z}\frac{y^2}{2} + Cy + D \qquad \textbf{Eq. A.9, A.10}$$

Applying the boundary conditions $u = U$, $w = W$ at $y = 0$ and $u = 0$, $w = 0$ at $y = h$ where U is the velocity of the flow in the axial direction and W is the velocity in the circumferential direction (rotor velocity), the following equations can be obtained,

$$u = \frac{1}{2\,\mu}\frac{\partial p}{\partial x}\left(y^2 - h\,y\right) + U\left(1 - \frac{y}{h}\right) \qquad \textbf{Eq. A.11}$$

$$w = \frac{1}{2\,\mu}\frac{\partial p}{\partial z}\left(y^2 - h\,y\right) + W\left(1 - \frac{y}{h}\right) \qquad \textbf{Eq. A.12}$$

The steady state continuity equation (Eq. A.2) can be integrated with respect to y to give,

$$[\rho v]_0^{h(x,z)} = -\int_0^{h(x,z)} \frac{\partial}{\partial x}\left(\rho\,u\right)\,\mathrm{d}y - \int_0^{h(x,z)} \frac{\partial}{\partial z}\left(\rho\,w\right)\,\mathrm{d}y \qquad \textbf{Eq. A.13}$$

As h only varies with v, the value of v at the boundary will be zero such that,

$$0 = -\int_0^{h(x,z)} \frac{\partial}{\partial x}\left(\rho\,u\right)\,\mathrm{d}y - \int_0^{h(x,z)} \frac{\partial}{\partial z}\left(\rho\,w\right)\,\mathrm{d}y \qquad \textbf{Eq. A.14}$$

Substituting for the expressions of u and w derived in equations A.11 and A.12 results in,

$$\begin{aligned} 0 \;=\; & -\int_0^{h(x,z)} \frac{\partial}{\partial x}\left(\frac{\rho}{2\,\mu}\frac{\partial p}{\partial x}\left(y^2 - h\,y\right) + \rho\,U\left(1 - \frac{y}{h}\right)\right)\,\mathrm{d}y \\ & -\int_0^{h(x,z)} \frac{\partial}{\partial z}\left(\frac{\rho}{2\,\mu}\frac{\partial p}{\partial z}\left(y^2 - h\,y\right) + \rho\,W\left(1 - \frac{y}{h}\right)\right)\,\mathrm{d}y \end{aligned} \qquad \textbf{Eq. A.15}$$

Applying Leibniz's Theorem for differentiation under an integral sign (Abramowitz and Stegun, 1965) which states that,

$$\frac{\mathrm{d}}{\mathrm{d}c}\int_{a(c)}^{b(c)} f(x,c)\,\mathrm{d}x = \int_{a(c)}^{b(c)} \frac{\partial}{\partial c} f(x,c)\,\mathrm{d}x + f(b,c)\frac{\mathrm{d}b}{\mathrm{d}c} - f(a,c)\frac{\mathrm{d}a}{\mathrm{d}c} \qquad \textbf{Eq. A.16}$$

Results in,

$$\begin{aligned}
&\frac{\partial}{\partial x}\int_0^{h(x,z)}\left(\frac{\rho}{2\,\mu}\frac{\partial p}{\partial x}\left(y^2-h\,y\right)+\rho\,U\left(1-\frac{y}{h}\right)\right)\mathrm{d}y\\
&=\int_0^{h(x,z)}\frac{\partial}{\partial x}\left(\frac{\rho}{2\,\mu}\frac{\partial p}{\partial x}\left(y^2-h\,y\right)+\rho\,U\left(1-\frac{y}{h}\right)\right)\mathrm{d}y\\
&\quad+\left(\frac{\rho}{2\,\mu}\frac{\partial p}{\partial x}\left(h^2-h\,h\right)+\rho\,U\left(1-\frac{h}{h}\right)\right)\frac{\mathrm{d}h}{\mathrm{d}x}\\
&\quad-\left(\frac{\rho}{2\,\mu}\frac{\partial p}{\partial x}\left(0^2-h\,0\right)+\rho\,U\left(1-\frac{0}{h}\right)\right)\frac{\mathrm{d}0}{\mathrm{d}x}
\end{aligned}$$ **Eq. A.17**

Now assuming that ρ and μ are independent of *y* and assuming that *U* and *W* are constant the integral in equation A.17 can be re-arranged and written as,

$$\frac{\partial}{\partial x}\left(\frac{\rho\,h^3}{\mu}\frac{\partial p}{\partial x}\right)+\frac{\partial}{\partial z}\left(\frac{\rho\,h^3}{\mu}\frac{\partial p}{\partial z}\right)=6\,U\frac{\partial}{\partial x}\left(\rho\,h\right)+6\,W\frac{\partial}{\partial z}\left(\rho\,h\right) \qquad \textbf{Eq. A.18}$$

The terms on the left hand side of equation A.18 are the diffusion terms (*Poiseuille*) and describe the net flow rates due the pressure gradients in the *x* and *z* directions, while the right hand side represents the convective (*Couette*) flow terms which describe the net entrained flow rate due to the shear caused by rotating the disc in *x* and *z* directions without the presence of a pressure gradient (Vasco, 2009).

Treating the fluid as an ideal gas and applying the equation of state $p = \rho RT$, equation A.18 can be expressed as,

$$\frac{\partial}{\partial x}\left(\frac{ph^3}{\mu T}\frac{\partial p}{\partial x}\right)+\frac{\partial}{\partial z}\left(\frac{ph^3}{\mu T}\frac{\partial p}{\partial z}\right)=6U\frac{\partial}{\partial x}\left(\frac{ph}{T}\right)+6W\frac{\partial}{\partial z}\left(\frac{ph}{T}\right) \qquad \textbf{Eq. A.19}$$

Hughes (1992) performed experiments where pad surface temperatures of a gas thrust bearing were measured which showed the residence time of the flow to be of too low a magnitude to cause significant changes in temperature and the flow can be assumed to be locally isothermal. For an isothermal domain equation A.19 can be simplified and re-written as,

$$\frac{\partial}{\partial x}\left(\frac{ph^3}{\mu}\frac{\partial p}{\partial x}\right)+\frac{\partial}{\partial z}\left(\frac{ph^3}{\mu}\frac{\partial p}{\partial z}\right)=6U\frac{\partial}{\partial x}(ph)+6W\frac{\partial}{\partial z}(ph) \quad \textbf{Eq. A.20}$$

In case of a face seal, while W is the rotor surface speed in the circumferential direction there is negligible motion in the axial x direction and U can be assumed to be zero resulting in the 2D compressible Reynolds equation,

$$\frac{\partial}{\partial x}\left(\frac{ph^3}{\mu}\frac{\partial p}{\partial x}\right)+\frac{\partial}{\partial z}\left(\frac{ph^3}{\mu}\frac{\partial p}{\partial z}\right)=6W\frac{\partial}{\partial z}(ph) \quad \textbf{Eq. A.21}$$

Pandian (1984) and Hughes (1992) postulated that for a gas based lubricant where the fluid film is essentially isothermal, viscosity be assumed to be constant. Neglecting viscous heating (Szeri, 1998) reduces equation A.21 to,

$$\frac{\partial}{\partial x}\left(ph^3\frac{\partial p}{\partial x}\right)+\frac{\partial}{\partial z}\left(ph^3\frac{\partial p}{\partial z}\right)=6\mu W\frac{\partial}{\partial z}(ph) \quad \textbf{Eq. A.22}$$

In the case of 2D incompressible flow, Reynolds equation (i.e. constant ρ) can be expressed as,

$$\frac{\partial}{\partial x}\left(h^3\frac{\partial p}{\partial x}\right)+\frac{\partial}{\partial z}\left(h^3\frac{\partial p}{\partial z}\right)=6\mu U\frac{\partial}{\partial x}(h) \quad \textbf{Eq. A.23}$$

While more straightforward in Cartesian coordinates, the code currently considered is based on a 2D compressible flow Reynolds equation in polar coordinates: *i.e.*

$$\frac{\partial}{\partial r}\left(\frac{rph^3}{\mu}\frac{\partial p}{\partial r}\right)+\frac{1}{r}\frac{\partial}{\partial \theta}\left(\frac{ph^3}{\mu}\frac{\partial p}{\partial \theta}\right)=6r\omega\frac{\partial(ph)}{\partial \theta} \quad \textbf{Eq. A.24}$$

Appendix B

Chapters 3 and 5: 3D CFD model Mesh Independence

A mesh independent solution in terms of leakage mass flow rate was achieved for the 3D CFD developed in *chapter 3* and also used in *chapter 5* with 20 nodes across the axial height of the primary gap. Figure B.1 shows a grid independence study for the 200 μm gap case running at an inlet pressure of 3.45 barg. Note that, other mesh zones were also refined but the focus of the study was on the number of nodes across the axial extent of minimum gap height.

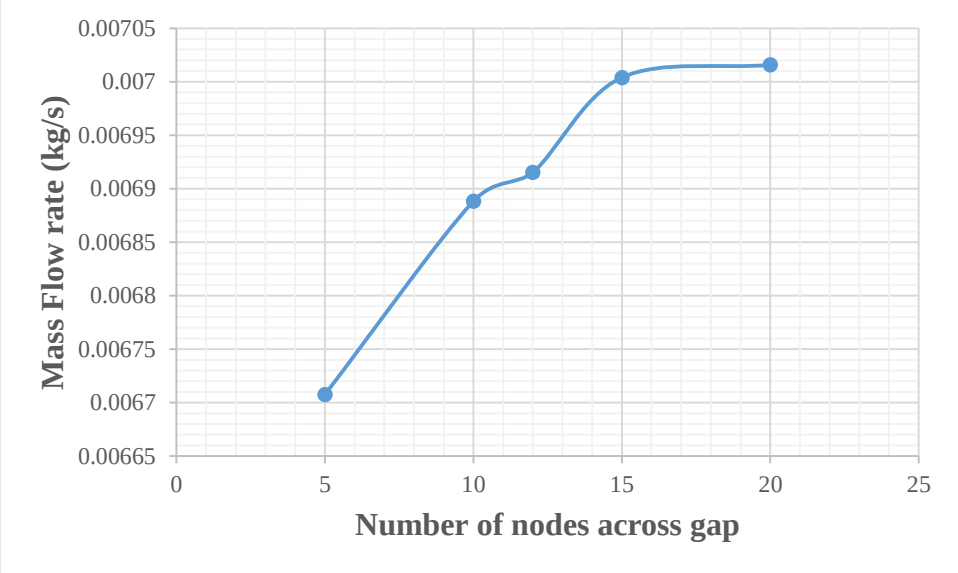

Figure B.1: <u>CH. 3 & 5</u> Mass flow rate grid independence, h_{min} = 200 μm, P_{in} = 3.45 barg

Chapter 6: 3D CFD model Mesh Independence

Similarly, the 3D CFD model developed in *chapter 6* to model the prototype seal has shown the solution to be grid independent in terms of leakage mass flow rate with 32 nodes across the axial extent of the minimum gap height. Figure B.2 shows the mesh independence study using the smallest of the front faces (Φ_3) running at a minimum gap height of 210 μm and an inlet pressure of 2.76 barg.

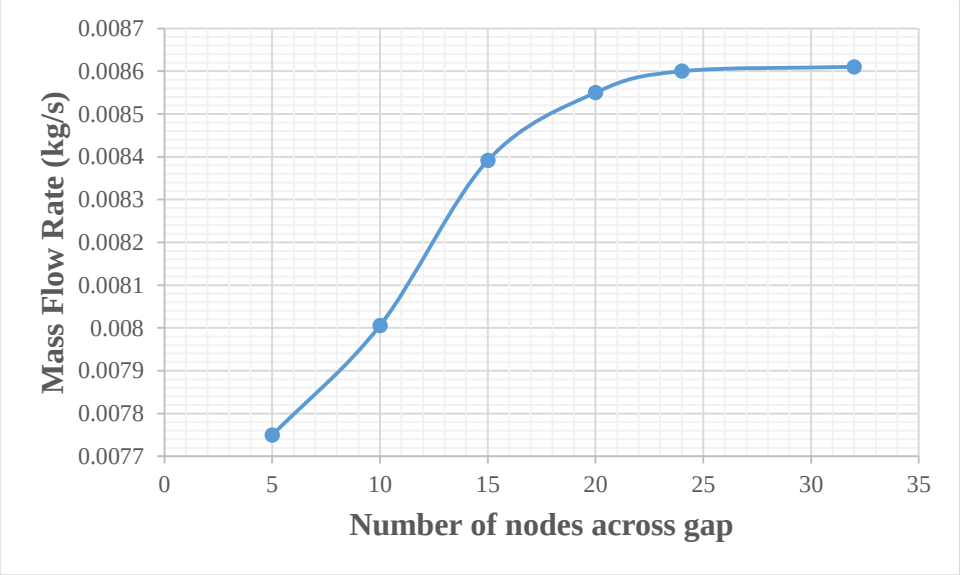

Figure B.2: CH. 6 Mass flow rate grid independence, Φ_3 ,h_{min} = 210 μm, P_{in} = 2.76 barg.